Experimental and Modeling Study of a Cold-Flow Fluid Catalytic Cracking Unit Stripper

A Thesis Submitted to the College of
Graduate Studies and Research
in Partial Fulfillment of the Requirements
for the Degree of Doctor of Philosophy
in the Department of Chemical Engineering
University of Saskatchewan
Saskatoon

By
Jason Samuel Wiens

Copyright Jason S. Wiens, June, 2010. All Rights Reserved

Permission to Use

In presenting this thesis in partial fulfillment of the requirements for a postgraduate degree from the University of Saskatchewan, I agree that the libraries of this university may make it freely available for inspection. I further agree that permission for copying of this thesis in any manner, in whole or in part, for scholarly purposes may be granted by the professor who supervised my thesis work, or in their absence, by the head of the Department of Chemical Engineering, or the dean of the College of Engineering. It is understood that any copying, publication, or use of this thesis or parts thereof for financial gain shall not be allowed without my written permission. It is also understood that due recognition shall be given to me and to the University of Saskatchewan in any scholarly use which may be made of any materials in my thesis.

Requests for permission to copy or to make other use of material in this thesis in whole or in part should be addressed to:

Head of the Department of Chemical Engineering
University of Saskatchewan
Saskatoon, Saskatchewan
S7N 5A9

“He who can no longer pause to wonder and stand rapt in awe is as good as dead; his eyes are closed”

-Albert Einstein

Abstract

Many particulate processes are preferably implemented in circulating fluidized beds (CFB) over traditional low-velocity fluidization to take advantage of the many benefits of circulating systems. Fluid catalytic cracking (FCC) is one of the most successfully applied processes in CFB technology, with more than 350 FCC units in operation worldwide. Despite its extensive use, an understanding of the complex behaviour of these units is incomplete.

A theoretical and experimental evaluation of the fluidization behaviour was conducted in the CFB riser, standpipe, and stripper. Initially, an extension of the existing CFB in the Fluidization Laboratory of Saskatchewan was designed. The experimental program conducted in this study included an examination of the solids flow behaviour in the riser, interstitial gas velocity in the downcomer, and stripping efficiency measurements. The hydrodynamic behaviour of the stripper was modeled using Multiphase Flow with Interphase eXchanges (MFIX) CFD code.

The solids flow behaviour in the bottom zone of a high-density riser was investigated by measuring the local upwards and downwards solids flux. Solids circulation rates between 125 and 243 kg/(m^2·s) were evaluated at a constant riser superficial gas velocity of 5.3 m/s. The effect of the riser superficial gas velocity of the local upflow at the riser centerline was also conducted at a solids circulation rate of 187 kg/(m^2·s). The results show that there is little variation in the local net solids flux at radial locations between $0.00 \leq r/R \leq 0.87$. The results indicate that a sharp regime change from a typical parabolic solids flux profile to this more radially uniform solids flux profile occurs at a gas velocity between 4.8 and 4.9 m/s.

To quantify stripping efficiency, the underflow of an injected tracer into the standpipe must be known. Quantification of the underflow into the standpipe requires knowledge of two main variables: the interstitial gas velocity and the tracer gas concentration profiles in the standpipe. Stripping efficiency was determined for stripper solids circulation rates of 44, 60, and 74 kg/(m^2·s) and gas velocities of 0.1, 0.2, and 0.3 m/s. For most conditions studied, the interstitial gas velocity profile was found to be flat for both fluidized and packed bed flow. The stripping efficiency was found to be sensitive to the operating conditions. The highest efficiency is attained at low solids circulation rates and high stripping gas velocities.

In the numeric study, stripper hydrodynamics were examined for similar operating conditions as those used in the experimental program. Due to an improved radial distribution of gas and decreasing bubble rise velocity, mass transfer is deemed most intense as bubbles crest above the baffles into the interspace between disc and donut baffles. Stripping efficiency is thought to improve with increasing gas velocity due to an increased bubbling frequency. Stripping efficiency is thought to decrease with increasing solids circulation rates due to a lower emulsion-cloud gas interchange coefficient and a decreased residence time of the emulsion in the stripper.

Acknowledgements

I would like to offer my most sincere gratitude to my supervisor for the past four years, Dr. Todd Pugsley. The guidance and support that was offered to me throughout the project was invaluable. I am especially thankful for the independence you entrusted in me in the project. Although the work was frustrating at times, the struggles truly enhanced the experience and the satisfaction of completing this dissertation.

I am appreciative for the work of all the faculty and staff in the college of engineering who have supported me over the years. Thanks to my graduate committee: Dr. Aaron Phoenix, Dr. Jim Bugg, Dr. Catherine Niu, and Dr. Ajay Dalai for the help and suggestions that undoubtedly improved the quality of the work. I am also appreciative of all faculty members in the Department of Chemical Engineering for their work during my time both as a graduate and undergraduate student at the University of Saskatchewan. Many thanks to the staff in the Department of Chemical Engineering and in the Engineering Machine Shops: Ted Wallentiny, Jean Horosko, Kelly Bader, Dragan Cekic, Dale Claude, Kevin Carter, and Henry Berg.

Over the years I have had the privilege of meeting and working with great colleagues and friends. Whether it was lending an ear to rant about everything that is going wrong with my project or enjoying a quick game of pick-up hockey in the basement of the pilot plant, my life was truly enriched by the friends I made. Thanks to Reza Malek, Dillon Petrucha (Herbie), Regan Gerspacher, Mariane Trepanier, Kevin Heppner, Erica Emery, Gareth Chaplin, and last but certainly not least, Mike Wormsbecker.

I am thankful for the support from all family and friends. I would like to thank my wife, Lindsay, for all the love and support through the past years and into the future as we build our new life together. A huge debt of gratitude to my parents, Murray and Laura, for their support over the many, many years I have spent at university (contrary to your predictions, I made it out before I needed a walker!). To all family, old and new, my warmest thanks.

Table of Contents

List of Tables

List of Figures

Nomenclature

A_b	bubble area (mm^2)
A_o	orifice plate open area (m^2)
A_{strip}	area of stripping vessel (m^2)
B_c	width of the rectangular inlet ducting of a cyclone (m)
C_A	concentration of species 'A' (mol/m^3)
$C_{A.S}$	concentration of active site complexes (mol/kg)
C_D	coefficient of discharge (-)
C_{Dor}	coefficient of discharge for the orifice (-)
C_{He}	concentration of helium (kg/m^2)
$C_{He,c}$	concentration of helium in bubble cloud (kg/m^2)
$C_{He,e}$	concentration of helium in emulsion phase (kg/m^2)
C_{ref}	concentration of reference gas used in TCD (v/v)
C_S	concentration of vacant catalyst sites (mol/kg)
D	pipe diameter (m)
d_b	bubble diameter (m)
D_c	inside diameter of the cyclone barrel (m)
d_c	bubble chord length (m)
D_e	inside diameter of the vortex finder in the cyclone (m)
$D_{fingers}$	inside diameter of the fingers extending from the header (m)
D_g	gas diffusivity (m^2/s)
D_{header}	inside diameter of sparger ring header (m)
D_{or}	orifice diameter (m)
d_p	particle diameter (m)
d_{pth}	particle diameter removed with 50% efficiency (m)
D_r	riser diameter (m)
e	gas expansion coefficient (-)
EBD	equivalent bubble diameter (mm)
F	fraction of particles with a diameter smaller than 45 μm (-)
F_{gs}	gas-solids drag force ($kg/(m^3 \cdot s)$)
FS	Fraction of full-scale defection on the TCD analyzer (-)
g	acceleration due to gravity (m^2/s)
G_s	solids circulation rate ($kg/(m^2 \cdot s)$)
$G_{s,down}$	downward solids flux ($kg/(m^2 \cdot s)$)
H	horizontal length of the L-valve (m)
H_c	height of the cyclone rectangular inlet duct (m)
H_{min}	minimum horizontal length of the L-valve (m)
H_r	riser height (m)
h_{strip}	height of baffled section in stripper (m)
J_c	diameter of the underflow duct in a cyclone (m)
K_{bc}	bubble-cloud gas interchange coefficient (s^{-1})
K_{be}	bubble-emulsion gas interchange coefficient (s^{-1})
K_{ce}	cloud-emulsion gas interchange coefficient (s^{-1})

k_D	desorption rate constant (s^{-1})
K_{DA}	equilibrium desorption constant (Pa^{-1})
L	length (m)
L_c	vertical length of the cyclone barrel (m)
L_{or}	orifice pitch (m)
M_{He}	molar mass of helium (kg/kgmol)
N	number of orifices (-)
N_d	orifice density (orifices/m^2 bed)
$N_{fingers}$	number of fingers extending from sparger grid header (-)
N_s	number of turns made by gas stream in a cyclone (-)
P	pressure (Pa)
p_A	partial pressure of 'A' at active site (Pa)
P_b	bubble perimeter (mm)
P_d	pressure drop of fluidized bed above air delivery system (Pa)
$P_{He\ inj}$	pressure in the stripper at point of helium injection (Pa)
P_{stand}	pressure in the standpipe at point of gas sampling (Pa)
P_1	air gauge pressure upstream of the orifice plate (Pa)
Q	gas volumetric flowrate (m^3/s)
$Q_{He,inj}$	volumetric flowrate of He tracer injected above the standpipe (m^3/s)
R	radius (m)
r	radial position (m)
Re_p	particle Reynolds number (-)
R_{gas}	universal gas constant (J/(kg·mol))
RR	reflux ratio (-)
r_D	rate of desorption (mol/(kg·s))
S_s	solids phase stress tensor (Pa)
S_c	length the vortex finder extends below the inlet duct in a cyclone (m)
T	temperature (K)
t	time (s)
t_{det}	time of detection of the helium pulse (s)
$t_{det,\ stat}$	statistically determined time of detection of the helium pulse (s)
t_p	pierced bubble time (s)
t_{res}	average residence time of solids in the stripper section (s)
U	gas velocity (m/s)
U_b	bubble velocity (m/s)
U_{br}	bubble rise velocity relative to emulsion phase (m/s)
$U_{ergun,sup}$	superficial slip gas velocity calculate using the Ergun equation (m/s)
U_g	interstitial gas velocity (m/s)
$U_{g,sup}$	superficial downward gas velocity in the standpipe (m/s)
U_{He}	superficial downward helium gas velocity in the standpipe (m/s)
U_{mb}	minimum bubbling fluidization velocity (m/s)
$U_{mb,I}$	interstitial minimum bubbling fluidization velocity (m/s)
U_{mf}	minimum fluidization superficial gas velocity (m/ s)
U_{or}	orifice gas velocity (m/s)
U_r	slip velocity between solid particles and interstitial gas (m/s)
$U_{rel,int}$	normalized interstitial gas velocity in the standpipe (-)

U_{riser}	riser superficial gas velocity (m/s)
U_{strip}	stripper superficial gas velocity (m/s)
V_b	differential voltage between the upper and lower leg (V)
$V_{b,\ post\text{-}inj}$	post-injection of helium pulse bridge voltage data (V)
$V_{b,\ pre\text{-}inj}$	pre-injection of helium pulse bridge voltage data (V)
V_t	voltage drop across the thermistor element (V)
Z	axial position (m)
Z_c	vertical length of the conical section of a cyclone (m)

Greek

α	stirring effect (-)
β	ratio of orifice diameter to piping diameter (-)
ε	voidage (-)
ε_{mf}	minimum fluidization voidage (-)
ε_{pb}	packed bed voidage (-)
ε_s	solids fraction (-)
Φ	bubble sphericity (-)
η_{strip}	stripping efficiency (-)
κ	isentropic exponent (-)
μ	gas viscosity (Pa·s)
Θ	fractional drag scaling factor (-)
θ_R	FCC catalyst angle of repose (degrees)
ρ_g	gas density (kg/m^3)
ρ_p	particle density (kg/m^3)
σ	standard deviation of bridge voltage (V)
τ_g	fluid phase deviatoric stress tensor (Pa)
υ_g	gas velocity (m/s)
υ_s	solids velocity (m/s)
ψ	particle porosity (-)

Chapter 1 - Introduction

1.1 Fluidization Regimes

When a fluid is passed upwards at a low velocity through a packed bed of particles, the fluid percolates through the void spaces between the stationary particles. By increasing the gas velocity, the drag force imparted by the fluid on the particles becomes greater. A point is reached where the drag force counterbalances the weight of the particles; the particles are lifted and separation of the particles occurs. At this point, the bed of particles has attained minimum fluidization.

Beyond the minimum fluidization velocity of gas-solids systems, two-phase theory (Toomey & Johnstone, 1952) dictates that any gas in excess of the minimum fluidization velocity will form gas bubbles; and the bed becomes a heterogeneous suspension of gas and solids. At elevated gas velocities the heterogeneous nature of the gas-solids flow begins to deteriorate, and the bed behaviour incrementally becomes dominated by a single-phase suspension of gas and solids. This incremental change in the behaviour of the bed, from heterogeneous to homogeneous gas-solids flow, is the basis for classification of fluidization regimes.

It is well accepted that there exists five regimes of fluidization (Grace, 1986). In order of low to high gas velocity, they are: bubbling, slugging, turbulent, fast fluidization, and pneumatic conveying (Figure 1-1). The transition between these regimes, and at times their very existence, is dictated by the physical properties of the solids in the bed. These properties include the particle density and diameter.

Geldart (1973) grouped the generalized fluidization behaviour of particles into four categories based on the bed density and particle diameter, known as the Geldart classification. The fluidization behaviour for these four particle groups is summarized below as described by Geldart (1973):

Group C: ‘Cohesive’ - fine, cohesive particles that are difficult to fluidize. Particles tend to channel or lift the bed as a plug. Interparticle forces are greater than that which the fluid can exert on the particles. Fluidization can generally be improved by the use of mechanical stirrers or vibrators. Typically, the diameter of a Geldart C particle is less than 20 μm.

Group A: ‘Aeratable’ – At the minimum fluidization velocity these particles expand homogeneously. Bubbling commences at an elevated gas velocity, known as the minimum bubbling fluidization velocity. Bubbles in these beds tend to split and re-coalesce very frequently. In freely bubbling beds the bubble velocity of very small bubbles (< 4 cm) tends to be approximately 30 – 40 cm/s regardless of the bubble size. The mean bubble size may be reduced in two ways: by having a wide

particle size distribution and/ or by having a small mean particle size. Bubbles can grow until a maximum stable bubble size is reached. For FCC catalyst, a typical Geldart A particle, the maximum stable bubble diameter is approximately 3 cm (Kunni & Levenspiel, 1991). Typically, the diameter of a Geldart A particle is between 30 and 100 μm.

Geldart B: Bubbling commences at or slightly above the minimum fluidization velocity. Coalescence is the predominant bubble-bubble interaction. Bubbles have no known maximum bubble size. Typically, the diameter of a Geldart B particle is between 100 and 800 μm.

Geldart D: Bubble formation does not commence until approximately 5 cm above the distributor. Bubble sizes may be the same as those in Geldart B class particles for the same excess gas velocity (gas velocity in excess of that which passes through the emulsion phase). These particles can be made to spout. Typically, the diameter of a Geldart D particle is greater than 1 mm.

The gas pressure and temperature can affect both the emulsion phase voidage in fluidized beds. It has been found that the emulsion phase voidage can undergo a small increase between 1 and 4 % with a rise in the operating pressure (Kunni & Levenspiel, 1991). However, the effect of temperature on the voidage can be more significant. An increase in the voidage up to 8% has been found at elevated temperatures up to 500°C for beds of fine particles, however for large particle systems the bed voidage appears unaffected by the gas temperature (Kunni & Levenspiel, 1991). This is significant because an elevated bed voidage increases the interstitial gas flow in a fluidized system. In most fluidized bed operations an elevated voidage would have a desirable effect on the bed performance, since there is more intimate contacting between gas and solids in the emulsion phase.

The most basic explanation of the behaviour of a bubbling fluidized bed was offered by Toomey & Johnstone (1952). Their theory considered the existence of two phases: an emulsion phase and a bubble phase. The emulsion phase consisted of solids suspended by interstitial gas, maintained at a voidage similar to that of minimum fluidization. Any gas in excess of minimum fluidization passed through the bed in the bubble phase, which was considered devoid of solids. This description has since been amended to include a bubble phase that is not completely devoid of solids and an emulsion phase with a voidage greater than minimum fluidization (Halow & Nicoletti, 1992, Kunni & Levenspiel, 1991). In the bubbling fluidization regime, bubble coalescence, involving the merging of an elongated trailing bubble into the wake of a leading bubble, is the dominant bubble interaction until the maximum stable bubble size is reached (Lim *et al.,* 1995).

A popular model for a bubble contained in a freely bubbling fluidized bed is that of the Murray bubble (Murray, 1965). Murray (1965) proposed a circular bubble with an indented base, giving the bubble a kidney-shaped appearance (Figure 1-2). The region underneath the indented base of the bubble is known as the bubble wake. A particle-laden region, known as the bubble cloud, often surrounds the gas bubble (Davidson & Harrison, 1963). The thickness of the bubble cloud is dependant on the rise velocity of the bubble through the emulsion. If the bubble rises

more slowly than the emulsion gas, the cloud is absent and the interstitial gas uses the bubble as a short-cut through the bed. The bubble cloud is present when the bubble rises through the bed more rapidly than the interstitial gas. The thickness of the cloud is greatest at low bubble rise velocities. The thickness of the bubble cloud is assumed negligible when the ratio of bubble rise velocity to interstitial gas velocity is in excess of approximately 5 (Kunni & Levespiel, 1991, Rowe *et al.,* 1964).

The solids circulation pattern in bubbling fluidized beds is a consequence of the bubble flow phenomenon. In beds of aspect ratio (bed height/ bed diameter) approaching unity, bubbles have a tendency to rise through the centre of the bed. Particles are vertically transported through the centre of the bed by the bubble wake. Particles in close proximity to the passing bubble freely enter the cloud, but can leave at random positions. This results in lateral mixing of solids. Downflow of particles is typically observed in the annular region adjacent to the vessel wall. However, there is evidence of non-centralized bubble flow and the potential for downflow of particles in the middle of the bed (Werther & Molerus, 1973, Bayle *et al.,* 2001, Abed, 1985).

Bubbles formed at the distributor in tall, narrow fluidized beds can grow to a sufficient size to occupy the bed diameter. These large bubbles are called slugs. The slugging fluidization regime does not occur in all particulate systems. For example, the maximum stable bubble size characteristic of Geldart A particles often prevents slug formation. In beds where slugging does occur, three types of slugging fluidization have been identified (Kunni & Levenspiel, 1991): axial slugs, wall slugs, and flat slugs (Figure 1-3). Axial slugs form in beds of particles that have good fluidity. The slugs rise through the centre of the bed, and particles fall downwards at the wall at the same rise rate as that of the slug. At elevated gas velocities and in beds containing particles that are angular or in a bed containing a rough vessel wall, wall slugs are formed. Wall slugs have a tendency to adhere to and slide up the vessel wall. The third type of slugs, known as flat slugs, are most commonly observed in beds of Geldart D particles. Flat slugs segregate the bed into alternating sections of gas and solids along the axis.

Turbulent fluidization represents the transition regime between heterogeneous and homogeneous fluidization behaviour. In this regime, there is no clearly defined continuous phase. Instead, there is either an intermittent continuum or interspersing gas voids and dense regions composing the bed (Bi *et al.,* 2000). Gas voids are in a continuous state of coalescence and splitting; and are of irregular shape (Rhodes, 1996). When turbulent fluidization is preceded by bubbling fluidization (rather than slugging), as is typically the case with Geldart A particles, the transition is denoted by the change from laminar to open turbulent bubble wakes (Bi *et al.,* 2000). Otherwise, a gradual transition from the slugging regime occurs involving intermittent slug-like structures interspersed with periods of fast-fluidization-like behaviour (Bi *et al.,* 2000). An increased rate of particle entrainment occurs in the turbulent regime due to a diffuse bed surface (Wiens & Pugsley, 2006).

Advantages of operating in the turbulent regime are many. A brief voidage lifetime, resulting from the splitting of bubbles, has been shown to increase gas-solids contacting (Bi *et al.,* 2000). This reduces the resistance to inter-phase mass transfer, often a limiting characteristic of bubbling and slugging beds. Improved solids mixing over that of the bubbling and slugging regimes results in increased heat transfer, improved temperature uniformity and decreased gas

back-mixing (Bi *et al.,* 2000). Also, it has been observed that the emulsion phase expands beyond the minimum fluidization voidage in the turbulent regime (Yamazaki *et al.,* 1991). These factors have made operation in the turbulent regime attractive for chemical reaction in a fluidized bed.

Transition from the turbulent fluidization regime to the next regime, fast-fluidization, occurs when the upper surface of the bed becomes undistinguishable due to significant entrainment (Bi *et al.,* 2000). To compensate for the high levels of entrainment, solids must be continuously fed into the fast-fluidized bed. Typically, a fast-fluidized bed will have an S-shaped axial voidage profile, with a high solids concentration at the bottom of the bed and a dilute region at the top. However, the solids circulation rate, total solids inventory, particle size and density, solids inlet configuration, bed exit structure, and level of solids re-introduction have all been shown to influence the axial voidage profile (Lim *et al.,* 1995). The dilute region of a fast-fluidized bed, referred to as the 'fully-developed' region, is a region of nearly constant average upwards solids velocity and voidage. In the dilute region, there is an up-flowing, dilute suspension of gas and solids in the central core of the column. At the wall there are dense, downward moving clusters of solids (Kunni & Levenspiel, 1991, Lim *et al.,* 1995). There is continuous re-fluxing of solids between the dilute core and particle clusters along the wall. This type of flow behaviour is referred to as core-annular flow.

In the pneumatic transport regime, the heterogeneous structure observed in lower-velocity fluidization disappears (Bai *et al.,* 1999), and the solids become evenly distributed within the gas phase. Operation in this regime requires a sufficiently high gas velocity to prevent choking and saltation. Solids concentrations less than 1% are typical (Kunni & Levenspiel, 1991). The solids concentration is constant along the axis.

1.2 Mass Transfer in Freely Bubbling Beds

1.2.1 Mass Transfer of an Adsorbed Species

Mass transfer of an adsorbed species from the internal skeleton of a porous catalyst particle to the bubble phase of a fluidized bed includes several individual steps. These steps include: desorption of the gas species from the active sites, diffusion from the internal porosity to the particle external boundary layer, mass transfer from the boundary layer to the emulsion gas, diffusive transfer from the emulsion gas into the bubble cloud, and finally convective and diffusive transfer from the bubble cloud to the bubble.

Consider the simple desorption of species 'A' from the catalyst active site 'S': AS↔A+S. The rate of desorption of species A is governed by the rate equation (Fogler, 1999):

$$r_D = k_D\left(C_{A\bullet S} - \frac{p_A C_S}{K_{DA}}\right) \qquad (1.1)$$

The rate of desorption is promoted by a high concentration of active site complexes, $C_{A\bullet S}$, but reduced by high values of the partial pressure of species A, p_A, and by a high concentration of vacant active sites, C_S. Because the stripping of an adsorbed species is a transient process, the

concentration of active complexes and the partial pressure of species 'A' continue to decrease while the concentration of vacant active sites increases. Therefore, the rate of de-sorption would decrease as a catalyst particle descends through the stripper. The desorption rate constant, k_D, and the equilibrium de-sorption constant, K_{DA}, both increase exponentially with temperature (Fogler, 1999). Therefore, desorption can be promoted at elevated temperatures.

From a material balance, it can be shown that the diffusivity of species A through a catalyst pore is given by the equation:

$$\frac{\partial C_A}{\partial t} = \frac{D\psi}{r^2}\frac{\partial}{\partial r}\left(r^2\frac{\partial C_A}{\partial r}\right) + r_D\rho_P \qquad (1.2)$$

It can be observed from equation 1.2 that the concentration of species 'A' inside the particle can be governed either by the rate of diffusion or by the rate of desorption. The diffusivity of gases increases with increasing temperature, therefore pore diffusion would be promoted at elevated temperatures.

The no-slip assumption in fluid flow states that the tangential fluid velocity at a solid surface is zero. As you move away from this surface, the fluid velocity increases rapidly. The surface of the solid forms what is called a boundary layer. Mass transfer is inhibited because of the lack of convective air flow, therefore species A must diffuse through the boundary layer in order to reach the bulk fluid (Incropera & DeWitt, 2002). However, due to high amounts of gas mixing and high slip velocities between the particles and interstitial gas in a fluidized bed, it is generally assumed that equilibrium of the gas species concentration is rapidly attained between the particle surface and the interstitial gas (Kunni & Levenspiel, 1991a). Therefore, mass transfer resistance due to the existence of a boundary layer in fluidized beds is typically ignored.

In the case of de-sorption and internal pore diffusion, the hydrodynamic behaviour in a fluidized bed cannot affect the rates of mass transfer to an appreciable extent. Of most interest when examining mass transfer operations in fluidized beds are hydrodynamic factors that affect the rate of gas interchange between the emulsion and bubble phases.

1.2.2 Mechanisms of Mass Transfer From Emulsion to Bubble Phase

In dense fluidized beds, it is well accepted that there exists two impediments to mass transfer between the emulsion and bubble phases: transfer between the emulsion phase and the bubble cloud, and transfer from the bubble cloud to the bubble gas (Kunni & Levenspiel, 1991). Mass transport occurs via diffusion and convection across the bubble-cloud boundary (Drinkenburg & Rietema, 1972). Convective transfer across this boundary is a result of the continuous circulation of gas (often termed the 'throughflow' of gas) between the cloud and the bubble caused by the shearing of particles against the cloud gas as the bubble rises through the emulsion phase. Across the cloud-emulsion boundary, transport occurs only by diffusion in the case of a non-adsorbable species and by diffusion and convection in the case of an adsorbable species (Drinkenburg & Rietema, 1972). However, further mechanisms exist that allow for convective transport across this interface. There are many physical properties that can affect the rates of mass transfer across the cloud-emulsion and emulsion-bubble boundaries. These include:

bubble diameter, bubble rise velocity, bubble growth, bubble interactions, cloud shedding, and adsorbable species.

The effect of the bubble diameter on mass transfer can best be illustrated by analyzing correlations for the gas interchange coefficients across the bubble-cloud boundary and the cloud-emulsion boundary. Physically, the interchange coefficient can be thought of as a rate of 'forward' transfer of gas across an interface, with an equal rate of 'backward' transfer across the same interface. The interchange coefficient across the bubble and cloud interface for a non-adsorbable gas can be correlated from the Higbie penetration model (Kunni & Levenspiel, 1991):

$$K_{bc} = 4.5\left(\frac{U_{mf}}{d_b}\right) + 5.85\left(\frac{D_g^{1/2} g^{1/4}}{d_b^{5/4}}\right) \qquad (1.3)$$

Equation 1.3 accounts for both convective transport across the bubble-cloud interface in the first term on the right hand side of equation 1.3 and for diffusive transport across the cloud-bubble boundary in the second term. For transfer across the cloud-emulsion interface, the gas interchange coefficient has been correlated as (Kunni & Levenspiel, 1991):

$$K_{ce} = 6.77\left(\frac{D_g \varepsilon_{mf} U_{br}}{d_b^3}\right)^{1/2} \qquad (1.4)$$

Only diffusive transport is accounted for when correlating mass transport across the cloud-emulsion interface. Equations 1.3 and 1.4 show that increasing the bubble diameter causes a decrease in both bubble-cloud and cloud-emulsion mass transfer coefficients, with the most significant effect of the bubble diameter being observed in the diffusive components of transfer. The effect of bubble diameter on the interchange coefficient predicted by the correlation is supported by the findings of Wakabayashi & Kunni (1971), which are summarized in Table 1-1. This trend is justified by examining the ratio of bubble surface area to volume. In the case of a perfectly spherical bubble, the ratio is $6/d_b$. This ratio shows that larger bubbles have a smaller surface area for mass transfer for each unit of bubble volume, and therefore the rate of gas interchange would be reduced for large diameter bubbles.

As a bubble ascends through the emulsion phase in a fluidized bed, the decrease in hydrostatic pressure is expected to result in an increase in the bubble diameter. However, it has been found that bubble growth well in excess of that expected by the change in pressure can occur (Sit & Grace, 1981, Chavarie & Grace, 1976). This growth must occur due to inward gas transpiration from the emulsion phase to the bubble phase. Chavarie & Grace (1976) found that failure to account for inward gas transpiration when modeling the interchange coefficient resulted in a 2.5 times overestimation of the interchange coefficient for a bubble rising in isolation. Sit & Grace (1981) also observed bubble growth to occur before the coalescence of two obliquely aligned bubbles. They found that the growth of these bubbles occurred at a faster rate than that of a single bubble rising in isolation. This inward gas transpiration, from the emulsion to the bubble phase, represents a mechanism for convective transport across the emulsion-cloud interface.

In addition to inward gas transpiration of pre-coalescing bubbles, Sit & Grace (1978) has shown that an increase in mass transfer can occur due to an increase in the cloud-bubble gas throughflow component in interacting bubbles. However, because cloud-bubble mass transfer is

typically only limiting in beds of large diameter particles (Sit & Grace, 1981), the effect of the increased throughflow component is typically only observed in beds of large diameter particles. The effect of particle diameter on the increase in the rate of mass transport via the gas throughflow component, as found by Sit & Grace (1981), is presented in Table 1-2.

The Murray bubble (Murray, 1965) is a popular model for describing the generalized bubble shape in bubbling fluidized beds. This model predicts a kidney-shaped bubble with an indented base; however bubble shapes often deviate from this idealized model (Drinkenburg & Rietema, 1973). Chavarie & Grace (1976) hypothesized that oscillatory stretching and local distortions may influence diffusive mass transport due to the unsteady nature of the cloud-emulsion interface. Drinkenburg and Rietema (1973) also cited irregularities in bubble shape, leading to a higher surface area for mass transport, for underestimation of the modeled rate of mass transport compared to experimental results. These results show that the assumption of a spherical bubble, typically used to correlate the gas interchange coefficient, may result in an underestimation of the true rate of mass transport across the cloud-emulsion interface.

Equation 1.4 illustrates the influence of the bubble rise velocity on the cloud-emulsion interchange coefficient. It shows that the cloud-emulsion gas interchange coefficient increases with the bubble rise velocity. This postulate is confirmed by Drinkenburg & Rietema (1972) for deep beds containing fast rising bubbles. In the case of shallow beds containing bubbles with a low rise velocity, Drinkenburg & Rietema (1972) found a dramatic increase in the mass transfer from the bubble cloud to the emulsion phase. This increase in the rate of mass transport is caused by the shedding of the cloud gas (the thickness of the bubble cloud is of increasing significance in bubbles with low rise velocities) to the emulsion phase when the bubble erupts from the surface of the fluidized bed (Drinkenburg & Rietema, 1972, Drinkenburg & Rietema, 1973).

Through a mechanism known as cloud shedding, it has been observed that discrete amounts of cloud gas are periodically expelled from the bubble cloud (Rowe *et al.,* 1964, Toei & Matsumo, 1969). These gas ‘pockets’ are expelled from the lobes of the bubbles. Toei & Matsuno (1969) proposed that cloud shedding occurs due to periodic variations in the bubble rise velocity. Rowe *et al.* (1964) calculated the half-life of the cloud gas based on expulsion by cloud shedding and compared it to that of diffusive transfer across the cloud-emulsion boundary for a 0.05 m bubble rising at 2.5 times the emulsion gas velocity. They found the half-life of cloud gas to be approximately 2 seconds based on cloud shedding and 1.1 seconds based on diffusion alone. Toei and Matsuno (1969) found that cloud shedding was responsible for one-third of the total mass transport. This shows that cloud shedding is a potentially important mechanism for convective transport across the cloud-emulsion interface.

The Murray model for bubbles in a fluidized bed (Murray, 1965) predicts that particles from the bed freely enter the gas cloud from the top and exit through the bottom but that particles are absent from the bubble phase. However, it has been established that the bubble phase contains a small amount of particles (Kunni & Levenspiel, 1991a). It has been found that mass transport in a fluidized bed is increased significantly using adsorbable tracers over non-adsorbable tracers. Kunni and Levenspiel (1991a) found that gases that adsorb on the bed particles experience up to ten times more rapid bubble-emulsion interchange than did non-adsorbing gases. It has been proposed that this increase is caused by the small fraction of

particles that are known to exist inside, and pass through, the bubble phase (Kunni & Levenspiel, 1991a, Drinkenburg & Rietema, 1972). Once inside the bubble phase, desorption of the tracer gas from the surface of the solids can occur. This form of transfer negates both the bubble-cloud and the cloud-emulsion resistances to mass transport. Convective transport of adsorbed gases is also thought to occur because of gas laden particles freely entering the cloud (Drinkenburg & Rietema, 1972). In addition to adsorbable species, particles with a high porosity would also benefit from this mechanism of mass transport.

Mass transport from the emulsion to bubble phase occurs through a complexity of additive mechanisms. To be able to explore all the mechanisms that may affect the mass transport would require a variety of experimental techniques and equipment, and would require predictive correlations which are not available to date. However, common elements exist through the mechanisms of mass transport discussed above that are able to qualitatively predict trends in mass transport. These common elements include the bubble diameter, rise velocity, and sphericity.

1.3 Circulating Fluidized Beds

Many particulate processes are preferably implemented in circulating fluidized beds (CFB) over traditional low-velocity fluidization. Some of these processes include: fluid catalytic cracking (FCC), fluid coking, and coal combustion. Unique to CFBs are that they use integrated solids separation and return systems in the reactor configuration. Chemical processes utilize CFBs to take advantage of the many benefits of circulating systems: the ability to have staged processes, improved gas-solids contacting, lower axial gas mixing, and lower temperature gradients (Grace & Bi, 1997).

Figure 1-4 presents a diagram of the Kellogg® FCC process. A CFB in the FCC process consists of a fast-fluidized riser, in which the zeolite catalyst particles are entrained with the upward flowing fluidizing steam and atomized heavy gas oil feed. The feed is typically in the 320 to 600 ºC boiling range (Avidan, 1997). Conversion of the heavy gas oil feed to lower molecular-weight products, called ‘cracking’, occurs in the riser. After conversion, the gas and solids are separated in the riser terminator. The vapour products exit the CFB and are sent to a fractionator; while the particles empty into a counter-current steam-catalyst stripper. The role of the stripper is to remove any entrained or adsorbed hydrocarbons from the pores and interstices of the catalyst stream. The stripper empties into the standpipe, a transport line that moves the catalyst to the regenerator. The regenerator burns any coke deposited on the catalyst from the cracking reaction. Aside from simply regenerating the catalyst, burning of the coke also provides the heat needed for the endothermic cracking reaction in the riser.

1.3.1 The Riser

A riser in the FCC process typically operates in the fast-fluidization regime. Table 1-3 presents typical operating conditions in an FCC unit riser. As can be seen in the table, the catalyst particles and vapourized crude oil feed have brief average residence times for the cracking reaction to occur. Gas backmixing can lead to over-cracking of the feed, and thus should be avoided. Several design features are implemented in the riser to limit backmixing,

including using a completely vertical riser geometry to limit non-uniformities in the gas and solids profiles, and even feeding of the atomized heavy gas oil feed across the riser cross section (Avidan, 1997). As discussed in Section 1.1, there is refluxing of solids at the vessel wall in the fast-fluidization regime. Inevitably, this would cause to gas backmixing. Despite this, it has been found that the residence time of gas in the riser closely resembles plug flow (Kunni & Levenspiel, 1991).

1.3.2 The Standpipe

The standpipe has two main functions: to transport solids and to build pressure in the CFB. The standpipe is the only part of the CFB loop where a pressure gain is achieved. This pressure build-up is the driving force for transporting the catalyst particles around the CFB. Gravity transfers solids from an area of low pressure to an area of high pressure. Gas flows upward relative to the downflowing solids, creating a 'sealing' pressure drop (Knowlton, 1997) (Figure 1-5). Gas flow may be either downwards or upwards relative to a stationary reference.

Standpipes normally operate in either fluidized or packed bed flow. In packed bed flow, the relative velocity, U_r, between the solids and gas are less than the minimum fluidization velocity and the pressure build can be predicted by the Ergun equation. When the relative velocity is equal to or above the minimum fluidization velocity, the standpipe operates in fluidized bed flow. For Geldart A particles, fluidized bed flow in standpipes can be further divided into two distinct regimes: bubbling and non-bubbling fluidized flow (Knowlton, 1997). Non-bubbling fluidized bed flow is the desired operating regime, as it allows for the maximum pressure build along the length of the standpipe. In bubbling fluidized flow, excess gas results in the formation of bubbles in the standpipe. Bubbling fluidized flow is undesirable for two reasons: it reduces the bulk density of the standpipe thus reducing the pressure build-up, and the bubbles can coalesce and potentially become large enough to span the standpipe diameter. These large bubbles can cause instability in the standpipe, which can result in unsteady standpipe flow (Karri & Knowlton, 1997).

Because the pressure can change significantly along the length of the standpipe, compression of the interstitial gas occurs. This gas compression can lead to defluidization of the emulsion towards the bottom of the standpipe; thus reducing the pressure build-up. To counteract this gas compression, aeration gas is added to the standpipe. In most cases, aeration is added in equal increments along the length of the standpipe to maintain solids in a fluidized state. This scheme is preferred over point injection at the site of defluidization because the large volume of gas required to counter-act defluidization can result in the formation of gas bubbles at the site of gas injection (Knowlton, 1997).

The standpipe geometry can be either vertical, angled, or hybrid (containing both angled and vertical sections). Angled and hybrid standpipes are used where there exists a vertical and horizontal separation between vessels in the CFB. Vertical standpipes can achieve higher solids circulation rates, and attain a higher pressure build-up than either angled or hybrid standpipes (Knowlton, 1997). In addition, the range of stable operation in vertical standpipes is wider than that of angled and hybrid standpipes. This is because separation of gas and solids occurs in angled and hybrid standpipes, resulting in gas bubbles traveling along the top of the inclined section. These bubbles can coalesce and bridge across the standpipe, resulting in erratic solids

flow. In a hybrid standpipe, this bridging occurs at the bottom of the upper vertical section. When bridging occurs, the maximum solids circulation rate in the standpipe is achieved (Karri *et al.,* 1995). However, the maximum stable solids circulation rate in the standpipe can be increased by incorporating a gas bypass line at the top of the angled section in a hybrid standpipe (Karri *et al.,* 1995).

1.3.3 The Regenerator

The regenerator combusts coke, deposited on the catalyst surface from the cracking reaction, and any un-stripped hydrocarbons to carbon monoxide, carbon dioxide, water, and sulfur and nitrogen oxides (Avidan, 1997). Typically, low velocity fluidized bed combustors operate in the turbulent fluidization regime (Avidan, 1997). However, some regenerator designs use a tapered geometry such that a transport regime occurs at the top of the bed to transport solids either into the riser or to re-circulate solids back into the regenerator. Due to a wide variety of regenerator designs, efficiencies ranging from 20 to 70% have been reported (van Deemter, 1980). Poor regenerator performance can often be remedied by improving air distribution, using a centralized spent catalyst distribution, and using counter-current flow of air and solids (Avidan, 1997).

1.3.4 The Stripper

The role of the stripper is to displace the entrained and adsorbed hydrocarbons from the solid catalyst particles by contacting with steam. Stripping is usually accomplished in a dense, moving fluidized bed. Steam is injected at the bottom of the stripper, and bubbles counter-current to the down-flowing catalyst stream that enters from the top. Table 1-4 presents typical industrial operating parameters of an FCC stripper. Hydrocarbons are displaced from the catalyst stream into the steam bubbles. Once it has passed through the stripper, the steam bubbles containing the stripped hydrocarbons are removed from the FCC unit, thus allowing for recovery of the stripped hydrocarbon product. Ideally, the gas and solids would be evenly distributed across the stripper cross-section for most efficient contacting. Because bubbles have a tendency to rise through the centre of freely bubbling beds (Bi *et al.,* 2000, Cui *et al.,* 2001), baffles are generally installed to promote a more even distribution of gas and solids.

Although stripping is a fluidized bed process, it differs from classical fluidization technology in that the stripper contains internal baffles. In addition, several unique bed geometries exist depending on the location of the stripper inside the FCC unit. One of the common geometries used is the annular stripper (Figure 1-6). The annular stripper has a central, vertical riser that creates an annular stripping vessel. Although convenient in design, this geometry leads to flow maldistribution problems due to asymmetric design of the standpipe withdrawal. The other common design is a fully cylindrical stripper (Figure 1-7). In this design, the riser is external to the stripper vessel. In an effort to improve stripping efficiency and alleviate operating problems, other stripper designs have been proposed. One of these designs is to add a secondary external stripping vessel operated in parallel to the primary stripping vessel (Letzsch, 2003).

An important design element that influences both effectiveness of the stripper at removing the entrained and adsorbed hydrocarbons as well as the operating window of the stripping vessel (i.e. the solids circulation rate and stripping gas velocity before flooding is observed) is the baffle configuration. In cold-flow experimental studies, baffles have been shown to improve stripping efficiency over that of an un-baffled striper (Padyen *et al.,* 2001, Rivault *et al.,* 1995). The purpose of baffles is to promote radial movement of gas and solids. Proper baffle design will ensure a more complete use of stripper cross-section, minimize short circuiting, and enhance gas-solids contacting.

1.4 Stripper Operating Problems

One of the purposes of implementing baffles in the stripper is to reduce the occurrence of operating problems. To date, three operating problems have been reported in the open literature. These problems include: flooding, bridging, and catalyst maldistribution.

Catalyst maldistribution is characterized by segregated use of the vessel cross section by steam and catalyst. For example, catalyst may channel down one side of the stripper, and steam up the other side. This leads to short-circuiting of the solids and gas through the stripper, and reduces stripping efficiency. Although maldistribution can occur even in a well-designed stripper, it can be minimized by a symmetric stripper design, implementing a central vertical standpipe, good baffle design, and good steam distribution (Senior *et al.,* 1998).

De-fluidization of the catalyst can occur if pockets of catalyst descend a significant distance before encountering steam bubbles (Senior *et al.,* 1998). The catalyst becomes de-fluidized because of the gas compression occurring when the catalyst traverses the stripper; moving from an area of lower pressure to an area of higher pressure. Catalyst de-fluidization can be either permanent, which renders that part of the stripper inactive, or intermittent (Senior *et al.,* 1998). Intermittent de-fluidization is known as bridging. When bridging occurs, catalyst becomes locked between the baffles. This catalyst bridge causes an accumulation of stripping steam below the obstruction. Eventually a fault in the bridge occurs, resulting in large clumps of de-fluidized catalyst to crash through the void space. This can cause hardware damage. Bridging can be detected by high amplitude fluctuations in the vessel differential pressure (Bi *et al.,* 2004). Bridging can be avoided by ensuring proper steam distribution, and proper baffle design (Senior *et al.,* 1998).

Flooding results when the local catalyst downward velocity is greater than the steam bubble rise velocity (Senior *et al.,* 1998). This condition causes steam to accumulate inside the stripper vessel, and the catalyst to rapidly cascade down the baffles. This leads to short catalyst residence times in the stripper as well as poor steam-catalyst contacting. Despite this, a flooded stripper generally continues to exhibit smooth catalyst circulation. Bi *et al.* (2004) identified four criterion to identify flooding in gas-solids counter-current strippers: underflow of stripping steam into the standpipe, poor stripping efficiency caused by reduced residence time of the solids in the stripper, and development of a region of high voidage below the baffles. Stripper operation at low stripping gas velocities and high solids circulation rates are a major cause of flooding (Senior *et al.,* 1998). In addition, baffle designs that redistribute gas as small bubbles in regions of high catalyst velocity are thought to promote flooding (Bi *et al.,* 2004). Bi *et al.* (2004) also

suggested that steep angled baffles and baffles that are separated by wider gaps (even though they occupy the same fractional cross-sectional area) can delay the onset of flooding.

1.5 Stripper Baffle Configurations

1.5.1 Disc-and-Donut Baffles

The industry standard in baffle design has traditionally been the disc-and-donut baffle (Figure 1-6). This configuration is used in annular stripper geometries, as the baffles are alternatively attached to the stripper and riser walls. Although stripping efficiency was a consideration in its design, the disc-and-donut baffle places a higher emphasis on operational reliability. The disc-and-donut baffles are slanted at steep angles, typically 45°, and leave large open areas, typically 50%. The steep baffle angle results in poor gas-solids contacting, but ensures that the catalyst flows smoothly since FCC catalyst has a tendency to de-fluidize if it encounters horizontal surfaces (Johnson & Senior, 1996). The steep baffle angle and the large open area of the disc-and-donut baffles prevent blockage of the stripper by dome coke and large pieces of concrete that can fall into the stripper (Johnson & Senior, 1996). Disc-and-donut baffles are typically designed to operate at solids circulation rates ranging from 49 – 65 kg/(m^2·s) (Letzsch, 2003). When the circulation rate is increased beyond 98 kg/(m^2·s) stripper efficiency decreases substantially (Letzsch, 2003).

1.5.2 Disc-and-Donut Baffles Modified with Flux Tubes™

Mobil Oil Corp. developed the technology known as Flux Tubes™. The design modifies existing disc-and-donut baffles instead of replacing them with a completely new internal. The purpose of the new design was to increase the operating window of the stripper beyond that of typical disc-and-donut baffles. In their design, vertical pipes are inserted into typical disc-and-donut baffles (Figure 1-8, Figure 1-9) (Johnson & Senior, 1996). The pipes are cut on the horizontal at the base, but at a shallower angle on the top so that a lip is created. The lip is provided to promote diversion of the flowing catalyst downwards through the pipe. The Flux Tubes™ are terminated above the base of the baffle to tap into the high pressure gas which tends to accumulate under the baffle, thereby promoting gas flow through the pipe. The pipes provide an alternate flow path for the steam and catalyst. The tubes also increase the open area of the stripper by 10%, which reduces the peak flow at the pinch points (Johnson & Senior, 1996).

Cold-flow testing of the Flux Tube™ design showed that stripping efficiency of a helium and carbon dioxide tracer is only moderately better using the Flux Tube™ design over conventional baffles (Miller *et al.,* 2000). However, conventional disc-and-donut baffles were found to flood at a critical solids flux, at which point a sharp decrease in the stripping efficiency was observed. Flux Tubes™ were able to maintain good stripping efficiency beyond this critical flux.

1.5.3 DynaFlux™ Technology

Mobil Oil Corp. and M.W. Kellogg Co. have jointly developed DynaFlux™ technology (Miller *et al.,* 2000). DynaFlux™ is a combination of Flux Tubes™ and Lateral Mixing Elements™. Lateral Mixing Elements™ are designed to increase the mean residence time of catalyst, correct catalyst maldistribution, and improve mixing (Miller *et al.,* 2000). As such, Lateral Mixing Elements™ are especially useful in annular strippers where there is an asymmetric catalyst withdrawal out of the stripper. In their industrial testing, Mobil Oil Corp. found that two-thirds of the catalyst flows down one-quarter of the cross-sectional area of their annular stripper without Lateral Mixing Elements™. After installation of Lateral Mixing Elements™ a uniform distribution of catalyst across the cross-section was observed, increasing the mean catalyst residence time by 10% (Miller *et al.,* 2000).

1.5.4 Shed Decks

Shed decks are composed of rows of sheds with their peaks pointing upwards (Figure 1-10). Like disc-and-donut baffles, these particular internals are designed with an emphasis on operational reliability. The baffles are typically slanted at 45° from the horizontal and are placed in a number of staggered rows. This design is popular in a process known as 'fluid coking', which cracks a higher molecular weight feed than does FCC. It is preferentially used in fluid coking due to rapid fouling of the baffles.

1.5.5 KFBE™ Structured Packing

Instead of modifying existing disc-and-donut baffles, Koch-Glitsch has taken the approach of designing completely new internals. Several structured packings were designed and tested, however their testing showed that KFBE™ structured packing optimized contacting between gas and solids (Figure 1-11) (Rall & DeMulder, 2000). Homogeneous fluidization was found to occur throughout the bed, without large variations in bed density or stagnant regions. The active volume of the stripper (where there is gas-solids contacting) was found to increase by 15 – 60% using the KFBE™ internals over standard disc-and-donut baffles (Rall & DeMulder, 2000). Because the fluidization was more uniform, the lowest possible catalyst velocity is maintained throughout the stripper containing KFBE™ internals (Rall & DeMulder, 2000). The emulsion velocity was reduced by as much as 80% in comparison to standard disc-and-donut baffles (Rall & DeMulder, 2000). Cold-flow testing showed that solids circulation rates in excess of 145 kg/(m^2·s) could be achieved in a stripper containing KFBE™ internals with no evidence of flooding.

1.5.6 Other Structured Packings

As of 2003, eight packed strippers were in operation worldwide (Letzsch, 2003). Strippers were packed with 8 – 10 layers of structured packing (Figure 1-12). Letzsch (2003) did not give details of the design(s) of the packing, however case studies were presented of refiners who retrofitted their strippers to structured packings. All refiners found that the retrofit resulted in a higher stripping efficiency and lower stripping steam requirements. No indication of

plugging or fouling was found (Letzsch, 2003). A pay-back period of 9 months for the retrofit was reported by one refiner.

1.6 Knowledge Gap and Thesis Objective

High consumer demand for gasoline has forced refiners to increase FCC unit throughput by increasing catalyst circulation and feed rates beyond original FCC unit design specifications. Although further increases in the FCC unit are possible, many refiners are limited by stripper capacity (McCarthy *et al.,* 1997). This bottlenecking of the stripper is reflected in the recent interest in baffle design. Knowledge of the operating conditions (stripping gas velocity and solids circulation rate) that lead to inadequate stripping would improve guidelines for stripper operating parameters and design. In addition, an understanding of the hydrodynamic behaviour of the industry standard disc-and-donut baffles would allow for improved design of second-generation baffles.

This dissertation describes an investigation of a CFB riser, downcomer, and stripper. Initially, an extension of the existing CFB in the Fluidization Laboratory of Saskatchewan was designed. The experimental program conducted in this study included an examination of the solids flow behaviour in the riser, interstitial gas velocity in the downcomer, and stripping efficiency measurements. The hydrodynamic behaviour of the stripper was modeled using Multiphase Flow with Interphase eXchanges (MFIX) CFD code.

To date, the behaviour of the bottom zone of the CFB riser remains largely unexplored. From the available literature, it is apparent that two types of solids flux profiles are prevalent at high-density conditions: parabolic with net upflow at all radial locations, and parabolic with net upflow at the centerline and net downflow at the wall. However, radially uniform and U-shaped profiles are also known to exist. The objective of this work is to explore the effect of operating conditions on the solids flux profiles in the bottom zone of a high-denstiy CFB riser. Riser solids circulation rates between 125 and 243 kg/(m^2·s) are tested at a constant riser superficial gas velocity of 5.3 m/s. The effect of the riser superficial gas velocity of the local upflow at the riser centerline is also examined at a constant solids circulation rate of 187 kg/(m^2·s). In addition to an exploration of the solids flux behaviour, the integrated solids flux profiles are used to determine the solids circulation rate in the experimental CFB. The solids circulation rate determined from the integrated solids flux profiles are related to the pressure drop in the solids feeding device for use as an on-line calibration of solids circulation rate in the CFB (Section 2.2).

The effect of operating conditions (stripping gas velocity and solids circulation rate) on the stripping efficiency and hydrodynamic behaviour of FCC strippers is not yet well understood. All previous studies examining the effect of operating conditions on the removal of a non-adsorbing tracer gas have found > 99% stripping efficiency. After accounting for experimental error, these high stripping efficiencies make it difficult to discern the influence of operating conditions on the stripping efficiency. In addition, these studies have relied on correlations to model the emulsion gas velocity profiles of the tracer gas underflow into the standpipe. Since this is a necessary variable for determining the stripping efficiency, there is obviously value in experimentally determining these profiles to improve the accuracy of the measured stripping efficiency. The objective in this work is to measure the effect of the solids circulation rate and

stripping gas velocity on the stripping efficiency of a FCC stripper containing disc-and-donut baffles. Stripping efficiency is studied for stripping gas velocities ranging from 0.1 to 0.3 m/s, and solids circulation rates ranging from approximately 45 to 75 kg/(m^2·s). These conditions were chosen because they correspond to typical commercial FCC stripper operation (Table 1-4). The stripping efficiency measurements will be fully experimental, requiring measurement of the tracer gas concentration and emulsion gas velocity profiles in the standpipe in order to close the steady state tracer gas mass balance.

The hydrodynamic behaviour of FCC strippers containing disc-and-donut baffles remains largely unknown. An understanding of the hydrodynamic behaviour would allow for improved design of second-generation stripper internals, as it helps to identify the occurrence and cause of unfavourable gas-solids contacting behaviours. The objective of this work is to investigate the hydrodynamic behaviour of FCC strippers at the same operating conditions examined in the experimental stripping efficiency study. Hydrodynamic data will be acquired from computational fluid dynamics (CFD) models. The hydrodynamic behaviour will be examined through qualitative observations, time-averaged voidage and bubbling frequency profiles, and an investigation of bubble properties: sphericity, rise velocity, and diameter.

This dissertation is formatted for individual publication of chapters 3, 4, 5, and 6. Chapter 2 describes the CFB apparatus used in the experimental program. Chapter 3 describes the results of select experiments examining the effect of solids circulation rate on riser solids flux profiles in the bottom zone of the CFB riser. Values of the solids circulation rate, derived from integrating the solids flux profiles, are used for calibration the experimental CFB (Section 2.2). Chapter 4 discusses the hydrodynamic behaviour of the stripper containing disc-and-donut baffles. The hydrodynamic data discussed in Chapter 4 is acquired from the results of CFD modeling. Chapter 5 details the results of an experimental program to determine the emulsion gas velocity profiles in the standpipe and un-baffled stripper. Finally, Chapter 6 presents the effect of the stripping gas velocity and solids circulation rate on the experimentally determined stripping efficiency. Measurement of the stripping efficiency utilizes the emulsion gas velocity profiles determined in Chapter 5 to close the helium tracer gas mass balance. The effect of the hydrodynamic behaviour of the FCC stripper on the stripping efficiency is interpreted through the emulsion-cloud gas interchange coefficient, determined from the hydrodynamic data presented in Chapter 4.

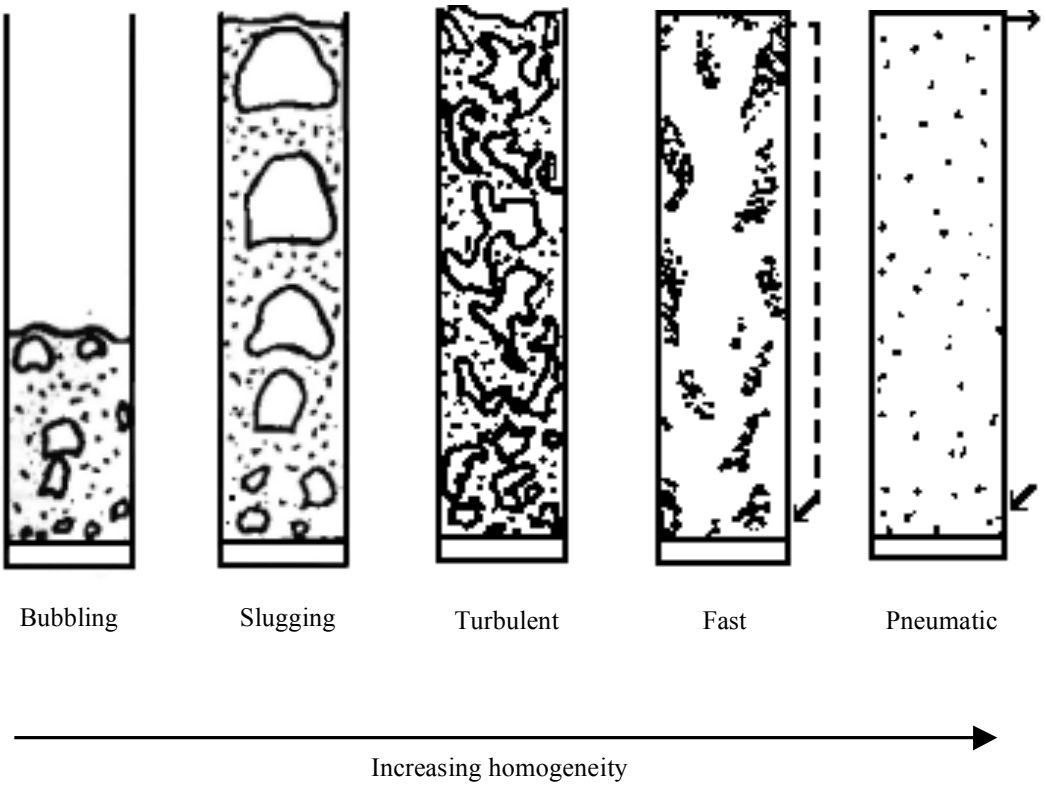

Figure 1-1: Fluidization regimes (Grace, 1986).

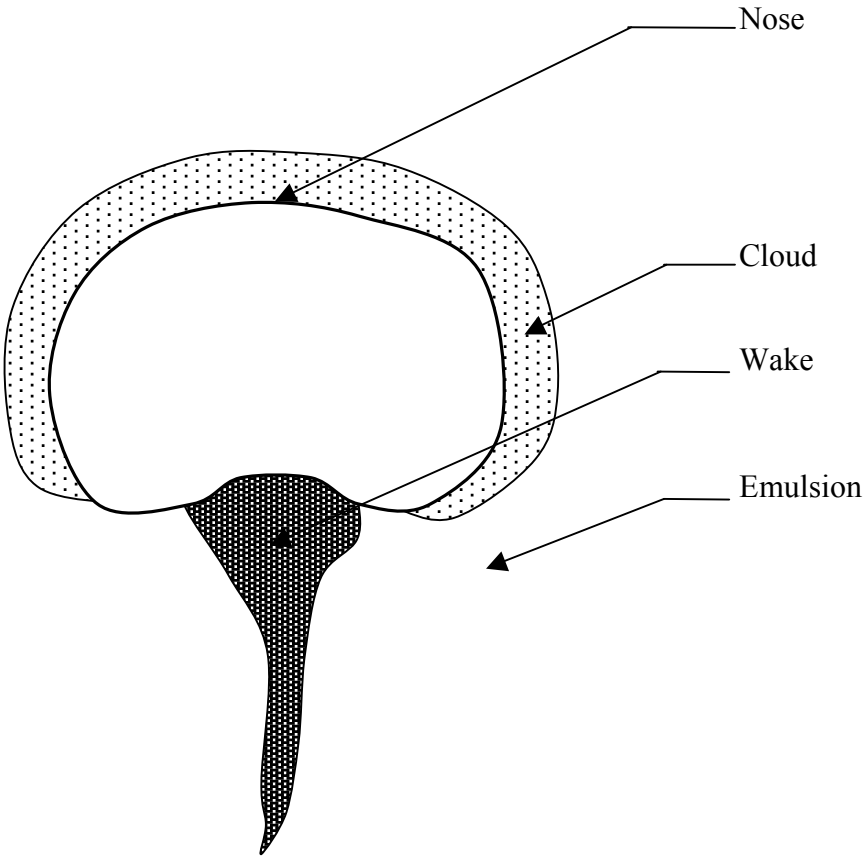

Figure 1-2: Murray bubble (Murray, 1965)

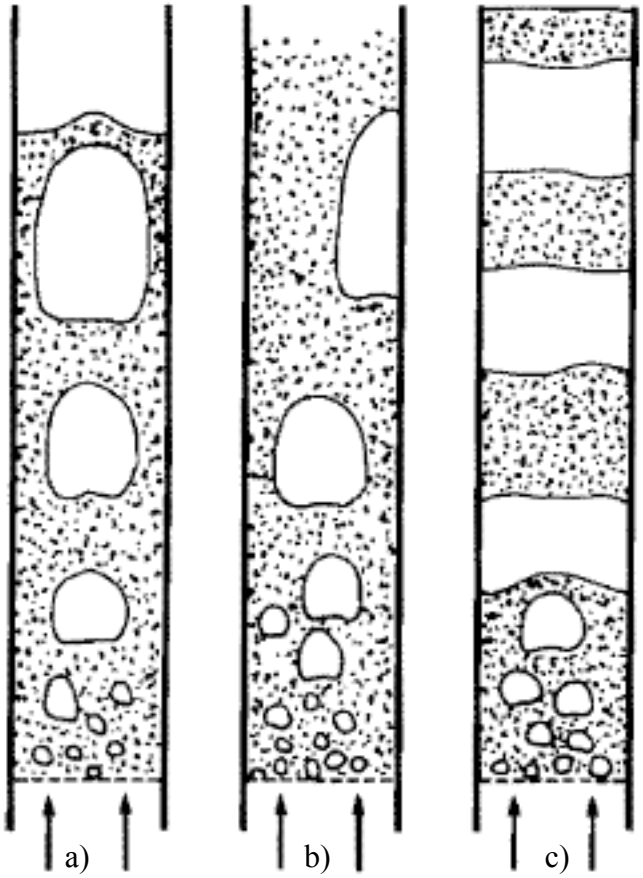

Figure 1-3: Types of slugs in the slugging fluidization regime a) axial slugs, b) wall slugs, and c) flat slugs (Kunni & Levenspiel, 1991).

Table 1-1: The effect of bubble diameter on the bubble-emulsion gas interchange coefficient (Wakabayashi & Kunni, 1971).

d_b , m	K_{be} , s^{-1}
0.04	11 - 16
0.06	9 - 18
0.08	8 - 14
0.11	7 - 11

Table 1-2: The effect of particle diameter on the increase in mass transport observed in coalescing bubbles relative to that of bubbles rising in isolation (Sit & Grace, 1981)

d_p, μm	% increase
390	34
320	35
160	15
93	3-8
90	small

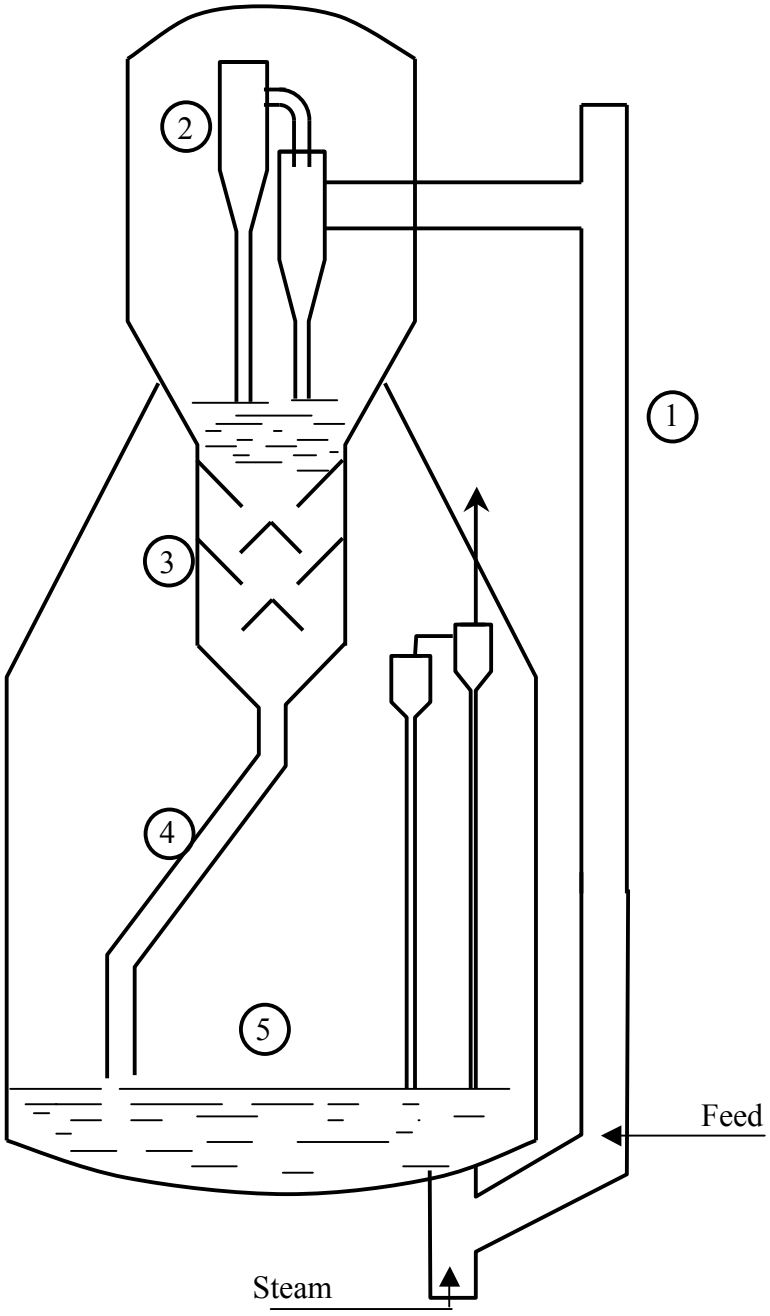

Figure 1-4: Kellogg® FCC process (Kunni & Levenspiel, 1991). Labels: 1) riser, 2) riser terminator, 3) stripper, 4) standpipe, 5) regenerator.

Table 1-3: Typical riser operating conditions (Avidan, 1997).

Property	Value
Feed temperature, ºC	150 - 300
Regenerated catalyst temperature, ºC	675 - 750
Riser top temperature, ºC	500 - 550
Catalyst/ oil ratio, wt.	4 - 10
Dispersion steam, wt%	0 - 5
Pressure, kPa	150 - 300
Oil residence time, s	1 - 5
Solids residence time, s	3 - 15

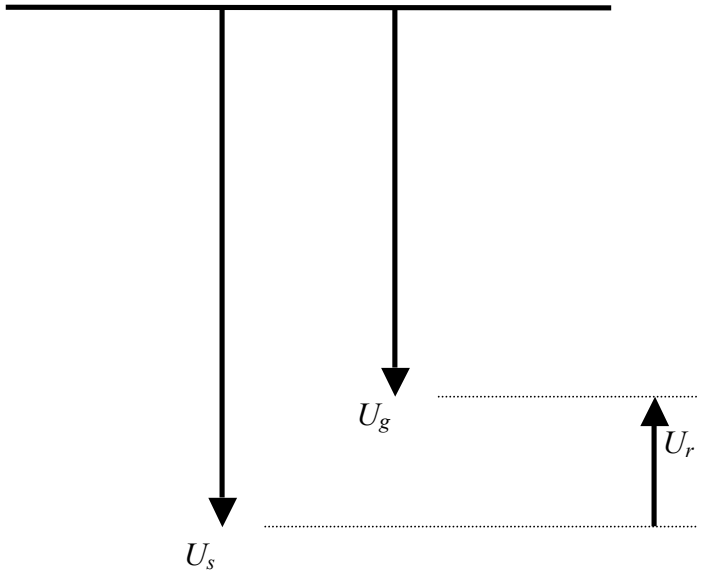

Figure 1-5: Relative velocity (U_r) between the solids (U_s) and gas (U_g) in standpipes.

Table 1-4: Key design operating conditions for industrial FCC unit strippers. * King (1992), ** Senior *et al.* (1998).

Property	Value
Stripping Steam Severity (kg steam/ 1000 kg catalyst) *,**	2 – 4
Superficial Steam Velocity (m/s) *	0.15 – 0.30
Superficial Catalyst Flux (kg/(m^2·s)) *,**	30 – 75
Maximum Restricted Catalyst Flux (kg/(m^2·s)) **	250
Mean Catalyst Residence Time (s) **	60 – 120
Stripper Temperature (ºC) **	495 - 565

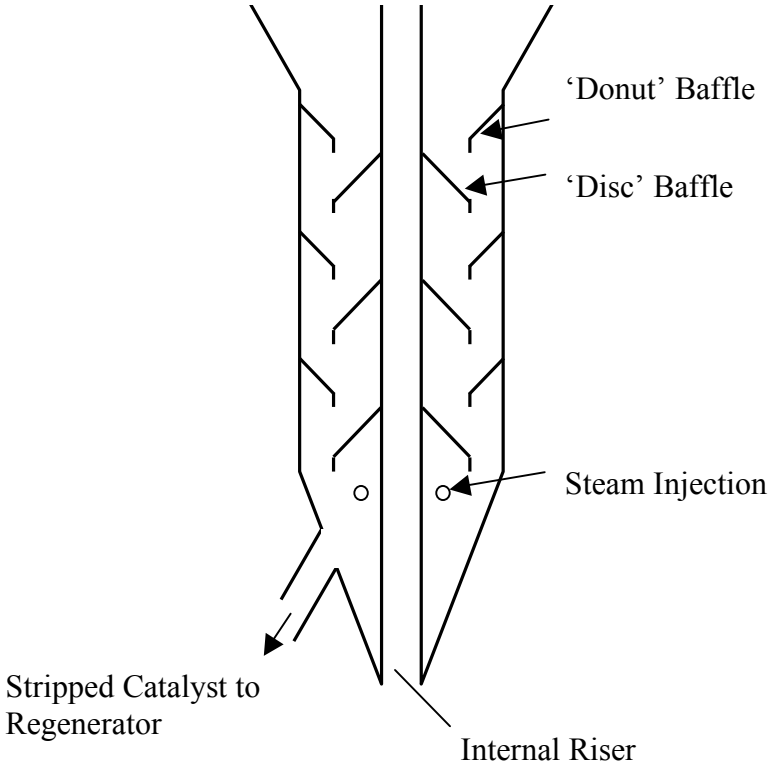

Figure 1-6: Annular stripping vessel containing disc-and-donut baffles.

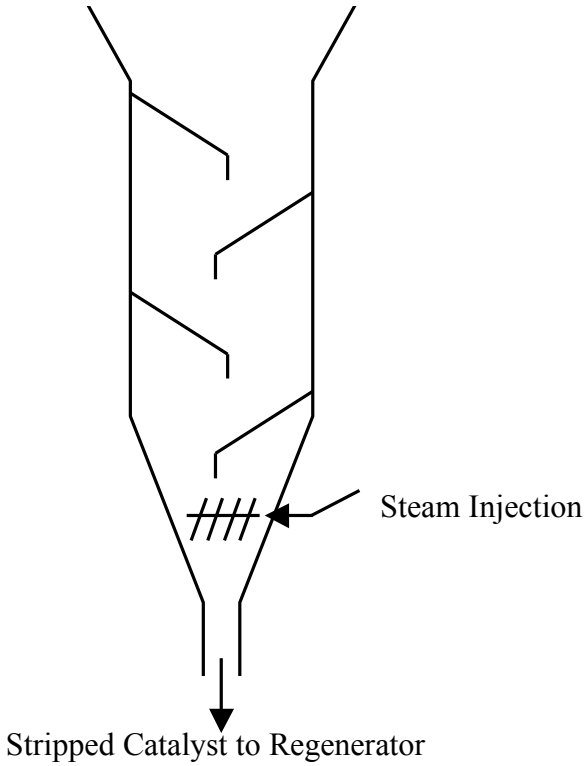

Figure 1-7: Cylindrical stripping vessel containing baffles.

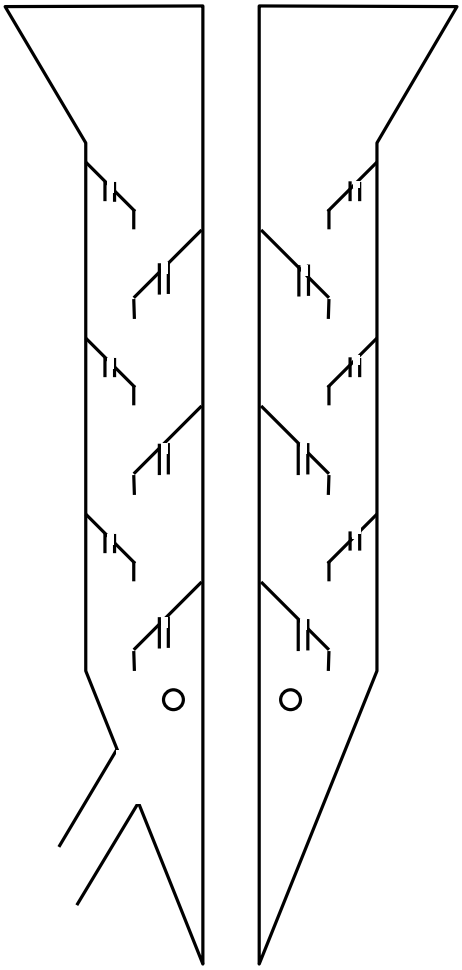

Figure 1-8: Annular stripper containing disc-and-donut baffles modified with Flux Tubes™.

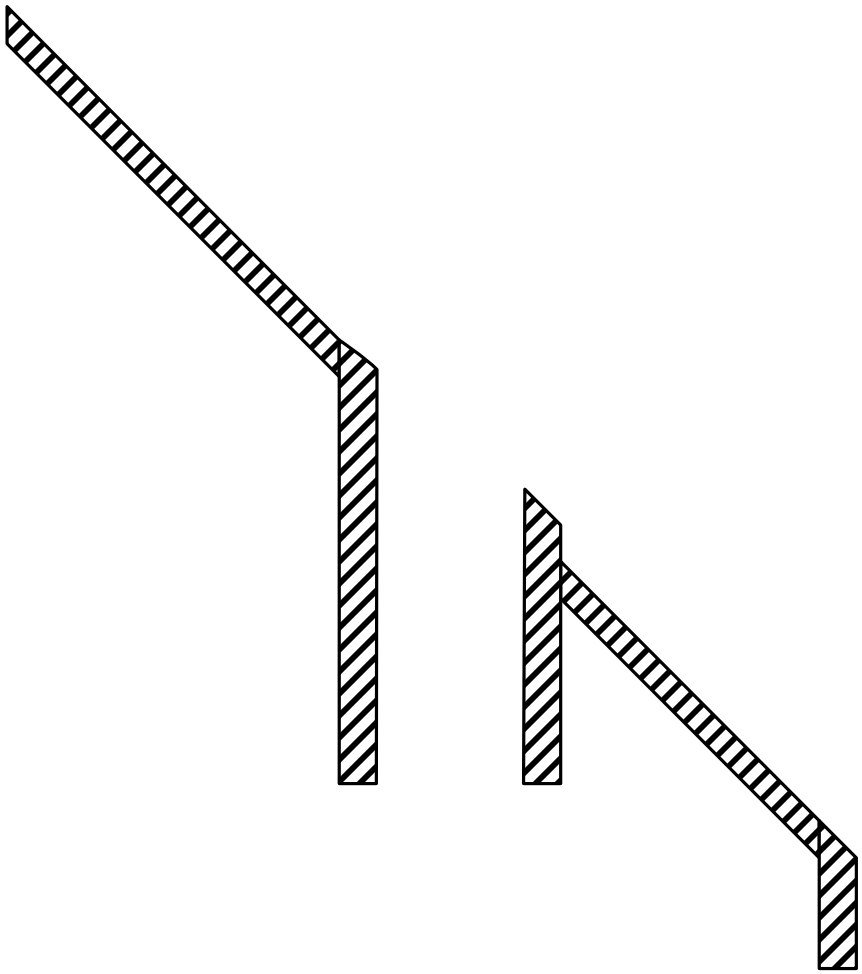

Figure 1-9: Cross sectional view of a donut baffle showing a Flux Tube™.

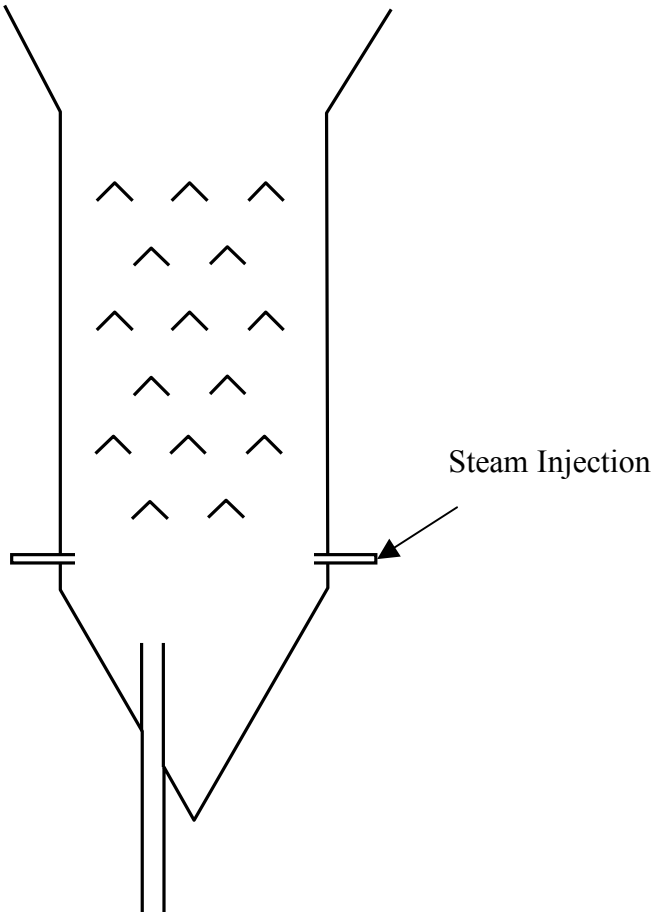

Figure 1-10: Fluid coker stripper containing shed baffles.

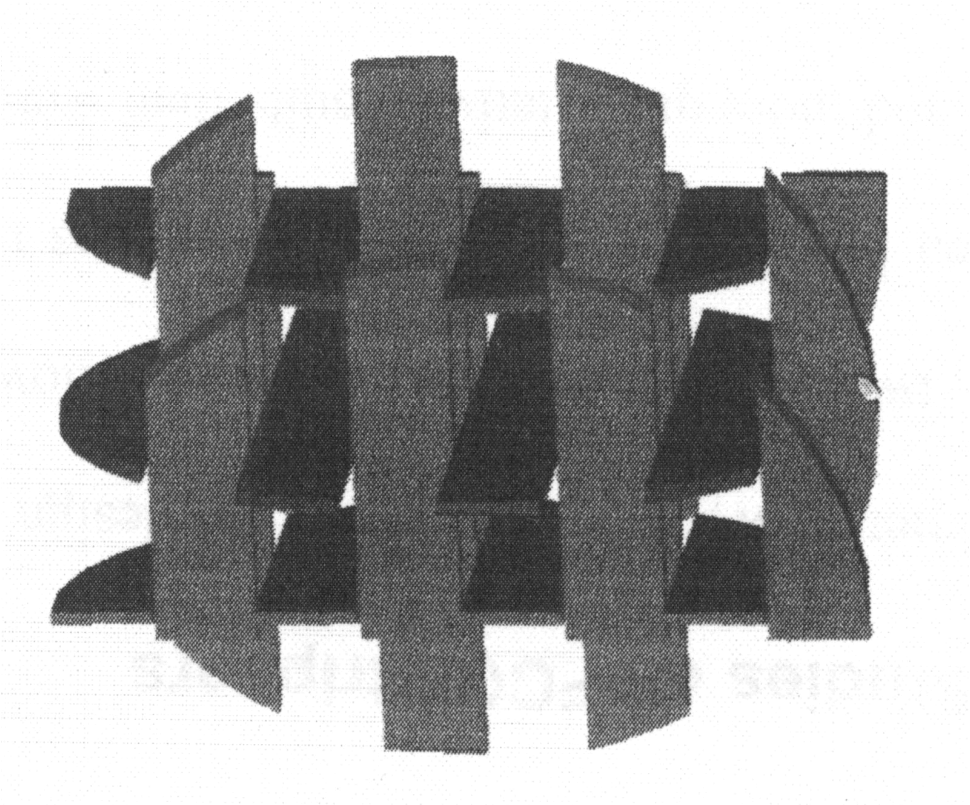

Figure 1-11: KFBE™ structured packing (Rall & DeMulder, 2000).

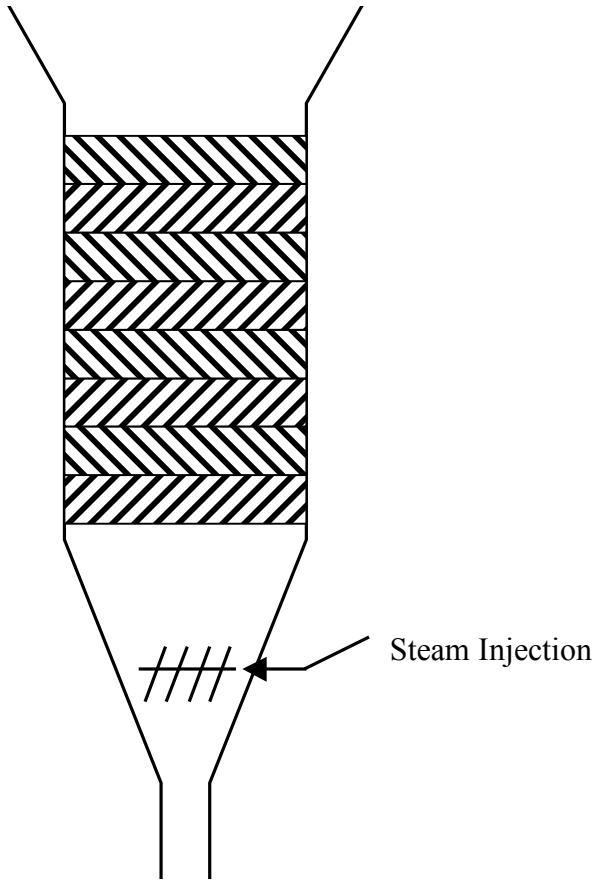

Figure 1-12: Cylindrical stripper containing eight rows of structured packing

Chapter 2 – Circulating Fluidized Bed Apparatus

2.1 Circulating Fluidized Bed

Appendix A outlines the start-up and shut-down procedures, as well as troubleshooting and maintenance guidelines for the circulating fluidized bed (CFB) apparatus. A diagram of the CFB apparatus used in the experimental program is presented in Figure 2-1. The CFB uses fluid catalytic cracking catalyst as bed material, and air as fluidizing gas. The CFB is constructed out of acrylic to allow for visual observation. The riser is a 13 m tall section with an inside diameter (I.D.) of 0.14 m. The differential pressure is measured at 13 locations along the length of the riser to aid in troubleshooting and for optimizing operating parameters. At the top of the riser, a 90° elbow changes the flow direction from vertical to horizontal. The horizontal section leads to the solids separation system, consisting of two cyclones placed in series. The intention of the designs of the primary and secondary cyclones is for high capacity and high efficiency, respectively. Details of the design of the cyclones are given by Malcus (2000). The solids are fed into the downcomer via L-valves on the cyclone underflow streams. Details on the design of these L-valves are provided in Section 2.5.2.

The downcomer is composed of two sections: the stripper and the standpipe. The stripper section is a 4.7 m tall, 0.29 m I.D. section that can be outfitted with baffles. While operating the CFB, however, approximately 2 m of this height is freeboard to help reduce entrainment. An internal cyclone is used to return any entrained particles back into the stripper. Details of the design of this cyclone are given in Section 2.5.5. At the bottom of the stripper, solids enter into a hybrid standpipe. Symmetrically located to the stripper, the standpipe is a 0.19 m I.D. pipe that contains two vertical sections and one 45° inclined section. The upper vertical section, located directly beneath the stripper, is 1.0 m in length. This section has taps for measuring the differential pressure, and also a single tap for providing aeration gas. The lower vertical section is 5.8 m in length. The differential pressure is measured at 4 locations along the length of the lower vertical section of the standpipe, and aeration taps are located every 1.0 m. In the 45° inclined section, aeration taps are separated by a 0.24 m distance. An air bypass line connects the top of the inclined section to the freeboard section above the stripper. Further details regarding the design of the 45° inclined section can be found in Section 2.5.1. The flowrate of aeration gas to all taps is individually measured using rotameters.

Solids are transferred between the riser and the standpipe via the annular bed (Figure 2-2). The design of the annular bed is based on the work of Pugsley (1995). Its purpose is to allow acute control over the solids circulation rate, and to provide a reliable method for measuring the solids circulation rate in the CFB. Solids are drained into the top of the annular bed from the standpipe, and are distributed throughout the annular space between the outer circumference of the riser (located centrally in the annular bed) and the wall of the annular bed. Aeration gas enters the annular bed through a windbox covered by a radial gas distributor. The windbox has an inside diameter of 0.76 m and an outside diameter of 1.06 m. The distributor is 0.76 m outside diameter, 70 mm high perforated plate with evenly spaced 3.2 mm diameter holes

in a triangular pitch. The open area of the perforated plate is 40%. Aeration is introduced into the windbox through eight symmetrically spaced ports around the circumference of the windbox to ensure even gas distribution. Aeration gas from the windbox entrains particles into the riser through eight 15 mm diameter symmetrically places orifices in the riser wall. The rate of solids entrainment into the riser, and thus the solids circulation rate in the CFB, is controlled by adjusting the aeration rate into the windbox. As will be discussed in Section 2.2, the solids circulation rate is correlated to the pressure drop in the annular bed.

The CFB could achieve a maximum solids circulation of 100 kg/(m^2·s) in the stripper (437 kg/(m^2·s) in the riser). However, installation of the internal cyclone limited the maximum attainable solids circulation rate to 75 kg/(m^2·s). This was thought to occur because of the added pressure drop caused by the cyclone preventing riser gas from entraining the solids through the primary cyclone L-valve. Improving the configuration of the cyclone underflow would reduce the pressure drop caused by conveying the solids, and thus would allow for gains in the attainable solids circulation rate.

2.2 Calibration of the Solids Circulation Rate

The solids circulation rate in the CFB was calibrated against the radial pressure drop in the annular bed (Figure 2-3). Pressure taps in the annular bed are located at radial distances of 0.10 and 0.25 m from the outside of the riser wall. The pressure drop was measured using an Omega PX139-001D4V differential pressure transducer. Malcus (2000) found a linear relationship between the radial pressure drop in the annular bed and the solids circulation rate. Malcus (2000) measured the solids circulation rate in the CFB by closing a porous butterfly valve in the CFB standpipe and measuring the height of solids accumulated on the valve over a known period of time. However, this method is disadvantageous because it interferes with the system by causing a drop of the solids inventory in the standpipe. This drop in the solids level reduces the pressure build-up in the standpipe, and thus causes a reduction in the solids circulation rate in the CFB. It is obvious, then, that a less-intrusive calibration technique is desired to improve the accuracy of the measured solids circulation rate in the CFB.

In the present study, measurement of the solids circulation rate was performed by measuring the local net solids flux (upflow – downflow) across the radius of the riser and integrating the resulting profile using Euler's method. The same technique and methods described in Chapter 3 of this report were used for measurement of the local solids upflow and downflow. Although the solids inventory in the standpipe was significantly lower during the calibration experiments than that used in most experiments, Maclus (2000) found that there was no effect of the solids inventory on the relationship between the radial pressure drop in the annular bed and the solids circulation rate. For the 10 experiments performed, the solids circulation rate was plotted against the recorded pressure drop in the annular bed to allow for on-line calibration of the solids circulation rate (Figure 2-4). Commensurate with the work of Malcus (2000), a linear calibration between the measured solids circulation rate and the annular bed pressure drop was developed. The equation describing the relation between the solids circulation rate in the riser and the pressure drop in the annular bed is:

$$G_s = 0.0516 \cdot \Delta P + 94.4 \qquad (2.1)$$

The maximum riser solids circulation rate that could be measured using this technique was 243 kg/(m^2·s). Beyond this circulation rate, choking in the upflow probe necessitated an increase in the sampling gas velocity well beyond the superficial gas velocity in the riser. Aguillon *et al.* (1995) found that if an interfacial probe velocity higher than the gas superficial velocity in the riser is used, there is an overestimation of the local solids flux. Therefore, calibration was terminated at solids circulation rates in excess of 243 kg/(m^2·s) to avoid bias error in the calibration. For later experiments requiring solids circulation rates beyond those measured in the calibration, the linear calibration curve was extrapolated to predict the values of the solids circulation rate.

Comparison between the solids circulation rates measured by the local mass flux measurement technique used in the present study and other techniques have been reported by Herb *et al.* (1992), Rhodes *et al.* (1988), and Issangya *et al.* (1998). The reported accuracy of the measured solids circulation rate and the standard method used to compare the measurement are presented in Table 2-1. As can be seen from the table, measurement of the local solids flux profiles reasonably correlates to the measurement using other techniques.

In the present study, uncertainty associated with the calibration of the solids circulation rate is derived from two sources: reproducibility of the local solids flux measurements (both upflow and downflow) and deviations of the experimentally determined solids circulation rate from that predicted by the linear calibration curve. Uncertainties are determined using the root-sum-square approach. The 95% confidence interval of the solids circulation rate determined using this method is 38 kg/(m^2·s) in the riser, 20 kg/(m^2·s) in the standpipe, and 9.0 kg/(m^2·s) in the stripper.

2.3 Riser Gas Velocity

An orifice meter, located along the 0.102 m I.D. inlet tubing to the CFB riser, is used to determine the superficial gas velocity of air in the riser. The orifice plate is built according to the American Society of Mechanical Engineers standards. The orifice has a diameter of 0.030 m. The pressure drop across the orifice is measured using an Omega PX139-001D4V differential pressure transducer. The gauge pressure of the orifice is measured on the upstream pressure tap and the temperature of the air is measured using a thermometer inserted into the inlet piping. Measurement of these variables allows for calculation of the gas density. The volumetric flowrate through an orifice meter is given by the equation:

$$Q = C_D e A_o \sqrt{\frac{2\Delta P \rho_g}{1-\beta^4}} \qquad (2.2)$$

The coefficient of dischange, C_D, was calculated by McKeen (2003a) to be a constant value of 0.60 for riser superficial velocities ranging from 3.8 to 15.2 m/s. β, defined as the ratio of the orifice diameter and the piping diameter, has a value of 0.294. The expansion factor, e, accounts for changes in air density in the orifice. It is determined from the equation:

$$e = 1 - (0.41 + 0.35\beta^4)\frac{\Delta P}{\kappa P_1} \qquad (2.3)$$

The isentropic exponent, κ, is a function of the air temperature and pressure. For air behaving as an ideal gas, the isentropic exponent takes on a constant value of 1.4. To find the riser superficial gas velocity, the volumetric flowrate determined from equation 2.2 is divided by the cross-sectional area of the riser.

2.4 Particle Characterization

The particles used in the experiments are FCC catalyst. These particles were chosen because they are same type of particle used in industrial FCC operations. The key particle properties are listed in Table 2-2. The bulk density of the catalyst was found by weighing a known volume of catalyst. The values for the packed and fluidized bed voidages are typical for FCC catalyst (Malcus, 2000, McKeen 2003). The Sauter mean diameter of the particles was determined from particle size analysis using a Malvern® Mastersizer S Long Bench (Figure 2-5). The minimum fluidization velocity, U_{mf}, was found using the correlation of Baeyens & Geldart (1974):

$$U_{mf} = \frac{\left(\rho_p - \rho_g\right)^{0.934} g^{0.934} d_p^{1.8}}{1110 \mu^{0.87} \rho_g^{0.066}} \tag{2.4}$$

The minimum bubbling velocity, U_{mb}, was found using the correlation of Abrahamsen & Geldart (1980):

$$U_{mb} = 2.07 \exp\left(0.716F\right)\left(\frac{d_p \rho_g^{0.06}}{\mu^{0.347}}\right) \tag{2.5}$$

The variable 'F' represents the fraction of particles smaller than 45 μm. This fraction consists of 4.43% of the FCC catalyst used in the experiments.

2.5 Design and Troubleshooting

2.5.1 Hybrid Standpipe

In hybrid standpipes, it has been observed that separation of the gas and solids occurs along the inclined section of the standpipe (Karri & Knowlton, 1993). Gas bubbles rise to the top of the inclined section, while solids occupy the lower portion. At low aeration rates Karri and Knowlton (1993) found that the bubbles moved downward with the flowing solids; while at elevated aeration rates the bubbles were observed to move counter-current to the downflowing catalyst. Downflow of gas bubbles results in stable standpipe operation. However, upflowing bubbles can coalescence and form gas bridges at the top of the inclined section, which severely limit the attainable solids circulation rate in the standpipe (Karri & Knowlton, 1993, Karri *et al.,* 1995). Karri *et al.* (1995) found that gas bridging in the upper vertical section of a hybrid standpipe could be eliminated by employing a gas bypass line connecting the upper section of the angled standpipe to the freeboard section above the solids in the standpipe.

A schematic of the angled section employed in the hybrid standpipe of the experimental CFB can be seen in Figure 2-6. The angled section of the standpipe is 1.2 m long, angled at 45º. There is a 1.0 m long vertical section from the top of the angle that connects the standpipe to the stripper section. Aeration taps are located 0.18 m, 0.42 m, 0.66 m, and 0.90 m from the base of

the angled section. A 0.51 m I.D. air bypass line is located 0.95 m from the base of the angled section. The bypass line is inserted perpendicular to the angled section at the top of the tube, and exits to the freeboard section above the solids in the standpipe. A valve is located on the bypass line to control the amount of gas being bypassed to the freeboard.

Before installation of the aeration lines and the gas bypass, it was observed that defluidization of the catalyst occurred in the angled section. Defluidization was evidenced by oscillations of the solids stream in the angled section. Gas bridging was commonplace at the union between the angled section and the lower vertical section of the standpipe. Gas bridging resulted in low frequency oscillations in the standpipe pressure profile near the angled section and necessitated a shut-down of the CFB. After installation of the gas bypass, stable operation of the standpipe could be achieved.

2.5.2 L-Valves

The following is a summary of the work of Knowlton (1997) on the design and operation of L-valves in circulating systems. L-valves are the most common type of non-mechanical valves used in CFBs. They are commonly implemented at the base of the standpipe to control the solids circulation rate through the CFB. The solids flux is controlled by tuning the amount of aeration in the L-valve, which affects the pressure drop caused by the flow of solids through the valve. Solids are forced through the valve by drag forces imparted on the solids by the aeration and interstitial gases.

L-valves are most successfully applied to systems containing particle sizes between 100 and 5000 μm, corresponding to Geldart B and D particles. For smaller Geldart A particles, control of the solids flux is difficult because of their tendency to maintain a fluidized state for a short time even in the absence of fluidizing gas. This tendency to remain fluidized causes the particles to flow through the L-valve constriction like a liquid.

Two parameters are important in design of L-valves: the location of aeration on the vertical section, and the length of the horizontal section (Figure 2-7). Optimum results are obtained when aeration is added at a height above the centre-line of the horizontal section greater than 1.5 times the L-valve diameter. Adding aeration below this level results in gas bypassing; while adding aeration above this level necessitates excessive aeration to achieve the equivalent solids flux. In some cases, aeration is also added along the horizontal section of the L-valve. The length of the horizontal section of the L-valve is crucial for encouraging a smooth flow of solids. If the horizontal section is too long, intermittent slugging of solids can occur. The minimum length of the horizontal section is based on the angle of repose of the solids in the system, θ_R. The horizontal length should be in the range of 1.5 – 2 times H_{min}, where H_{min} is defined as:

$$H_{\min} = \frac{D}{\tan(\theta_R)} \tag{2.6}$$

The purpose of applying L-valves in the experimental CFB was not for control of the solids flux through the system, but rather as a means of solids conveyance from the primary and secondary cyclone into the downcomer. The L-valve, rather than a conventional vertical cyclone

dipleg, was required because the cyclones were external to the downcomer. This required transporting solids over a horizontal distance in order to empty into the downcomer. Full design specifications for the primary and secondary cyclone L-valves can be found in Table 2-3. The horizontal separations between cyclones and the downcomer necessitated a horizontal length of 0.53 and 0.29 m for the primary and secondary cyclone L-valves, respectively. These horizontal lengths exceed the proper design specifications presented earlier. The primary cyclone L-valve should have a horizontal section measuring between 0.22 m and 0.30 m, while the secondary cyclone L-valve should have a horizontal section measuring between 0.18 m and 0.24 m.

The original locations of the aeration for the cyclone L-valves was along the centerline for the primary cyclone L-valve, and at L/D = 3.5 and along the centerline for the secondary cyclone L-valve. While this scheme resulted in satisfactory performance for the secondary cyclone L-valve, defluidization was found to occur in the primary L-valve. Defluidization resulted in accumulation of solids in the primary cyclone. As a result, intermittent slugging of solids was observed to occur. Slugging resulted in a high velocity slug of solids to pass through both the primary and secondary cyclone. This intermittency in the operation of the L-valves caused back-pressure in the system, which in turn caused oscillations of the solids circulation rate in the CFB. These oscillations required shut-down of the apparatus. To remedy the slugging behaviour in the primary cyclone L-valve, five aeration taps were added to the horizontal section of the L-valve. Taps were placed on 60º angles and separated by distance of 0.0075 m. This aeration scheme resulted in stable operation of the CFB.

2.5.3 Helium Sparger Grid

Ensuring an even distribution of helium into the downflowing catalyst stream is paramount in the proper design of an experimental stripping program. Previous studies (i.e. Cui *et al.,* 2006) have used point injection of helium into the catalyst stream. Point injection would result in a high concentration of helium tracer at the point of injection. It is possible that excessive amounts of helium could easily be stripped from the catalyst stream before becoming properly mixed across the stripper cross section; thus resulting in higher than expected stripping efficiencies. To avoid this, a gas sparger grid was designed for injecting helium tracer above the stripper.

A sparger grid is commonly used in cylindrical FCC strippers to provide stripping steam. A header, connected to an external gas supply, supplies air to several ‘fingers’ extending to the periphery of the stripper vessel (Figure 2-8). The manifold and fingers contain orifices through which gas can enter the catalyst stream. The guidelines of Karri & Werther (2003) were used to design the sparger grid.

To ensure even distribution of gas into the catalyst, the pressure drop across the grid is typically designed to be 30% of the bed pressure drop. Full design specifications can be seen in Table 2-4. A median bed height of 1.2 m was assumed for the design, and the desired gas flowrate was assumed to be $3U_{mb}$. The orifice velocity was calculated using the equation (Kunni & Levenspiel, 1991):

$$U_{or} = C_{Dor}\sqrt{\frac{2\Delta P_d}{\rho_g}} \tag{2.7}$$

A typical value of 0.8 was used for the coefficient of discharge (Karri & Werther, 2003). The relation between the number of orifices and the orifice diameter is given by:

$$D_{or} = \sqrt{\frac{4Q}{\pi N U_{or}}} \tag{2.8}$$

A triangular orifice pitch was used in the sparger grid. The grid orifice pitch, L_{or}, is related to the orifice density (orifices per unit area of bed), N_d, through the relation:

$$L_{or} = \left(N_d \sin 60^\circ\right)^{-1/2} \tag{2.9}$$

The approximate number of orifices in the sparger grid sized for the stripper is given by:

$$N = N_d A_{strip} \tag{2.10}$$

For the design, 84 holes of 1.4 mm diameter were chosen. This results in an orifice velocity of 54 m/s. The relation between the header diameter and the diameter of the fingers is given by:

$$\left(\frac{D_{header}^2}{N_{fingers} D_{fingers}^2}\right)^2 > 5 \tag{2.11}$$

For the design, it was desirable to have two headers so that four connections to the external air supply could be made. This was done so the force of the downflowing solids does not cause the grid to twist while in the column. The headers in the final design are 11 and 22 mm I.D.. Each quadrant of the grid contains five - 5 mm fingers extending from the 22 mm header to the periphery of the stripper (Figure 2-9).

2.5.4 Air Sparger Ring

To supply stripping air to the experimental stripper, an air sparger ring was designed (Figure 2-10). The sparger ring has four independently metered inlets for stripping air that connect to the ring. The sizing of the orifices in the ring is based on the median operating conditions used in the stripper: a bed height of 1.6 m and a superficial stripping gas velocity of 0.25 m/s. The criterion of Kunni & Levenspiel (1991) for designing air distributors in fluidized beds was used. Key design parameters are presented in Table 2-5.

Kunni & Levenspiel (1991) state that the pressure drop across the distributor should be 30% of the pressure drop caused by the fluidized head of solids in the bed. The orifice velocity is found from the equation 2.7. The coefficient of discharge, C_{Dor}, is based on the Reynolds number of the gas in an empty stripping vessel. For the calculated Reynolds number of 4200, the coefficient of discharge is 0.6. Based on the orifice velocity determined from equation 2.7, it is important to determine the stirring effect, α:

$$\alpha = \frac{\rho_g U_{or}^2 g}{2\Delta P_d} \tag{2.12}$$

If $\alpha > 1$, jetting occurs which results in gas bypassing through the bed. If $\alpha << 1$, the distributor does not contribute to solids mixing. The orifice velocity, U_{or}, is used to calculate the diameter of orifices and the number of orifices:

$$D_{or} = \sqrt{\frac{4U_{strip}}{\pi U_{or} N_{or}}} \tag{2.13}$$

For the present design, 28 orifices of 14 mm diameter were placed around the circumference of the ring.

2.5.5 Internal Cyclone

Cyclones are the most common gas-solids separation units. Particle-laden gas tangentially enters a cylindrical section and separation of gas and solids occurs due to the high inertia of the solids. Gas leaves the cyclone through the exit duct on the top of the unit, while solids leave through the underflow (Figure 2-11). The design of a cyclone is a compromise between high efficiency (being able to remove sufficiently small particles) and pressure drop.

The theoretical particle size removed at 50% efficiency, d_{pth}, is found by the equation (Pell & Dunson, 1997):

$$d_{pth} = \sqrt{\frac{9\mu\, B_c}{\pi N_s \left(\rho_p - \rho_g\right)}} \tag{2.14}$$

Equation 2.14 allows for calculation of the width of the rectangular inlet, B_c. All other dimensions of the cyclones are determined from the correlations presented in Table 2-6. The particle diameter removed with 50% efficiency in equation 2.14 applies to dilute systems. When an appreciable amount of solids are present, the efficiency increases due to smaller diameter particles being entrained with the larger diameter particles as they move towards the wall of the cyclone. The total pressure drop in a cyclone has five contributions: inlet contraction, particle acceleration, barrel friction, gas flow reversal, and exit contraction. Information on the calculation of these losses is provided by Pell & Dunson (1997).

Significant entrainment of particles from the stripper bed surface required installation of a cyclone. The dimensions of the cyclone can be found in Table 2-6. The cyclone was designed to remove 23 μm particles at 50% efficiency. All design guidelines of Pall & Dunson (1997) were followed, except for the exit duct diameter. The diameter of the exit duct was reduced in the design to account for the width of the exit duct tube. This was done because obstruction of the inlet duct can reduce cyclone efficiency.

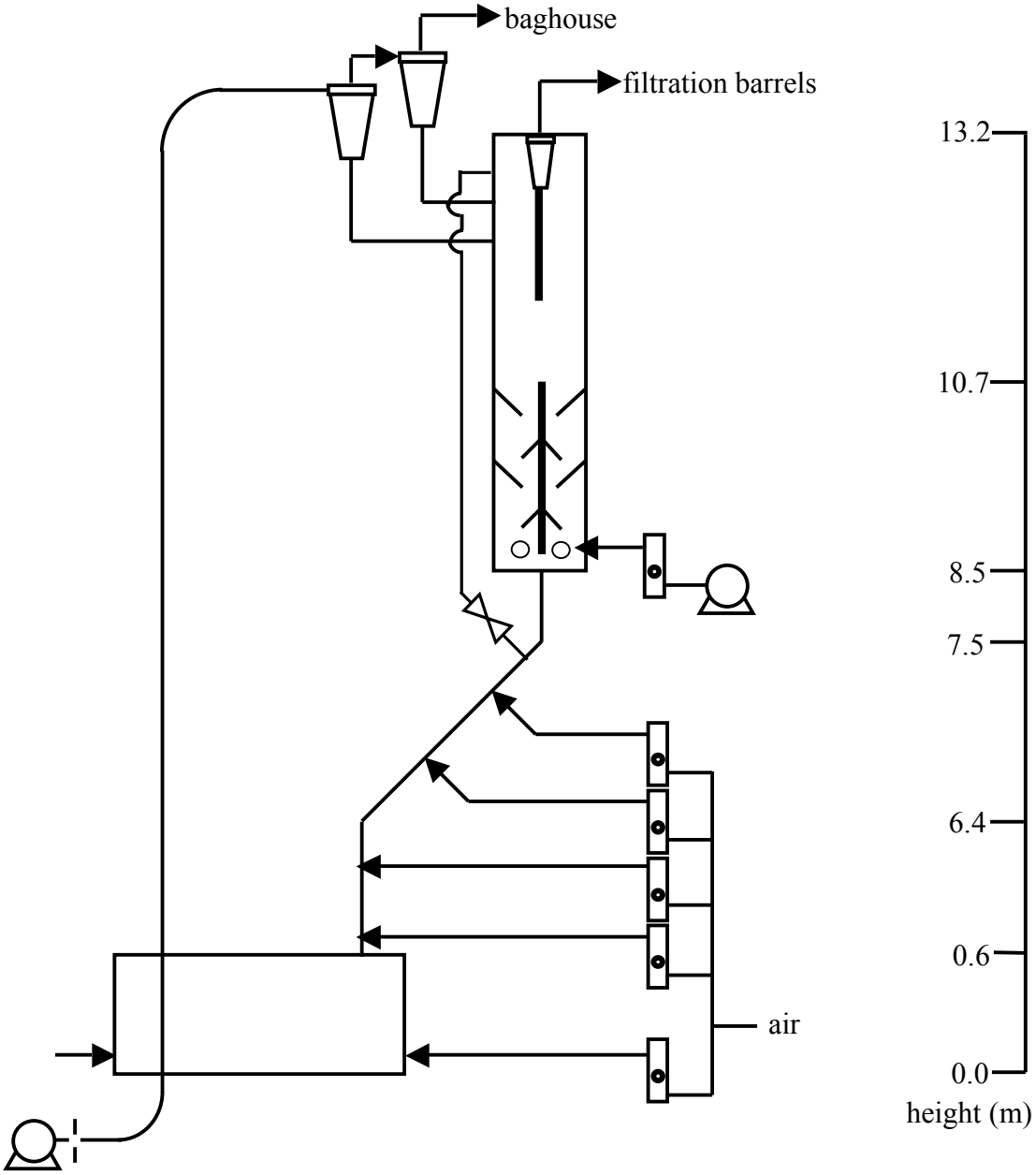

Figure 2-1: Diagram of the circulating fluidized bed used in experiments.

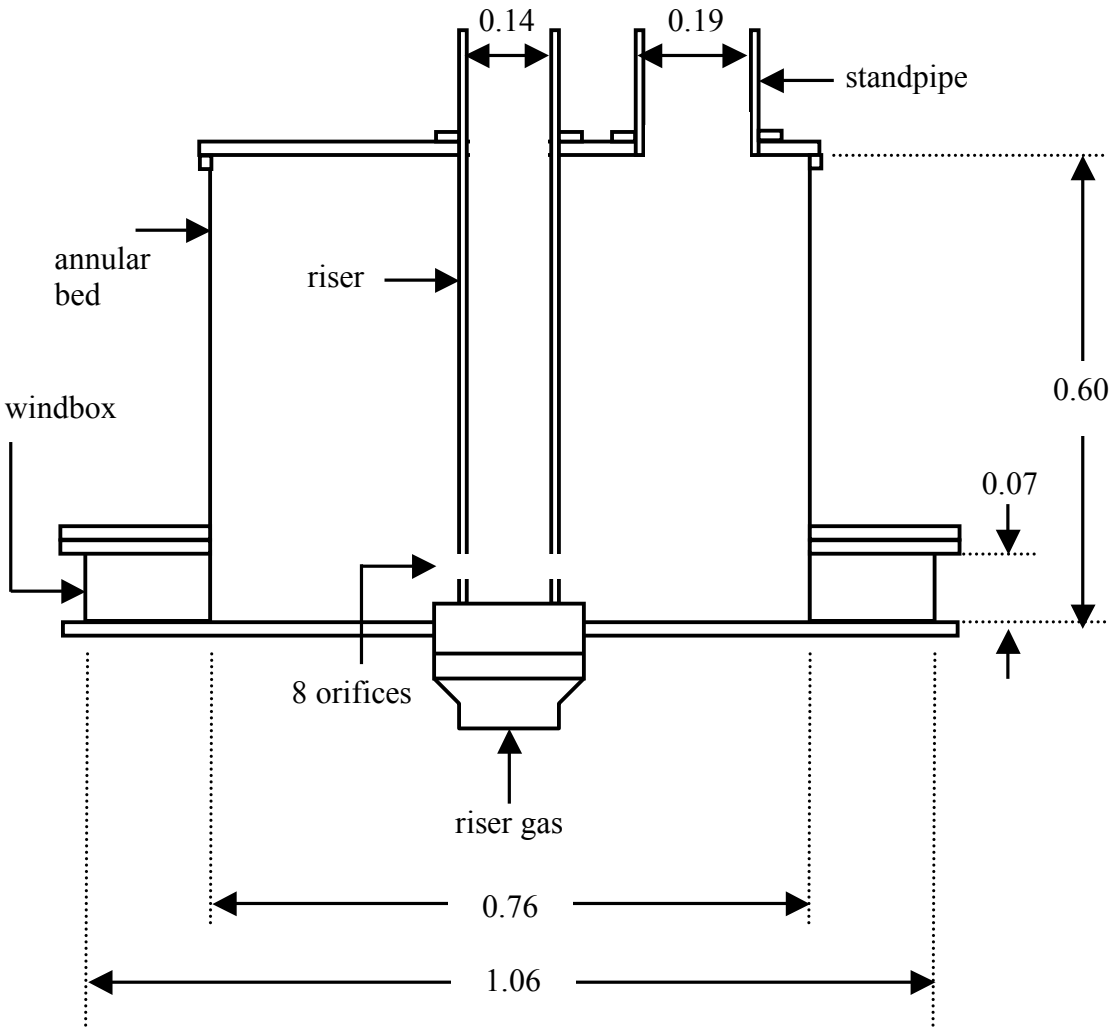

Figure 2-2: Annular bed used to control the solids circulation rate in the CFB.

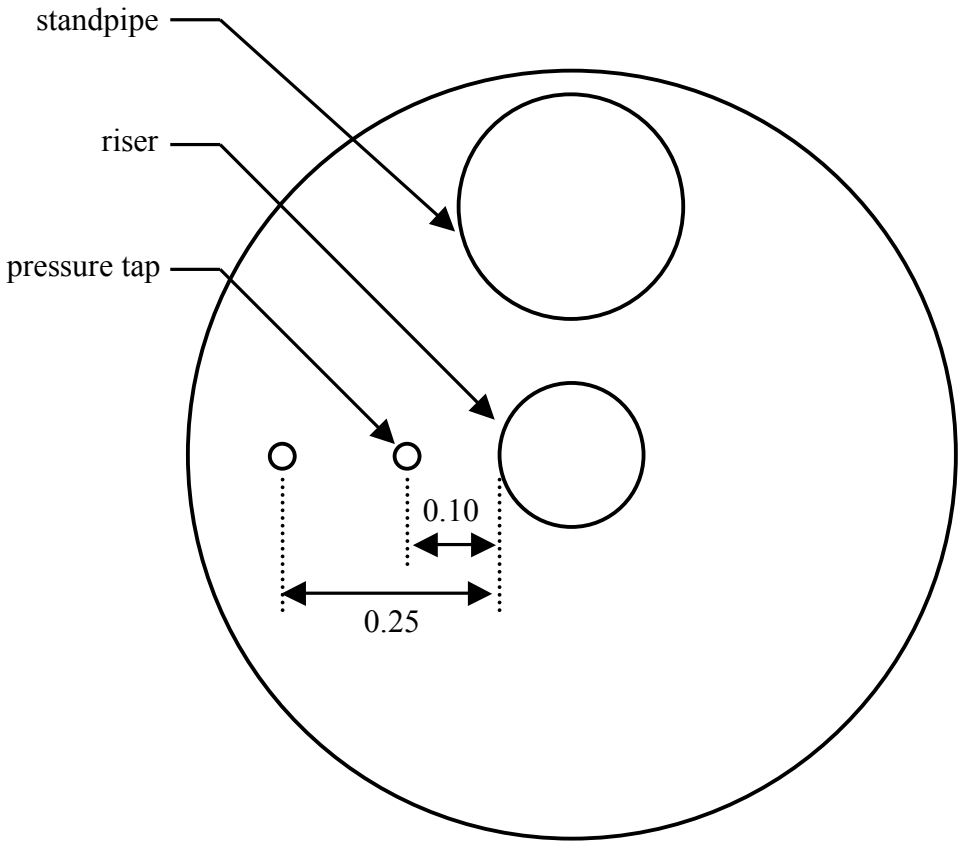

Figure 2-3: Location of pressure taps on the bottom of the annular bed. All dimensions in m.

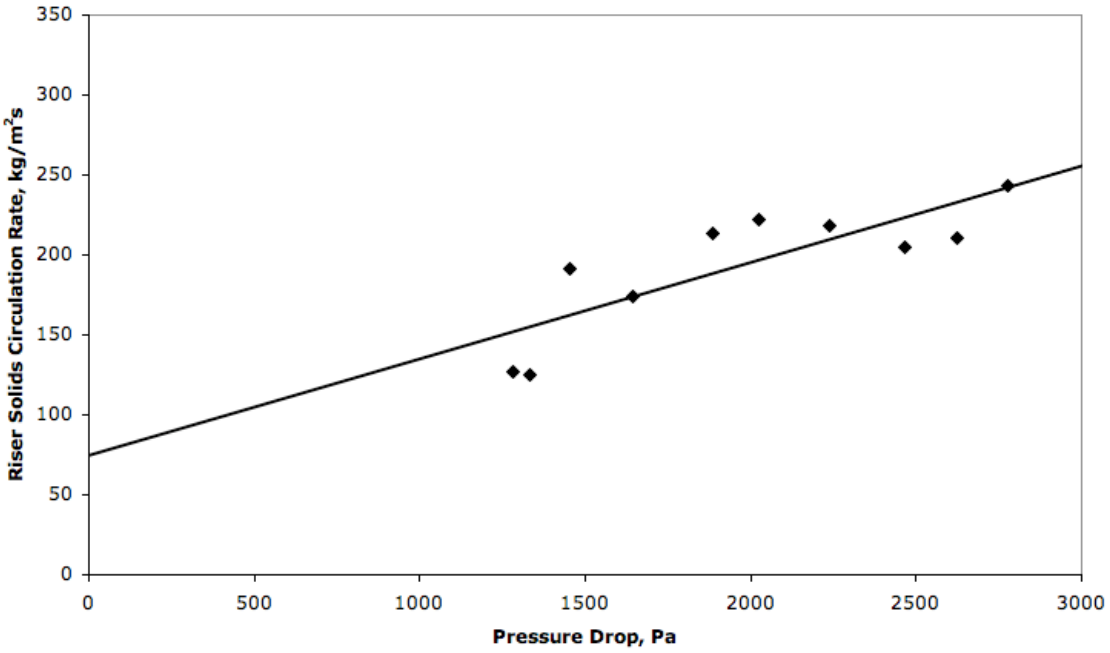

Figure 2-4: Relationship between the radial pressure drop in the annular bed and the riser solids circulation rate used for calibration in the CFB.

Table 2-1: Reported accuracy of the local solids flux technique for determining the solids circulation rate in a CFB.

Study	Standardizing Technique	Reported Accuracy
Herb *et al.* (1992)	unknown	20% difference for a single comparison
Rhodes *et al.* (1988)	Solids diverted into an external bed and weighed	Maximum 11.6% difference; always lower
Issangya *et al.* (1998)	Butterfly valve in standpipe	Average 25% difference

Table 2-2: Particle properties of the fluid catalytic cracking catalyst used in the experimental program.

Property	Value
Bulk density (kg/m^3)	975
Particle density (kg/m^3)	1550
Packed bed voidage (-)	0.37
Fluidized bed voidage (-)	0.45
Sauter mean diameter (μm)	98
Minimum fluidization velocity (m/s)	0.0059
Minimum bubbling velocity (m/s)	0.0094

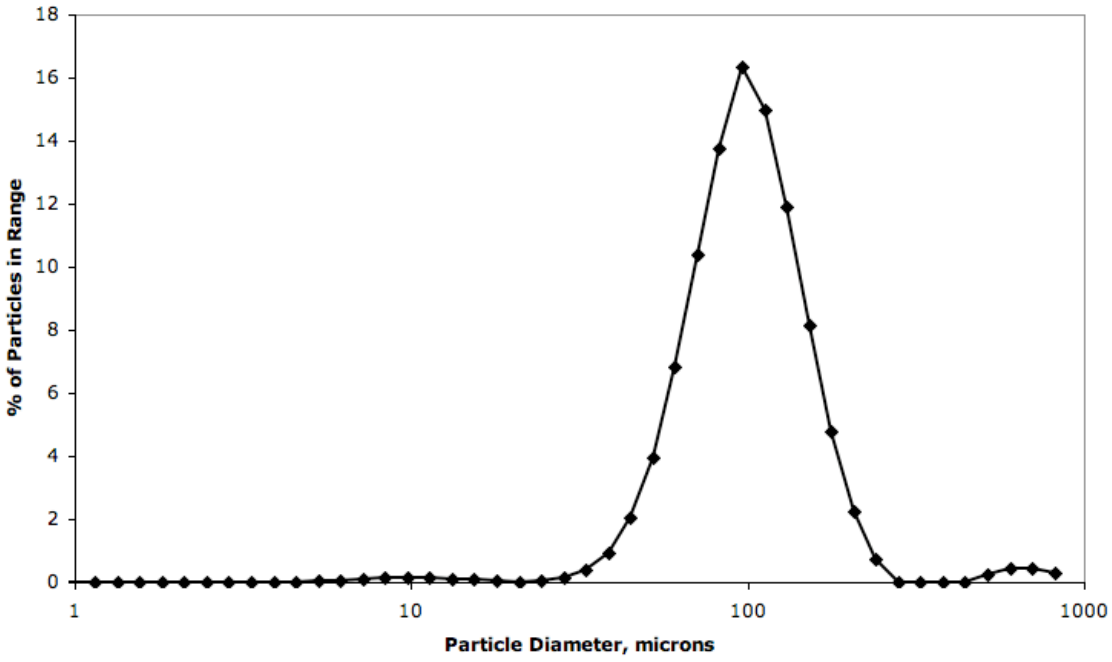

Figure 2-5: Particle size distribution of FCC catalyst used in experimental program.

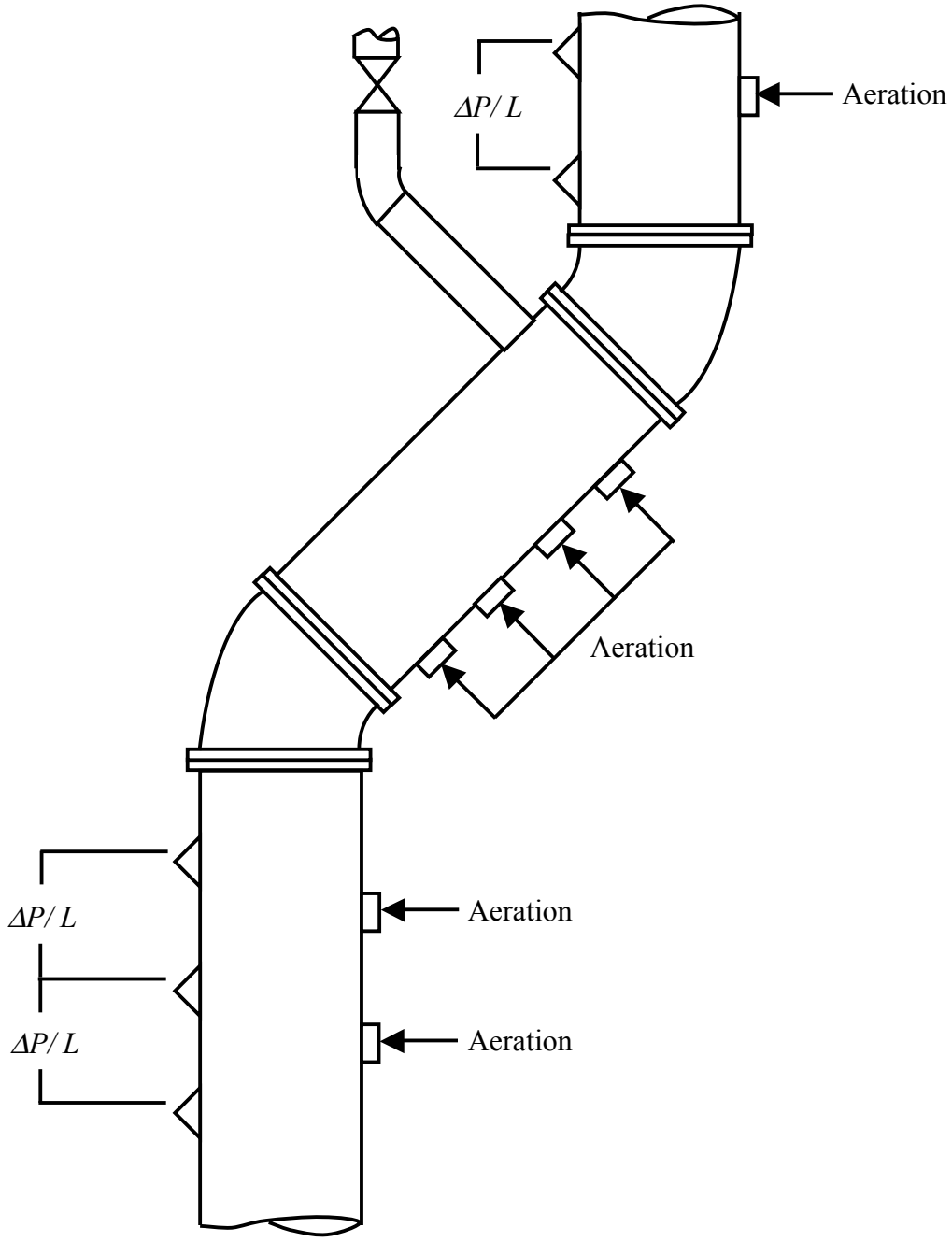

Figure 2-6: 45° inclined section of standpipe.

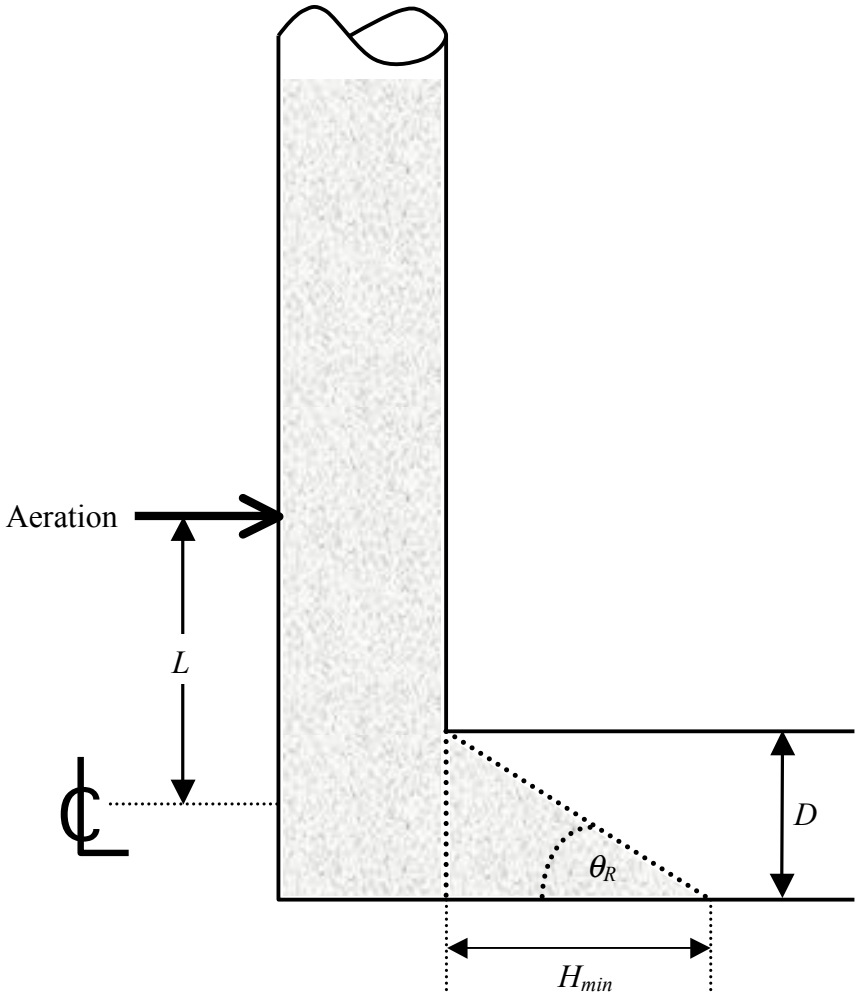

Figure 2-7: Typical L-valve design used in circulating fluidized beds.

Table 2-3: Design parameters of the L-valve on the primary and secondary cyclone underflow streams.

	Primary Cyclone	Secondary Cyclone
Inside diameter (m)	0.14	0.11
Vertical length (m)	0.07	0.53
Horizontal length (m)	0.53	0.29
H/H_{min}	3.6	2.4
Aeration location	• $L/D = 0$ • 5 - 60° inclined jets along horizontal	• $L/D = 3.5$ • $L/D = 0$

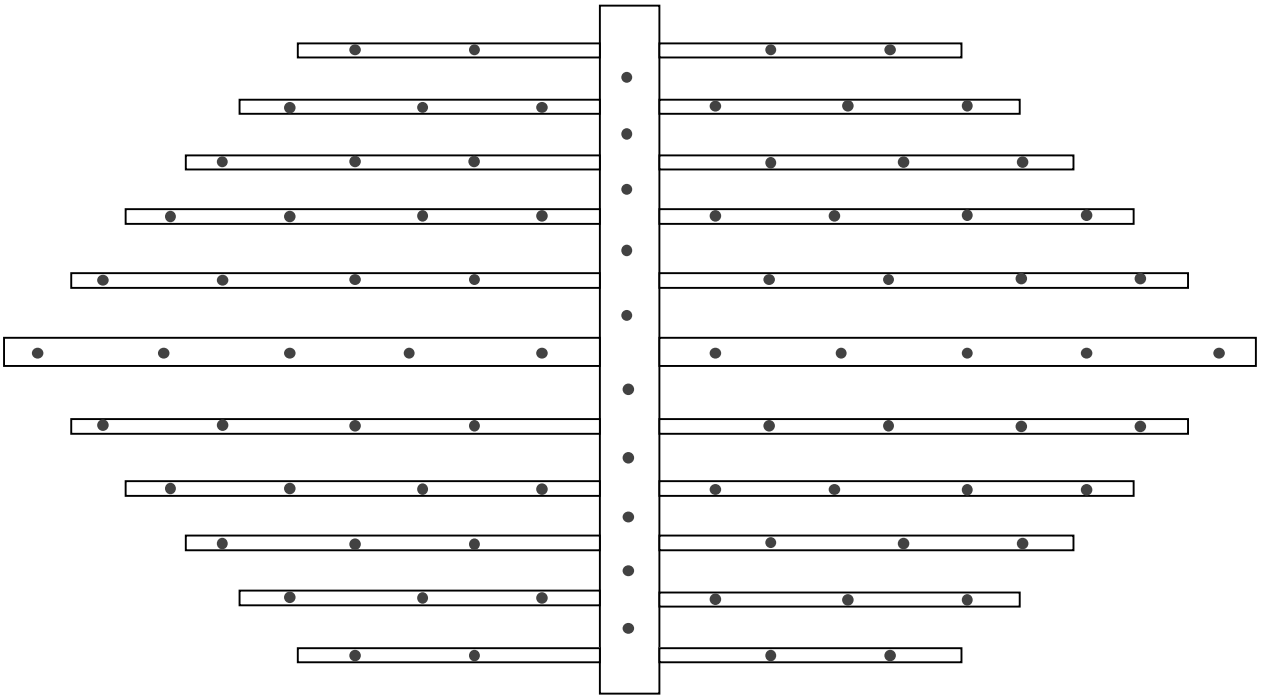

Figure 2-8: Sparger grid used to inject helium into emulsion phase.

Table 2-4: Design parameters of the helium sparger grid.

Parameter	Value
Grid pressure drop (Pa)	2719
Orifice velocity (m/s)	54
Number of orifices (-)	84
Orifice diameter (mm)	1.4
Orifice lateral spacing (mm)	27.9
Header diameters (mm)	11 & 22
Finger diameter (mm)	5
Number of fingers per quadrant (-)	5

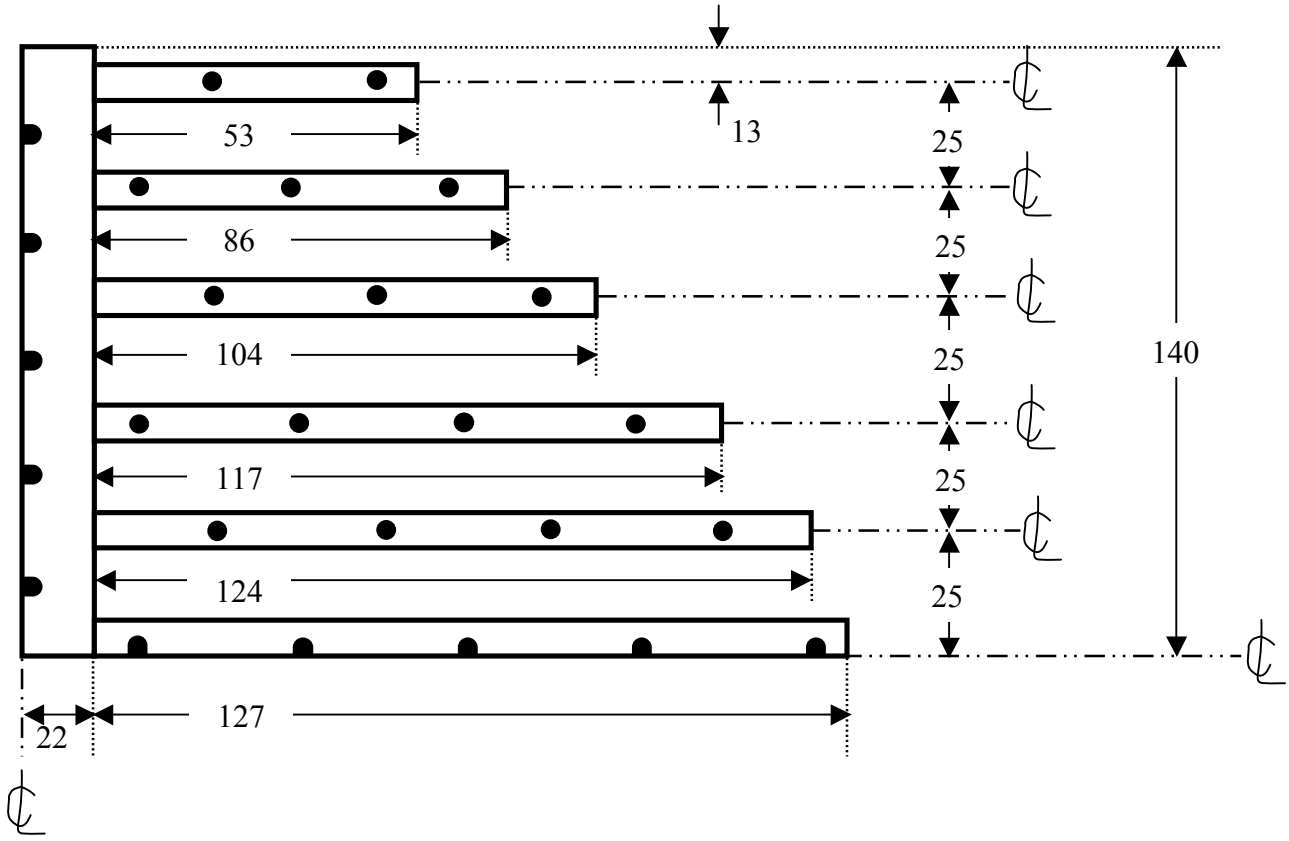

Figure 2-9: Dimensions of one quadrant of the sprager grid. All dimensions in mm.

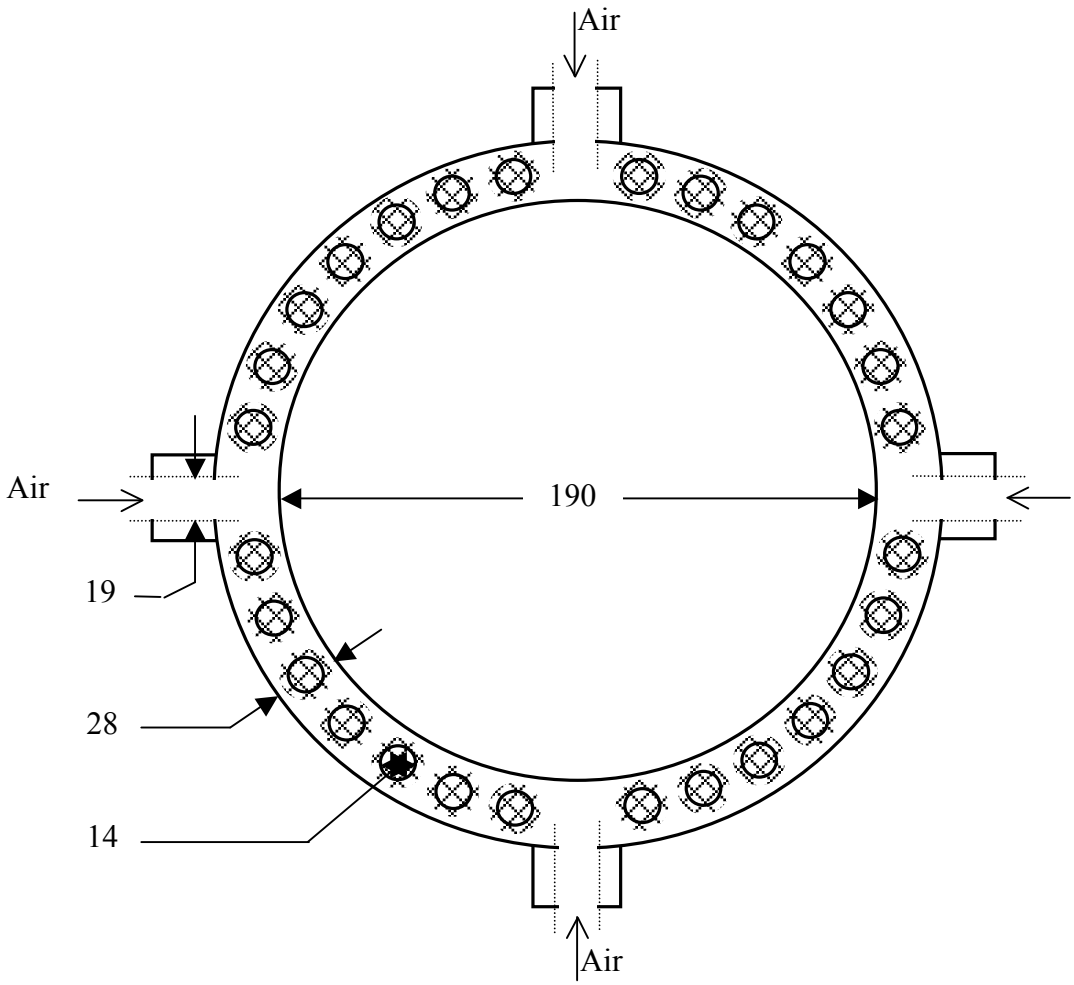

Figure 2-10: Air sparger ring used in the experimental stripper. All dimensions in mm.

Table 2-5: Design parameters of the air sparging ring in the stripper.

Parameter	Value
Diameter of sparging ring (mm)	28
Sparger pressure drop (Pa)	3900
Orifice velocity (m/s)	50.5
Coefficient of discharge (-)	0.6
Stirring effect (-)	0.36
Orifice diameter (mm)	14
Number of orifices (-)	28

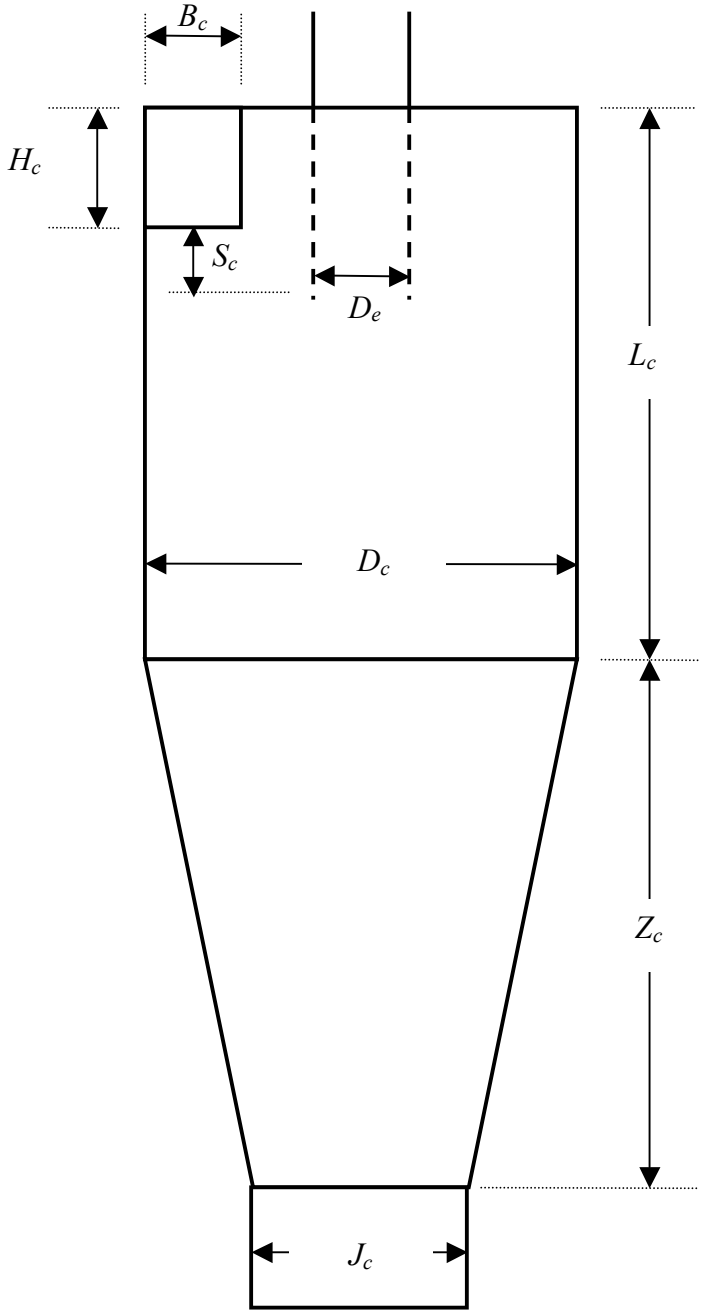

Figure 2-11: Diagram of the internal cyclone implemented in the stripper showing locations of the design dimensions.

Table 2-6: Design equations for cyclone (Pell & Dunson, 1997).

Parameter	Design equation	Dimension (mm)
Cyclone diameter	$D_c = 4B_c$	102
Cyclone exit duct diameter	$D_e = D_c/2$	38
Height of rectangular cone inlet duct	$H_c = D_c/2$	51
Length of cyclone cylindrical body	$L_c = 2D_c$	203
Offset between inlet duct footprint and exit duct	$S_c = D_c/8$	13
Length of conical body	$Z_c = 2D_c$	203
Diameter of solids outlet tube	$J_c = usually\ D_c/4$	25

Chapter 3 – Solids Flux Profiles in the High-Density Bottom Zone of a FCC Unit Riser

A summarized version of the contents of this chapter have been submitted to the 'Fluidization XIII: New Paradigm in Fluidization Engineering' conference for publication as a conference manuscript.

Contribution of the Ph.D. Candidate

Experiments were planned and performed by Jason Wiens. Dillon Petrucha provided some assistance for the experimental measurements. Todd Pugsley provided consultation regarding the experimental program. The software for data collection and analysis was developed by Jason Wiens. All of the writing of the submitted manuscript was done by Jason Wiens with Todd Pugsley providing editorial guidance regarding the style and content of the paper.

3.1 Objective

To date, the behaviour of the bottom zone of the CFB riser remains largely unexplored. From the available literature, it is apparent that two types of solids flux profiles are prevalent at high-density conditions: parabolic with net upflow at all radial locations, and parabolic with net upflow at the centerline and net downflow at the wall. However, radially uniform and U-shaped profiles are also known to exist. It is hypothesized that operation at moderate solids circulation rates and riser superficial gas velocities, which result in high-density conditions in the bottom zone of the riser, results in a parabolic net solids flux profile with upflow at all locations. The objective of this study is to examine the effect of solids circulation rate on the shape of the solids flux profiles in a high-density CFB riser. Solids flux profiles are examined for solids circulation rates of 125, 174, 213, and 243 kg/(m^2·s) operated at a constant superficial riser gas velocity of 5.3 m/s. The effect of the riser gas velocity on the solids upflow at the riser centerline is also tested. Riser gas velocities between 4.4 and 5.6 m/s are examined at a constant solids circulation rate of 187 kg/(m^2·s). Hydrodynamic inferences are made based on the location of maxima and minima in the solids flux profiles, as well as the overall shape of the profiles. The integrated net solids flux profiles also provide a means for measuring the solids circulation rate, used for calibration of the CFB apparatus discussed in Section 2.2.

3.2 Introduction

An understanding of the complex hydrodynamic behaviour in a circulating fluidized bed (CFB) riser is critical in design and evaluation of reactor performance. It is well accepted that the riser can be classified into four sections of unique hydrodynamic behaviour (Werther & Hirschberg, 1997). These sections, starting from the bottom of riser to the top, include: the bottom zone, the transition zone, the upper dilute zone, and the exit zone. By far the majority of the literature published to date has focused on the upper dilute zone. However, an understanding of the hydrodynamic behaviour of the bottom zone is of interest since it serves the important function of mixing gas and solids and atomized liquids before these mixtures enter the dilute zone of the riser. Proper mixing is important for optimum reactor performance.

Among the most obvious distinguishing characteristics of the bottom zone are its high density ($0.80 \leq \varepsilon \leq 0.90$ in the bottom zone versus $\varepsilon \leq 0.99$ in the dilute zone (Werther & Hirschberg, 1997) and unique hydrodynamic behaviour compared to that of the dilute zone. The hydrodynamic behaviour in a high-density bottom zone has historically been likened to that of either a bubbling (Svensson *et al.,* 1996) or turbulent fluidized bed (Bai *et al.,* 1995). More recently, however, there has been a movement away from this standard classification. Zhu & Zhu (2008) concluded that a single regime classification did not apply to their high-density bottom zone. They found that the hydrodynamic behaviour showed a gradual transition from a dilute phase transport regime to the turbulent flow regime when moving from the riser centerline to the wall. Grace (2000) has pushed to re-classify the behaviour in the high-density bottom section of a CFB riser as a distinct fluidization regime, termed ‘dense suspension upflow’ (DSU). Unique to the DSU regime is that a net upflow of particles occurs at all radial locations. Other distinguishing characteristics of DSU are that the flow is more homogeneous and there is a higher gas-solids slip velocity than that observed in turbulent fluidization (Grace, 2000).

One common method of analyzing flow properties in the CFB riser is through the use of solids flux probes. This technique provides valuable information on the local solids mass flux in the riser, a crucial element for understanding local gas and solids mixing and slip. Table 3-1 presents a summary of the past studies and current study examining the solids flux profiles in the bottom zone of the riser. From the table, it can be seen that the present study employs a range of operating conditions consistent with previous studies. However, the axial location of the measurement plane used in the current study is lower than most previous studies.

Issangya *et al.* (1998) examined the solids flux profiles in a 0.076 m inside diameter (I.D.), 6.1 m tall CFB containing FCC particles. Measurements were performed at solids circulation rates between 38 and 325 kg/(m^2·s) and gas velocities between 4.5 and 7.5 m/s. Experiments were performed at a measurement height of 2.8 m. For all conditions studied, they found that the solids flux profile was parabolic in shape with a maximum at the centerline and the minimum at the riser wall. For G_s > 170 kg/(m^2·s), increasing the solids circulation rate caused a corresponding increase in the local flux in the central region of the riser. Depending on the operating conditions, either net upflow or downflow near the wall was observed. Upflow was observed at voidages lower than 0.85, whereas downflow was observed at more dilute conditions. They reasoned that this was due to an increase in momentum transfer from the upflowing suspension in the central region to the increasingly dense phase near the wall.

Karri & Knowlton (1999) examined the effect of the solids circulation rate and gas velocity on the net solids flux profiles in a 0.3 m I.D., 13 m tall CFB riser containing FCC particles. The CFB was operated at solids circulation rates ranging from 49 to 586 kg/(m^2·s) and riser gas velocities ranging from 4.6 to 18.3 m/s. Measurements were made at a height of 3.7 m; slightly higher than their dense bed height of 2 m. Operating at a constant gas velocity of 4.6 – 4.9 m/s, they found that a parabolic net solids flux profile was prevalent for the range of solids circulation rates tested. These parabolic profiles had a maximum flux at the centerline and downflow at the wall. When increasing the solids circulation rate, the largest increase in the net flux profile was observed in the central region whereas relatively little change was observed at the wall. Karri and Knowlton (1999) also examined the effect of changing the gas velocity from 4.9 to 18.3 m/s on the net solids flux profiles while maintaining a constant solids circulation rate of 583 kg/(m^2·s). They found that as the gas velocity was increased from 4.9 to 12.2 m/s the solids flux profile changed from parabolic with downflow at the wall to a flat profile with upflow at all radial locations. Further increase to 18.3 m/s resulted in U-shaped profile where the maximum of the profile was located at the riser wall, and minimum at the centerline.

Wei *et al.* (1997) measured solids flux profiles in their 0.19 m I.D., 8.5 m tall CFB riser containing FCC particles. The riser was operated at solids circulation rates ranging from 18 to 235 kg/(m^2·s) and gas velocities ranging from 1.8 to 10.5 m/s. Measurements were made at heights of 1.8 and 3.9 m corresponding to the bottom zone and dilute zone, respectively. They identified three different solids flux profiles in their work: parabolic/core-annular, radially uniform, and U-shaped. The parabolic/core annular profile was reported at voidages of 0.77 and 0.95 in the bottom zone and dilute zone respectively. In this case, the riser gas velocity was 2.5 m/s and the solids flux was 101 kg/(m^2·s). In the lower measurement plane, increased downflow was observed at the wall and increase upflow in the central region compared to that of the higher measurement plane. The radially uniform solids flux profile was only reported at elevated bed

voidages ($\varepsilon = 0.97$) in the upper measurement plane. This type of profile is characterized by a near-constant local solids flux across the entire riser cross-section, with upflow at all locations. Like the radially uniform profile, the U-shaped profile was found to exist only at high bed voidages ($\varepsilon \geq 0.97$). This high bed voidage was observed at combinations of high riser gas velocities ($6.9 \leq U_{riser} \leq 10.1$ m/s) and low solids circulation rates ($48 \leq G_s \leq 127$ kg/(m^2·s)). The U-shaped profile had the maximum local solids flux at the wall and the minimum at the centerline.

Malcus *et al.* (2002) measured solids flux profiles in a 0.14 m I.D., 7.0 m tall CFB riser containing FCC particles. The riser was operated at solids circulation rates ranging from 148 to 264 kg/(m^2·s) and a constant gas velocity of 4.7 m/s. The solids flux profiles were measured at heights of 1.6 and 2.1 m, the lowest reported in the literature. The bed voidage at the 1.6 m measurement height ranged from 0.88 to 0.81 for solids circulation rates of 148 and 264 kg/(m^2·s) respectively. At the measurement height of 2.1 m, the bed voidage ranged from 0.95 to 0.81 for the same range of solids circulation rates. In all cases, with the exception of $G_s = 148$ kg/(m^2·s) at the upper measurement plane, net upflow was observed at all radial locations. For both measurement planes, the solids flux profiles were found to be mostly parabolic in shape at radial locations $0 \leq r/R \leq 0.87$ for most of the solids circulation rates tested. For $G_s \geq 184$ kg/(m^2·s) a sharp increase in the net flux was observed at $r/R > 0.87$. Malcus *et al.* (2002) described the overall shape of these profiles as being 'hook' shaped. A complementary study of solids mixing by Malcus & Pugsley (2001) found a high degree of lateral solids flux towards the wall at the same axial position. They reasoned that the high local solids flux at the wall could be achieved by a high concentration of particles in the wall region, caused by a high lateral solids flux, moving at a high particle velocity. Malcus *et al.* (2002) found that moving from the lower to the upper measurement plane resulted in a redistribution of solids upflow from the wall region to the central region. This resulted in a less pronounced hook shape in the flux profile at the upper measurement plane. They concluded that the hook in the local solids flux at the wall was characteristic of a developing flow in the dense bottom zone of the riser.

Based on the findings of the previous studies, it is evident that several types of radial solids flux profiles may exist in the bottom region of a CFB riser: parabolic in shape with net downflow near the wall, parabolic with net upflow at all locations, radially uniform, and U-shaped. At high-density conditions, parabolic profiles with either upflow or downflow are prevalent (Issangya *et al.,* 1998, Malcus *et al.,* 2002). Radially uniform and U-shaped profiles have been reported by Wei *et al.* (1997) and Karri & Knowlton (1999), however they have only been found to exist at high bed voidages and/or combinations of high gas velocities and low solids circulation rates.

To date, there have been a limited number of studies examining the flow behaviour in the bottom zone of a CFB riser. Amongst the available literature, there is no clear consensus on the prevailing flow regimes. The aim of this study is to present data on the solids flux profiles in a high-density bottom zone of a CFB riser to further the understanding of the complex behaviour of the bottom zone of a CFB riser. Hydrodynamic inferences are made based on the location of maxima and minima in the solids flux profiles, as well as the overall shape of the profiles.

3.3 Experimental

Measurement of the net solids flux requires both the upflow and downflow of solids be known at a single measurement plane in the CFB riser. The upflow and downflow measurement probes were inserted into the riser at a height of 1.6 m above the riser gas distributor plate. The upflow probe was inserted horizontally into the riser, whereas the downflow probe was inserted at a -45° angle to the horizontal.

A schematic of the upflow probe can be seen in Figure 3-1. The probe is similar in construction to those used in previous studies (Wei *et al.,* 1997, Aguillon *et al.,* 1995, Malcus *et al.,* 2002). The upflow probe is constructed of 6.4 mm O.D., 4.6 mm I.D. stainless steel. The probe has a 0.29 m horizontal section, after which a -90° bend creates a 60 mm vertical probe section. The open end of this section is the measurement tip of the upflow probe. Purge air is added downstream of the probe to prevent solids from entering the probe when measurements are not being taken. Purge air is metered using a Dwyer® RMA-23 rotameter, and on/off control of the aeration air into the probe is achieved using a Swagelok® B-1GS4 toggle valve. Downstream of the purge air injection point, a Swagelok® B-4P4T plug valve allows for on/off control of solids entering the solids collection jars. The plug valve is connected via 4.3 mm I.D. polyethylene tubing to the solids collection jars. The primary solids collection jar is a sealed 1000 mL pyrex container, while the secondary jar is a sealed 500 mL plastic container. Two collection vessels are necessary to prevent solids from being entrained with the sample air and exiting the solids collection system. Downstream of the solids collection system, a Dwyer® RMA-21 rotameter measures the gas flowrate through the system. Sampling of gas and solids out of the CFB riser is accomplished using a vacuum pump. Care was taken during design of the solids upflow measurement system to ensure that there were no changes in the inside diameter between components, as this was found to cause probe choking in early experiments.

The gas flowrate through an upflow probe system is known to influence the measured local solids flux in regions of high density (de Diego, 1995, Rhodes *et al.,* 1988). In regions of low solids density, as typically observed at the riser centerline, there is practically no influence (Aguillion *et al.,* 1995, Rhodes *et al.,* 1988). Two modes of operation of solids flux probes are possible: isokinetic and non-isokinetic. Because the emulsion gas velocity is typically not known in the riser, non-isokinetic sampling is typically performed. Aguillion *et al.* (1995) found that if the suction velocity at the probe tip was matched to the riser superficial gas velocity, the solids circulation rate could be accurately predicted using non-isokinetic solids sampling probes. This finding is confirmed by Azzi *et al.* (1991), who stipulated that the suction velocity should be maintained within ±1.5 m/s of the superficial gas velocity to accurately predict the solids circulation rate. For this study, a non-isokinetic gas sampling approach was used.

De Diego *et al.* (1995), found that using a typical suction downflow probe resulted in severe overestimation of the downward solids flux in the near-wall region. To overcome this problem, Issangya *et al.* (1998) developed a gravity-based downflow probe. In the present study, a similar probe design as that of Issangya *et al.* (1998) was used (Figure 3-2). The downflow probe is constructed of 9.5 mm O.D. stainless steel. The measurement tip is cut on a 45° angle so that the probe face is horizontal when inserted into the bed. Part of the measurement tip is covered to minimize solids reflection back into the riser. The open area of the measurement tip is

25.7 mm^2. The probe consists of a horizontal section that has a -45° bend located 240 mm from the measurement tip. A 9.5 mm ball valve, located 50 mm from the -45° bend, allows for on/off control of the solids entering the solids collection system. The ball valve is connected to a sealed 500 mL Erlenmeyer flask, used as the solids collection jar, via 6.4 mm I.D. Tygon® tubing. Because any solids that enter the collection jar must displace an equal volume of air out of the jar, the collection jar was connected via polyethylene tubing back to the riser. The air bypass was connected at the same axial position as the downflow measurements so to not induce a pressure gradient in the sampling system that would result in convective air flow. Aeration was added 200 mm from the measurement tip. Similar controls and meters were used for the downflow aeration as in the upflow aeration.

The local solids flux profiles were tested at solids circulation rates of 125, 174, 213, and 243 kg/(m^2·s) and a constant superficial riser gas velocity of 5.3 m/s. The effect of the riser gas velocity on the solids upflow at the riser centerline was also tested. Riser gas velocities between 4.4 and 5.6 m/s were examined at a constant solids circulation rate of 187 kg/(m^2·s). Measurement of the solids upflow and downflow were conducted at an axial position of 1.6 m above the riser air distributor plate.

3.4 Results

3.4.1 Effect of Gas Sampling Velocity

Figure 3-3 presents the effect of sampling gas velocity on the measured local solids mass flux for two radial position, r/R = 0.00 and r/R = 0.87. From the figure, it can be seen that there is little effect on the measured flux at the centerline. This is consistent with the findings of Aguillon *et al.* (1995) who found little effect of the sampling velocity on measured flux in the dilute central region of the riser. In the wall region, however, the measured flux is clearly affected by the sampling velocity. This is consistent with the findings of de Diego *et al.* (1995) for solids sampling in the dense region of the riser. This highlights the importance of selecting the proper gas sampling velocity on the measured solids flux.

3.4.2 Solids Concentration Profiles

Figure 3-4 presents the solids concentration profiles for the range of solids circulation rates tested. The solids concentration is calculated from the measured differential pressure along the axis of the riser. The profiles show that the measurement plane is contained in the high-density bottom zone of the CFB riser. The term ‘high-density’ generally refers to solids concentrations of 10% or higher in the riser. Solids concentrations of 0.12, 0.15, 0.16, and 0.16 were found at the measurement plane for solids circulation rates of 125, 174, 213, and 243 kg/(m^2·s), respectively.

3.4.3 Solids Flux Profiles

The upflow and downflow profiles in the CFB riser are presented in Figure 3-5a,b, respectively for solids circulation rates ranging from 125 to 243 kg/(m^2·s). The error bars in the

figures represent the 95% confidence intervals, derived from repeat measurements. To facilitate the discussion, it is convenient to differentiate the profiles into two groups based on location of maxima and minima, as well as the overall shape of the profile. One group consists of solids circulation rates ranging from 174 – 243 kg/(m^2·s), while the other consists of the solids circulation rate of 125 kg/(m^2·s).

The group consisting of solids circulation rates of 174, 213, and 243 kg/(m^2·s) show a maximum in the solids upflow profile (Figure 3-5a) at the wall and the minimum at the riser centerline. Increasing the riser solids flux results in a slight increase in the slope of the upflow profile, and a more pronounced 'hook' at the wall. The solids downflow profiles (Figure 3-5b) are sigmoidal in shape, with the maximum downflow occurring close to the riser wall and the minimum occurring at the centerline. There is no solids downflow present at the centerline. In this group, there is not a strong influence of the solids circulation rate on the local values in the downflow profile.

The upflow and downflow profiles for a solids circulation rate of 125 kg/(m^2·s) exhibit several distinctions to the group discussed above. While the maximum in the upflow profile (Figure 3-5a) still occurs at the wall, the minimum occurs at an intermediate radial position of r/R = 0.71. The downflow profile (Figure 3-5b) is parabolic, with the minimum downflow at the centerline and the maximum at the wall. This profile shows significant quantitative deviation in the local downward flux from the group composed of solids circulation rates of 174, 213, and 243 kg/(m^2·s). This, combined with the different overall shaped of the upflow and downflow solids flux profiles, suggest a change in bed behaviour occurs when increasing the flux from 125 to 174 kg/(m^2·s).

Although direct measurement of the hydrodynamic behaviour in the riser is not possible using the solids flux probe method, several inferences can be made. The lack of solids downflow and the relatively low amount of solids upflow at the centerline suggests the formation of a dilute core with a high particle velocity. Moving towards the wall region, the increased intermittency of the flow (both upflow and downflow) suggests an increase in bed density with a lower particle velocity. These observations appear consistent with the findings of Zhu & Zhu (2008) that there exists a dilute core that transitions to a dense bed towards the wall.

Figure 3-6 presents the net solids flux profiles for the range of solids circulation rates tested. For the range of solids circulation rates tested, net upflow is observed at all radial locations. This is characteristic of the DSU fluidization regime as defined by Grace (2000). For a solids circulation rate of 125 kg/(m^2·s), a maximum flux of 187 kg/(m^2·s) is observed at the centerline; decreasing to a minimum of 92 kg/(m^2·s) at r/R = 0.80. At r/R > 0.8, there is a flattening of the profile to the wall. The solids circulation rates ranging from 174 to 243 kg/(m^2·s) all have a local maxima at r/R = 0.36 and the global maxima at the riser wall. The minimum local flux over this range is found at an intermediate location $0.71 \leq r/R \leq 0.87$, however it is not significantly lower than the local flux observed at the centerline. There is, however, an apparent forming of a depression with increasing solids circulation at this intermediate radial position.

Superficially, the profiles presented in Figure 3-6 could be described as radially uniform or U-shaped. However, the riser solids concentration and gas velocity are inconsistent with those of Karri & Knowlton (1999) and Wei *et al.* (1997) when these types of profiles were observed. The solids concentration, solids circulation rate, and gas velocity are more consistent with authors who have observed parabolic shaped solids flux profiles (Malcus *et al.,* 2002, Issangya *et al.,* 1998). For this reason, it would be expected that the bottom zone in the current study would operate in a hydrodynamic regime more characteristic of parabolic solids flux profiles. However, it appears possible that a transition to a more radially uniform regime can occur at gas velocities and solids concentrations more typical of a high-density CFB riser.

For all solids circulation rates tested, the net flux profiles show little deviation in the local flux at the riser centerline. The values at the centerline range from a minimum of 181 kg/(m^2·s) to a maximum of 212 kg/(m^2·s) at solids circulation rates of 174 kg/(m^2·s) and 243 kg/(m^2·s), respectively. When increasing the solids circulation rate, the largest gain in the local solids flux profile is observed at the wall. This is consistent with the description of a developing flow in an FCC riser given by Parssinen & Zhu (2001). They found that flow development at the centerline in the bottom zone of a CFB riser is nearly instantaneous. In the wall region, however, they found that development is delayed by increasing the solids circulation rate through the riser.

Qualitatively, the solids flux profiles presented here are most similar to those of Malcus *et al.* (2002). To date, Malcus *et al.* (2002) are the only study to have found an increase in flux at the wall, resulting in the characteristic hook-shaped net flux profile. However, the net flux profiles presented here differ from those presented by Malcus *et al.* (2002) in the magnitude of the local solids flux near the riser wall and at central core (Figure 3-7a,b). It is seen from Figure 3-7a,b that the contribution of the local net solids flux to the total solids circulation rate in the present study are consistently lower than that of Malcus *et al.* (2002) at radial positions of $r/R < 0.60$. However, at radial positions of $r/R > 0.60$ the contribution of the local solids flux in the current study is always greater than that of Malcus *et al.* (2002). Malcus *et al.* (2002) concluded that the hook-shaped profile was indicative of early flow development in the riser, as they found a migration of solids from the wall to the centre with increasing height in the riser. Based on this conclusion, it is possible that the solids flux profiles in the current study are indicative of an earlier stage of flow development than that observed by Malcus *et al.* (2002).

Considering that the current study and that of Malcus *et al.* (2002) use a riser of equivalent diameter operated at similar solids circulation rates, it is worthwhile to consider why the solids flux profile indicate a lesser-developed flow than that of Malcus *et al.* (2002) at the same measurement height. The cause of the deviation appears to be a sharp transition in the hydrodynamic behaviour that occurs between a riser gas of 4.8 and 4.9 m/s in the riser. At this transition velocity, the local solids flux upflow at the centerline is found to drop precipitously from approximately 300 kg/(m^2·s) to less than 200 kg/(m^2·s) (Figure 3-8). This drop in the local flux indicates a transition from a more dense core to a more dilute core. However, the sharp transition to a more radially uniform regime found in this study is in contrast to the more gradual transition observed by Wei *et al.* (1997). This suggests that the profiles observed in the present work appear based on a different mechanism than that of Wei *et al.* (1997).

3.4.4 Influence of the Solids Feeding Device

Malcus *et al.* (2002) attributed the uniqueness of the hook shaped profile to the fact that they had conducted their measurements at the lowest axial locations presented in the literature, and thus was a phenomenon of flow development in the dense section of a CFB riser. In the present work, a similar conclusion has been reached. However, it is conceivable that the 'hook' shape is an artifact of the unique solids feeding devices used both by Malcus *et al.* (2002) and in the present study.

It has been well documented that the exit geometry affects the solids distribution in the fully-developed region near the exit of a CFB riser (Mabrouk *et al.,* 2008, van der Meer *et al.,* 2000, Reddy & Nag, 2001). The exit affect is usually manifested as an asymmetry in the voidage profile that dissipates upstream of the exit. Although the length of this exit affect is varied, in most cases it is observed over considerable distances. For example, Reddy & Nag (2001) observed an exit affect over 2 m of their 5.3 m riser. Although exit effects indicate that geometry can affect the solids distribution in CFB risers, the low solids concentration in the upper section of the riser is not indicative of the conditions in the dense bottom zone. Therefore, any conclusions reached by studying exit affects can only indicate a 'proof of concept' rather than in indication of the behaviour one would expect in the dense lower section.

To date, there has been much less attention given to the effect of solids feeding devices on the solids distribution profiles in the riser. Van Engelandt *et al.* (2007) examined the influence of the solids feeding device on the riser gas velocity profile at several axial positions in a 0.1 m I.D., 4 m tall riser operated at solids fluxes ranging from 0.5 to 4.5 kg/(m^2·s) and gas velocities ranging from 5.3 to 7.4 m/s. Their solids feeding device was a 35° inclined side inlet located between 0.38 and 0.54 m of the riser entrance. They found an asymmetrical gas velocity profile in the vicinity of their solids feeder with an off-centre maximum. Within 0.6 m of the riser entrance they found the velocity profile to become fully developed. Increasing the solids circulation or decreasing the riser gas velocity introduced larger gradients in the profile near the feeder, however they did not find it to significantly affect the length to fully develop the flow. Unlike the present study, however, the combination of solids circulation rates and riser gas velocities used by van Engelandt *et al.* (2007) led to dilute conditions in the riser. As such, the applicability of the findings of van Engelandt *et al.* (2007) to the present study is unknown.

Yan *et al.* (2003) examined the voidage distribution in a 0.07 m I.D., 10 m tall CFB riser operated at solids circulation rates between 50 and 550 kg/(m^2·s) and riser gas velocities between 5.5 and 10.0 m/s. Solids were fed to the riser using a -45° inclined transfer line located 0.17 – 0.25 m above the riser entrance. At a measurement height of 0.98 m, a symmetric voidage and solids velocity profile was found on a plane perpendicular to the feed introduction. However, along the plane parallel to the point of solids injection there was a lower concentration of particles along the wall compared to the perpendicular plane for $G_s \geq 300$ kg/(m^2·s). At the lower circulation rates tested, a higher particle concentration at the wall along the parallel plane was found. Non-uniformities were also noted along the parallel plane. On this parallel plane, they found a higher particle concentration and lower particle velocity near the wall containing the solids feeder compared to that opposite the feeder. Asymmetry in the solids concentration profiles was found over the entire range of operating conditions studied and at all axial locations

in the dense region of their riser, however it was intensified at elevated solids circulation rates. In the dilute zone of the riser, the asymmetries were no longer present.

Based on the findings of Yan *et al.* (2003) it seems likely that the solids feeding device can affect the solids distribution in the dense section of a CFB riser. The most common feeding devices implemented today are L-valves, J-bends, and inclines that introduce solids asymmetrically into the riser through a single transfer line. In the current study, solids are introduced into the riser through a high pressure drop solids feeding device. Solids enter the riser through eight symmetrically placed orifices around the riser periphery. Although the results of Yan *et al.* (2003) are not directly comparable to the current study due to the different solids feeders used, it seems plausible that the solids feeding device could contribute to the unique shape of the solids flux profile in the current study. On the plane parallel to the solids feeder Yan *et al.* (2003) found an increased solids concentration near the wall, as well as a steeper gradient in the particle concentration profile at $G_s < 300$ kg/(m^2·s). Because multiple solids feed points are used in the current study, it is likely that there is a higher particle concentration around the entire periphery of the riser, leading to high local flux in the near-wall measurements. While the same argument of an increased solids concentration at the periphery could be extended to any solids feeding device, measurement of a high-flux wall in a riser using a single-entry solids feeding device would be dependant on selection of the radial location of solids flux measurements. It is also unknown what the effect of the asymmetry resulting from using a single entry point would be on the stability of the solids concentration and solids velocity profiles compared to that of the more symmetric solids feeding device used in the present study.

3.4.5 Solids Refluxing

Solids refluxing in a CFB riser is known to cause gas backmixing (Arena, 1997). Gas backmixing is undesirable in the riser as it can cause over-cracking of the crude oil feed. Van der Meer *et al.* (2000) defined the reflux ratio as:

$$RR = \frac{G_{s\,down}}{G_s} \tag{3.1}$$

Figure 3-9 presents the reflux ratio at each radial position. For solids circulation rates ranging from 174 to 243 kg/(m^2·s), the maximum solids refluxing occurs at an intermediate position ($0.80 \le r/R \le 0.87$) and the minimum at the centerline. As the solids circulation rate is increased from 174 to 243 kg/(m^2·s), refluxing at $r/R > 0.71$ decreases while remaining relatively constant elsewhere. At a solids circulation rate of 125 kg/(m^2·s), lower refluxing is observed at $r/R \le 0.71$ than is observed for higher circulation rates. At this solids circulation rate, the highest flux is observed at the riser wall. Figure 3-10 presents the effect of riser solids circulation rate on the cross-sectional average solids refluxing. The plot shows that a similar amount of refluxing occurs at 125 and 174 kg/(m^2·s). At $G_s > 174$ kg/(m^2·s), the average refluxing is reduced. It is expected, therefore, that gas backmixing would be reduced at elevated solids circulation rates in the bottom region of a CFB riser.

3.5 Conclusions

The solids flux profiles in a 0.14 m I.D., 14 m tall CFB riser were examined for solids circulation rates ranging from 125 to 243 kg/(m^2·s) operated at a riser gas velocity of 5.3 m/s. The effect of the riser gas velocity on the local solids flux at the centerline was also examined for riser gas velocities ranging from 4.4 to 5.6 m/s operated at a constant solids circulation rate of 187 kg/(m^2·s). The measurement height of 1.6 m was located in the high-density bottom zone of the riser. It was found that the bed operates in dense suspension upflow; with a maximum in the net solids flux profile located near the wall, giving the profiles a hook-shaped appearance. There is evidence to suggest that hook-shaped solids flux profiles are a consequence of the solids feeding device, however further experimentation needs to be performed to confirm this. The solids flow is in an early stage of development, evidenced by the sharp increase in solids flux near the wall and by the near-constant local solids flux at the centerline with changing solids circulation rates. Measurement of the local upflow at the riser centerline indicates that a sharp transition from a more-dense to a more-dilute core can occur in the bottom zone of a high-density riser by changing the riser superficial gas velocity. This sharp transition has not been previously reported. The sharp change in the local upflow suggests a transition from a parabolic solids flux profile to a more radially uniform profile. The solids reflux ratio was calculated for the range of solids circulation rates tested. It was found that solids refluxing decreases for $G_s >$ 174 kg/(m^2·s).

Table 3-1: Summary of the conditions used in previous studies and the present study.

Reference	G_s kg/(m^2·s)	U_{riser} (m/s)	ε	D_r (m)	H_r (m)	Meas. Z (m)	Test Material
Malcus et al. (2002)	150-264	4.7	0.80-0.88	0.14	7.0	1.6, 2.1	FCC
Wei et al. (1997)	18-235	1.8-10.5	0.73-0.99	0.19	8.5	3.9	FCC
Issangya et al. (1998)	38-325	4.7-7.5	0.75-0.97	0.076	6.1	2.8, 4.6	FCC
Karri & Knowlton (1999)	49-586	4.6-18.3	0.74-0.90	0.305	13.0	3.7	FCC
Present study	125-243	5.3	0.84-0.88	0.14	14.0	1.6	FCC

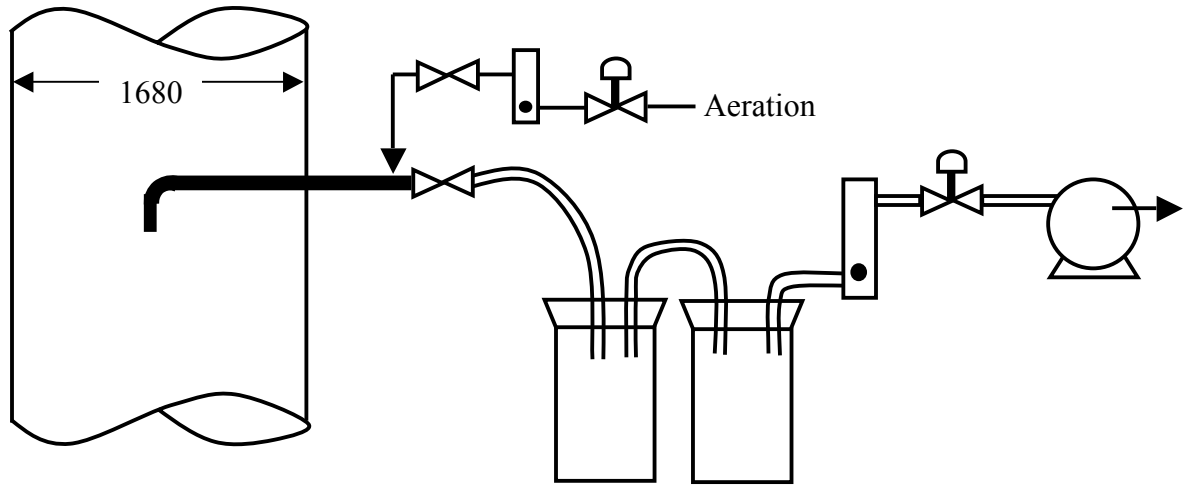

a)

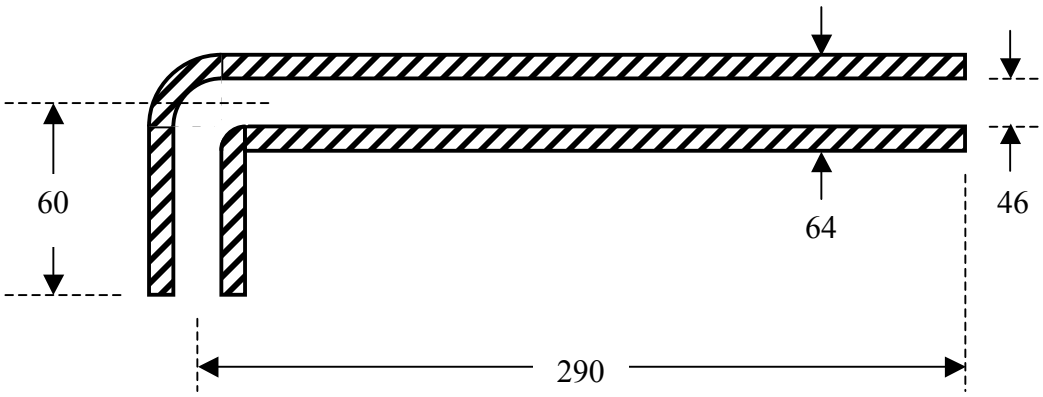

b)

Figure 3-1: Solids upflow probe in CFB riser (a) schematic of measurement system, (b) dimensions of upflow probe (all dimensions in mm).

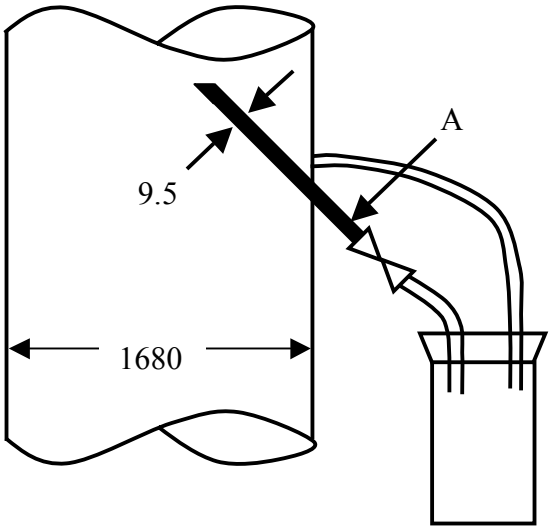

a)

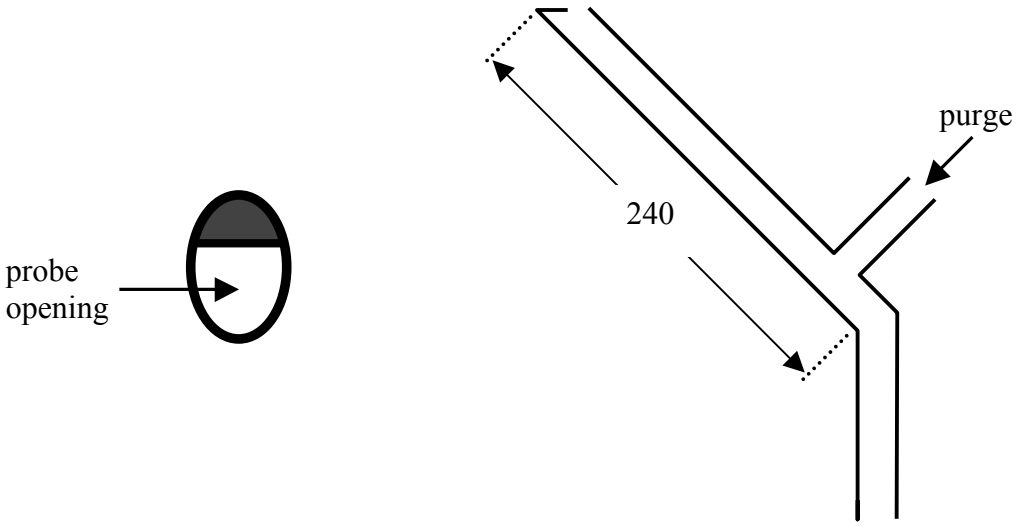

b)

Figure 3-2: Solids downflow probe in the CFB riser (a) schematic of measurement system, (b) dimensions of upflow probe. All dimensions in mm.

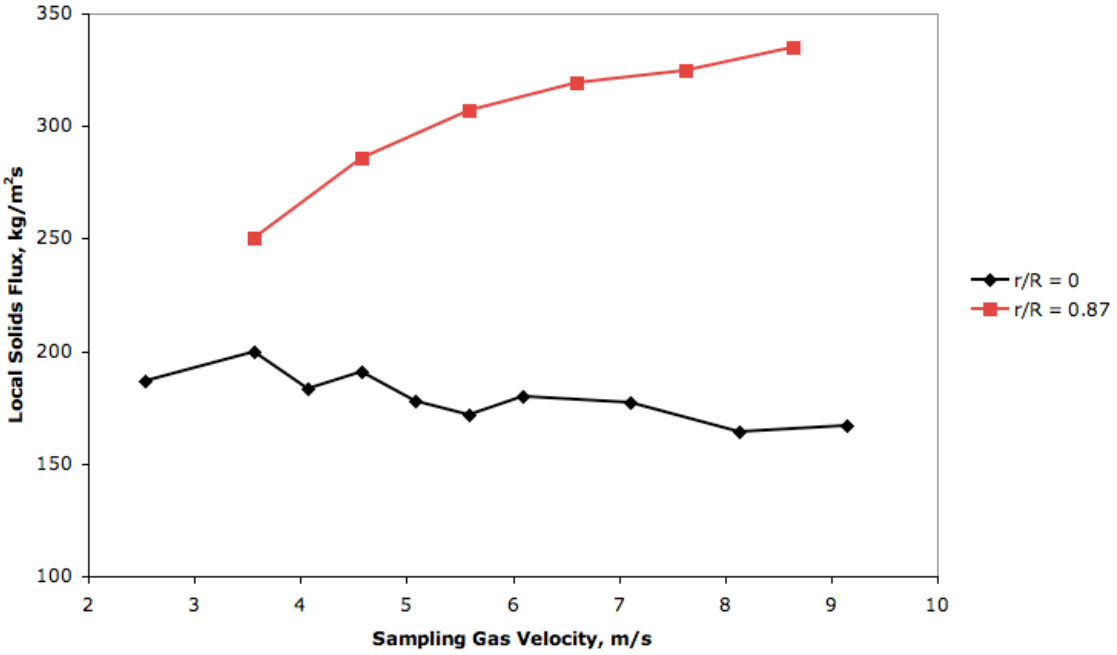

Figure 3-3: Effect of sampling gas velocity on the measured solids upflow in the riser. Riser solids circulation rate is 205 kg/(m^2·s).

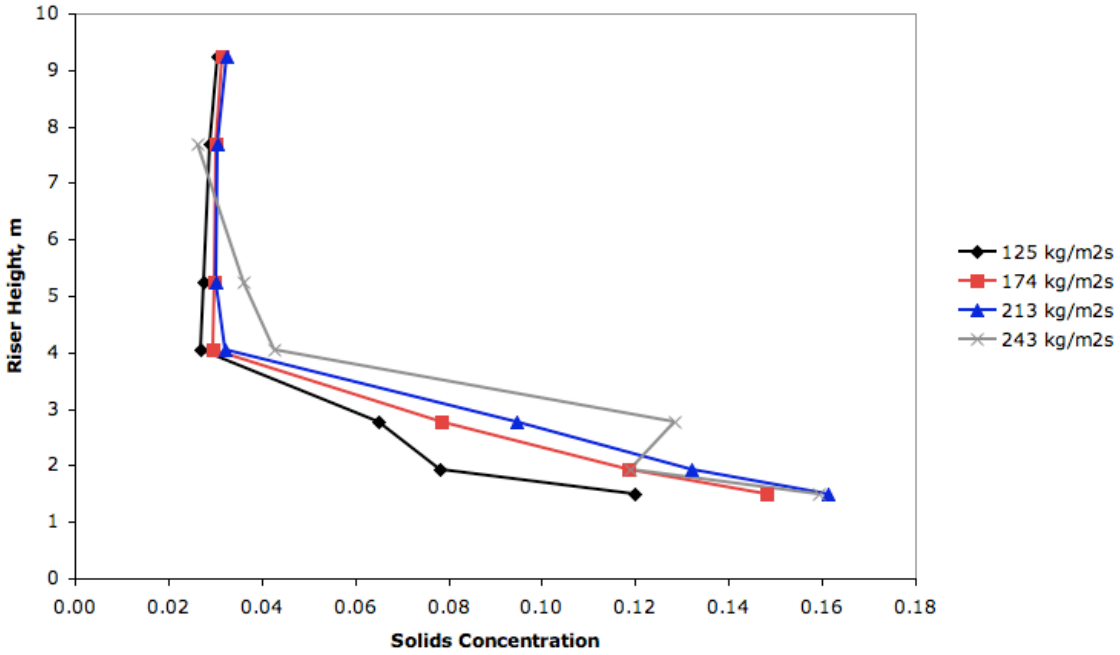

Figure 3-4: Effect of solids circulation rate on the solids concentration profiles in the CFB riser. Riser superficial gas velocity is 5.3 m/s.

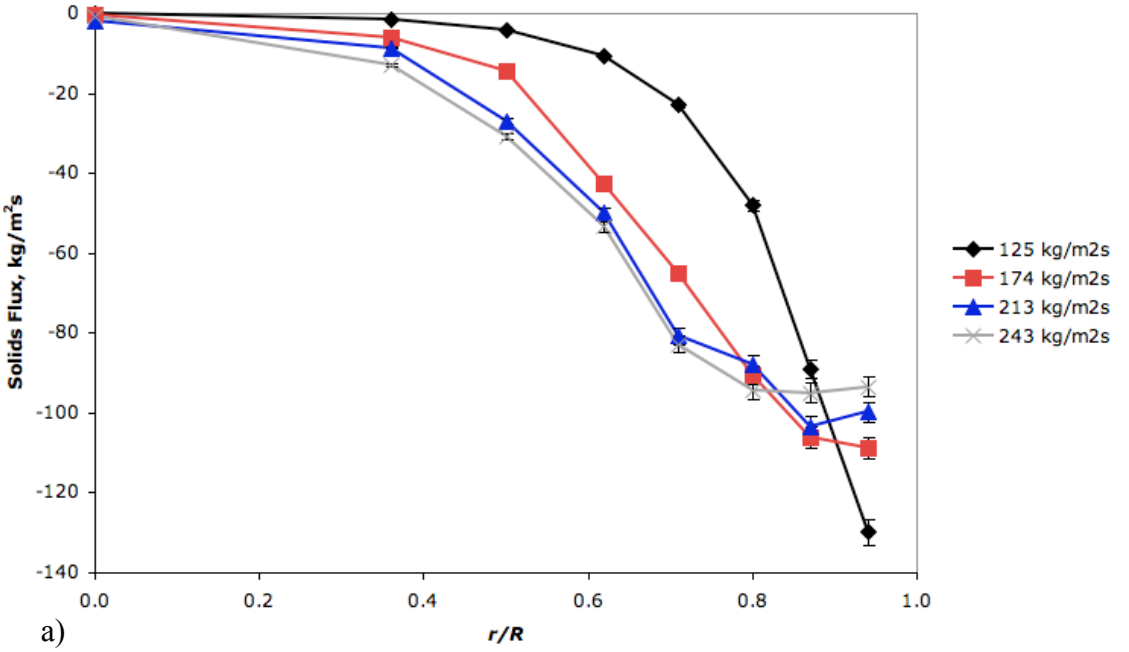

a)

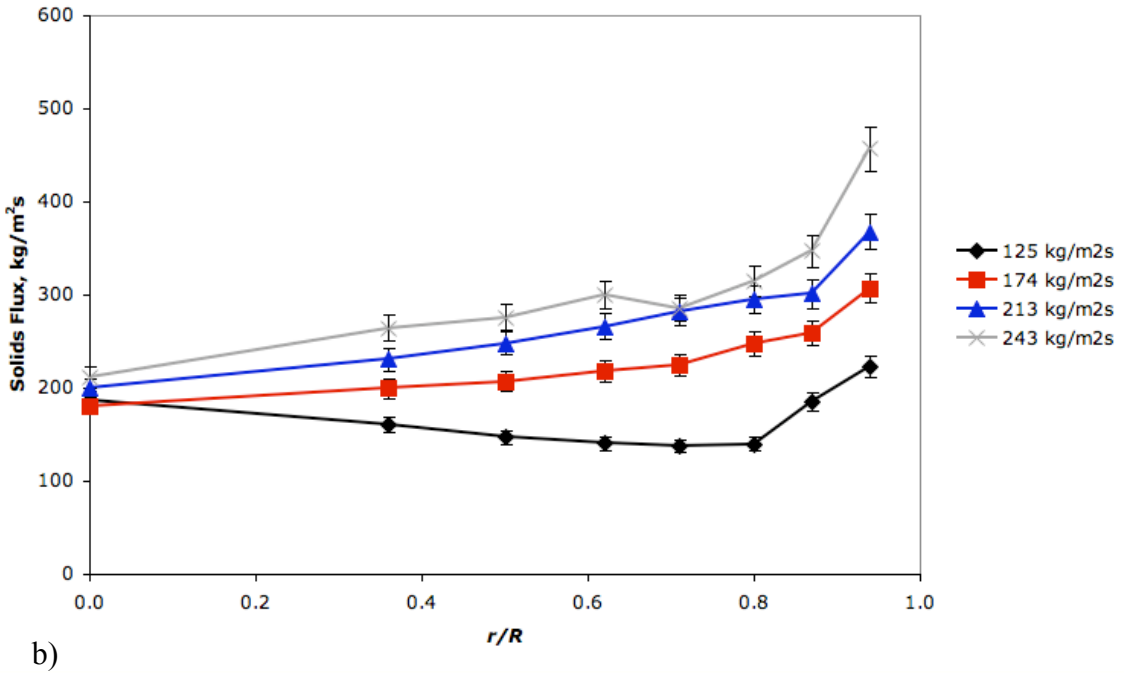

b)

Figure 3-5: Effect of solids circulation rate on the local solids flux profiles a) upflow, b) downflow, plotted with the 95% confidence interval. Riser superficial gas velocity is 5.3 m/s.

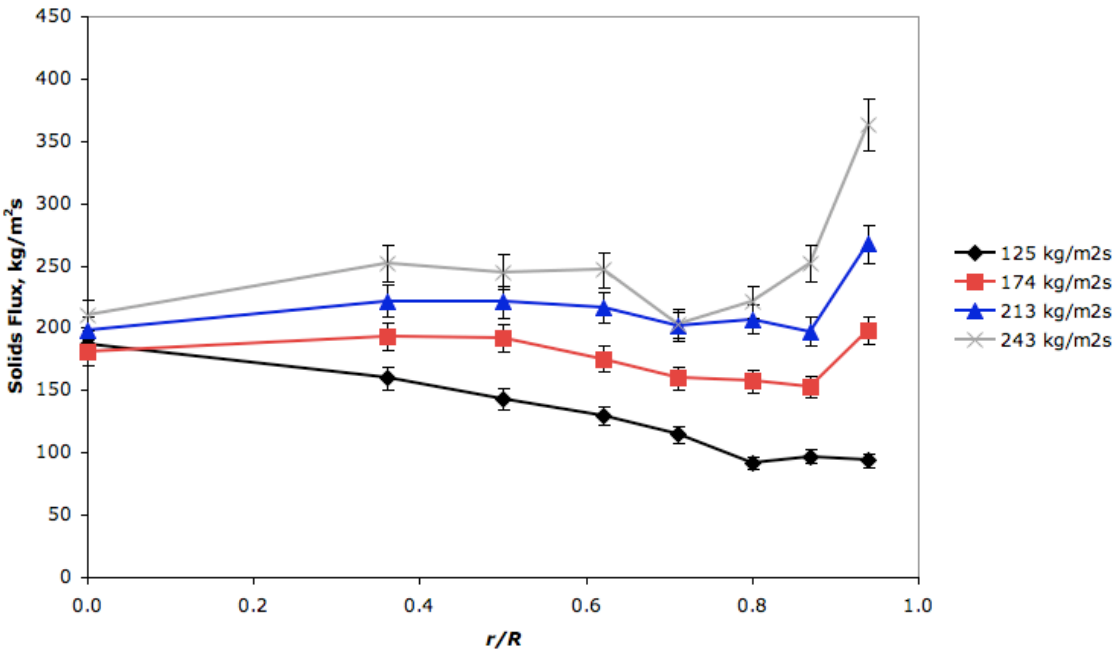

Figure 3-6: Effect of solids circulation rate on the net solids flux profiles, plotted with the 95% confidence interval. Riser superficial gas velocity is 5.3 m/s.

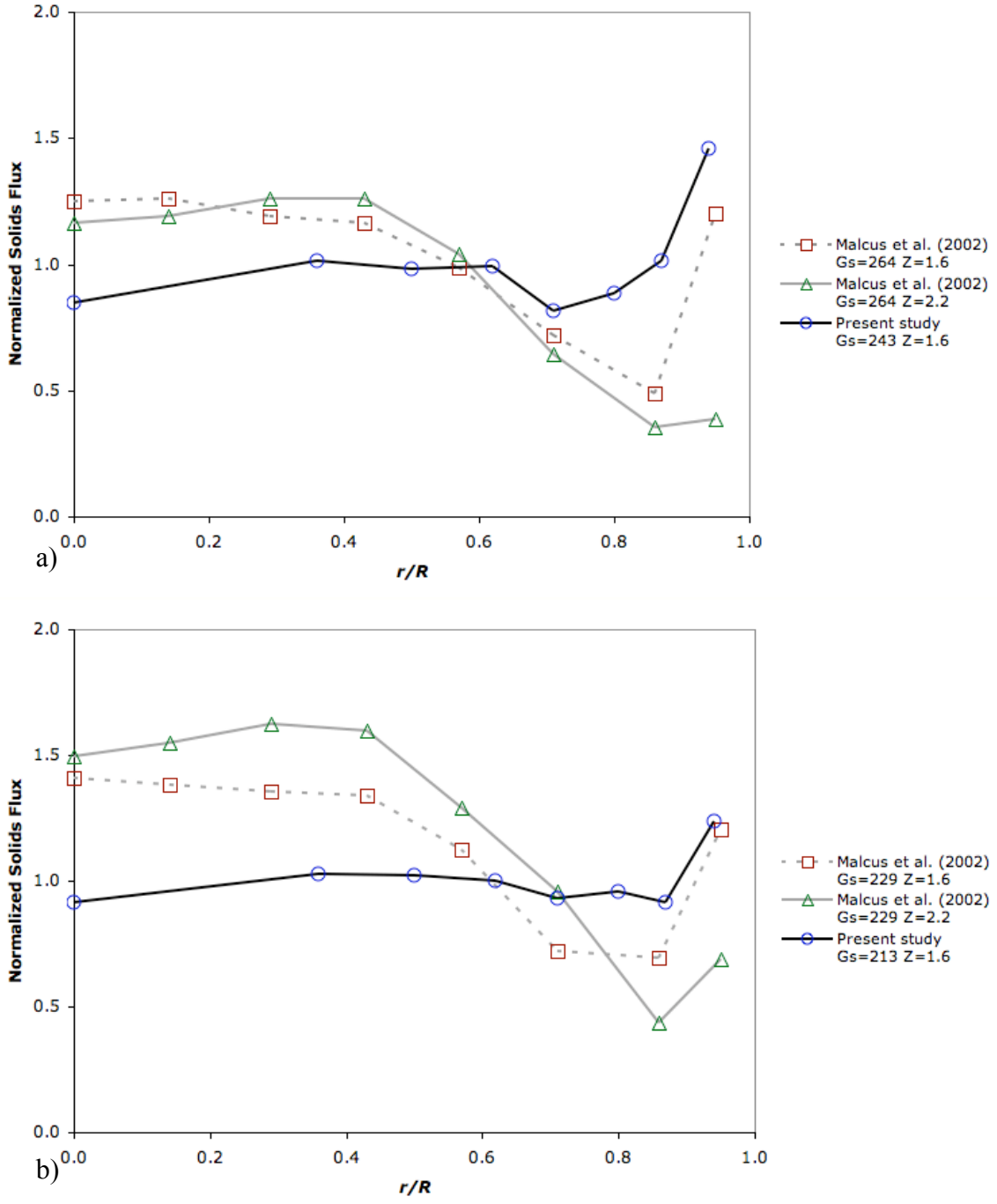

Figure 3-7: Comparison of normalized solids flux profiles for Malcus *et al.* (2002) and the current study operated at similar solids circulation rates a) G_s (Current study) = 216 kg/(m^2·s), b) G_s (Current study) = 249 kg/(m^2·s).

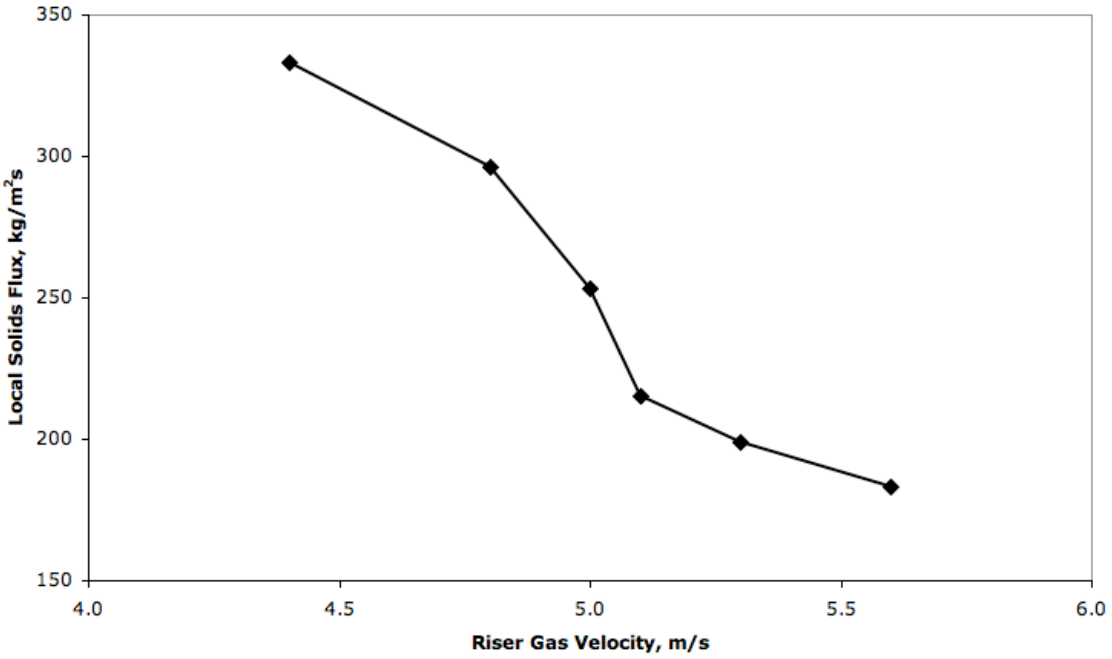

Figure 3-8: Effect of the riser gas velocity on the local solids flux at the riser centerline. Riser solids circulation rate is 187 kg/(m^2·s).

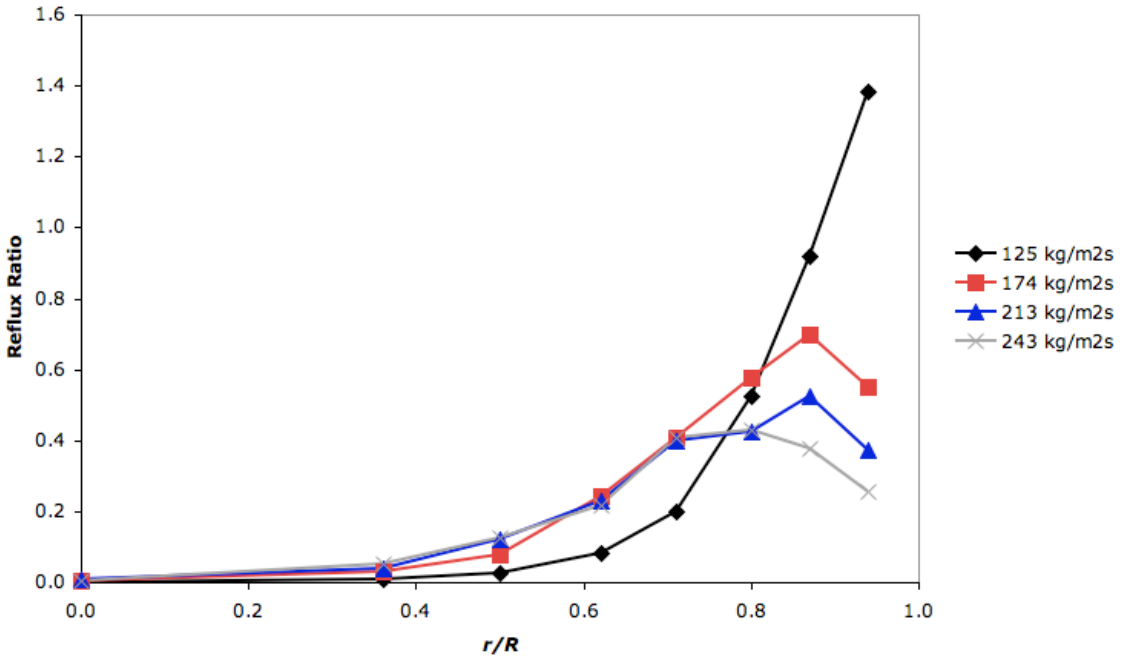

Figure 3-9: Effect of solids circulation rate on the local reflux ratio in the CFB riser. Riser superficial gas velocity is 5.3 m/s.

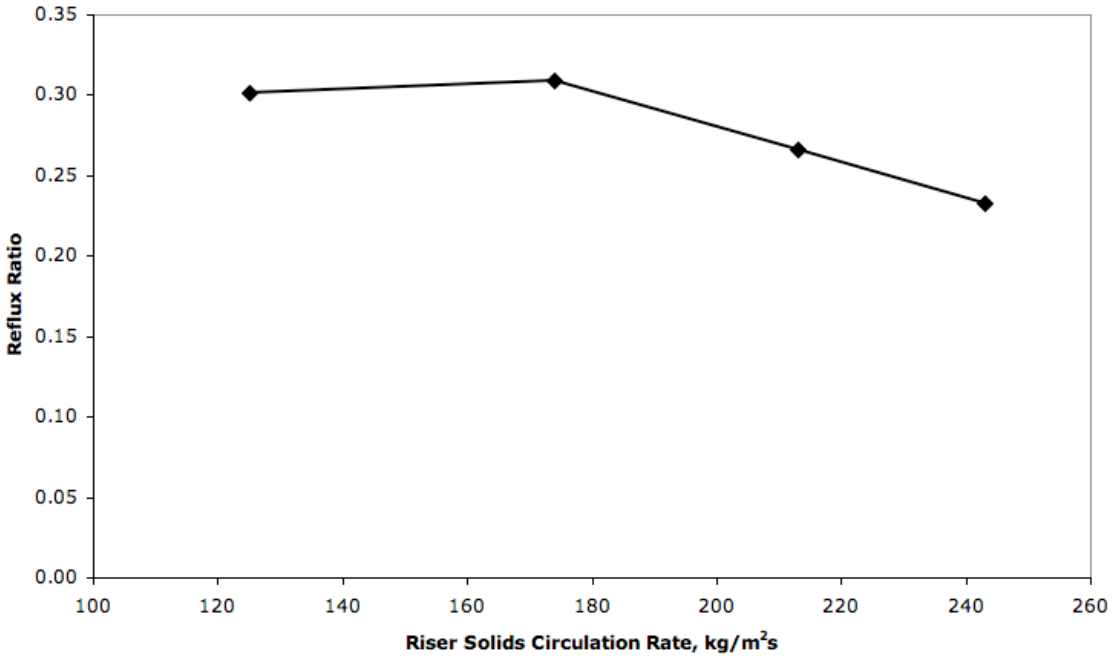

Figure 3-10: Effect of the riser solids circulation rate on the average reflux ratio. Riser superficial gas velocity is 5.3 m/s.

Chapter 4 – CFD Modeling of the Hydrodynamic Behaviour of an FCC Stripper

Contribution of the Ph.D. Candidate

The models were prepared by Jason Wiens. Todd Pugsley provided consultation regarding the model development. All models were run on Multipase Flow with Interphase exchanges (MFIX) software, a freely available CFD modeling software package developed by the United States National Energy Technology Laboratory (NETL).

4.1 Objective

The hydrodynamic behaviour of FCC strippers remains largely unexplored. Fluid catalytic cracking strippers can be distinguished from freely bubbling beds in two ways: there is counter-current flow of gas bubbles and solids, and strippers contain internal baffles. It is hypothesized that these two factors would cause distortion of the bubble shape and an intricate bubble rise path. The objective of this work is to investigate the hydrodynamic behaviour of FCC strippers for solids circulation rates ranging from 45 to 75 kg/(m^2·s) and stripping gas velocities ranging from 0.1 to 0.3 m/s. The hydrodynamic behaviour will be examined through qualitative observations, time-averaged voidage and bubbling frequency profiles, and an investigation of bubble properties: sphericity, rise velocity, and diameter.

4.2 Introduction

Computational Fluid Dynamics (CFD) is a useful tool for predicting the hydrodynamic behaviour in fluidized beds. Application of CFD to analyze bed behaviour is advantageous because predictions of hydrodynamics can be made in geometries and locations that would be impossible to measure using conventional experimental techniques, or that would require highly specialized equipment. The resulting abundance of hydrodynamic data can also assist in identifying important details that affect global bed performance, such as heat and mass transfer or reactor conversion and yield.

CFD modeling has been successfully applied to dense fluidized beds containing Geldart B particles. However, simulation of beds containing finer Geldart A particles has been mostly unsuccessful to date. This is thought be a result of the inability of two-fluid CFD models to adequately account for interparticle forces in fluidized beds containing Geldart A particles (Krishna & van Baten, 2001, McKeen, 2003). The only interparticle force accounted for in most CFD models is particle-particle collisions. However, there is evidence that cohesive particle forces may be significant in beds of fine particles (Massimilla & Donsi, 1976, Rietema, 1991).

McKeen & Pugsley (2003) were the first to successfully apply two-fluid CFD modeling to dense beds of Geldart A particles. They modeled a bubbling fluidized bed of FCC catalyst at superficial gas velocities ranging from 0.05 to 0.20 m/s. Model validation was based on comparison of bed expansion, bubble diameter, and bubble velocities between their two-dimensional CFD model and their three-dimensional experimental system. McKeen & Pugsley (2003) accounted for particle cohesive forces by modifying the Gibilaro gas-solids drag law (Gibilaro *et al.,* 1985) to the form:

$$F_{gs} = \Theta\left(\frac{17.3}{\mathrm{Re}_p} + 0.336\right)\frac{\rho_g\left|\overline{v_s} - \overline{v_g}\right|}{d_p}\varepsilon_s\varepsilon^{-1.8} \qquad (4.1)$$

McKeen & Pugsley (2003) suggested that a fractional drag scaling factor, Θ, between 0.2 and 0.3 should be used. This drag scaling factor effectively increases the particle diameter of the FCC catalyst from 75 μm to an agglomerate diameter of between 135 and 170 μm. Hence the factor reflects the clustering that is known to occur in beds of FCC catalyst with the corresponding reduction in the gas-solid interfacial drag force.

The modified form of the Gibilaro gas-solids drag law developed by McKeen & Pugsley (2003) has been implemented in CFD codes to study the behaviour of fluid catalytic cracking strippers (McKeen, 2003, Gao *et al.,* 2008). McKeen (2003) simulated a two-dimensional, geometrically scaled version of the experimental system of Rivault *et al.* (1995). Solids circulation rates between 28 and 85 kg/(m^2·s) and stripping gas velocities between 0.1 and 0.33 m/s were examined for the stripper containing disc-and-donut baffles. Qualitative comparisons were made between McKeens's simulated FCC stripper and the experimental findings of Rivault *et al.* (1995). Similar to the findings of Rivault *et al.* (1995), McKeen (2003) found that a void space developed below each baffle. Gas was found to bubble up from underneath the baffle and move vertically and laterally to the void space beneath the next baffle; while the solids were found to slide down the face of the trays. The baffles were found to be effective in breaking up bubbles as they rise between the trays. Validation of the model was based on comparison of the bubbling frequency profiles between McKeen's simulation and the experimental work of Rivault *et al.* (1995). Good quantitative agreement of the bubbling frequency profiles was observed at a solids circulation rate of 28 kg/(m^2·s) and stripper gas velocity of 0.18 m/s. At a stripper gas velocity of 0.33 m/s, however, significant deviation was observed.

Gao *et al.* (2008) simulated a two-dimensional stripper containing 'V-baffles'. V-baffles are similar to standard disc-and-donut baffles except that they do not have the vertical skirt attached to the base of the baffle. A solids circulation rate of 27 kg/(m^2·s) was examined for stripping gas velocities between 0.05 and 0.20 m/s. Gao *et al.* (2008) used qualitative analysis, radial bed density profiles, and radial particle velocity profiles to analyze their results. Although several data types were presented, limited interpretation of their data severely limits its usefulness for furthering the understanding of the hydrodynamic behaviour of FCC strippers. Similar to the findings of McKeen (2003), particles were found to slide down the face of the tray. They found that the V-baffles were effective in breaking up bubbles, yielding 'a great number of small bubbles'.

An important contribution to the understanding of the hydrodynamic behaviour in FCC strippers was the experimental study by Rivault *et al.* (1995). Solids circulation rates between 28 and 108 kg/(m^2·s) were tested for stripping gas velocities between 0.1 and 0.4 m/s in a stripper containing disc-and-donut baffles. They found that the average bubble chord length was insensitive to the solids circulation rate and the stripping gas velocity. The chord length remained between 0.044 and 0.065 m, however only 10 to 30% of the bubbles could be processed to determine the chord length either due to bubble deformation or non-vertical rise. The accuracy of these results is questionable, however, since it was found that the peak bubbling frequency decreased from 4.6 to 2.6 Hz upon increasing the stripping gas velocity from 0.18 to 0.33 m/s. Rivault *et al.* (1995) found that increasing the solids circulation did not affect the bubbling frequency, but did promote a more even distribution of bubbles across the vessel cross-section.

To date, the hydrodynamic behaviour of FCC strippers remains relatively unexplored. The most important contribution to the understanding of the bubbling behaviour of FCC strippers remains the experimental study by Rivault *et al.* (1995), however the advantages of CFD modeling provides an opportunity for a more thorough investigation of stripper behaviour. FCC strippers differ from freely bubbling beds in two important ways: 1) the net flow of the emulsion phase is counter-current to the bubble phase and 2) the stripping vessel contains baffles that are

designed to re-distribute gas. It is evident, then, that relying on hydrodynamic principles adapted from freely bubbling beds would likely be erroneous for interpreting stripper behaviour. The purpose of the current study is to utilize CFD simulations to investigate bed hydrodynamic behaviour and important bubble properties in an FCC stripper containing disc-and-donut baffles. The hydrodynamic behaviour is interpreted through qualitative analysis, time-averaged voidage profiles, bubbling frequency profiles, and analysis of bubble properties.

4.3 Model Set-Up and Parameters

Multiphase Flow with Interphase eXchanges (MFIX) version MFIX-2007-4 code was used to simulate the FCC stripper. Appendix B provides samples of the MFIX data, output, and log files. Table 4-1 presents the conservation equations used in the MFIX CFD code for a single solids phase and a single gas phase. The default numerical solution parameters and constitutive relations were used in the simulations (www.mfix.org), except for the gas-solids drag. The default gas-solids drag relation was replaced with the modified Gibilaro drag law developed by McKeen & Pugsley (2003). The recommended value of 0.25 was used for the drag law scale factor (McKeen & Pugsley, 2003). An axisymmetric cylindrical coordinate system with a 5 mm by 5 mm grid was used in the active area (gas and solids flow) of the stripper. The grid size was chosen based on the mesh refinement study performed by McKeen & Pugsley (2003) for bubbling beds containing FCC catalyst. The second-order Superbee discretization was used for all governing equations. This was chosen over the default first-order upwinding scheme because first-order discretization is known to produce unrealistic pointed capped bubbles. To achieve steady state operation in the stripper, new simulations were run for 60 s whereas re-start simulations were run for 40 s. For both cases, the last 10 s of data were used to examine bed hydrodynamic behaviour.

Due to the large number of simulations required, an axisymmetric two-dimensional model was used to simulate the FCC stripper. Two-dimensional modeling of fluidized beds has been frequently used in the open literature because of the low computation times required compared to that of three-dimensional models. However, because of the three-dimensional nature of bubbling fluidized bed flow it is obvious that superior results could be attained with three-dimensional models. To date, there has been little comparison between the validity of two- versus three-dimensional models in two-phase flows. Peirano *et al.* (2001) found that a two-dimensional model could not satisfactorily predict the static and dynamic behaviour of their bubbling fluidized bed. However, their validation was performed at a single gas velocity in a square cross-section bed of Geldart B particles. However, many authors (i.e. McKeen & Pugsley, 2003, Gamwo *et al.,* 1999) have found qualitative and quantitative agreement of the behaviour in two-dimensional models and three-dimensional experimental systems. Regardless of the debate surrounding the use of two-dimensional models, it is still a useful tool for comparative and sensitivity analysis (Peirano *et al.,* 2001).

Figure 4-1 and Figure 4-2 present the bed geometry and initial and boundary conditions used in the FCC stripper simulations. The dimensions of the simulated stripper are based on geometric scaling of the experimental system (Chapter 6). The simulated stripper is composed of five donut baffles and four disc baffles. The total length of the baffled section of the stripper is 1.2 m. The bases of the disc and donut baffles extend 40 mm and 80 mm horizontally from their

points of attachment on the 'dummy-riser' and east wall, respectively. Each baffle has a 10 mm skirt extending from the base of the baffle. Based on the axisymmetric assumption, each baffle blocks approximately 50% of the open area at the pinch point. The dummy riser extends 25 mm from the west wall. Eighty mm of unbaffled space separates the apex of the lower baffle and the base of the skirt on the top baffle.

Table 4-2 presents the particle and air properties used in the simulations. The particle density of 1550 kg/m^3 and mean particle diameter of 98 μm are identical to the properties of the FCC catalyst used in the experimental program (Section 2.4). The restitution coefficient for particle-particle collisions is chosen based on the work of Benyahia *et al.* (2000) for FCC particles. The angle of internal friction used is typical for FCC particles (Khoe *et al.,* 1991).

4.3.1 Boundary Conditions

Four boundary conditions (BC) were specified in the simulations to control the stripping gas velocity and solids circulation rate (Figure 4-2). Two boundary conditions specify the outflow of gas and solids at the southernmost and northernmost planes of the computational domain and two boundary conditions specify the inflow of gas and solids at intermediate locations within the computational domain.

At the southernmost horizontal plane of the simulation, a uniform particle velocity profile boundary condition was specified. The downward particle velocity was set equal to the particle velocity for the desired solids circulation rate in the simulation, and an equivalent downward gas velocity was specified. At the northern boundary of the simulation a constant pressure boundary condition equal to atmospheric pressure was specified. The constant pressure boundary condition theoretically allows entrained solids to leave the computational domain, however it was observed that convergence at this boundary condition was sensitive to bubbles erupting from the surface of the bed near this boundary.

The other boundary conditions, namely solids and gas inflow into the simulation, govern the solids circulation rate and stripping gas velocity in the simulation. The gas inflow boundary condition is located 120 mm from the southern boundary of the simulation (185 mm below the 1st donut baffle), and extends from 95 to 105 mm from the western wall. A fixed local gas velocity was specified at this location, and scaled to the desired superficial stripping gas velocity in the simulation. The horizontal length of the air inflow boundary condition was chosen such that the orifice velocity was maintained between the simulations and the experimental apparatus. The solids inflow boundary condition is located 1.870 m from the southern boundary of the simulation (340 mm above the last donut baffle), and extends from 70 to 100 mm from the western wall. A fixed downward solids velocity profile was specified at this location, and scaled to the desired solids circulation rate in the simulation. An equal downward gas velocity was specified at this boundary. To avoid accumulation of solids in the simulated stripper, it was important to ensure the solids velocity at the inlet and outlet boundary conditions satisfied the steady-state material balance.

In addition to boundaries that establish the solids circulation rate and stripping gas velocity, several bed internal structures needed to be constructed. These internals include: the

'dummy-riser', the disc-and-donut baffles, and enclosures for the solids dipleg and the gas velocity. No-slip boundaries were defined for all bed internals. The dummy riser was constructed of 25 mm by 5 mm cells that extend from the south to the north boundary of the computational domain. The cells extend horizontally 25 mm from the western wall. The disc-and-donut baffles were constructed of 5 mm by 5 mm no-slip walls. The 45° angle of the baffles was mimicked by creating 'steps' in the computational domain. Finally, enclosures were constructed of 5 mm by 5 mm cells to cover the solids and gas inflow boundaries. These enclosures are necessary to prevent bed dynamic behaviour from interfering with the desired solids and gas inflow.

4.3.2 Initial Conditions

Initial conditions were specified for the two distinct phases in the simulation: the freeboard region and the dense bed region. In both cases, the parameters were set to the minimum fluidization conditions. In the dense bed region, gas velocity was set to the interstitial gas velocity at minimum fluidization, and the particle velocity was set to zero. The dense bed height was initially set at 1.685 m. In the freeboard section, the gas velocity was set equal to the superficial gas velocity at minimum fluidization. Two different freeboard heights were used in the simulations because of divergence of some of the simulations caused by bubbles erupting near the constant pressure boundary condition at the northern boundary. A freeboard height of 1.175 m was used for simulations using operating conditions of (solids circulation rate & stripper gas velocity): 45 kg/(m^2·s) & 0.1 m/s, 60 kg/(m^2·s) & 0.1 m/s, 60 kg/(m^2·s) & 0.2 m/s, 75 kg/(m^2·s) & 0.1 m/s, 75 kg/(m^2·s) & 0.2 m/s, and 90 kg/(m^2·s) & 0.1 m/s. A freeboard height of 1.675 m was used for simulations using operating conditions of (solids circulation rate & stripper gas velocity): 45 kg/(m^2·s) & 0.2 m/s, 45 kg/(m^2·s) & 0.3 m/s, 60 kg/(m^2·s) & 0.3 m/s, and 75 kg/(m^2·s) & 0.3 m/s.

4.4 Model Validation

Figure 4-3 presents the apparent solids concentration, measured from the pressure drop across the stripper section in the experiments (Chapter 6) and in the simulation. As can be seen in the figure, model predictions are within 7% of the experimental data for the low flux, low gas velocity operating conditions. For solids circulation rates of 60 and 75 kg/(m^2·s) operated at stripper gas velocities of 0.3 and 0.2 m/s, respectively, the model predictions deviate by 13% and 26% from the experimentally measured solids concentration. Therefore, it is expected that the model would be able to closely predict the hydrodynamic behaviour of the stripper at the low solids circulation rates and low stripping gas velocities examined. Simulations at solids circulation rates of 60 and 75 kg/(m^2·s) operated at stripper gas velocities of 0.3 and 0.2 m/s, respectively, would be less capable of predicting stripper hydrodynamics. Because the simulations are used to predict bubbling frequency profiles and bubble diameter data, it is obvious that use of these quantities would be the preferred method of model validation. However, these quantities were not measured in the experimental program.

4.5 Results

4.5.1 Bubbling Bed Qualitative Analysis

This section describes the bubble formation, interactions, and movement based on observations in the modeled FCC stripper. The discussion pertains to simulations operating at conditions that exhibit smooth bubbling behaviour (Table 4-3). For simulations exhibiting bubbling behaviour, similar bubble motion and interactions are observed. However, the frequency and intensity of bubble-bubble interactions is found to be sensitive to the solids circulation rate and stripping gas velocity in the simulation.

Figure 4-4, Figure 4-5, and Figure 4-6 present macroscopic time-lapse views of the simulated stripper operating at a solids circulation rate of 45 kg/(m^2·s) and stripper gas velocities 0.1, 0.2, and 0.3 m/s, respectively. Under each baffle there is a permanent void space that extends horizontally from the bottom of the skirt to the wall where the baffle is attached. Gas bubbles are found to cascade from baffle to baffle as they move upwards through the stripper. A similar bubble shape and size is maintained throughout the length of the baffled section of the stripper. When the gas bubbles ascend past the last baffle of the stripper, large gas slugs are formed that occupy most of the vessel cross section. This description of the gas motion is similar to that observed experimentally by Rivault *et al.* (1995) and modeled by McKeen (2003).

In the active area between the disc and donut baffles, the gas exhibits complex hydrodynamic behaviour never reported in the literature. This behaviour can be classified into three distinct stages of development based on the proximity of the formed bubbles to the lower and upper baffle: bubble formation, developing bubble flow, and baffle encroachment.

The bubble formation stage occurs at the pinch point (the site of highest particle velocity, located adjacent to the baffle skirt at the base of a baffle) adjacent to the lower baffle skirt. At this stage, the gas bubble grows while remaining attached to the gas void contained under the lower baffle. Growth of the bubble generally causes a vertically elongated shape, however the bubble can sometimes become wide enough to nearly encompass the entire open area at the pinch point. Once the bubble has reached a sufficient diameter for the buoancy to overcome the force of the down-flowing solids, it detaches from the baffle and begins ascending. This bubble growth is similar in appearance to the sketch of a slotted pipe gas distributor operated at low gas velocity prepared by Massimilla (1985). In the bubble formation stage, it is common for a bubble rising from a lower baffle pair to coalesce with the developing bubble. While maintaining a static gas velocity of 0.1 m/s, increasing the solids circulation rate in the system results in larger bubbles being formed. At elevated gas velocities, the increased volume of gas in the stripper causes rapid bubble growth. Additionally, the increased bubble frequency causes a sharp increase in the incidence of coalescence with the growing bubble.

The moment of detachment of the formed bubble from the gas void under the baffle demarcates the transition to the second stage of bubble development: developing bubble flow. Developing bubble flow is characterized by frequent bubble-bubble interactions, and changes to the shape and trajectory of the rising bubbles. Immediately after detachment from the lower baffle, the bubble accelerates, elongates, and moves towards the wall of the vessel (vertically aligning with the upper baffle). At elevated solids circulation rates, the bubbles appear more

elongated and are of more uniform size than at low solids circulation rates. Increasing elongation of the bubbles is likely due to the increased drag enacted on the bubbles by the down-flowing catalyst stream at elevated solids circulation rates.

Bubble coalescence between two vertically aligned bubbles is a regular occurrence in the developing bubble flow stage. Coalescence is most frequently observed soon after detachment of the bubble from the baffle. During encroachment of the coalescing bubbles, the lagging bubble is observed to elongate and accelerate before coalescing with the leading bubble. This is similar to the description of bubble coalescence offered by Sit & Grace (1981). Due to the increased bubble frequency, coalescence is more often observed at elevated gas velocities. Commonly, especially at positions approaching the upper baffle, coalescence does not actually result in the merging of the leading and lagging bubble. Instead, encroachment of the bubbles simply results in elongation and acceleration of the lagging bubble.

Two modes of bubble splitting have also been observed in developing bubble flow: knifing and wake shedding. One mode, known as 'knifing', was described by Rowe *et al.* (1964) as occurring when "the leading edge of a bubble is frequently penetrated by small 'fingers' of particles…". This is observed in the current work as a streak of low voidage cutting through a large diameter bubble, typically rising in isolation, at approximately a ±15° angle (Figure 4-7a). However, knifing was never observed to successfully produce two daughter bubbles from the parent bubble. Instead, the smaller bubble was swept around the parent bubble then re-absorbed into the parent bubble. This type of bubble splitting appears most commonly at low solids circulation rates and low gas velocities. The second mode of bubble splitting, known as wake shedding (Rowe *et al.,* 1964), produces small diameter bubbles that are independent from the parent bubble (Figure 4-7b). These bubbles are expelled from the lobes in the wake of the bubble. Although this is rarely observed, it appears to be promoted when bubbles rise in vertical alignment but are too far apart to coalesce. Wake shedding typically occurs in the lagging bubble. It is most commonly observed at high solids circulation rates operated at high stripping gas velocities.

The third stage of development, coined 'baffle encroachment', is demarcated by a flattening of the bubble to a more spherical shape. Flattening of the bubble occurs gradually at first, but accelerates as the bubble approaches the upper baffle. This is especially evident at elevated stripping gas velocities, where encroachment of bubbles often produces very distorted and elongated bubbles. This flattening of the bubble is likely promoted by a low catalyst velocity in the area directly below the baffle space not producing as much drag on the bubbles. In the latter stages of baffle encroachment, the bubbles shift their trajectory away from the wall towards the outside of the top baffle.

It is apparent that bubbles in the baffle encroachment phase have a stronger affinity to bubbles forming adjacent to the upper baffle rather than to the gas void trapped beneath the upper baffle. As the bubbles approach the upper baffle, they will preferentially coalesce with bubbles in the bubble formation stage or in the early developing bubble stage rather than be absorbed into the void space beneath the upper baffle, despite having to traverse a large lateral distance from the wall. Because of this preference, an interesting gas circulation pattern emerges by one of two similar mechanisms (Figure 4-8a-c, Figure 4-9a-c). Peculiar to this gas circulation

pattern is that a small 'stray' bubble is released via either mechanism that is swept into the emulsion phase and moves either downwards or is nearly stationary. This is deemed a circulation pattern since it occurs continuously, especially at high gas velocities.

Figure 4-8a-c shows the prominent mechanism causing the stray bubble circulation pattern. In this mechanism, a bubble in the baffle encroachment stage (lagging) approaches a bubble in the formation or early developing bubble flow stage (leading) at an oblique angle. Because of the oblique angle of approach (Figure 4-8a), a 'finger' of gas extends from the far side of the leading bubble around the lagging bubble (Figure 4-8b). As the leading and lagging bubbles coalesce, the finger is released as a distinct bubble into the emulsion stream (Figure 4-8c). This stray bubble usually coalesces with either the original parent bubble or a trailing bubble. Occasionally, the stray bubble simply disperses into the emulsion stream.

The secondary mechanism leading to the stray bubble circulation pattern is shown in Figure 4-9a-c. In this mechanism, the leading bubble is generally in the developing bubble flow stage (Figure 4-9a). In order to catch up to the leading bubble, the lagging bubble stretches across the baffle. In doing so, the bubble cross section thins near the edge of the baffle skirt (Figure 4-9b). A rupture occurs across the stretched section of the bubble, releasing the tail of the lagging bubble into the emulsion stream. The stray bubble either coalesces with a later bubble or disperses into the catalyst stream.

4.5.2 Bubble Distribution and Frequency

The hydrodynamic behaviour in a fluidized bed is often expressed in terms of time-averaged voidage profiles. These voidage profiles are useful because they provide information on the spatial distribution of bubbles in a fluidized bed. This has a considerable impact on fluidized bed operation, as non-uniform bubble distribution over the bed improves the overall mass transport between the emulsion and bubble phases. The following discussion pertains to the simulated stripper operating at a solids circulation rate of 45 kg/(m^2·s) and a stripping gas velocity of 0.1 m/s. Because the simulations outlined in Table 4-3 all exhibit similar bubbling behaviour, most of the discussion presented here is valid for that entire range of simulations. The effects of changing operating conditions will be discussed in Section 4.5.3.

Figure 4-10 presents the time-averaged voidage profile for the active area (ignores the permanent void space under the baffle) of the simulated stripper operated at a solids circulation rate of 45 kg/(m^2·s) and a stripping gas velocity of 0.1 m/s. In this plot, the bottom of the skirt of the disc baffle (the 'lower' baffle) is located at a height of 0 mm, and the bottom of the skirt of the donut baffle (the 'upper' baffle) is located at 165mm (Figure 4-11). The local time-averaged voidage underneath the baffles was excluded from the plot. Thus, at low axial positions a full cross-sectional profile is not presented.

At a distance of 15 mm above the skirt of the disc baffle, Figure 4-10 shows a sharp increase in the voidage immediately adjacent to the disc baffle (the disc baffle extends from $0 \leq r/R \leq 0.69$). The profile peaks at $r/R = 0.78$, then decreases towards the vessel wall. At this baffle interspace height, the time-averaged voidage is considerably higher than the minimum fluidization voidage at nearly all radial locations. This implies that there is some gas-solids

contacting at most radial locations. However, due to the high-velocity of the emulsion stream at the pinch point there would be limited contacting time between the gas and solids. Also noteworthy is that the gas hold-up at this measurement level is higher than that at the 50 mm baffle interspace height (Figure 4-12). This increased gas hold-up supports the observation that bubbles are stationary or slowly rising as they grow. Based on the high voidage adjacent to the baffle and the high gas hold-up, it is apparent that at a height of 15 mm the bed operates in the bubble formation stage.

At a baffle interspace height of 50 mm, it is observed that the maximum in the time-averaged voidage profile has shifted to a radial position of $r/R = 0.88$ (Figure 4-10). Consistent with the observations made in Section 4.5.1 for the developing bubble stage, this implies that bubbles have a tendency to move towards the wall as they ascend from the lower baffle. Movement of bubbles towards the wall is confirmed by the bubbling frequency profiles taken at the same height (Figure 4-13). This figure shows that moving from a baffle interspace height of 15 to 50 mm results in an increased bubbling frequency in the near-wall region, indicated by a shift in the frequency profile towards the wall. Also notable from this figure is that a small decrease in the peak frequency is observed when moving from the 15 to 50 mm baffle interspace height, indicating some bubble coalescence between these two heights. Acceleration of bubbles is confirmed by the cross-sectional averaged voidage (Figure 4-12), which indicates the lowest gas hold-up at any measurement height tested.

At a baffle interspace height of 50 mm, the time-averaged voidage profile at $r/R \leq 0.64$ is maintained at or near the minimum fluidization voidage. This indicates a segregated flow of solids down the face of the disc baffle. This is confirmed by analyzing the time-averaged solids velocity vectors (Figure 4-14). The figure shows a high solids concentration (as illustrated by the darker region of lower voidage and the low-magnitude solids velocity vectors) above the face of the disc baffle that diminishes towards the eastern wall. Segregated emulsion flow along the face of the baffles was also observed by Rivault *et al.* (1995) and McKeen (2003).

At a baffle interspace height of 85 mm, located 5 mm (one computational cell) above the apex of the disc baffle, the time-averaged voidage profile (Figure 4-10) has flattened considerably. There are two phenomena that were discussed in Section 4.5.1 that could account for the flattening of the profile: changing of the bubble shape from elongated to more-spherical, or drifting of the bubbles away from the wall.

It is hypothesized that bubbles change from elongated to spherical in shape because they become sheltered from the high-velocity catalyst flow as they approach the baffle above. This hypothesis is confirmed by Figure 4-15, which presents the instantaneous solids velocity vector field as bubbles ascend from the disc to the donut baffle. This figure indicates that, as the bubbles crest above the apex of the disc baffle, they escape the high-velocity solids streaming along the top of the baffle. Although the bubbles still stream near the stripper wall at this baffle interspace height, they have a tendency to increase in width away from the wall (flattening of the bubble). This appears to be the most probable reason for the flattening of the time-averaged voidage profile at a baffle interspace height of 85 mm. This increasing bubble width implies the bubbles have entered the final stage of development: baffle encroachment.

Drifting of the bubbles away from the wall region could potentially result in a flattening of the time-averaged voidage profile at a baffle interspace height of 85mm. However, the frequency profiles (Figure 4-13) show that the bubbling frequency does not change considerably in the near-wall region between the baffle interspace heights of 50, 85, and 120 mm. If significant drifting of the bubbles did occur, one would expect a shift of the frequency profiles towards the western wall. Shifting of the frequency profile is not observed in Figure 4-13; instead it is found that a tail is formed that extends towards the western wall at the 85 mm height. Formation of this tail is likely a result of the widening of bubble discussed earlier. Thus, it seems unlikely that there is any significant bubble drifting away from the wall between these baffle interspace heights and therefore would not contribute significantly to the flattening of the voidage profile.

At a baffle interspace height of 120 mm, the time-averaged voidage profile continues to flatten to the extent where the voidage is above minimum fluidization at nearly all radial locations. Similar to the findings at a height of 85mm, it seems that the flattening of the profile is caused by an increase in the width of the bubbles. There does not appear to be significant drifting of the gas bubbles, as indicated by a constant peak bubbling frequency near the wall as compared to baffle interspace heights of 85 and 50 mm (Figure 4-13). Instead, there is a widening of the tail extending to the centre of the bed. As discussed earlier, this is indicative of an increasing bubble width.

The baffle interspace height of 155 mm is located 10 mm (2 computational cells) below the donut baffle skirt. At this height, the time-averaged voidage profile is nearly linear at a radial locations $0.74 \leq r/R \leq 0.98$. This radial location corresponds to the same area occupied by the void space under the donut baffle ($0.76 \leq r/R \leq 1.0$). The location of the linear time-averaged voidage profile also corresponds to the maximum voidage at this measurement height. It is expected that the high voidage at this location is caused by sloshing of gas that results when rising bubbles are partly absorbed into the void space under the baffle. At $r/R \leq 0.71$ the voidage decreases towards the centerline. In Section 4.5.1 it was observed that the bubbles had a high amount of lateral movement towards the outer edge of the upper baffle as they approach the void space under the baffle. This is confirmed by the frequency profiles in Figure 4-13, which show a significant shift in the bubbling frequency to $r/R < 0.74$. Also of note is the increased bubbling frequency at 155 mm, indicating a break-up of bubbles between the baffle interspace heights of 120 and 155 mm.

The data suggests that the baffle encroachment phase would offer the best opportunity for mass transfer in the stripper (baffle interspace heights ≥ 85 mm). This height corresponds to the interspace located between the apex of the lower baffle and the void space under the upper baffle. Superior mass transfer would occur due to improved use of the vessel cross section indicated by the time-averaged voidage profiles (Figure 4-10), a decreased bubble rise velocity indicated by the increased gas hold-up (Figure 4-12), and a decreased emulsion velocity resulting from the full-cross section of the stripper being available to gas and solids flow. Conversely, at baffle interspace heights < 85 mm it is thought that a high bubble rise velocity, high emulsion velocity, and streaming of bubbles would result in poor gas-solids contacting. This suggests inefficient use of the available volume of the stripper vessel at baffle interspace heights < 85 mm. The volume of the stripper vessel is further underutilized at interspace heights < 85 mm due

to the gas voids that form under the baffles, since there is no gas-solids contacting at this location.

4.5.3 Effect of Operating Conditions on the Hydrodynamic Behaviour

The preceding discussion only presented hydrodynamic data for bubble flow from the disc baffle on the bottom to the donut baffle on top at a solids circulation rate of 45 kg/(m^2·s) operated at a stripping gas velocity of 0.1 m/s. However, it is found that changing these conditions has little influence on the overall hydrodynamic behaviour. This section discusses the effects of these variables: baffle order, stripping gas velocity, and solids circulation rate.

4.5.3.1 Effect of the Baffle Order

Figure 4-16 presents the time-averaged voidage profile for the bubble ascending from the donut baffle on the bottom to the disc baffle on top. The figure shows that a similar bubbling behaviour occurs when bubbles ascend from the donut to the disc baffle as that observed when bubbles ascend from the disc to the donut. At the lowest baffle interspace height, 15 mm above the donut skirt, a sharp increase in the voidage is observed adjacent to the donut baffle located at $0.72 \leq r/R \leq 1.0$. At higher baffle interspace heights, the profile first shifts towards the western wall, then flattens across the vessel width. One notable dissimilarity between Figure 4-10 and Figure 4-16 are that the bubbles do not stream as close to the wall when the donut is on the bottom. This is likely due to the increased width of the upper disc baffle creating a wider 'sheltering' effect from the high catalyst velocity at the pinch point.

4.5.3.2 Effect of the Solids Circulation Rate

Changing the solids circulation rate is found to have minimal impact on the hydrodynamic behaviour in the stripper at a gas velocity of 0.1 m/s. Figure 4-17 presents the effect of changing the solids circulation rate on the time-averaged voidage profiles at a baffle interspace height of 50 mm. As can be seen in Figure 4-17, there is slightly higher preference for gas to travel along the wall at elevated solids circulation rates. Figure 4-18 presents the bubbling frequency profiles at a baffle interspace height of 50 mm. The figure shows that the peak frequency is decreased at elevated solids circulation rates. This decreased frequency suggests that the bed contains fewer bubbles of larger diameter.

At a gas velocity of 0.2 m/s, changing the solids circulation rate has a less predictable impact on the time-averaged voidage profiles. Increasing the solids circulation rate from 45 to 60 kg/(m^2·s) results in a less complete use of the vessel cross-section at baffle interspace heights of 85 and 120 mm (Figure 4-19). This observation is consistent with that observed at a stripping gas velocity of 0.1 m/s. Further increasing the solids circulation rate from 60 to 75 kg/(m^2·s), however, results in vastly improved use of the vessel cross section at these heights (Figure 4-19). This increased use of the vessel cross section is thought to occur because of gas accumulation under the upper donut baffle causing earlier lateral movement of the bubbles towards the outer edge of the upper baffle. This hypothesis is confirmed by the bubbling frequency profile in Figure 4-20. This figure shows a strong shift in the frequency profile towards the western wall at

a baffle interspace height of 120 mm for a solids circulation rate of 75 kg/(m^2·s) compared to the other, lower solids circulation rates simulated. It should be noted that, while this appears to be beneficial from a gas-solids mixing standpoint, the increase in the gas accumulation under the baffle reduces the active area (where both gas and solids are present) of the stripper. Thus, gas-solids contacting would be reduced. Increased gas accumulation under the baffles is one of the criterion set forth by Bi *et al.* (2004) to indicate flooding in an FCC stripper. However, as will be discussed in Section 4.5.5, the stripper simulated at a solids circulation rate of 75 kg/(m^2·s) and a stripping gas velocity of 0.2 m/s is not yet flooded.

In the discussion of the generalized bubble behaviour, it was noted that a decrease in the peak bubbling frequency between baffle interspace heights of 15 and 50 mm indicated some degree of bubble coalescence between these locations. For all other operating conditions simulated, no change in the peak bubbling frequency was found to occur. This implies insignificant bubble coalescence between these measurement heights. It appears that the bulk of bubble coalescence at elevated solids circulation rates and stripping gas velocities occurs before the baffle interspace height of 15 mm; while bubbles are forming adjacent to the baffle skirt.

The gas hold-up in the stripper is also affected by the solids circulation rate (Figure 4-12). As can be seen in the figure, increasing the solids circulation rate results in small increases in the gas hold-up at most measurement heights. This is especially evident for a solids circulation rate of 75 kg/(m^2·s), however as discussed earlier the stripper is approaching a flooded state at this solids circulation rate.

The results presented here are not in agreement with the experimental study of Rivault *et al.* (1995). Rivault *et al.* (1995) found that the bubbling frequency was not sensitive to the solids circulation rate between 28 and 108 kg/(m^2·s), but observed an increased use of the vessel cross section at elevated solids circulation rates. In this study, the model predicted a lower bubbling frequency and reduced use of the vessel cross-section at elevated solids circulation rates. The reasons for this discrepancy between the results presented here and those of Rivault *et al.* (1995) may be the axial location of the measurement plane used to determine the frequency profiles. In the present work, the bubbling frequencies are insensitive to the solids circulation rate only at the highest baffle interspace height of 155 mm. At this height, the increased gas hold-up adjacent to the upper baffle could also cause an earlier shift in the bubble trajectory from the wall to the outside edge of the upper baffle. This lateral movement of bubbles would give the appearance of improved use of the vessel cross section. In the work by Rivault *et al.* (1995) the location of measurement plane used to acquire bubble frequency data at different solids circulation rates is not specified, and thus it is uncertain whether this is indeed the cause of the discrepancy.

4.5.3.3 Effect of the Stripping Gas Velocity

The effect of changing the gas velocity while maintaining a static solids circulation rate of 45 kg/(m^2·s) and 60 kg/(m^2·s) on the time averaged voidage profile is presented in Figure 4-21 and Figure 4-22, respectively for a baffle interspace height of 85 mm. It is found that increasing the stripping gas velocity causes a more complete use of the stripper cross-section, indicated by a lateral extension towards the western wall of the time-averaged voidage profile (Figure 4-21, Figure 4-22). This effect is more pronounced at elevated solids circulation rates, and is probably

influenced by decreased spacing of bubbles causing an earlier shift of the bubble trajectory away from the wall towards the outside of the upper baffle. This hypothesis is supported by a small shift in the bubbling frequency profile (Figure 4-23).

Changing the gas velocity has a significant effect on the bubbling frequency profiles. Aside from the expected increase in the peak bubbling frequency, it is found that increasing the gas velocity results in the formation of a secondary peak in the bubbling frequency profiles at a measurement height of 85 mm (Figure 4-23). As discussed in Section 4.5.1, a unique circulation pattern is prevalent at high gas velocities that results in the formation of a small stray bubble that moves either downwards or is stationary. The secondary peak in the frequency profiles appears to be caused by the stray bubble formation in the circulation pattern.

4.5.4 Bubble Properties

Measurement of the bubble diameter is very important in beds of FCC catalyst because mass transfer is typically limited between the emulsion and the bubble cloud in fine-particle systems (Sit & Grace, 1981). A popular method for measuring the bubble diameter is via the pierced chord length:

$$d_c = U_b t_p \tag{4.2}$$

The bubble chord length is defined as the vertical length of bubble as it rises through a defined point in space. This method, commonly applied to fibre optic probe measurements, requires the bubble velocity to be known. The bubble velocity is found by determining the time required for a bubble to traverse a known distance in the bed. The pierced bubble time, t_p, is the time taken for the bubble to move through the cell used to sample the dynamic bed voidage.

In the case of spherical bubbles, the bubble chord length at the centre of the bubble is equivalent to the bubble diameter. Because bubbles are not always pierced through the centerline, Lim & Agarwal (1990) proposed a correlation between the mean pierced bubble chord length and the true mean bubble diameter:

$$d_b = 1.35 d_c \tag{4.3}$$

It is important to note that the correlation developed by Lim & Agarwal (1990) is only applicable to mean values of the bubble chord length. While it is possible to calculate an actual distribution of bubble sizes, it would require assuming a bubble shape (Lim *et al.,* 1995). As noted earlier, bubble shapes appear elongated due to the downflow of catalyst in a CFB stripper. It would, therefore, be tenuous to assume a conventional or consistent bubble shape in the stripper.

The goal of the current work is to develop a correlation relating the bubble chord length to an equivalent spherical bubble diameter. In the simulation, a computational cell was considered to be a gas bubble when $\varepsilon \geq 0.80$ (McKeen, 2003). Appendix C.3 presents the MatLab® computer code used to calculate the pierced chord length and bubble frequency from the MFIX simulation data. The pierced bubble time was calculated at a baffle interspace height of 85 and 75 mm above the disc baffle skirt. The bubble velocity was measured by dividing the separation distance (10 mm) by the time lag between detection of the rising bubble at the lower and upper planes. Voidage data was sampled at 1000 Hz to calculate the bubble rise and pierced bubble time. Lim & Agarwal (1992) concluded that procedures need to be incorporated to reject non-vertically rising bubbles. In the current study, bubbles in the two measurement planes whose

pierced time differed by more than 15% were rejected from the bubble diameter measurements. Bubble properties were calculated at a radial location of r/R = 0.84 in the simulated FCC stripper. This location, corresponding to the maximum in the frequency profiles, was chosen because the pierced bubble time showed the least deviation in the pierced time calculations between the two planes used to sample the voidage data.

Figure 4-24 shows the effect of solids circulation rate and stripping gas velocity on the mean bubble chord length. It can be seen from the figure that the bubble chord length increases with both an increase in solids circulation rate and stripper gas velocity. Given that the cross-section of the simulated stripper available for gas and solids flow is 120 mm, the plot implies that a spherical bubble would approach slug flow at elevated solids circulation rates and stripper gas velocities. Because gas slugging was not observed in the simulations, it is probable that the bubble chord length highly misrepresents the true bubble diameter.

Due to the significance of bubble diameter measurements and the practicality of fibre optic probes to study the hydrodynamic behaviour in fluidized beds, it is beneficial to be able to correlate the pierced chord length of a bubble to its true diameter. To do so, it is first convenient to define the equivalent bubble diameter. The equivalent bubble diameter in this work is defined as the diameter of a perfectly circular bubble whose area is equal to that of the area of the elongated bubbles present in the modeled CFB stripper. The area of the simulated bubbles was found by 'photographing' the bubble as it breached the 85 mm baffle interspace height. At each time step in the simulation, the 85 mm plane was sampled and tested to see if any computational cell had a voidage that would indicate the presence of a bubble ($\varepsilon \geq 0.8$). If a bubble was detected, the next row of cells (h = 80 mm) was sampled, continuing until a bubble could no longer be detected in the plane. Each cell containing $\varepsilon \geq 0.8$ was assigned a value of 1, and every other cell was assigned a value of 0 (Figure 4-25). The area of the bubble could then be found by summing the matrix containing the 'on/off' data and multiplying by the area of the computational cells, 25 mm^2. The pierced chord length of the bubble was found by summing the vertical components of the bubble 'picture' sequence at a radial location of r/R = 0.84. The MatLab® computer code used to calculate the bubble area and circumference from the MFIX simulation data can be found in Appendix C.2.

Figure 4-26 presents the relationship between the pierced chord length and the equivalent bubble diameter. As can be seen in the figure, the equivalent bubble diameter is reasonably well represented by a linear relationship to the pierced chord length measured at the radial location of maximum local bubbling frequency. In this particular simulation, the ratio between the equivalent bubble diameter (*EBD*) and the pierced chord length (*PCL*) is *EBD/PCL* = 0.60. A ratio of *EBD/PCL* less than unity indicates that bubbles are elongated.

It was found that the ratio of *EBD/PCL* is relatively insensitive to the operating conditions exhibiting smooth bubbling. The average ratio of the equivalent bubble diameter to the pierced chord length is *EBD/PCL* = 0.59 ± 0.05 (95% confidence interval) at a baffle interspace height of 85 mm. Tests were also undertaken to see if this ratio was sensitive to the baffle interspace height used to sample the voidage data. At measurement heights of 50 mm and 120 mm, the ratio of *EBD/PCL* was found to be 0.65 and 0.70, respectively, at a solids circulation rate of 45 kg/(m^2·s) and a stripper gas velocity of 0.1 m/s. It is obvious that there is an

influence on the measurement height on the ratio of *EBD/PCL*. This is consistent with the discussion in Section 4.5.1 that found a changing bubble shape with their positions relative to the lower and upper baffle. This demonstrates the need to develop specific correlations for use in CFB strippers. It also may indicate a need for tomographic measurements for properly interpreting the hydrodynamic behaviour in FCC strippers.

Bubble diameter is of specific importance in mass transfer operations because it quantifies the surface area available for mass transport between the emulsion phase and bubble cloud. However, due to the distorted nature of the bubbles in the stripper one would expect a higher rate of mass transport than that predicted by the equivalent bubble diameter. It is useful, therefore, to relate the sphericity of the bubbles in the CFB stripper. In this work, the sphericity (Φ) is defined by the equation:

$$\Phi = \frac{A_b / P_b}{EBD/4} \tag{4.4}$$

The term on the bottom, *EBD*/4, represents the area-to-perimeter ratio of a perfect circle. The top term, A_b/P_b, represents the area-to-perimeter ratio calculated using the 'picture' method described earlier. The perimeter was found by summing the distances between adjacent cells on the exterior of the bubble. Because of the inherent errors in calculating the perimeter using this method, it should be noted that a perfectly spherical bubble represented in the simulation cells would have a sphericity of approximately 0.92.

Figure 4-27 presents the relationship between the bubble sphericity and the equivalent bubble diameter at a solids circulation rate of 45 kg/(m^2·s) and gas velocity of 0.1 m/s. The data in the figure shows a mostly linear trend of increasing sphericity with decreasing *EBD*. Although all operating conditions exhibited the same mostly linear trend between sphericity and *EBD*, a generalized correlation could not be established because of differences in the individual relationships. Table 4-4 provides the values of sphericity for the mean *EBD* for the range of simulations.

The bubble velocity affects the rate of mass transfer in the bed because it defines the contact time between the emulsion phase and bubbles. The bubble rise velocity with respect to the emulsion phase can be correlated to the bubble diameter for bubbles rising in isolation. One such correlation, based on two-phase theory, is that of Davidson & Harrison (1963):

$$U_{br} = 0.711(g d_b)^{1/2} \tag{4.5}$$

The variable 'U_{br}' represents the rise velocity of a bubble with respect to the emulsion phase. The velocity of a bubble with respect to a stationary reference, U_b, can be found from the equation (Davidson & Harrison, 1963):

$$U_b = U_{strip} - U_{mf} + U_{br} \tag{4.6}$$

Figure 4-28 presents the average bubble velocity determined from the simulation compared to the predicted bubble velocity found from equation 4.6. The bubble rise velocity was calculated from equation 4.5 using the average *EBD* for each of the conditions simulated (Table 4-4). It can be seen that, for most operating conditions simulated, the correlation can reasonably predict the bubble velocity. However, a higher sensitivity to the stripper gas velocity is observed in the simulations compared to that predicted by the correlation. The correlation best predicts the

bubble velocity at a stripper gas velocity of 0.2 m/s. At lower stripper gas velocities, the correlation overpredicts the bubble velocity; while at higher gas velocities the correlation underpredicts the bubble velocity. It is thought that the high sensitivity to the stripper gas velocity observed in the simulations occurs due to a high frequency of bubble encroachment at elevated gas velocities. As discussed in Section 4.5.1, bubble encroachment was observed to cause acceleration of the lagging bubble. Encroachment is more frequent at elevated gas velocities due to a decreased spacing of bubbles, and thus is likely to be the reason for this high sensitivity of the bubble velocity to the stripping gas velocity.

It should be noted that the bubble rise velocity is expected to vary in the interspace between disc and donut baffles. This conclusion is based on the increasing gas hold-up that is observed between baffle interspace heights of 85 and 120 mm (Figure 4-12). Unlike the axisymmetric two-dimensional case simulated, however, in a fully three-dimensional bed the bubbles can take multiple pathways to ascend the baffles. This would likely increase spacing between and result in a lesser incidence of bubble encroachment in the three-dimensional bed compared to that observed in the simulations. This would result in a lower bubble rise velocity in the three-dimensional beds. However, the strong affinity between leading and lagging bubbles observed in the simulations does suggest the possibility for streaming flow of bubbles in three-dimensional beds, especially at elevated gas velocities. This may be reason Rivault *et al.* (1995) found a decrease in the bubbling frequency at elevated gas velocities – it is possible that measurement of the radial bubbling frequency is sensitive to the polar angle that the probe inserted into the vessel.

4.5.5 Flooded Stripper Analysis

The previous discussion does not pertain to simulations for solids circulation rates of 75 kg/(m^2·s) and 90 kg/(m^2·s) operated at stripping gas velocity of 0.3 and 0.1 m/s, respectively. Based on qualitative analysis at these operating conditions, the stripper was deemed to be flooded. This assertion is based on observation in the simulation of the criteria set forth by Bi *et al.* (2004) to indicate flooding in FCC strippers: gas underflow from the stripper into the standpipe, and a development of a region of high voidage under the baffles.

Figure 4-29a,b shows time-lapse images of the simulations exhibiting flooding behaviour. As can be seen in the figure, the void space under the baffles becomes expanded at these conditions. The void space extends downwards along the wall; extending on an angle towards the outer edge of the baffles. A similar behaviour was observed in the simulation operating at a solids circulation rate of 75 kg/(m^2·s) and stripping gas velocity of 0.2 m/s, however the principal difference between this simulation and those deemed flooded is absence of the large area of voidage extending from the bottom donut baffle to the southern boundary of the simulation. This area of voidage if thought to be an indicator that gas underflow from the stripper into the standpipe would occur. However, because the southern boundary condition establishes a constant solids and gas velocity, gas underflow into the standpipe does not actually occur in the simulation.

The operating conditions leading to flooding in the simulation are not expected to correspond to the flooding point in true stripper operation. This is because the catalyst velocity at

the pinch point in the two-dimensional simulation is more significantly affected by passing bubbles than would occur in a true three-dimensional system. In the three-dimensional system, bubbles would occupy only a small fraction of the open area at the pinch point. This is in contrast to the two-dimensional simulation, where bubbles are observed to nearly span the pinch point. The significant cross-section occupied by the bubbles in these instances would significantly perturb the catalyst velocity. Senior *et al.* (1998) speculated that flooding occurs in FCC strippers when the downward catalyst velocity through the pinch point exceeds the bubble rise velocity. It is obvious, then, that flooding would be predicted at lower solids circulation rates and stripping gas velocities in a axisymmetric two-dimensional simulation than would actually occur in a three-dimensional bed. Use of a fully three-dimensional model would be expected to more closely predict the true flooding point in the experimental system.

4.6 Conclusions

Hydrodynamics were examined in a simulated FCC unit stripper containing geometrically scale disc-and-donut baffles. Solids circulation rates ranging from 45 to 90 kg/(m^2·s) were simulated at stripping gas velocities ranging from 0.1 to 0.3 m/s. Most simulations exhibited smooth bubbling behaviour, however flooding was observed for some operating conditions. The bubbling behaviour in the interspace between disc and donut baffles exhibited complex behaviour never reported in the literature. After release of the bubble from the void space under the baffle, the bubble accelerates and elongates while moving towards the wall. When the bubble breaches the apex of the baffle it begins to take on a more-spherical shape as it approaches the upper baffle. The hydrodynamic behaviour is heavily influenced by leading bubbles, especially at high stripping gas velocities. Bubble properties, including the pierced diameter, rise velocity, sphericity, and equivalent bubble diameter were evaluated. These properties were found to be sensitive to the axial position between an upper and lower baffle.

Table 4-1: Conservation equations used in MFIX.

Gas Continuity	$\frac{\partial}{\partial t}\left(\varepsilon\rho_g\right)+\nabla\cdot\left(\varepsilon\rho_g\vec{v}_g\right)=0$
Solids Continuity	$\frac{\partial}{\partial t}\left(\varepsilon_s\rho_p\right)+\nabla\cdot\left(\varepsilon_s\rho_p\vec{v}_s\right)=0$
Gas Momentum	$\frac{\partial}{\partial t}\left(\varepsilon\rho_g\vec{v}_g\right)+\nabla\cdot\left(\varepsilon\rho_g\vec{v}_g\vec{v}_g\right)=-\varepsilon\nabla P+\nabla\bar{\bar{\tau}}_g+F_{gs}\left(\vec{v}_s-\vec{v}_g\right)+\varepsilon\rho_g\vec{g}$
Solids Momentum	$\frac{\partial}{\partial t}\left(\varepsilon_s\rho_p\vec{v}_s\right)+\nabla\cdot\left(\varepsilon_s\rho_p\vec{v}_s\vec{v}_s\right)=-\varepsilon_s\nabla P+\nabla\bar{\bar{S}}_s+F_{gs}\left(\vec{v}_s-\vec{v}_g\right)+\varepsilon_s\rho_p\vec{g}$

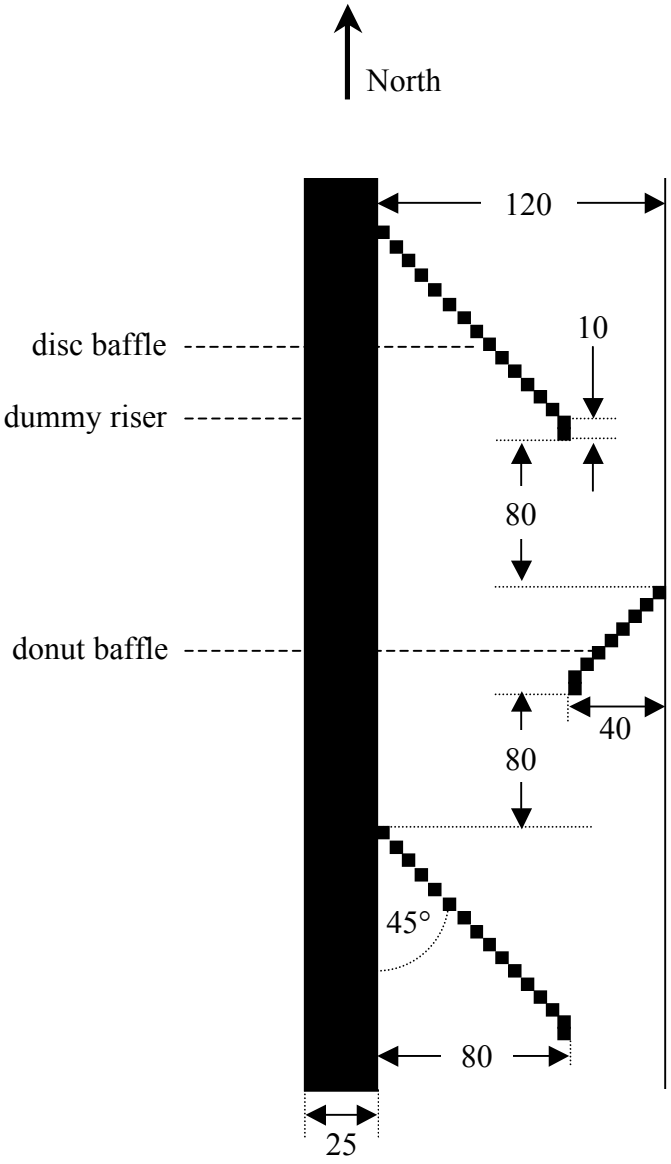

Figure 4-1: Baffle geometry used in simulations. All dimensions in mm.

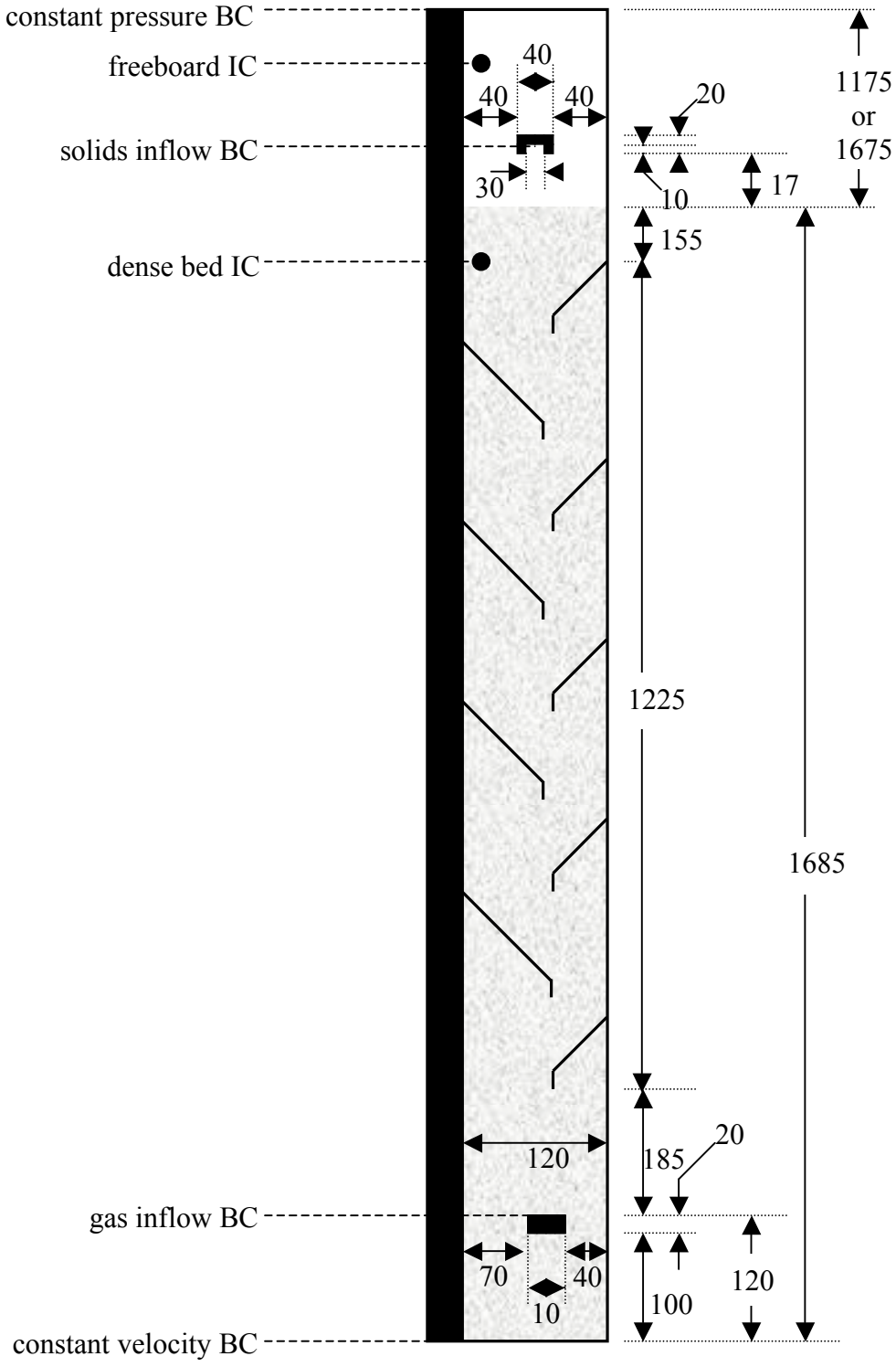

Figure 4-2: Stripper geometry used in simulations. All dimensions in mm.

Table 4-2: Gas and particle properties for simulated FCC stripper.

Property	Value
Particle density (kg/m^3)	1550
Mean particle diameter (μm)	98
Maximum packing voidage	0.45
Gas viscosity (Pa·s)	1.98×10^{-5}
Temperature (K)	298
Restitution coefficient	0.95
Internal angle of friction	30°

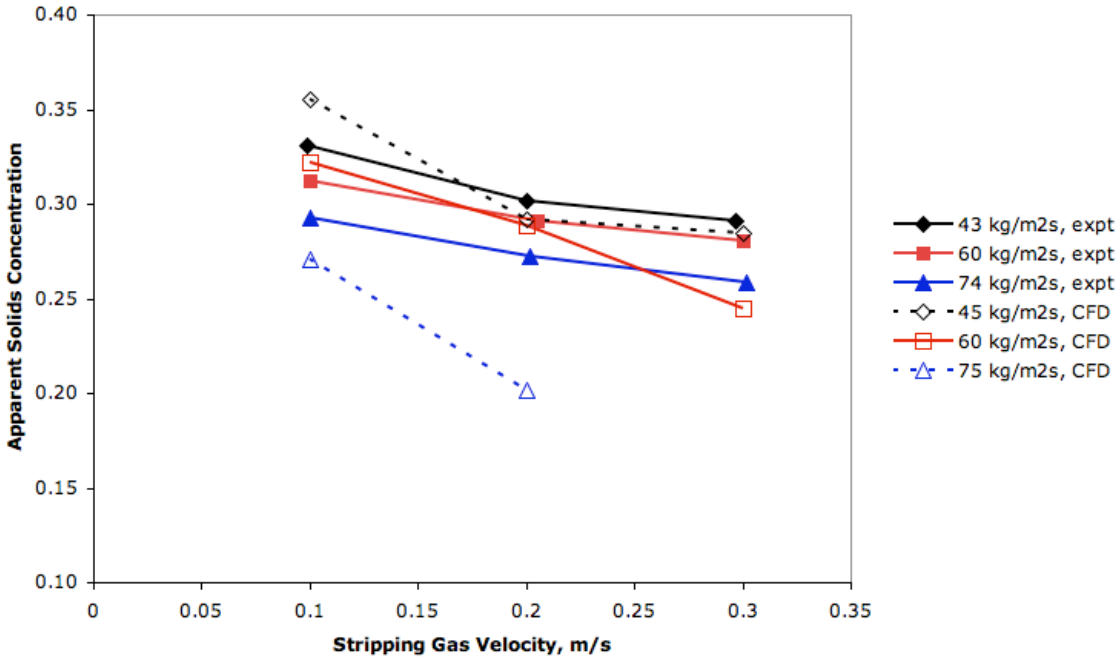

Figure 4-3: Comparison of the stripper apparent solids concentration predicted by the CFD model with experimental data.

Table 4-3: The hydrodynamic behaviour observed at different simulated operating conditions.

Hydrodynamic Behaviour	Solids Circulation (kg/(m^2·s))	Gas Velocity (m/s)
Bubbling	45	0.1, 0.2, 0.3
Bubbling	60	0.1, 0.2
Bubbling	75	0.1, 0.2
Flooding	75	0.3
Flooding	90	0.1

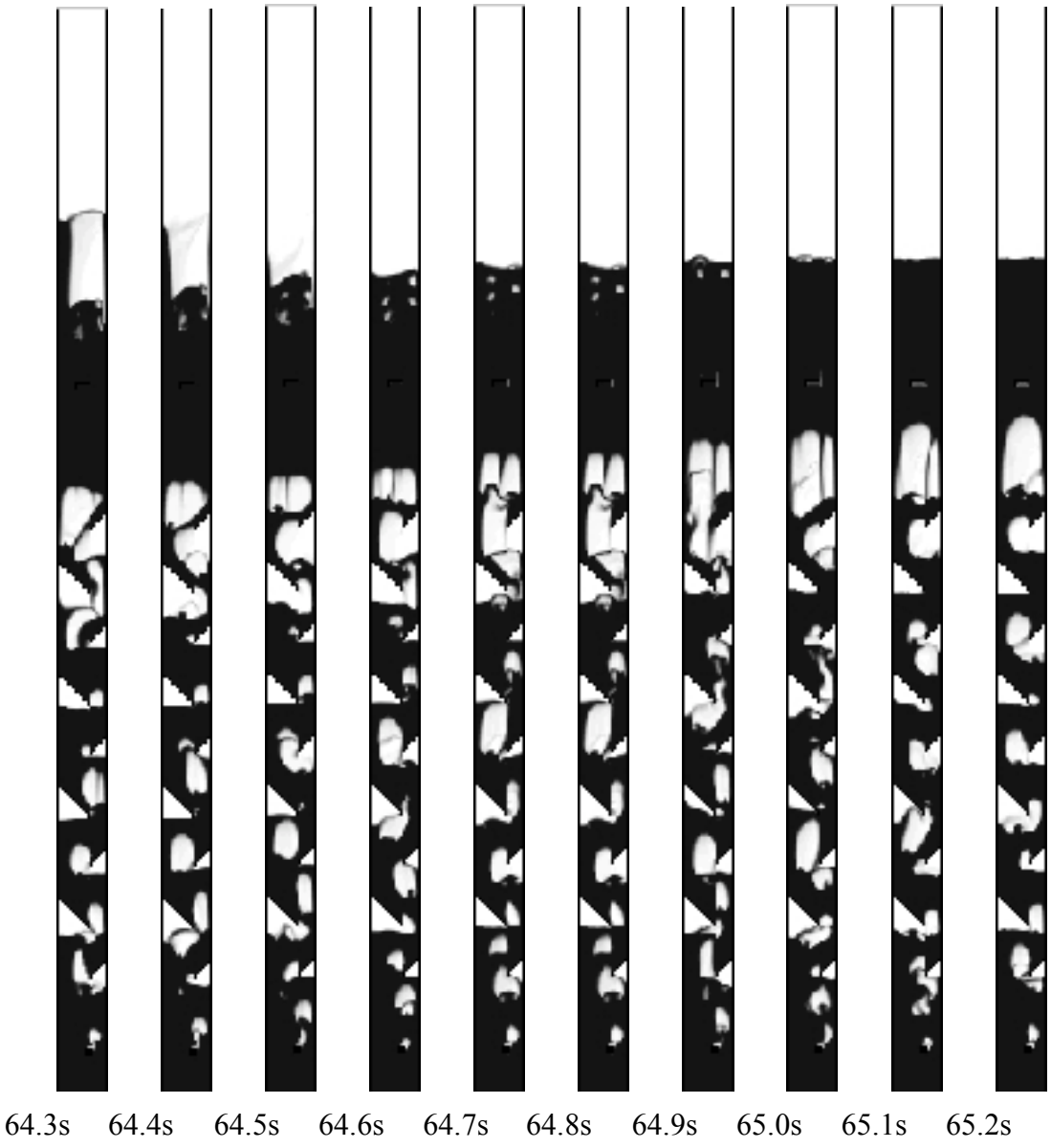

Figure 4-4: Time lapse images of simulated CFB stripper operating at a solids circulation rate of 45 kg/(m^2·s) and stripping gas velocity of 0.1 m/s. White areas indicate gas phase and black areas indicate emulsion phase.

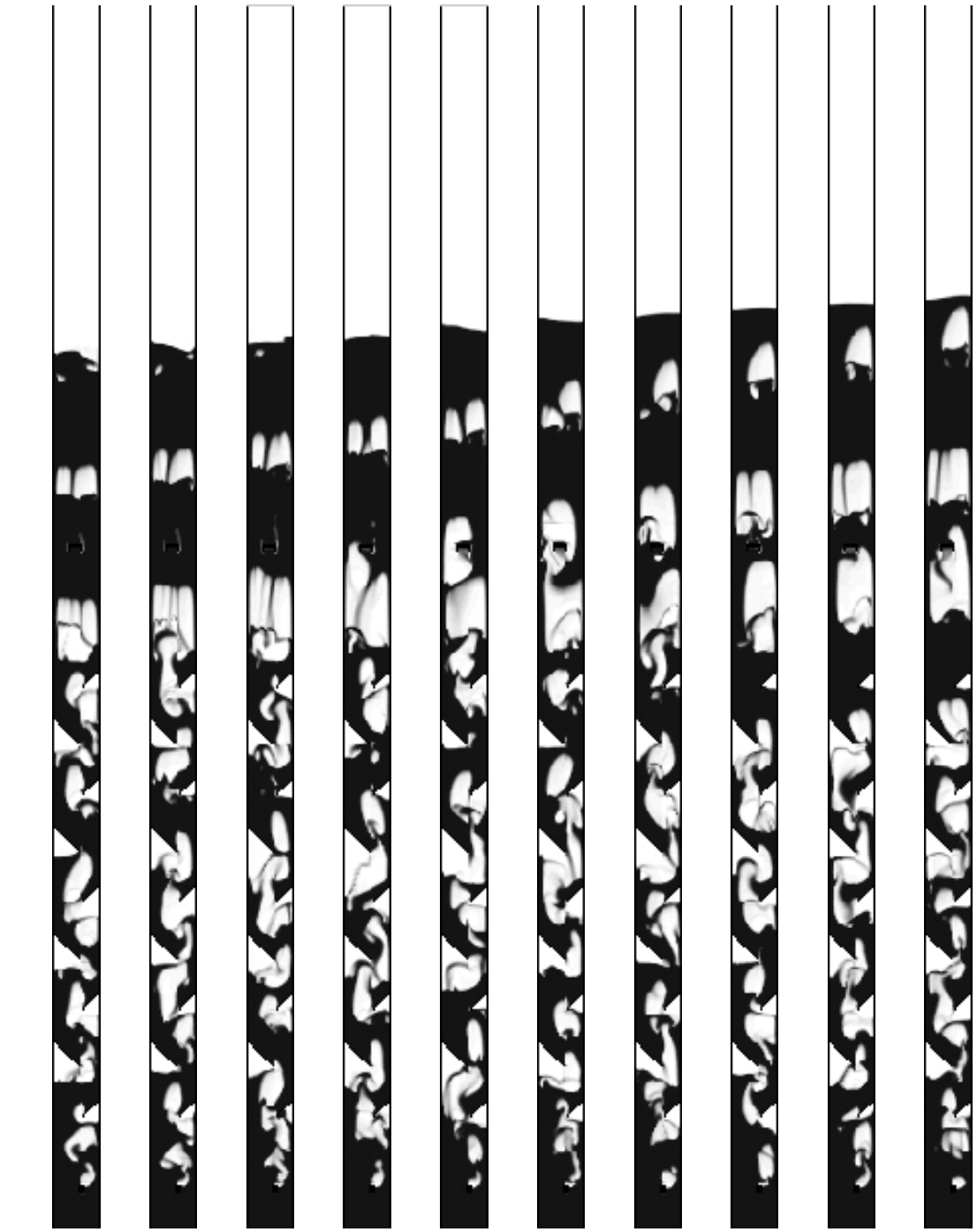

Figure 4-5: Time lapse images of simulated CFB stripper operating at a solids circulation rate of 45 kg/(m^2·s) and stripping gas velocity of 0.2 m/s. White areas indicate gas phase and black areas indicate emulsion phase.

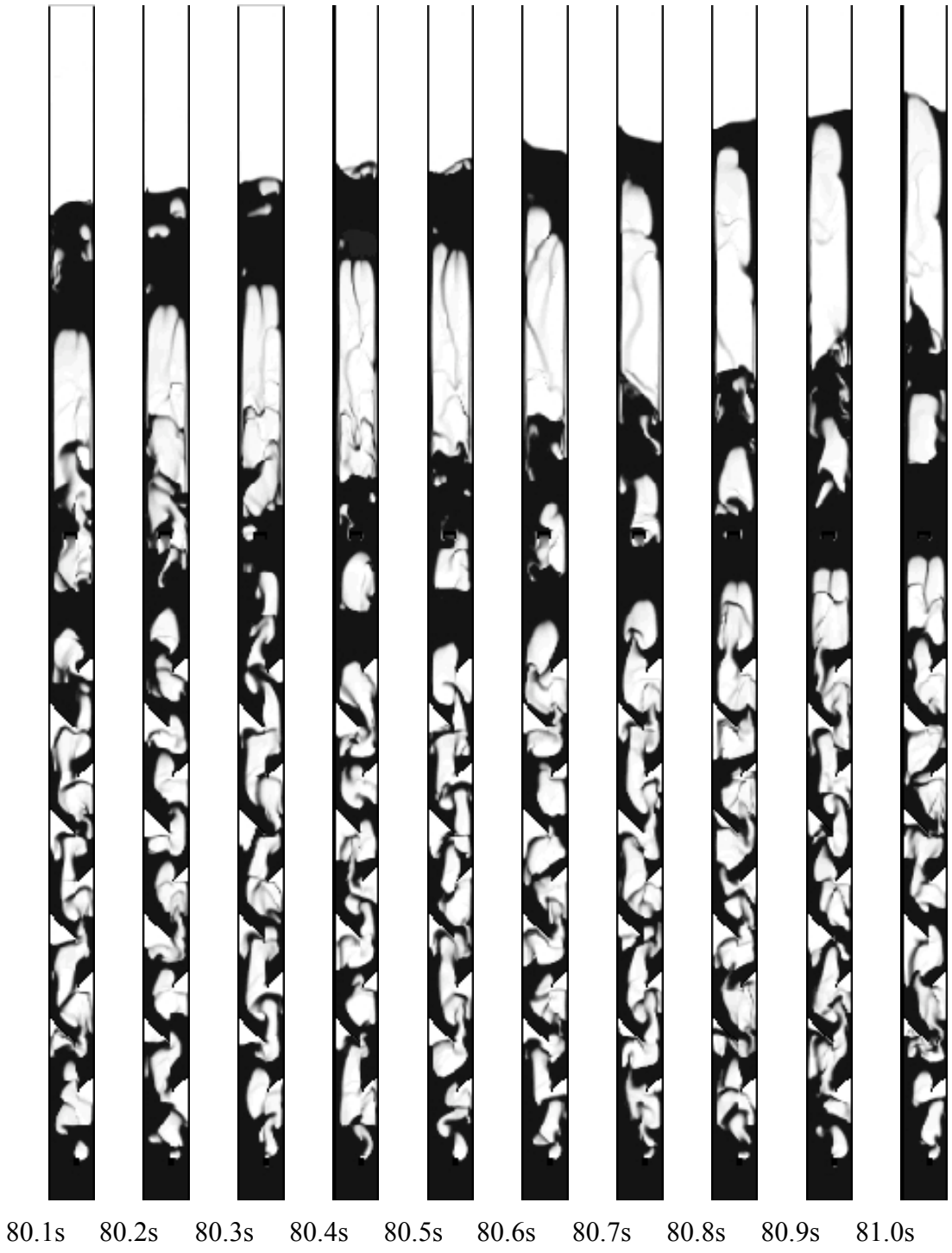

Figure 4-6: Time lapse images of simulated CFB stripper operating at a solids circulation rate of 45 kg/(m^2·s) and stripping gas velocity of 0.3 m/s. White areas indicate gas phase and black areas indicate emulsion phase.

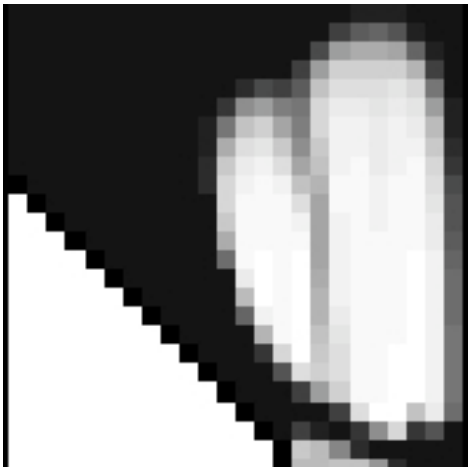

a)

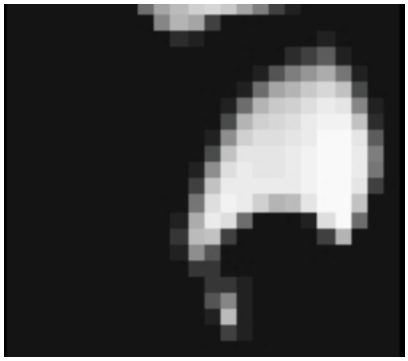

b)

Figure 4-7: Bubble splitting in the simulated CFB stripper a) knifing b) wake shedding.

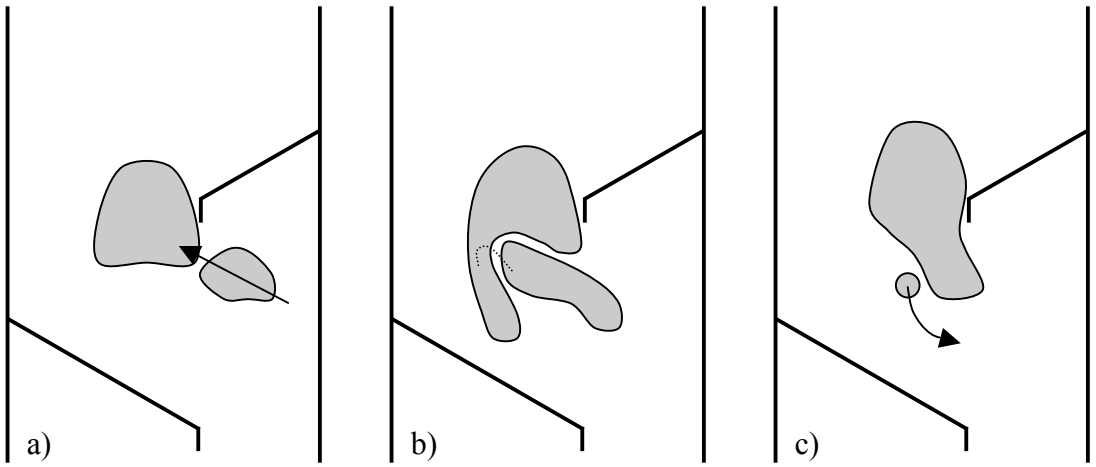

Figure 4-8: Sequence showing the primary mechanism resulting in the release of a stray bubble.

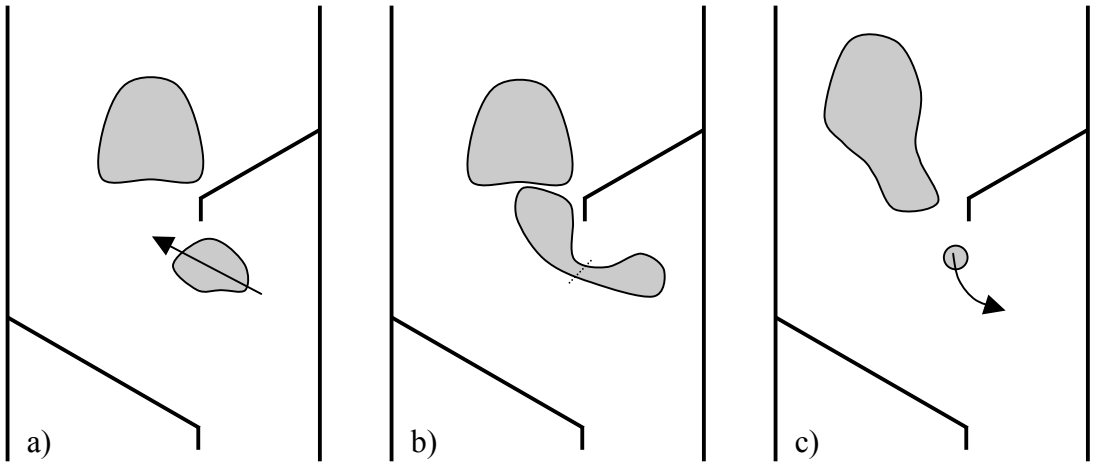

Figure 4-9: Sequence showing the secondary mechanism resulting in the release of a stray bubble.

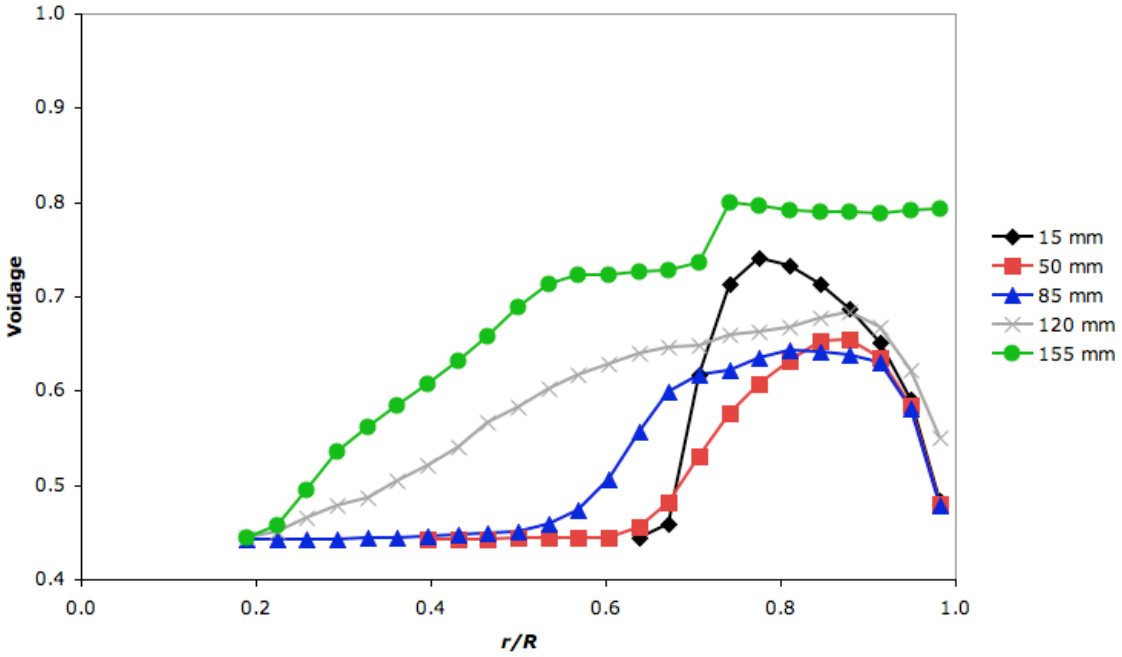

Figure 4-10: Time-averaged voidage profiles of the simulated CFB stripper at various distances above the disc baffle skirt. Simulation conditions: solids circulation rate = 45 kg/(m^2·s), stripper gas velocity = 0.1 m/s.

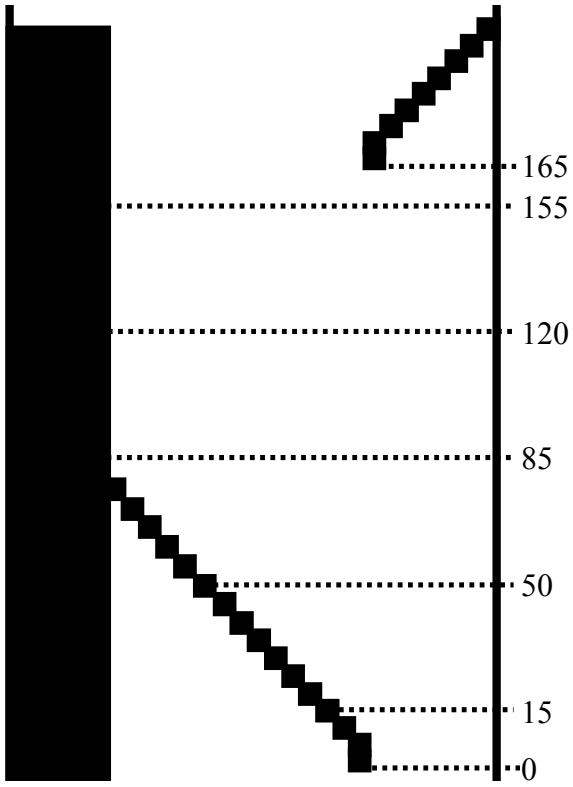

Figure 4-11: Locations in baffle interspace used to determine bubble properties.

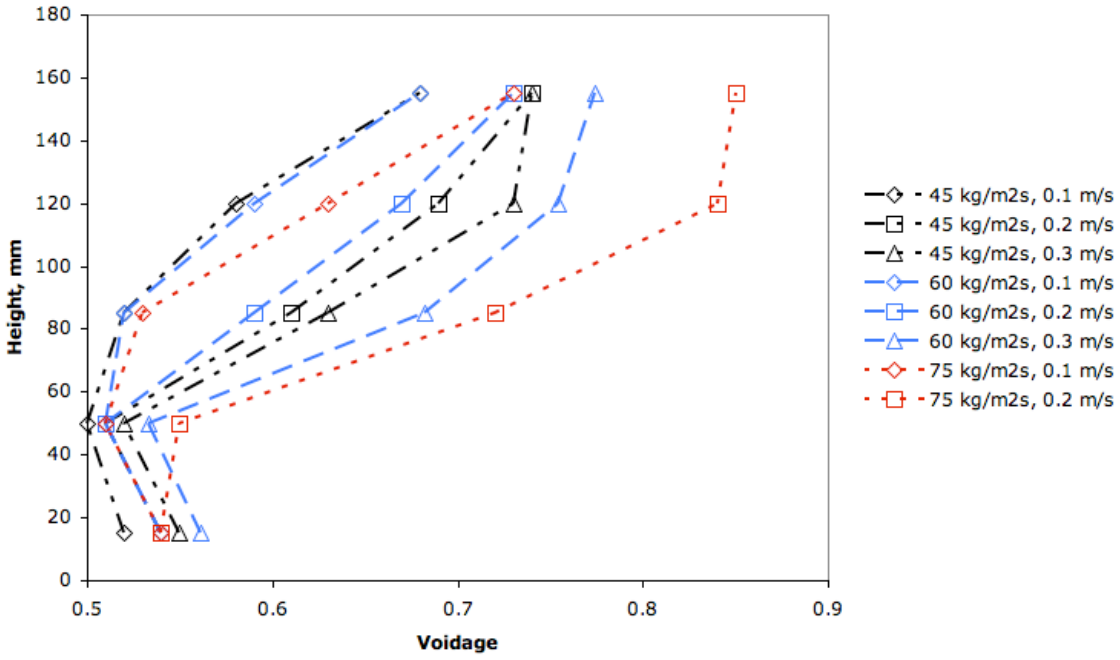

Figure 4-12: Effect of measurement height on the cross-sectional averaged voidage.

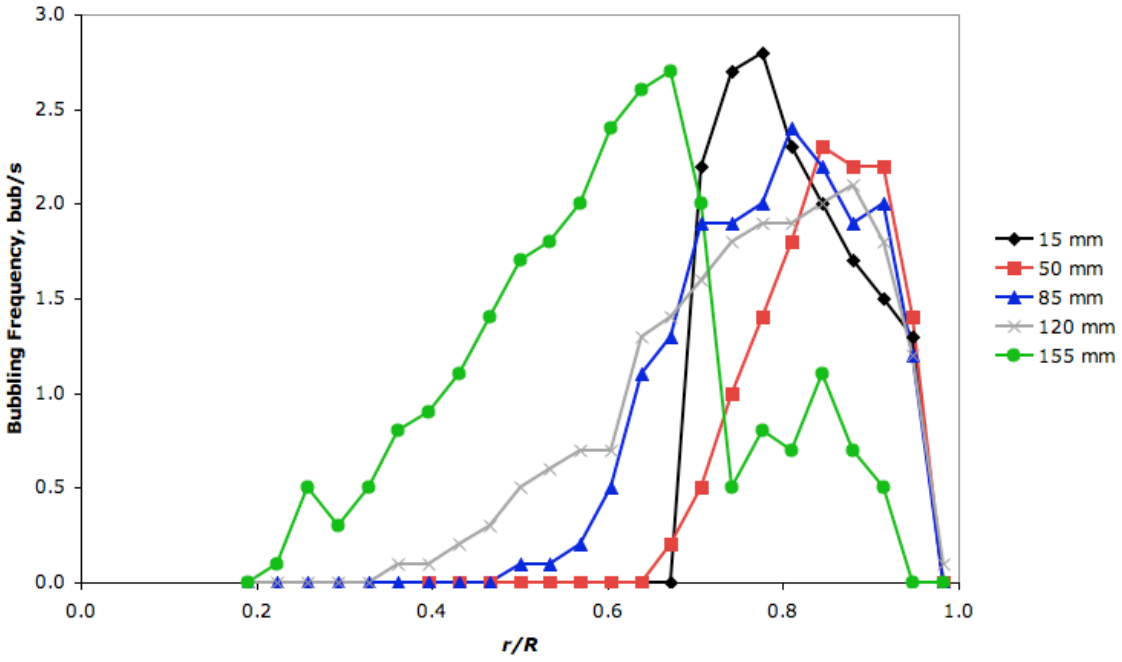

Figure 4-13: Bubbling frequency profiles of the CFB stripper simulation at various distances above the disc baffle skirt. Simulation conditions: solids circulation rate = 45 kg/(m^2·s), stripper gas velocity = 0.1 m/s.

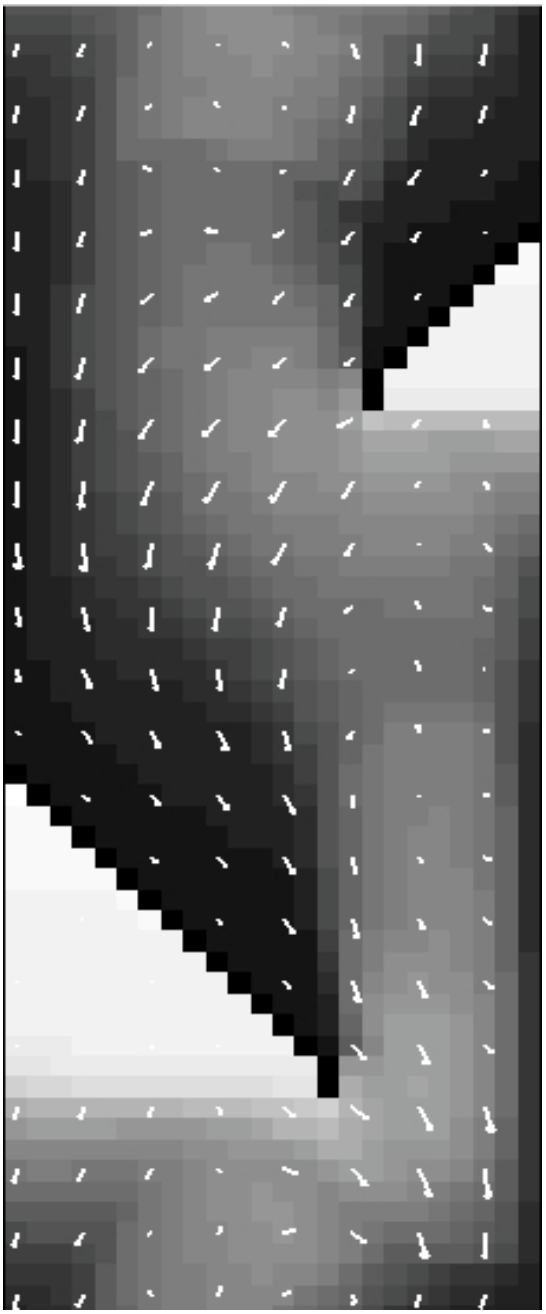

Figure 4-14: Time-averaged solids velocity vector field. Simulation conditions: solids circulation rate = 45 kg/(m^2·s), stripping gas velocity = 0.1 m/s. White areas indicate gas phase and black areas indicate emulsion phase.

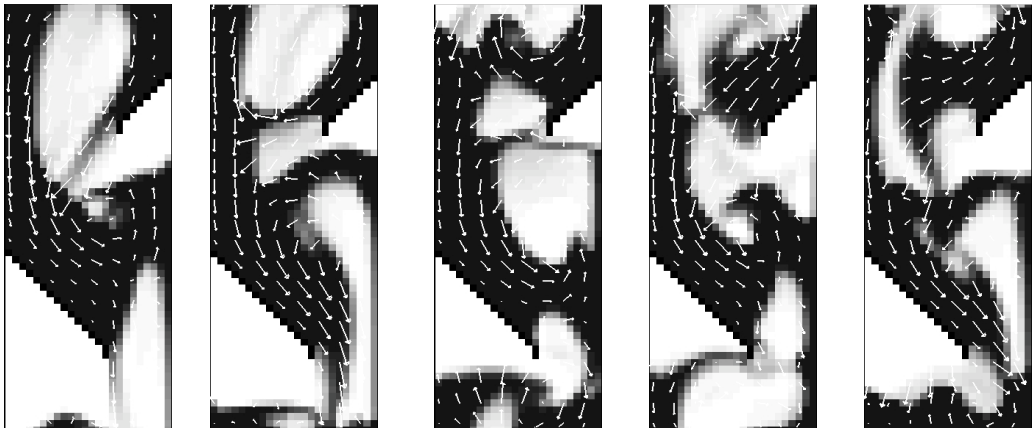

Figure 4-15: Time lapse images of simulated CFB stripper showing solids velocity vectors. Simulation conditions: solids circulation rate = 45 kg/(m^2·s), stripping gas velocity = 0.1 m/s. White areas indicate gas phase and black areas indicate emulsion phase.

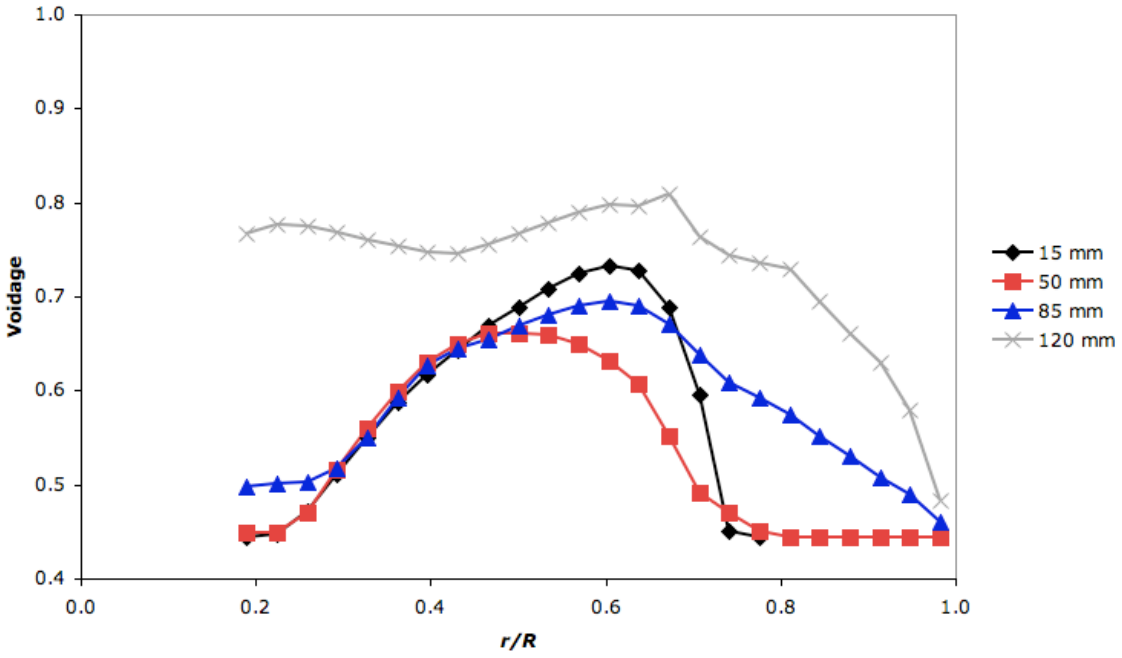

Figure 4-16: Time-averaged voidage profiles of the simulated CFB stripper at various distances above the donut baffle skirt. Simulation conditions: solids circulation rate = 45 kg/(m^2·s), stripper gas velocity = 0.1 m/s.

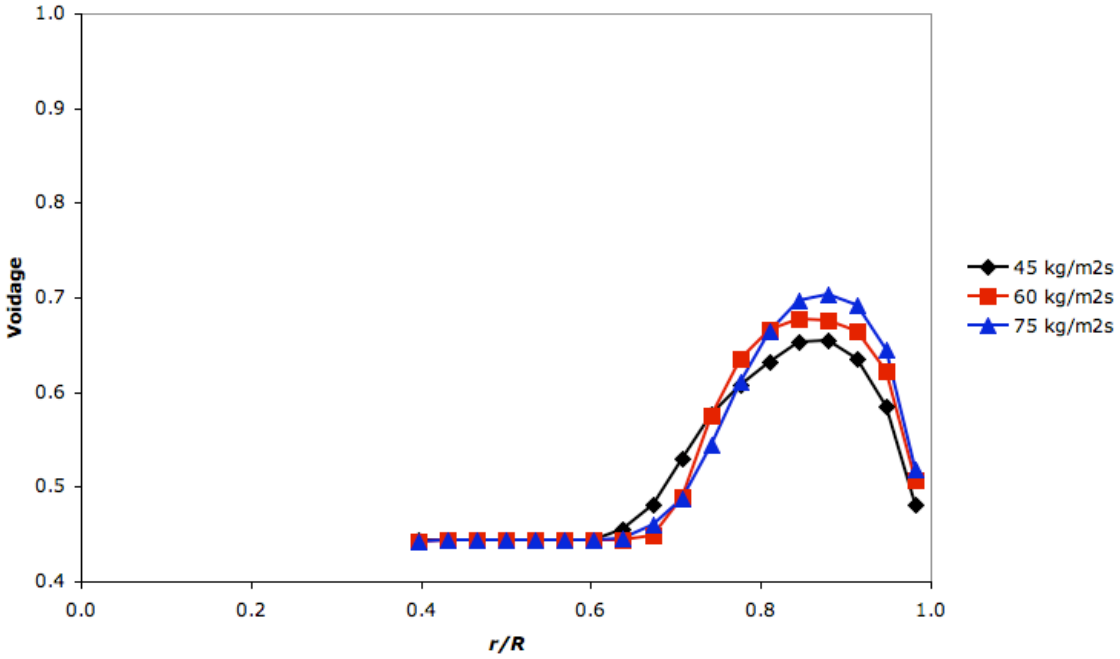

Figure 4-17: Time-averaged voidage profiles of the simulated CFB stripper at various solids circulation rates. Simulation conditions: measurement height = 50 mm above the disc baffle skirt, stripper gas velocity = 0.1 m/s.

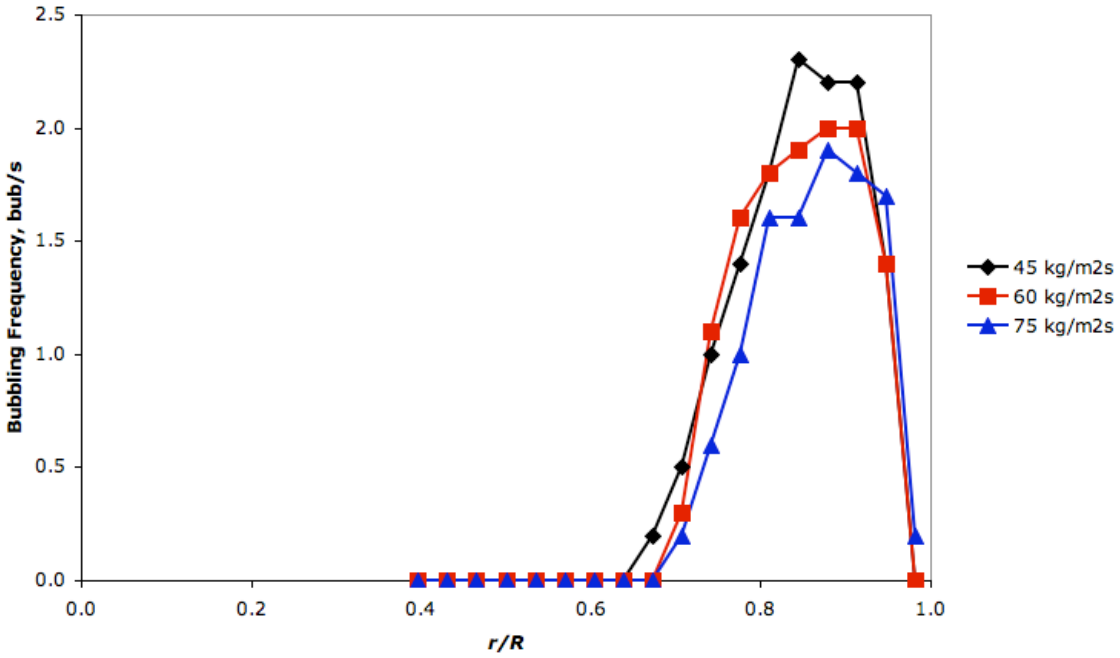

Figure 4-18: Bubble frequency profiles of the simulated CFB stripper at various solids circulation rates. Simulation conditions: measurement height = 50 mm above the disc baffle skirt, stripper gas velocity = 0.1 m/s.

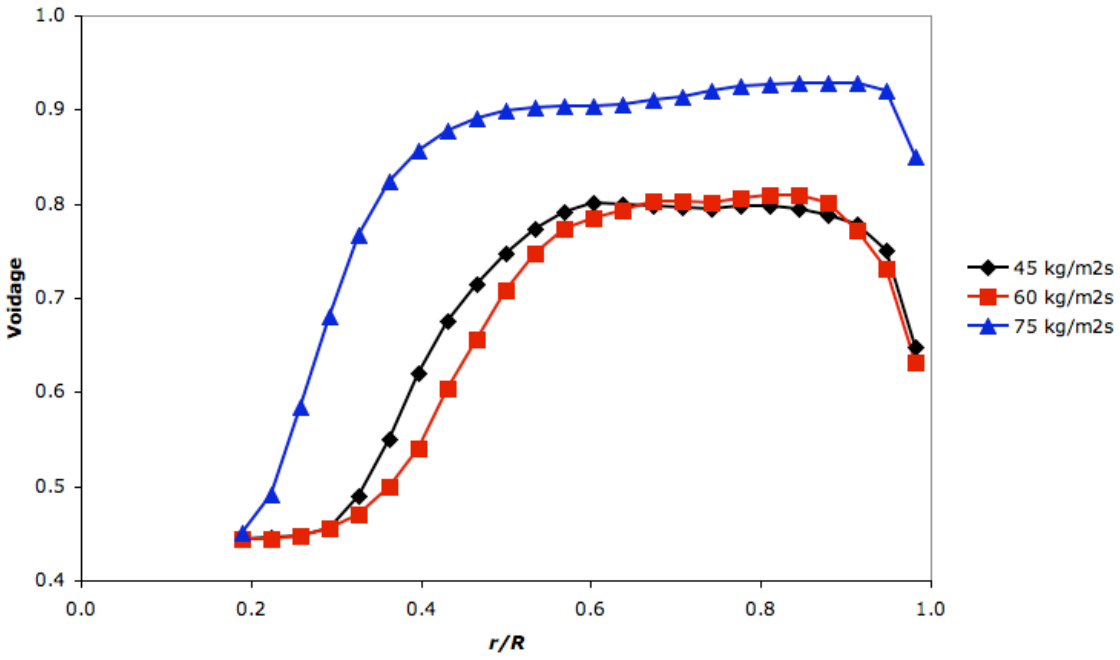

Figure 4-19: Time-averaged voidage profiles of the simulated CFB stripper at various solids circulation rates. Simulation conditions: measurement height = 120 mm above the disc baffle skirt, stripper gas velocity = 0.2 m/s.

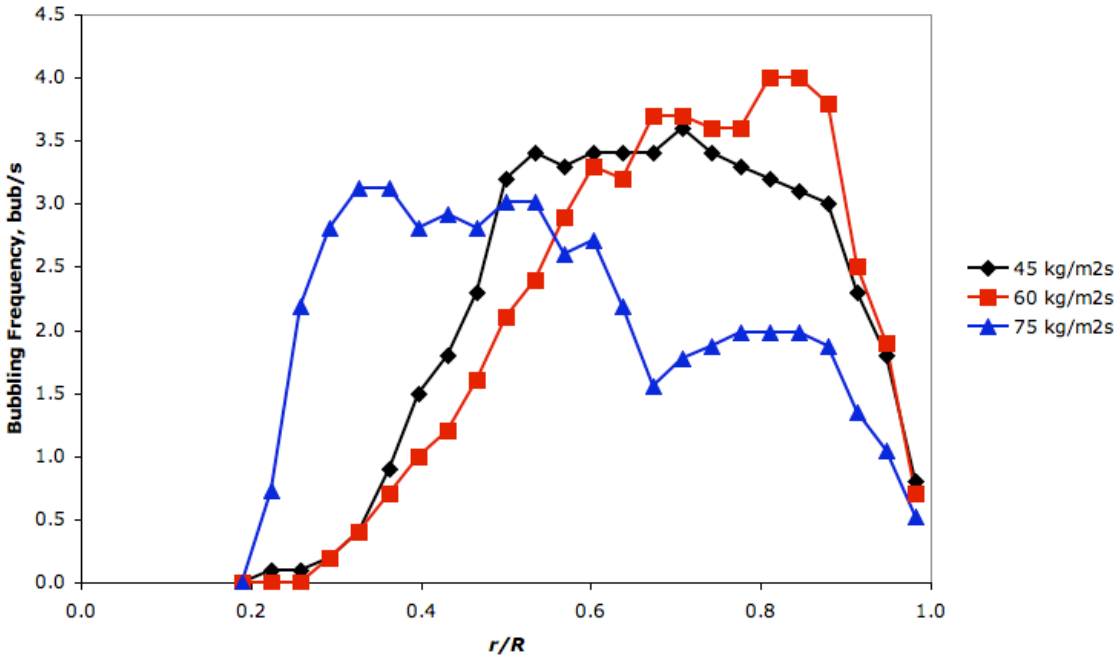

Figure 4-20: Bubble frequency profiles of the simulated CFB stripper at various solids circulation rates. Simulation conditions: measurement height = 120 mm above the disc baffle skirt, stripper gas velocity = 0.2 m/s.

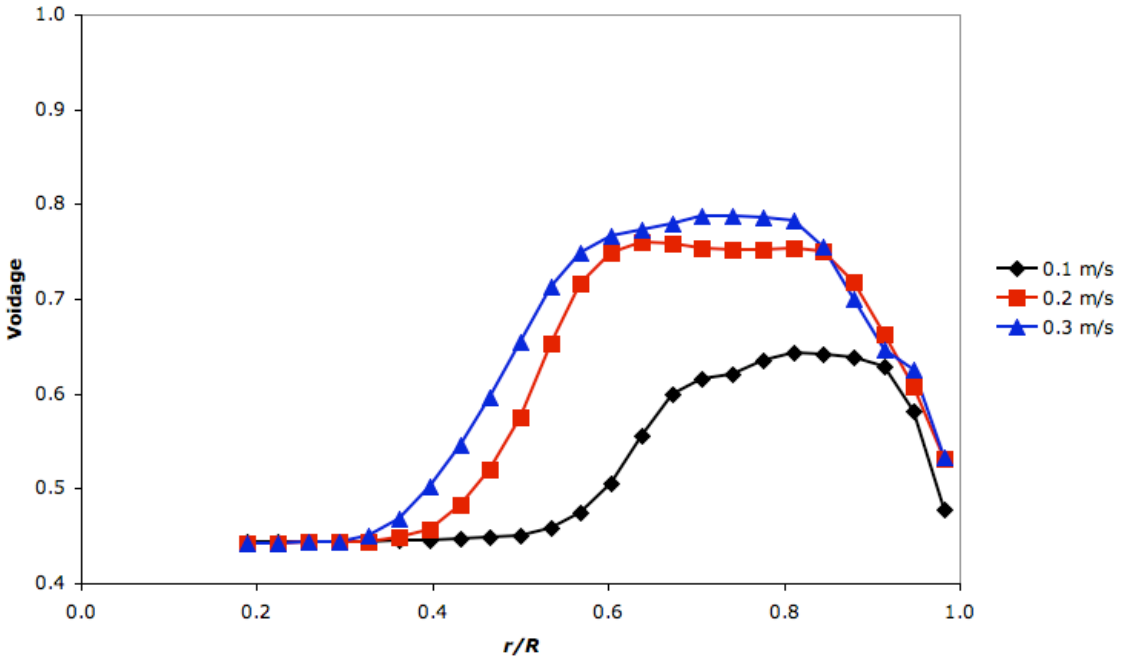

Figure 4-21: Time-averaged voidage profiles of the simulated CFB stripper at various gas velocities. Simulation conditions: measurement height = 85 mm above the disc baffle skirt, solids circulation rate = 45 kg/(m^2·s).

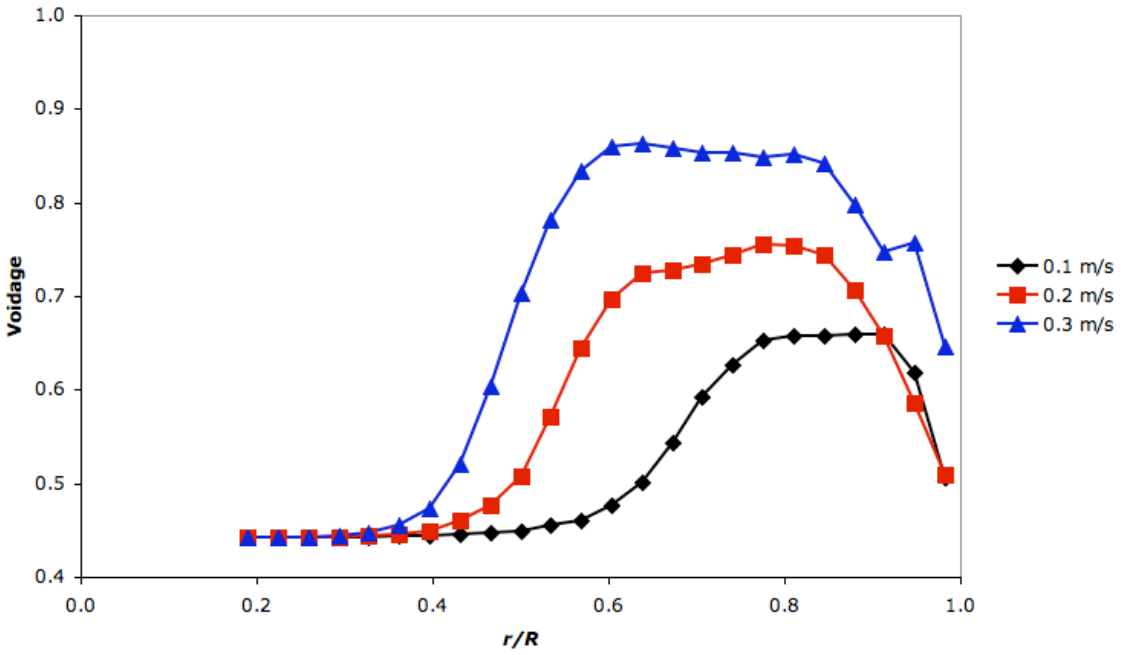

Figure 4-22: Time-averaged voidage profiles of the simulated CFB stripper at various gas velocities. Simulation conditions: measurement height = 85 mm above the disc baffle skirt, solids circulation rate = 60 kg/(m^2·s).

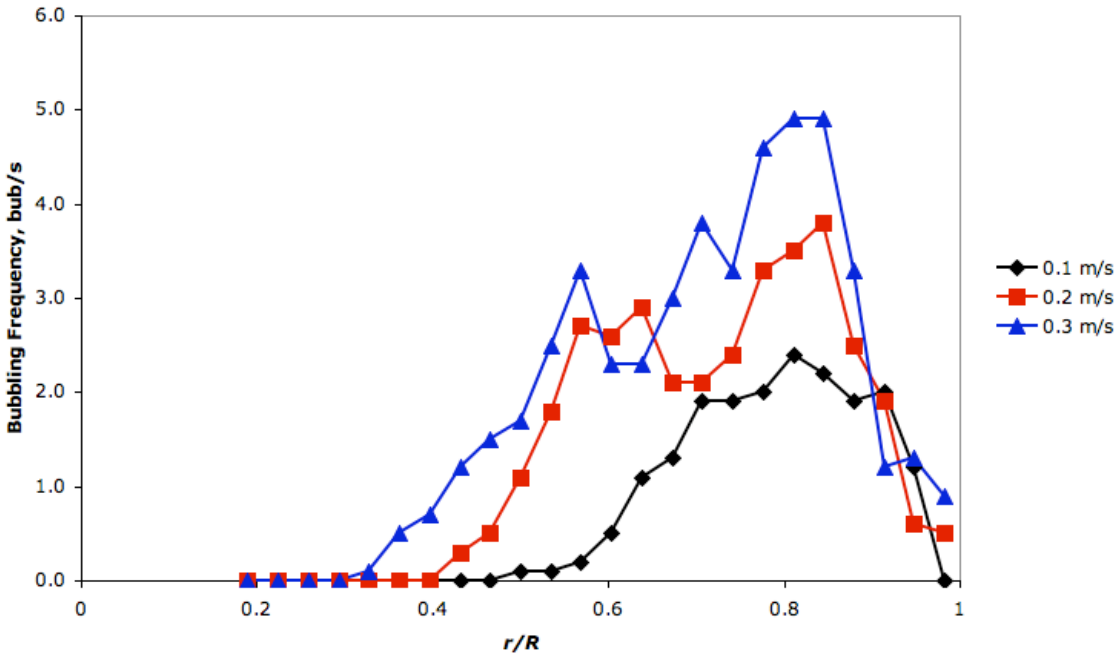

Figure 4-23: Bubble frequency profiles of the simulated CFB stripper at various stripper gas velocities. Simulation conditions: measurement height = 85 mm above the disc baffle skirt, solids circulation rate = 45 kg/(m^2·s).

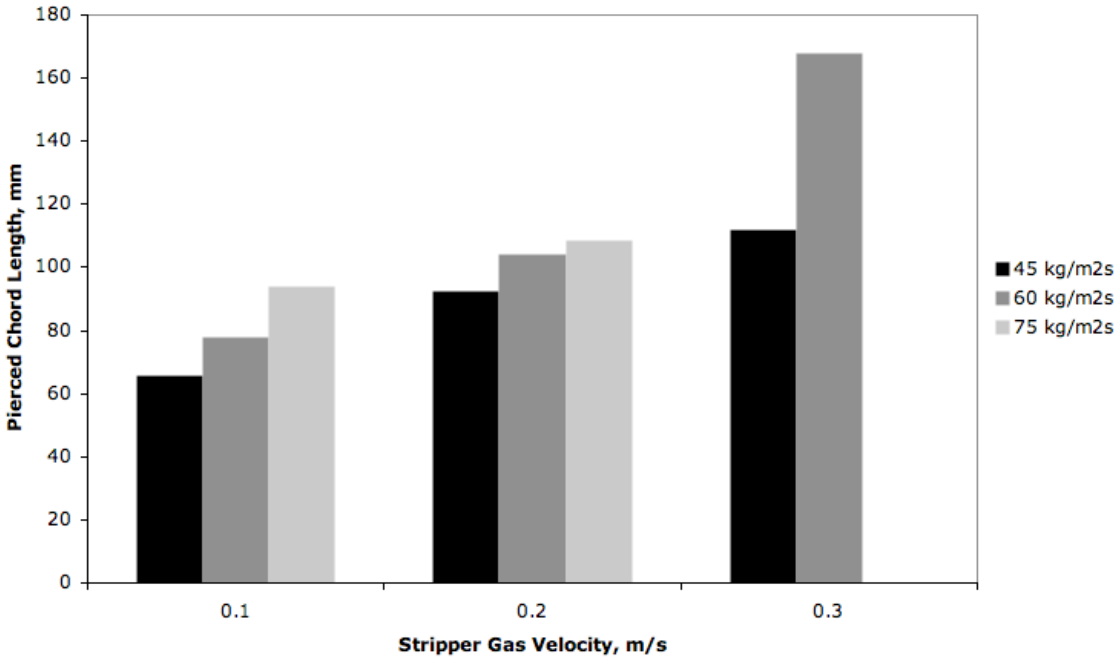

Figure 4-24: Mean pierced chord length of bubbles at solids circulation rates ranging from 45 to 75 kg/(m^2·s) and stripping gas velocities ranging from 0.1 to 0.3 m/s. Measurement height is between 85 and 75 mm above the disc skirt.

0 0 0 1 1 0 0 0
0 0 1 1 1 1 0 0
0 0 1 1 1 1 0 0
0 0 1 1 1 1 0 0
0 0 1 1 1 1 0 0
0 0 1 1 1 1 0 0
0 1 1 1 1 1 0 0
0 1 1 1 1 1 0 0
0 1 1 1 1 1 1 0
0 1 1 1 1 1 1 0
0 1 1 1 1 1 1 0
0 1 1 1 1 1 1 0
0 1 1 1 1 1 1 0
0 1 1 1 1 1 1 0
0 0 1 1 1 1 1 0
0 0 1 1 1 1 1 0
0 0 1 1 1 1 1 0
0 0 0 0 1 1 0 0
0 0 0 0 0 0 0 0

Figure 4-25: 'Picture' method used to determine the bubble volume at a measurement height of 85 mm. '1' indicated a voidage $\varepsilon \geq 0.8$, and '0' indicates a voidage $\varepsilon < 0.8$.

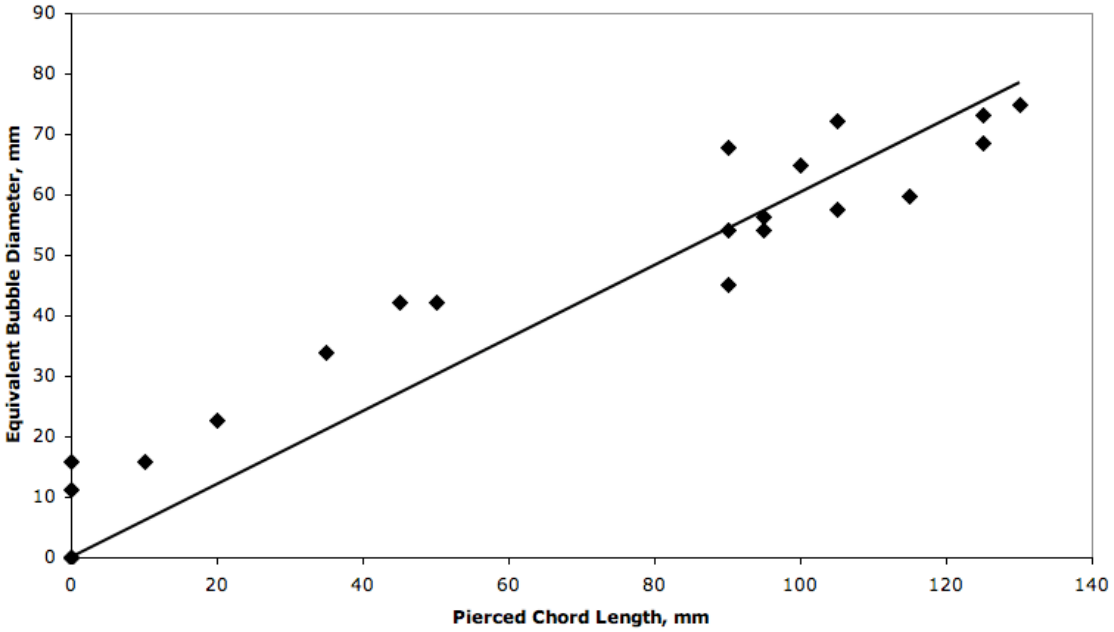

Figure 4-26: Relationship between the equivalent bubble diameter and the pierced chord length for the simulated CFB stripper operating at a solids circulation rate of 45 kg/(m^2·s) and a stripper gas velocity of 0.1 m/s.

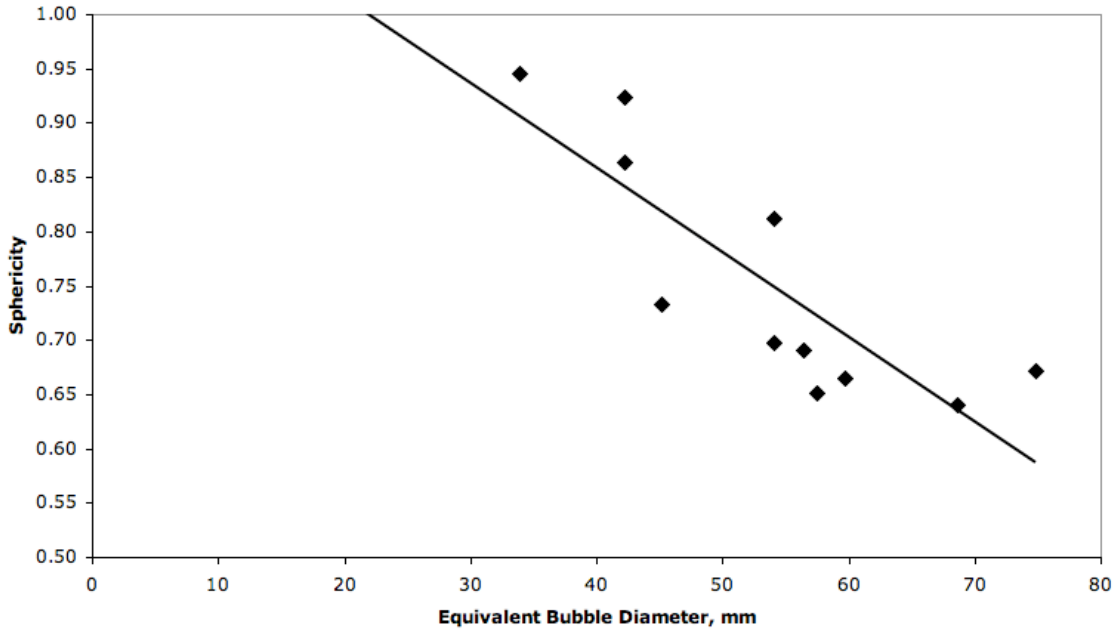

Figure 4-27: Relationship between the area-perimeter ratio and the equivalent bubble diameter for the simulated CFB stripper. Simulation conditions: measurement height = 85 mm above the disc baffle skirt, solids circulation rate = 45 kg/(m^2·s), and stripper gas velocity = 0.1 m/s.

Table 4-4: Values of bubble sphericity for the average *EBD* found for simulation conditions.

Solids Circ. Rate ($kg/(m^2 \cdot s)$)	Stripper Gas Vel. (m/s)	*EBD* (mm)	Sphericity (-)
45	0.10	39	0.85
45	0.20	55	0.76
45	0.30	66	0.68
60	0.10	46	0.77
60	0.20	62	0.69
60	0.30	99	0.59
75	0.10	56	0.73
75	0.20	64	0.59

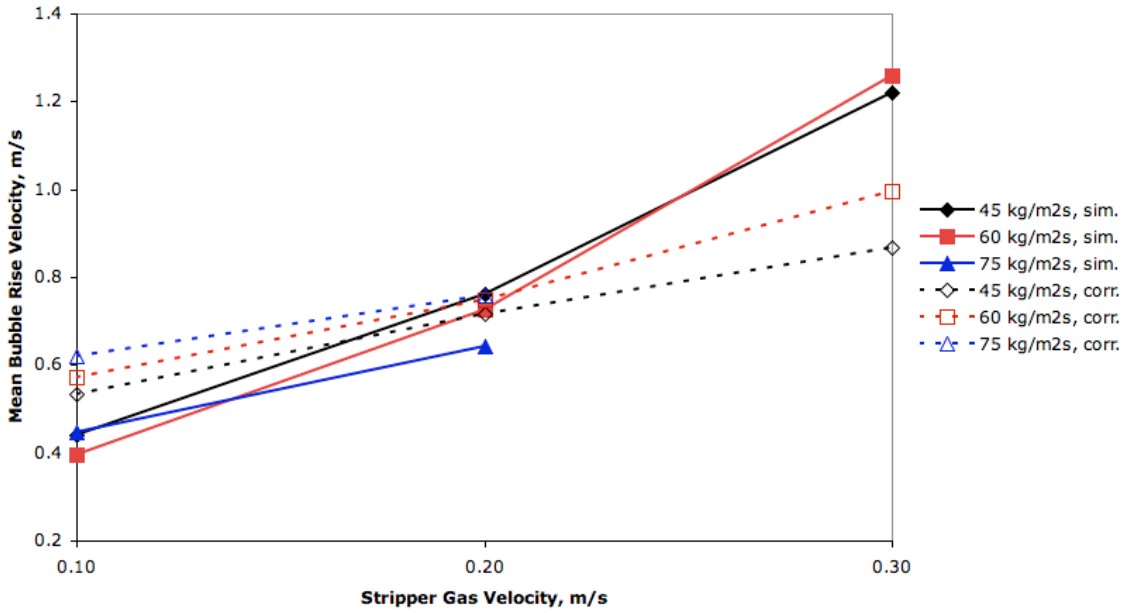

Figure 4-28: Comparison between simulated (sim.) bubble velocity and correlated (corr.) bubble velocity for bubbling stripper.

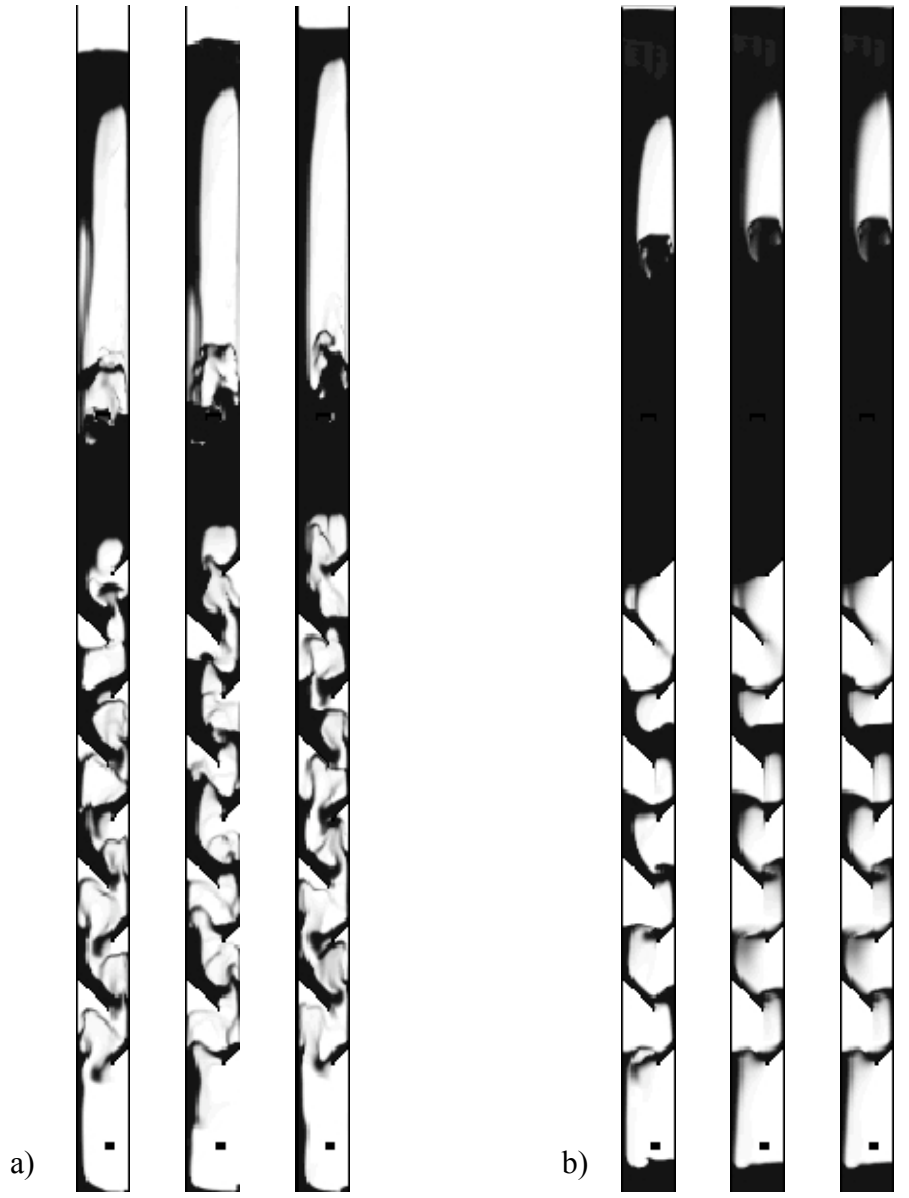

Figure 4-29: Time lapse images of a flooded CFB stripper operating at a) a solids circulation rate of 75 kg/(m^2·s) and stripping gas velocity of 0.3 m/s, and b) a solids circulation rate of 90 kg/(m^2·s) and stripping gas velocity of 0.1 m/s. White areas indicate gas phase and black areas indicate emulsion phase.

Chapter 5 – Emulsion gas velocities in the Downcomer

Contribution of the Ph.D. Candidate

Experiments were planned and performed by Jason Wiens. Dillon Petrucha provided some assistance for the experimental measurements. Todd Pugsley provided consultation regarding the experimental program. The software and hardware for all data collection and analysis was developed by Jason Wiens.

5.1 Objective

Knowledge of the emulsion gas velocity profile in the standpipe is required for calculating the volumetric flowrate of un-stripped gas tracer entering the standpipe; needed for closing the steady-state tracer mass balance in stripping efficiency studies. To date, this measurement has not been reported in the literature. Previous studies (i.e. Cui *et al*., 2006) have modeled this quantity as fully-developed laminar gas flow, which results in a parabolic emulsion gas velocity profile. It is hypothesized that the emulsion gas velocity profile would closely resemble the solids velocity profile in the standpipe, which is expected to be radially uniform. The objective of this study is to measure the emulsion gas velocity profiles in the standpipe and un-baffled stripper at stripper solids circulation rates ranging from 45 to 75 kg/(m^2·s).

5.2 Introduction

The standpipe is a length of pipe that transports solids from a region of low pressure to a region of high pressure. Gas is normally carried downwards with the solids, and creates a sealing pressure drop based on the relative velocity between the gas and solids, known as the slip velocity. For the following discussion, it is useful to first define the slip velocity between the gas and solids, U_r. The slip velocity is given by the equation:

$$U_r = \frac{G_s}{\rho_p(1-\varepsilon)} - U_g \qquad (5.1)$$

The first term on the right side of the equation is the downward interstitial particle velocity and U_g is the downward emulsion gas velocity. Depending on the slip velocity, a standpipe will normally operate in either a fluidized-bed flow or a packed-bed flow regime (Knowlton, 1997).

Fluidized-bed flow is the desirable operating regime since it allows for the maximum pressure build-up along the length of the standpipe. Fluidized-bed flow occurs when the slip velocity exceeds the minimum fluidization velocity: $U_r \geq U_{mf}/\varepsilon_{mf}$ (Knowlton, 1997). At slip velocities in excess of minimum fluidization the bed voidage can increase beyond the minimum fluidization voidage (Knowlton, 1997, Chong *et al.* 1987). Also, it has also been shown that the voidage can change along the length of a fluidized standpipe (Knowlton, 1997, Leung & Jones, 1978).

For packed-bed flow of solids in a standpipe, two sub-regimes exist depending on the slip velocity (Leung & Jones, 1978). When $U_r \leq 0$, the bed becomes maximally compressed and has a voidage equal to that of a vibrated packed bed. This sub-regime, termed slip-stick flow, occurs when the emulsion gas moves at the same velocity or a higher downward velocity than the solids. Slip-stick flow is characterized by oscillations in the solids flow at a frequency between 0.1 and 1 Hz (Leung & Jones, 1978).

The second sub-regime in packed-bed flow occurs when the slip velocity is bounded between $0 < U_r < U_{mf}/\varepsilon_{mf}$. This sub-regime is termed transitional packed bed flow (Leung & Jones, 1978). The voidage of the standpipe in this regime varies between the vibrated packed bed voidage and the minimum fluidization voidage depending on the slip velocity. In this regime, Knowlton *et al.* (1978) found the voidage could be determined from the relation:

$$\varepsilon = \varepsilon_{pb} + (\varepsilon_{mf} - \varepsilon_{pb}) \cdot \frac{U_r}{U_{mf} / \varepsilon_{mf}} \qquad (5.2)$$

Interaction between gas and solids in standpipe flow has been established on a macroscopic scale, however the need exists for establishing local phenomenon in standpipe flow. One such example is in the calculation of stripping efficiency in an FCC stripper. Quantification of the carry-under of tracer gas requires knowledge of the local emulsion gas velocity in the standpipe. To date, this measurement has not been reported in the literature. The purpose of this study is to measure the emulsion gas velocity profiles in the downcomer at various solids circulation rates.

5.3 Experimental

Three probes were constructed for the emulsion gas velocity tests. One probe, known as the injection probe, was designed to pulse inject a known volume of helium into the downcomer. The other two probes, known as detection probes, were designed to detect the passing helium pulse. The probes were placed into the downcomer in vertical alignment. The injection probe was placed at the top of the measurement stack. A vertical distance of 0.10 m separated the injection probe and the upper detection probe. A vertical distance of 0.19 m separated the two detection probes.

The injection probe is constructed out of a 13 mm outside diameter (O.D.), 0.36 m long stainless steel tube (Figure 5-1). The probe has a filter element attached to the injection tip containing eight 17 mm by 3 mm rectangular openings around the circumference, which are covered in a coarse screen. The entire filter element is wrapped with a 325 mesh screen to prevent particles from entering the injection probe. An Asco® 8210G1 solenoid valve is attached to the non-injection end of the injection probe to control the helium injections. The flowrate of helium through the probe is measured using a Porter® B-125-60 rotameter containing a stainless steel measurement bead.

The solenoid valve is activated on a specified time interval using LabView® software. LabView® directs a 5 V analog output (AO) signal from a Keithley® kpci-3116 data acquisition board (Figure 5-2), which in turn activates a Crydom® DC60S5 solid state relay. Activation of the solid state relay closes the switch on the circuit containing the solenoid valve, causing the solenoid valve to open and inject helium into the downcomer. Power is supplied to the solenoid valve via an MW® MW123A regulated 12Vdc power supply. The voltage signal (AI) from the Keithley ® kpci-3116 data acquisition board is routed to the primary data acquisition board, a Keithley® kpci-3101, so that the time of the solenoid valve activation can be recorded.

The detection probes are 8 mm inside diameter (I.D.), 10 mm O.D., 0.36 m long stainless steel tubes with 90º bends at the detection tip. There is 10 mm of vertical distance from the probe centerline to the open end of the probe after the 90º bend (Figure 5-3). Each probe contains an Omega® TH-44004-36-T thermistor element located immediately below the opening at the detection tip. The thermistors have a specified resistance of 2252 Ω at 25ºC, and a specified maximum response time of 1 s. The detection tip is covered with a double-layer of 325 mesh screen to prevent particles from entering the probe. Gas samples are continuously drawn through

the probes at an interfacial velocity of 0.078 m/s. The flowrate of sampled gas through both of the detection probes is measured using a Dwyer® RMA-1-SSV rotameter.

Each thermistor element comprised one leg of a separate Wheatstone bridge circuit (Figure 5-4). The rheostats ('R1', 'R2', 'R3') used in the Wheatstone bridge have an adjustable electrical resistance of between 0 and 1000 Ω. The resistance of rheostat 'R3' was maintained at 400 Ω. The rheostat 'R1' was adjusted until a steady-state voltage of 6.9 V was measured across the thermistor, V_t. The rheostat 'R2' was then adjusted until the bridge voltage, V_b, read between 0.4 and 0.6 V at steady-state. Adjustment of R1 and R2 was iterated until the desired thermsitor voltage drop and bridge voltage was attained. The wheatstone bridge circuits were powered using MW® MW123A 12Vdc regulated power supplies. The bridge voltage was sampled using a Keithley® kpci-3101 data acquisition board.

The interstitial gas velocity was measured at two locations in the downcomer of the CFB: one in the 0.29 m I.D. un-baffled stripper, and the other in the 0.19 m I.D. standpipe. Solids circulation rates of 44, 60, and 74 kg/(m^2·s) were tested in the un-baffled stripper, while 98, 135, and 170 kg/(m^2·s) were tested in the standpipe (the solids mass flowrates in the stripper and standpipe are equivalent). Five emulsion gas velocity measurements were made across the radius of both the un-baffled stripper and standpipe. In the un-baffled stripper, a sparger grid located 0.56 m upstream of the measurement stack was used to vigorously bubble the bed; thus ensuring fluidization conditions. The height of solids above the top of the measurement stack was 1.0 m in the un-baffled stripper. In the standpipe, the top of the measurement stack was located 0.37 m below the standpipe entrance (below the un-baffled stripper), and had a 3.7 m column of solids above the stack. During operation of the CFB, the fluidizing air relative humidity was maintained at approximately 50%. The pressure drop across the measurement stack was measured using an Omega® PX139-001D4V pressure transducer.

For all solids circulation rates tested, helium was injected into the column in 1 s pulses. The volume of helium pulses varied between experiments, ranging from 58 to 92 mL. The volume of helium injected was varied in an attempt to achieve a consistent peak-to-peak response in the bridge voltage between experiments. The time between successive helium pulses also varied between experiments, ranging from 30 to 60 s. In all experiments, at least 30 injection cycles were completed at each measurement position. All data was sampled at 1000 Hz.

To accurately measure the emulsion gas velocity, it is important that any errors associated with the measurement system be minimized. Error in the measurement system can arise from two sources: uncertainty associated with the experimental equipment, and time delay between when the helium pulse actually reaches the thermistor elements and when the bridge voltage increase can be detected in the measurements. The uncertainty in the latter is minimized by utilizing a robust scheme to accurately pinpoint the time of detection of the helium pulse in the acquired data. The error in the former is accounted for through calibration of the detection system.

5.3.1 Quantifying the Time of Detection

Figure 5-5 presents the response of the bridge voltages to the passing helium pulse. After initial detection of the helium pulse, the bridge voltage linearly increases with time until the maximum bridge voltage is attained. After peaking, the bridge voltage slowly decreases back to its resting state. To determine the time of detection of the helium pulse for the upper and lower measurement probes, a two-stage data analysis was used. In the first stage, the preliminary time of detection was determined using a statistical analysis of the measured bridge voltage. In the second stage, the preliminary time of detection was used as a starting point to collect data for linear interpolation of the post-detection data. The MatLab® computer code used to calculate the time of detection of the helium pulses can be found in Appendix C.1.

The statistical time of detection, $t_{det,\ stat}$, of the helium pulse is defined as the time where the post-injection bridge voltage is greater than the mean plus the 95% confidence interval of the pre-injection bridge voltage for five consecutive data points. Pre-injection and post-injection data is defined differently for the upper and lower helium detection probes (Figure 5-6). For the upper detection probe, the pre-injection data is defined as the bridge voltage data before activation of the solenoid valve is recorded by the data acquisition system, and post-injection data is the bridge voltage after activation of the solenoid has been detected. For the lower detection probe, the pre-injection data is defined as the bridge voltage data taken before the statistical time of detection of the helium pulse in the upper probe and the post-injection data is the bridge voltage after the statistical time of detection in the upper probe. For both the lower and upper detection probes, 1000 data points (1 s) of pre-injection bridge voltage data was used to calculate the mean and 95% confidence interval of the bridge voltage. The statistical time of detection, $t_{det,\ stat}$, was then defined as the first data point in a series of five that met the condition:

$$V_{b,\ post-inj}(t) > \frac{\sum_{t=1}^{100} V_{b,\ pre-inj}}{100} + 2\sigma \qquad (5.3)$$

Although the statistical method could acutely determine the time of detection of the helium pulse, it was found that the amplitude of the peak-to-peak bridge voltage response to the helium pulse influenced the time of detection. This is important because the peak-to-peak amplitude of the bridge voltage at the lower detection probe was always significantly lower than the response of the upper probe. This is likely due to back-mixing of the helium tracer in the downcomer causing a different concentration of helium tracer at the upper and lower detection probes. Thus, the volume of helium injected would influence the time lag between detection at the upper and lower detection probes. To remedy this, the time of detection was determined by a linear regression method. The time of detection, t_{det}, via the linear regression method is defined as the point of interception of two lines of best-fit: one comprising of the pre-injection data (Figure 5-7), and the other comprising of 500 data points (0.5 s) after the statistical time of detection. As can be seen in Figure 5-8, the linear regression method lessens the influence of the volume of helium injection on the time lag between detection of the helium pulse at the upper and lower detection probes compared to that of the statistical method.

5.3.2 Calibration

The two detection probes are operated at identical suction velocities, have the same steady-state voltage drop across the thermistors, and contain the same model of thermistor elements. Therefore, it is not expected that there would be any bias error associated with measuring the time delay between detection of the helium pulses at the upper and lower measurement probes. However, good practice dictates that these potential errors be accounted for. To test for bias error in the time delay between detection probes, the two detection probes were touched to the circumference of the injection tip of the helium injection probe. There was no separation distance between the injection probe and the face of the detection probes. Experiments were conducted in a similar manner to that described in Section 5.3. Data was reconstructed using the linear regression technique, however, instead of using the pre-injection bridge voltage data for the bottom detection probe shown in Figure 5-6 the pre-solenoid activation data was used (similar methodology to the upper detection probe). Using the linear regression technique, the calibration associated with the time lag between the upper and lower detection probes (t_{cal}) was -0.003 ± 0.088 s.

5.4 Results

The interstitial gas velocity was calculated from the relation:

$$U_g = \Delta Z / (\Delta t - t_{cal}) \tag{5.4}$$

where ΔZ represents the separation distance of the vertically aligned detection probes and Δt represents the measured time lag between detection of the helium pulse at the lower and upper detection probes. The relation represents the emulsion gas velocity since the injected helium tracer travels through the interstices of the emulsion phase.

Figure 5-9 presents the interstitial gas velocity profiles in the un-baffled stripper section of the CFB. The error bars in this figure represent the standard deviation of the measured interstitial gas velocity from the repeat measurements. A pressure drop of 7.6, 8.4, and 6.8 kPa/m was measured for solids circulation rates of 44, 60, and 74 kg/(m^2·s), respectively. From the figure it can be seen that a nearly constant emulsion gas velocity is detected across the radius of the un-baffled stripper for solids circulation rates of 60 and 74 kg/(m^2·s). This finding is supported by Chan *et al.* (2009) who found a flattening of the solids velocity profile upstream of an L-valve using positron emission particle tracking.

The flat interstitial gas velocity profile can be justified by relating the fluidized solids flow in the standpipe to single-phase liquid flows in a pipeline. Studies have found that the rheological behaviour of fluidized solids is likened to those of either a Newtonian or Bingham single-phase fluid, with a viscosity typically of magnitude 10^{-2} or 10^{-1} Pa·s (Zhao & Wei, 2000). In laminar fluid flow through a pipeline, the velocity gradient at any radial position is given by the equation:

$$\frac{dU}{dr} = \frac{-\Delta P}{L} \cdot \frac{r}{2\mu} \tag{5.5}$$

In fluidized standpipe flow, the pressure drop per unit length is independent of solids circulation rate. At constant pressure drop per unit length, the velocity gradient at any radial position, *r*, can

then be shown to be inversely proportional to the viscosity. Because fluidized solids have a much higher viscosity than typical single-phase fluids, it is expected that the velocity gradient across the radius would be small compared to single phase fluids, and thus a flat emulsion profile. Furthermore, solids flow is not restricted by the no-slip assumption at the vessel wall so wall stresses in standpipe flow would have a lesser effect than in single-phase liquid or gas flows.

Unlike the emulsion gas velocity profiles observed at solids circulation rates of 60 and 74 kg/(m^2·s), at a solids circulation rate of 44 kg/(m^2·s) the emulsion gas velocity is highest at the centerline and decreases towards the wall (Figure 5-9). While this appears to be a contradiction to the earlier justification of a flat velocity profile, it was observed during experimentation that bubbles from downstream aeration would regularly breach the measurement stack. Passing bubbles must accelerate the solids in the vicinity of the bubble boundary, and this acceleration would be intensified closer to the bubble flow (typically in the centre of the bed). Acceleration of the particles is reflected in the higher average downward velocity of the interstitial gas near the centerline of the stripper. The intermittency of bubble flow reflected in the higher standard deviation of the calculated velocity at r/R = 0.00 and 0.45.

Figure 5-10 presents the interstitial gas velocity profiles in the standpipe of the CFB. In this section, solids circulation rates of 98, 135, and 170 kg/(m^2·s) were tested. The error bars in this figure represent the standard deviation of the measured interstitial gas velocity from repeat measurements. The pressure drops across the measurement stack for these experiments were -0.1, -0.3, and -1.2 kPa/m, respectively. These pressure drops suggest there is a tendency for defluidization of the solids to occur after entering the standpipe. Defluidization upon entry into the standpipe was also predicted by Tsinontides (1999) in CFD simulations. For solids circulation rates of 98 and 135 kg/(m^2·s), a flat interstitial gas velocity profile is observed. For a solids circulation rate of 170 kg/(m^2·s) a relatively flat velocity profile is observed between $0.00 \leq r/R \leq 0.63$. Beyond r/R = 0.63 there is an increase in the downward interstitial gas velocity. Coinciding with this increase in the downward interstitial gas velocity is an increase in the standard deviation of the measured velocity. The high interstitial gas velocity near the wall for a solids circulation rate of 170 kg/(m^2·s) appears to be a characteristic of slip-stick flow. This assertion is supported by an observed intermittency of the solids flow at the wall and the large negative pressure drop across the measurement stack.

Figure 5-11presents the ratio of the experimentally determined slip velocity to the interstitial minimum bubbling fluidization velocity for the range of solids circulation rates tested. The error bars in this figure represent the 95% confidence interval calculated using the root-sum-square approach. The sources of uncertainty are the 95% confidence intervals in the helium injection/detection system and in the solids circulation rate calibration. For the un-baffled stripper, the experimental slip velocity was calculated using bed voidages calculated from the measured pressure drop. The pressure drop data indicates bed voidages of 0.50, 0.45, and 0.55 at solids circulation rates of 44, 60, and 74 kg/(m^2·s), respectively. In the standpipe, the slip velocity was calculated assuming the minimum fluidization voidage of 0.45. In all cases, the slip velocity is well in excess of the minimum bubbling velocity. There are two reasons the slip velocity in the un-baffled stripper could exceed the minimum bubbling velocity. These include: an interstitial gas velocity beyond that accounted for by two-phase theory or formation of particle agglomerates.

According to two-phase theory (Toomey & Johnstone, 1952), the slip velocity should never exceed the minimum bubbling velocity. However, in practice this has often been shown untrue (Rowe *et al.,* 1978, Kunni & Levenspiel, 1991, Grace & Clift, 1974, Baumgarten & Pigford, 1960). For example, Baumgarten & Pigford (1960) found that 8 to 27 times more gas passed through the bed rather than being contained in the bubble phase than that predicted by two-phase theory in their freely bubbling bed of FCC catalyst. It is thought that this excess gas is divided between the interstitial gas and a bubble flow-through component (Grace & Clift, 1974). This shows that the true slip velocity may be highly underestimated by the calculated interstitial minimum bubbling velocity. Although it is noted that bubble flow was only actually observed for one solids circulation rate tested (44 kg/(m^2·s)), it is possible that interstitial gas flow in the un-baffled stripper may be elevated due to vigorous bubbling of the sparger grid located 0.56 m above the measurement stack.

It has been well established that FCC particles can form agglomerates due to cohesive interparticle forces (McKeen & Pugsley, 2003, Massimilla & Donsi, 1976). Particle agglomerates would increase the slip velocity needed to attain minimum fluidization (and minimum bubbling if applicable) and therefore could account for the high slip velocities determined in the experiments. In the un-baffled stripper, the measured slip velocity would be matched to the theoretical minimum fluidization velocity if particle agglomerates measuring between 170 and 270 μm were formed. This agglomerate size is 1.7 to 2.8 times the actual particle diameter of 98 μm. This is similar to the ratio of particle agglomerate size to actual particle size of 1.8 to 2.3 used by McKeen & Pugsley (2003) to successfully model a bubbling bed of FCC catalyst. It appears likely, therefore, that the high slip velocity could be attributed to the formation of particle agglomerates.

In the standpipe the pressure drop data and calculated slip velocity are in contradiction. The pressure drop data indicates that the solids are de-fluidized, but the slip velocity indicates the bed is fluidized. It is believed that the slip velocity determined through experimentation is erroneous due to localized fluidization caused by injecting the helium tracer gas into the otherwise de-fluidized catalyst. How this has altered the shape of the velocity profile developed is unknown. However, because flow patterns in the standpipe are so highly dependant on the downstream and upstream operation it is thought that the experimental profiles would offer a good qualitative indication of the transition to slip-stick flow but that the predicted slip velocity would be quantitative erroneous.

5.5 Conclusions

An experimental program was conducted that examined the interstitial gas velocity profiles in an un-baffled CFB stripper and standpipe. In the stripper, the solids were maintained in a fluidized state, whereas defluidization of solids in the standpipe was found to occur. For both the fluidized and defluidized conditions, a flat interstitial gas velocity profile was most commonly observed. However, two notable exceptions were found. When bubbles were found to breach the measurement plane, the maximum downward velocity was found at the centerline; linearly decreasing towards the wall. In the defluidized standpipe when slip-stick flow was observed, a higher average velocity was observed near the wall. The experimentally determined

slip velocity in the fluidized section suggests particle agglomerates of order 1.7 to 2.8 times the measured particle size are forming.

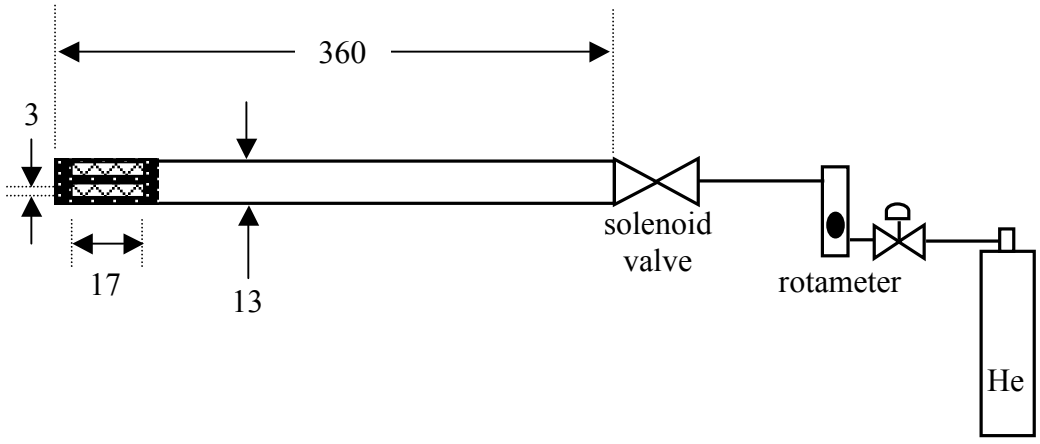

Figure 5-1: Schematic of the injection probe. All dimensions in mm.

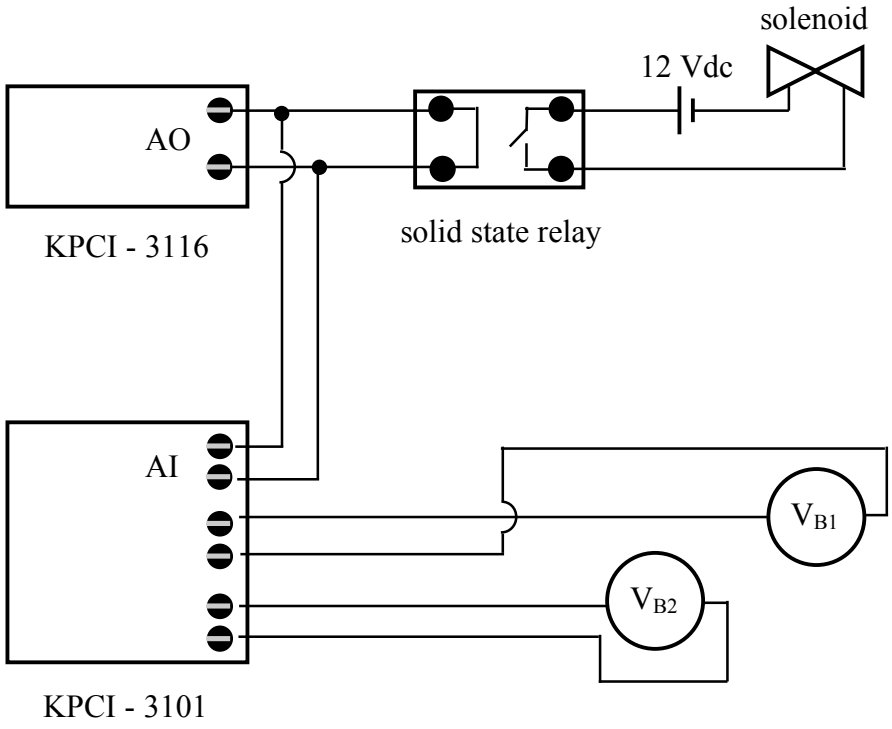

Figure 5-2: Data acquisition equipment used to control solenoid activation and measure wheatstone bridge voltage.

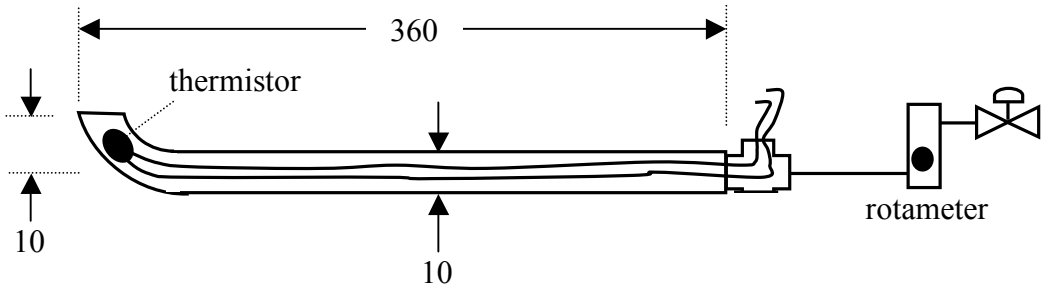

Figure 5-3: Schematic of the detection probe. All dimensions in mm.

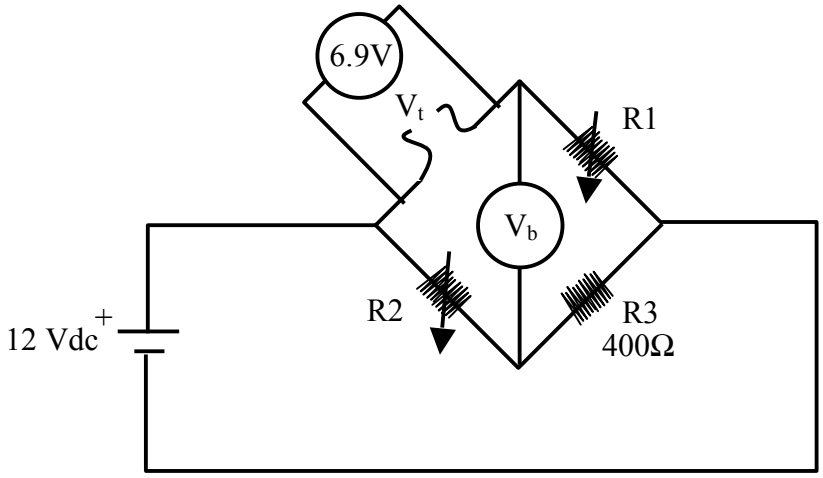

Figure 5-4: Wheatstone bridge used to detect voltage changes in the thermsitor element.

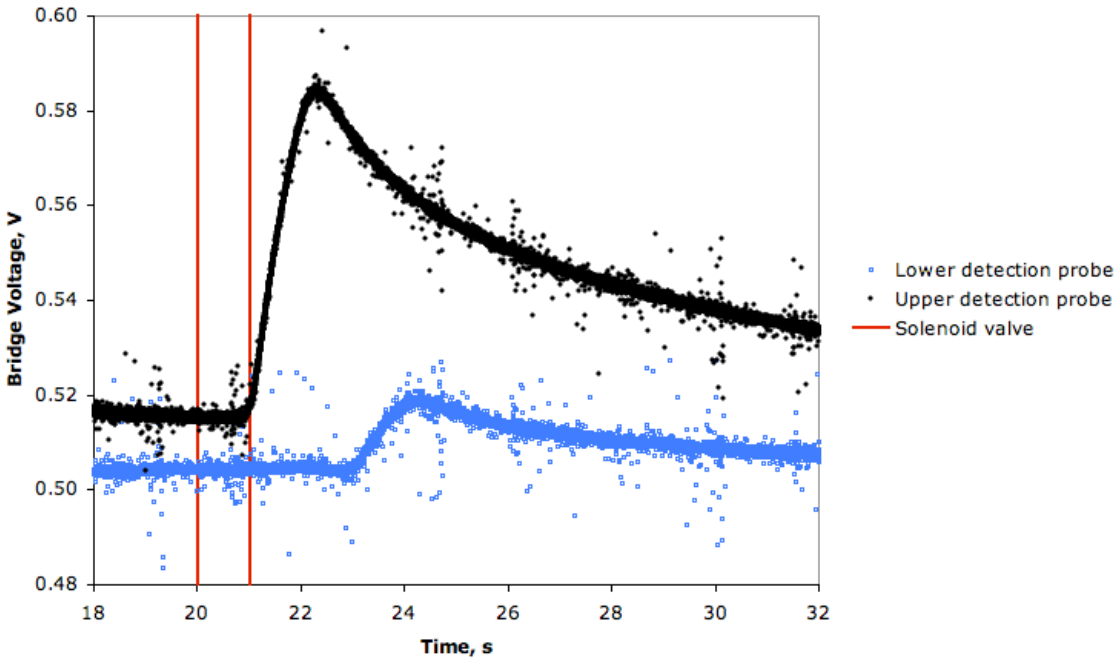

Figure 5-5: Response of the wheatstone bridge voltages of the upper and lower detection probes to a single pulse of helium. Operating conditions: solids circulation rate = 170 kg/(m^2·s) in the standpipe, $r/R = 0$.

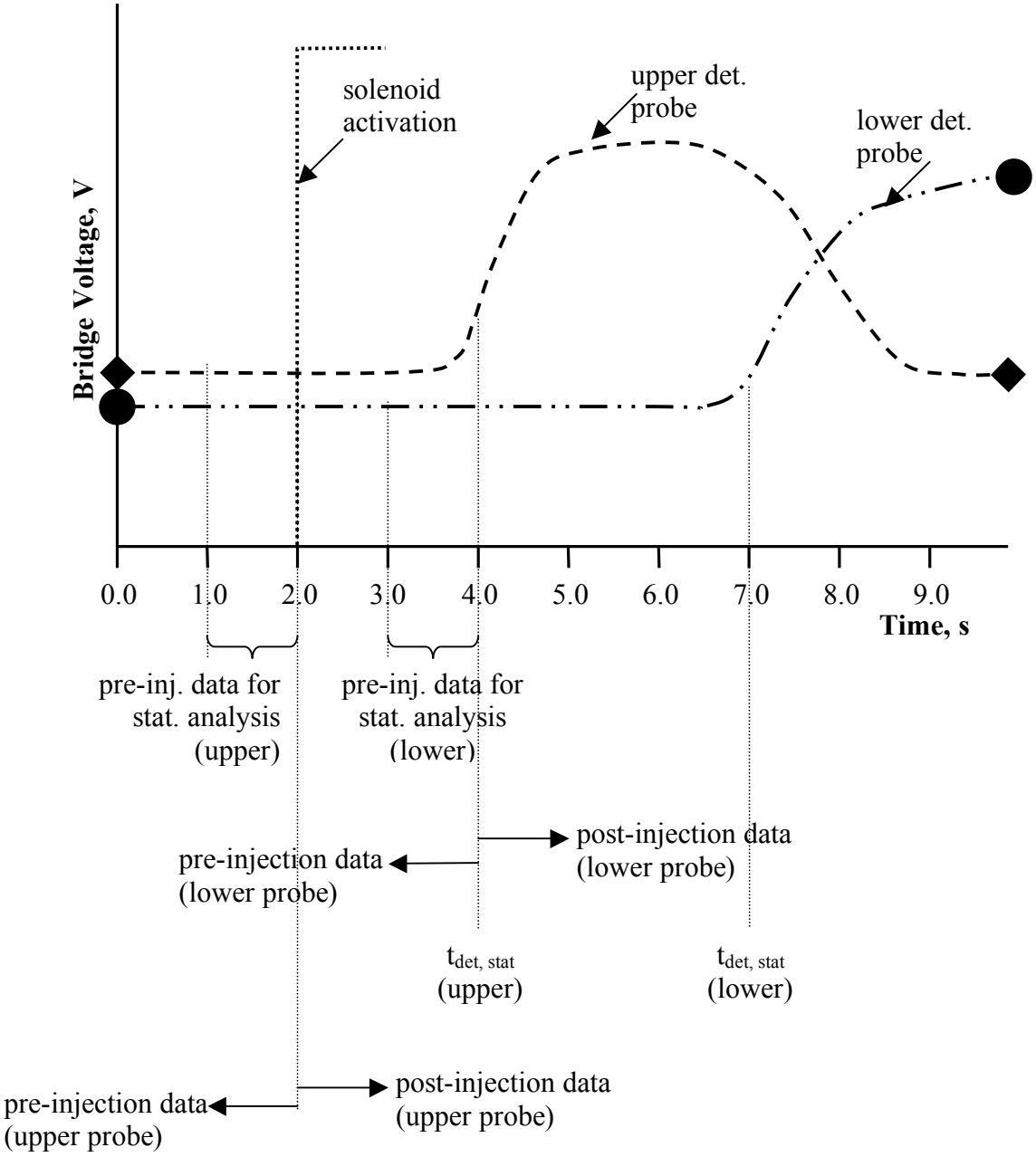

Figure 5-6: Illustration of the data used to statistically determine the time of detection of the upper and lower detection probes.

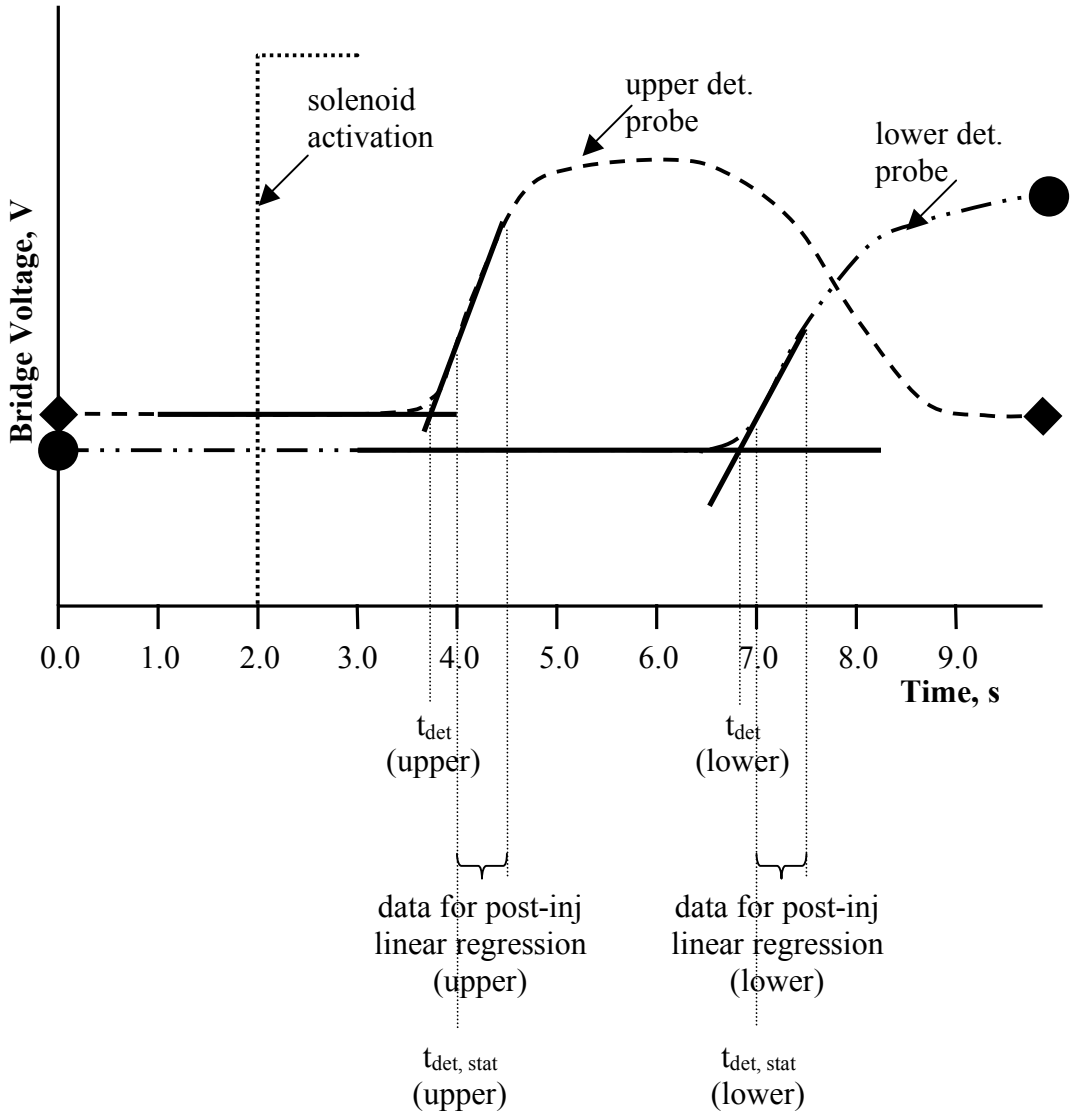

Figure 5-7: Illustration of the data used to determine the time of detection via the linear regression method for the upper and lower detection probes.

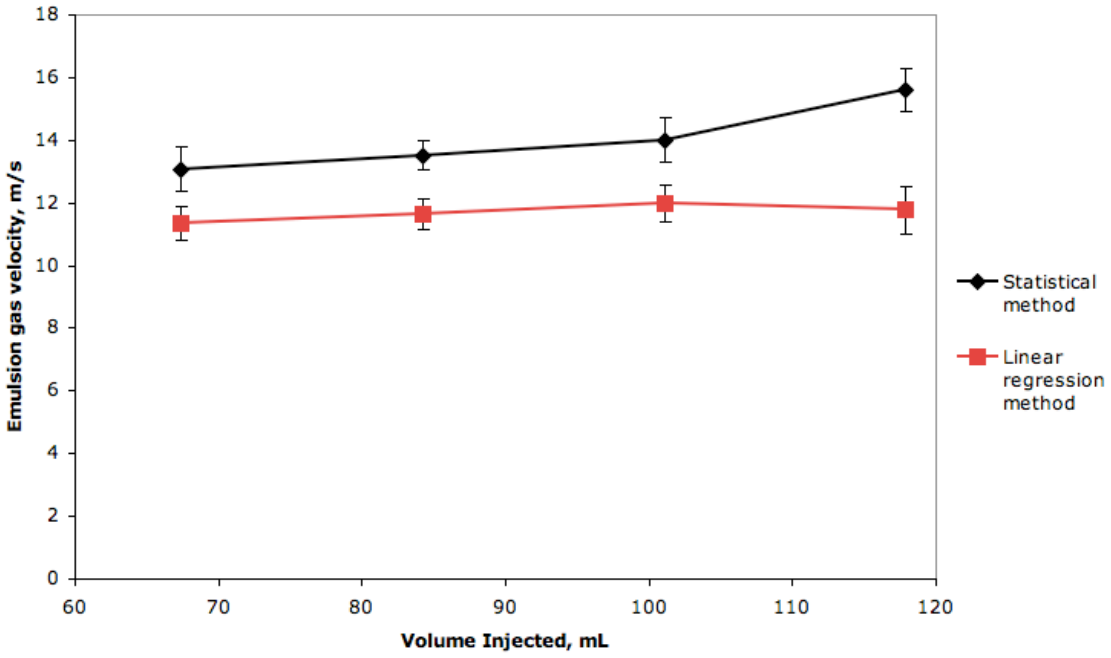

Figure 5-8: Effect of the methodology for determining the time of detection on the emulsion gas velocity.

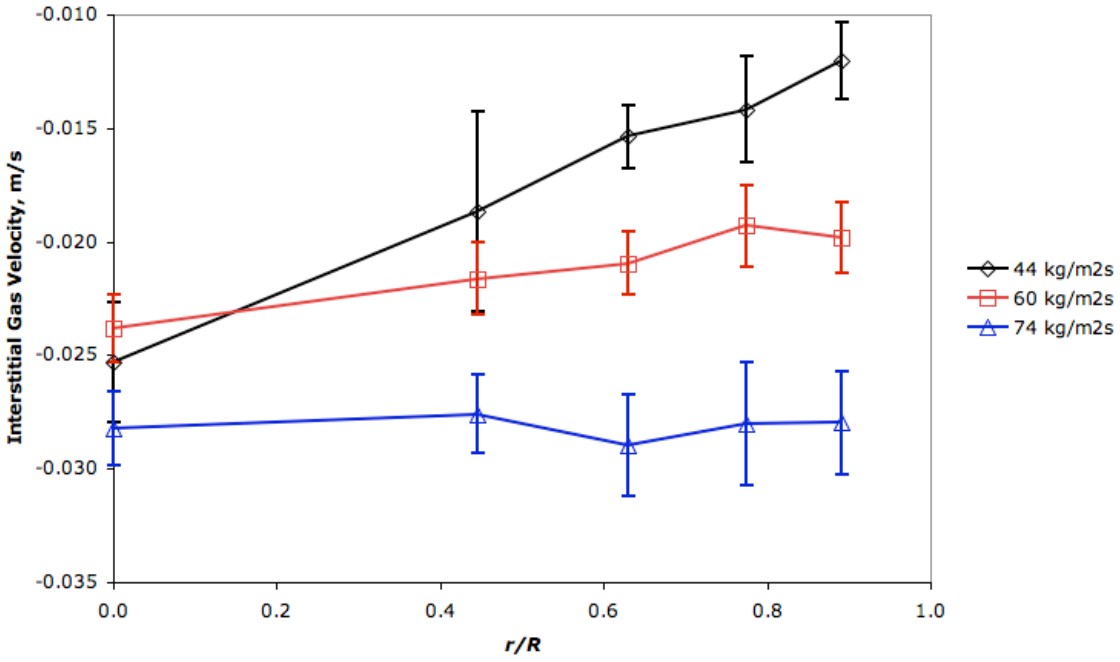

Figure 5-9: Interstitial gas velocity profiles at various solids circulation rates in the unbaffled stripper (fluidized). Error bars represent the standard deviation of the measured value.

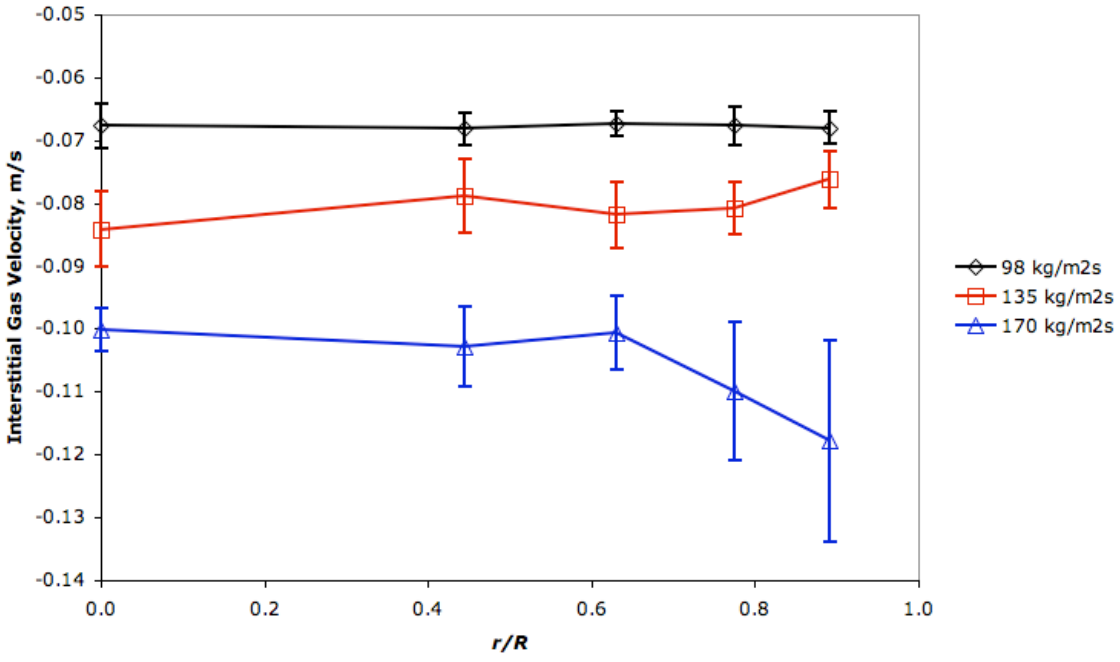

Figure 5-10: Interstitial gas velocity profiles at various solids circulation rates in the standpipe (de-fluidized). Error bars represent the standard deviation of the measured value.

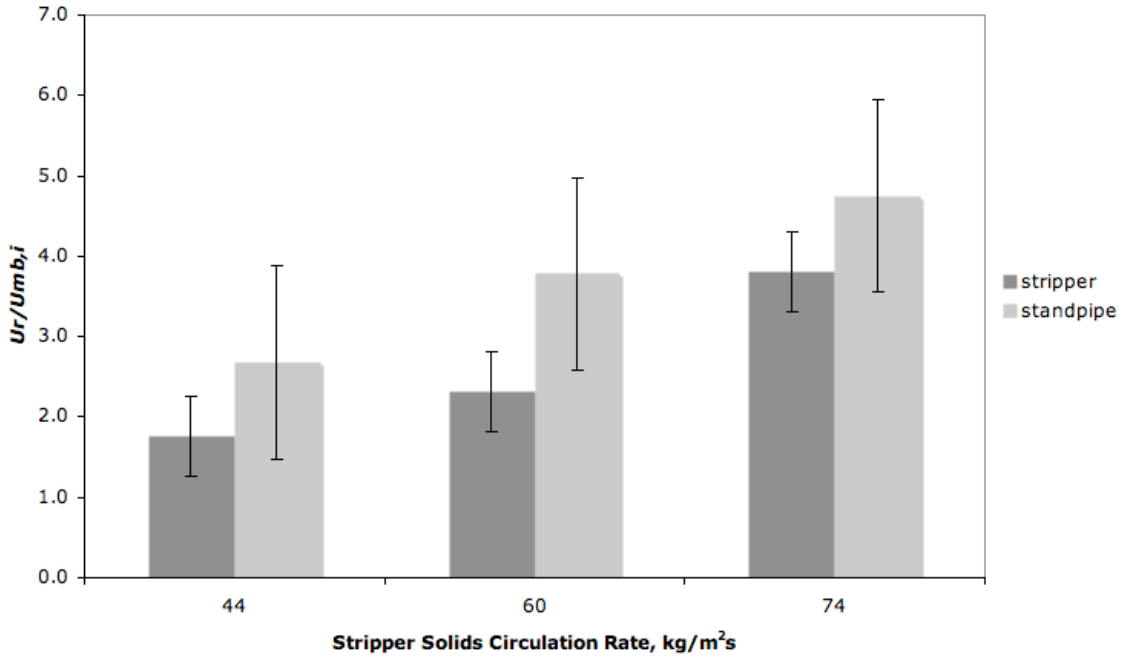

Figure 5-11: Effect of testing conditions on the ratio of the gas-solids slip velocity to the interstitial minimum bubbling velocity. Stripper solids circulation rates of 44, 60, and 74 kg/(m^2·s) correspond to standpipe solids circulation rates of 98, 135, and 170 kg/(m^2·s), respectively. Error bars represent the 95% confidence intervals.

Chapter 6 – Stripping Efficiency in an FCC Stripper Containing Disc-and-Donut Baffles

Contribution of the Ph.D. Candidate

Experiments were planned and performed by Jason Wiens. Todd Pugsley provided consultation regarding the experimental program. The software and hardware for all data collection and analysis was developed by Jason Wiens.

6.1 Objective

The effect of operating conditions (stripping gas velocity and solids circulation rate) on the stripping efficiency in FCC strippers is still not well understood. Previous studies that have investigated this phenomenon all measured efficiencies greater than 99% for all conditions tested. This makes it difficult to discern the relative effect of changing operating conditions on stripping efficiency. It is hypothesized that designing an experimental program that shows a greater variation in measured stripping efficiency would allow for greater differentiation of the effect of operating conditions on FCC stripping efficiency. This would allow for straightforward optimization of the design and operating parameters in these units. The objective of this study is to determine the effect of industrially relevant operating conditions on the measured stripping efficiency for a stripper containing standard disc-and-donut baffles. Operating conditions of interest include solids circulation rates between 45 and 75 kg/(m^2·s) and stripping gas velocities between 0.1 and 0.3 m/s. The stripping efficiency is then related to the hydrodynamic behaviour of the FCC stripper, acquired from CFD simulations (Chapter 4).

6.2 Introduction

Fluid catalytic cracking (FCC) is the main conversion process in a petroleum refinery. The FCC process converts heavy crude oil fractions into gasoline and other light distillates with the aid of solids catalyst particles. After conversion, the cracked product and catalyst particles are separated in the riser terminator. However, some hydrocarbons inevitably remain entrained in the catalyst pores and interstices, and adsorbed on the catalyst surface. Proper operation of the FCC unit requires that these hydrocarbons be removed prior to catalyst regeneration. Removal of these hydrocarbons is accomplished in a counter-current steam-catalyst stripper.

High consumer demand for gasoline has forced refiners to increase FCC unit throughput by increasing catalyst circulation and feed rates beyond original FCC unit design specifications. Although further increases in the FCC unit are possible, many refiners are limited by stripper capacity (McCarthy *et al.,* 1997). This bottlenecking of the FCC stripper is reflected in the recent interest of the research community in the stripping process.

To date there have been three studies examining stripping efficiency in cold-flow strippers (Rivault *et al.,* 1995, Payden *et al.,* 2001, Cui *et al.,* 2006). Figure 6-1 presents a parametric map of the operating conditions investigated in these studies, as well as those investigated in the current study. Variables of interest when examining stripping efficiency are the solids circulation rate, the stripping gas velocity, and the baffle configuration used in the stripper. In all studies, air was used as the stripping gas, FCC as the particles, and helium was used to mimic the entrained hydrocarbon gas. Since helium does not adsorb on FCC catalyst, helium tracer gas mimics interstitial gas and gas contained within the catalyst pores, but does not mimic the stripping of adsorbed hydrocarbons that also occurs in an industrial FCC unit. It is, however, a valuable technique for discerning the relative stripper performance for different operating conditions.

Padyen *et al.* (2001) studied stripping efficiency in a 0.29 m inside diameter (I.D.) semi-cylindrical FCC stripper containing three pairs of disc-and-donut baffles. The disc baffles were attached to a central, vertical riser. In their study, solids circulation rates ranging from 3 to 18

kg/(m^2·s) and stripping air velocities ranging from 0.01 to 0.15 m/s were tested. These conditions are not representative of industrial stripping operations. In all experiments, the closure of the helium tracer mass balance indicated 100% stripping efficiency. Measurements of the helium tracer concentration in the middle of the bed indicated that high solids circulation rates and low stripping gas velocities reduce stripping efficiency. It was speculated that reduced stripping efficiency at elevated solids circulation rates was caused by a decrease in the catalyst residence time in the stripper.

Cui *et al.* (2006) examined stripping efficiency in a dynamically scaled fluid coker stripper. The stripper was a 0.61 m I.D. semi-cylindrical vessel contained eight staggered rows of 90º sheds. The stripper open area at the pinch point was 50%. Data was presented for a stripping gas velocity of 0.24 m/s operated at solids circulation rates between 24 and 57 kg/(m^2·s). The stripping efficiency at these conditions varied from 99.97% to 100.00%. Similar to the findings of Payden *et al.* (2001), stripping efficiency was found to decrease at most of the high solids circulation rates tested. However, the stripping efficiency was found to increase when the stripper became flooded at high solids circulation rates. Cui *et al.* (2006) speculated that stripping efficiency increased at the flooding condition because a gas pocket formed under the sheds that prevented the injected tracer gas injected in the upper reactor to penetrate through to the stripper.

Rivault *et al.* (1995) examined stripping efficiency in a 0.50 m I.D. semi-cylindrical vessel containing four donut baffles and three disc baffles. Solids circulation rates between 28 and 108 kg/(m^2·s) were tested for gas velocities ranging from 0.1 to 0.4 m/s. For all conditions tested, the stripper exhibited smooth solids circulation. The measured stripping efficiency varied from 99.000% to 99.999% for the conditions tested. Stripping efficiency was found to decrease at elevated solids circulation rates and low gas velocities. Based on some measured hydrodynamic data, Rivault *et al.* (1995) reasoned that the decrease in stripping efficiency at high solids circulation rates was a result of a lower catalyst residence time in the stripper. At elevated gas velocities the stripping efficiency was thought to improve due to a higher frequency of consistent diameter bubbles. However, the presented data is inconsistent with this conclusion. Their data shows a decrease in bubbling frequency from 4.6 Hz to 2.6 Hz occurred upon increasing the gas velocity from 0.18 m/s to 0.33 m/s.

From the available studies, a general theme has arisen: stripping is most efficient at low solids circulation rates and high gas velocities. However, the high stripper efficiencies found in previous studies (all > 99% efficient) make it difficult to discern the relative effect of changing operating conditions on stripper performance. In addition, interpretation of the stripping efficiency with hydrodynamic data is lacking. The purpose of this study is to determine the effect of the stripping gas velocity, solids circulation rate, and number of baffle pairs on the stripping efficiency of a helium tracer gas at industrially relevant operating conditions for FCC units. The stripping efficiency is then related to the hydrodynamic behaviour of the stripper, determined from CFD simulations of the geometrically scaled stripper.

6.3 Experimental

The experimental stripper is a 0.29 m inside diameter (I.D.) vessel containing standard disc-and-donut baffles. The dimensions of a single baffle pair can be seen in Figure 6-2. A 0.051 m I.D. dummy riser is located at the centre of the stripper. The dummy riser is used to simulate an annular geometry, common in many industrial units. The disc baffles are attached to the dummy riser, and extend 0.074 m from the dummy riser. The donut baffles extend 0.039 m horizontally from the periphery of the stripper. Both baffles are slanted at 45º angles, and block approximately 50% of the open area at the pinch point. There is 0.078 m of vertical separation between adjacent baffles. The number of disc baffles used in the experiments varied from 2 to 4. There was always one more donut baffle than disc (both the top and bottom baffle were always donut baffles).

Stripping air is provided through an air sparger ring located 0.185 m below the last donut baffle (Figure 6-3). The sparger ring was designed according to pressure drop specifications provided by Kunni & Levenspiel (1991) for gas distributors. The ring is 0.028 m I.D. copper tube with 26 – 0.014m bores placed symmetrically around the ring. The inside diameter of the ring is 0.028 m. Air is supplied to the sparger ring via four individual supply lines. Each supply line is individually metered using a Dwyer® RMC-108 rotameter. Each rotameter has a specified uncertainty of 2% full scale, or 2.52×10^{-4} m^3/s. The stripping air flowrate is temperature and pressure corrected using an Omega® G-0-50C-6-PB dial-type temperature gauge and an Omega ® PGL-25L-100 Bourdon-type pressure gauge, respectively. Stripping air was provided from a 1.5 kW regenerative blower.

Helium was continuously injected 0.15 m above the top baffle of the stripper using a gas sparger grid. Helium was chosen as a tracer gas because it has a significantly different thermal conductivity than does the fluidizing air. This difference in thermal conductivity between the tracer and fluidizing gas is required for determining the concentration of tracer in the interstitial gas. The helium sparger grid was designed according to the specifications of Karri & Werther (2003). The helium flow rate was metered using a Porter® B-250-4 precision rotameter containing a glass bead. The specified accuracy of the rotameter is 5% full scale, or 1.94×10^{-5} m^3/s. The flowrate of helium was held constant at 3.88×10^{-4} m^3/s for experiments examining the effect of stripping gas velocity and solids circulation rate on the stripping efficiency. When testing the effect of the number of baffles on the stripping efficiency, a constant helium flow rate of 2.98×10^{-4} m^3/s was used.

The concentration of helium tracer carry-under was measured 0.48 m below the entrance to the standpipe. Gas samples were vacuum-drawn through a horizontally placed L-shaped sampling probe (the sampling face of the probe was facing into the solids flow) containing a sintered metal filtering tip at a constant flow rate of 7.866×10^{-6} m^3/s. The samples are drawn through a GOW-MAC® 20-series dual pass thermal conductivity detector (TCD). The TCD compares the conductivity of the sampled gas to that of a reference gas containing air with a known concentration of tracer gas. Two reference gases were used for these experiments: 4.49% v/v helium/air and 2.04% v/v helium/air. The 4.49% v/v reference gas was used in experiments to determine the effect of the number of baffles in the stripper, whereas the 2.04% v/v reference gas was used to determine the effect of operating conditions (solids circulation rate and stripper gas velocity). The voltage signal from the TCD was routed through a Keithley® MB-40 signal

conditioner module to a Keithley® KPCI-3101 data acquisition module. Data was logged using LabView® software at a frequency of 1 Hz. Using electronically logged data, the TCD analyzer has a specified uncertainty of 1% of full scale.

Helium concentration measurements were made at six radial locations across the 0.095 m I.D. standpipe. For each measurement, 180 s of data was logged to determine the helium concentration. The sampling probe was then moved to the next measurement location, and the next measurement was started after waiting 300 s for the system to come to steady state. Experiments were conducted for solids circulation rates of 43, 60, and 74 kg/(m^2·s) and stripper superficial gas velocities of 0.1, 0.2, and 0.3 m/s. To test the effect of number of baffles on the stripping efficiency, the stripper was fitted with 4, 3, and 2 disc baffles (5, 4, and 3 donut baffles) operated at a solids circulation rates of 74 kg/(m^2·s) and a stripper gas velocity of 0.1 m/s. To test the effect of operating conditions, the stripper was fitted with 2 disc baffles (3 donut baffles). For all experiments, height of solids above the sparger grid was maintained at approximately 0.9 m.

6.4 Results

6.4.1 Calculation Procedure

To calculate the stripping efficiency, the flowrate of the helium tracer gas entering the stripper and the underflow of helium into the standpipe must be known. To quantify underflow of the helium tracer in the standpipe, the profile of the local helium tracer gas velocity must be integrated across the standpipe radius. The helium tracer gas velocity is found from two measured quantities: the superficial emulsion gas velocity profile in the standpipe and the helium tracer gas concentration profile. The velocity profile of helium tracer gas in the standpipe is then calculated from the equation:

$$U_{He}(r) = \frac{\left|U_{g,\sup}(r)\right| \cdot \%FS(r) \cdot C_{ref}}{100} \qquad (6.1)$$

The deflection of the TCD analyzer, $\%FS(r)$, measures the concentration of helium in the sampled gas compared to a reference gas of known concentration (C_{ref}). The product of $\%FS(r)$ and C_{ref} gives the concentration of helium in the sampled gas at the measurement position, r.

Measurement of the local gas velocity in the standpipe has not been previously attempted in the literature. Most previous studies that measured the stripping efficiency provide little information on how this quantity is determined. The most detailed information on the calculation of this variable was provided by Cui *et al.* (2006). Cui *et al.* (2006) calculated the gas velocity profile as fully-developed laminar flow with the no-slip assumption at the vessel boundaries. This resulted in a parabolic-shaped emulsion gas velocity profile. In the present work, the emulsion gas velocity in the standpipe was determined using a novel measurement system. Results from this study are presented in Chapter 5.

The emulsion gas velocity profiles discussed in Chapter 5 indicated a discrepancy between theory and the experimentally determined results. While the pressure drop measurement across emulsion gas velocity detector stack indicated moving packed bed flow regime, the slip velocity (the relative velocity between the interstitial gas and solids) implied fluidization

conditions. It is thought that injecting the helium into the catalyst stream caused local fluidization; resulting in the fully-fluidized slip velocity measured by the system. However, because flow patterns are so highly dependant on downstream and upstream conditions, it is thought that the experimental profiles would offer a good qualitative indication of the moving packed bed velocity profiles, but be quantitatively erroneous. Therefore, the emulsion gas velocity profile was normalized and the Ergun equation was used to calculate the superficial slip velocity from pressure drop measurements in the standpipe. The superficial gas velocity, $U_{g,sup}(r)$, was found from the equation:

$$U_{g,\sup}(r) = \left(\frac{G_s}{\rho_p} \frac{\varepsilon}{(1-\varepsilon)} - U_{ergun,\sup} \right) U_{rel,\text{int}}(r) \qquad (6.2)$$

In calculating the slip velocity from the Ergun equation, particle agglomerates of 200 μm were assumed. This agglomerate diameter is based comparison of the measured slip velocity to the theoretical minimum fluidization velocity in emulsion gas velocity tests where fully-fluidized conditions were present. This is consistent with the particle agglomerate size used by McKeen & Pugsley (2003) to successfully model a bubbling bed of Geldart A particles.

Because of the large diameter probes required for the emulsion gas velocity tests, the emulsion gas velocity was only tested at five radial locations. However, six measurements of the helium concentration in the standpipe could be measured using the same spacing regime between measurements. Because it is important to quantify the helium velocity across as much of the standpipe radius as possible, interpolation of the emulsion gas velocity data was used to estimate the emulsion gas velocity at $r/R = 0.95$. Interpolation was performed by assuming a parabolic velocity profile with symmetry about the standpipe centerline ($dU_{g,sup}/dr = 0$ at $r = 0$).

With the helium tracer gas superficial velocity profile in the standpipe known, the stripper efficiency is calculated from:

$$\eta_{strip} = \left(1 - \frac{\frac{P_{s\tan d} M_{He}}{R_{gas} T} 2\pi \int_0^r U_{He}(r) \cdot r \cdot dr}{\frac{P_{He\,inj} M_{He}}{R_{gas} T} Q_{He,inj}} \right) 100 \qquad (6.3)$$

Equation 6.3 corrects for the pressure difference between the standpipe where the helium underflow is measured and above the baffled section of the stripper where the helium is injected. The uncertainty associated with the above calculation was calculated using the 'root-sum-square' approach.

6.4.2 Stripping Efficiency

Figure 6-4 presents typical plots of the downward superficial emulsion gas velocity profile. The figure shows that a mostly flat emulsion gas velocity was used to quantify gas underflow for the conditions tested. The uncertainty in the emulsion gas velocity profiles is mostly a result of the uncertainty (± 17 kg/(m^2·s)) associated with the calibration of the solids circulation rate in the CFB. The uncertainty in the solids circulation rate is propagated through the calculation of the stripping efficiency by calculation of the local slip velocity using the Ergun equation (equation 6.2).

Figure 6-5 presents typical plots of the helium concentration measured in the standpipe. For solids circulation rates of 43 and 60 kg/(m^2·s), a mostly constant helium concentration is measured throughout the radius of the vessel. At a solids circulation rate of 74 kg/(m^2·s), however, the highest concentration of helium is observed at the centerline; generally decreasing towards the wall. At r/R = 0.60, there is a sharp drop in the helium concentration. This sudden decrease in the helium concentration was observed for all gas velocities at a solids circulation rate of 74 kg/(m^2·s), however was more pronounced at the lower gas velocities tested. It is believed that the decreased concentration at this radial location is caused by underflow of the stripping gas from the sparger ring into the standpipe. This is significant because it is one of the criterions set forth by Bi *et al.* (2004) to indicate flooding. Although flooding was not observed in any experiments, it may indicate that operation of the stripper is approaching a flooded state.

Figure 6-6 presents the effect of operating conditions on the stripping efficiency for the stripper containing 2 disc and 3 donut baffles. At a solids circulation rate of 43 kg/(m^2·s) near complete stripping of the helium tracer gas occurs for the range of stripping gas velocities tested. Stripping efficiencies range from 96.0% to 99.3% for gas velocities ranging from 0.1 to 0.3 m/s at this solids circulation rate. For solids circulation rates of 60 and 74 kg/(m^2·s), increased sensitivity to operating conditions is observed. Stripping performance is poor at a gas velocity of 0.1 m/s, with only 57% and 71% of the helium tracer being removed at solids circulation rates of 74 and 60 kg/(m^2·s), respectively. Increasing the stripping gas velocity to 0.2 m/s at these solids circulation rates greatly improves stripper performance, while further increasing the velocity to 0.3 m/s offers only marginal gains. However, regardless of the stripping gas velocity used, significantly improved stripping efficiency is always found at a solids circulation rate of 43 kg/(m^2·s).

In beds of Geldart A particles, it is thought that mass transfer via diffusion from the emulsion phase to the bubble cloud is the limiting step in mass transport (Sit & Grace, 1981). The gas interchange exchange coefficient between the bubble cloud and the emulsion phase, K_{ce}, can be approximated by modifying the Higbie penetration model (equation 1.4) to the form:

$$K_{ce} = 4.515\left[\frac{D_g \varepsilon_{mf} U_{br}}{EBD^3 \Phi^2}\right]^{1/2} \qquad (6.4)$$

where the bubble rise velocity, U_{br}, is the velocity of the bubble relative to the emulsion phase, give by the equation (Davidson & Harrison, 1963):

$$U_{br} = U_b - U_{strip} + U_{mf} \qquad (6.5)$$

Physically, the interchange coefficient can be thought of as a rate of diffusion of gas from the emulsion phase into the thin cloud surrounding the bubble, with an equal rate of diffusion from the cloud back to the emulsion. The bubble velocity, U_b, equivalent bubble diameter, *EBD*, and bubble sphericity, Φ, are predicted from two-dimensional CFD models of the geometrically scaled stripper. The values of EBD and sphericity can be found from Table 4-4, and the values for the bubble velocity can be found from Figure 4-28. These parameters were acquired 85 mm above the disc baffle skirt in the simulation, located just above the apex of the disc baffle (Chapter 4). Based on analysis of the bed hydrodynamics from simulation data, it is thought that mass transfer would be most effective between this measurement height and the skirt of the

upper baffle. The change in the helium tracer concentration along the height of the bed can be found from:

$$\frac{dC_{He}}{dZ} = \frac{-K_{ce}}{U_{br}}\left(C_{He,e} - C_{He,c}\right) \tag{6.6}$$

It can be seen from equation 6.6 that the amount of helium tracer gas transferred from the emulsion to the bubble phase is proportional to the ratio of K_{ce}/U_{br}. Because equation 6.6 is developed with reference to a plane moving at the same speed as the interstitial solids, the true length, Z, with respect to a stationary reference can be found from:

$$Z = L\left(1 - \frac{G_s}{\rho(1-\varepsilon)U_b}\right) \tag{6.7}$$

Figure 6-7 shows the effect of operating conditions on the ratio of K_{ce}/U_{br}. Data from the simulations operated at a solids circulation rate of 75 kg/(m^2·s) and a stripper gas velocity of 0.3 m/s are excluded due to flooding conditions in the stripper. As can be seen in the figure, the ratio of K_{ce}/U_{br} is at a maximum for conditions of low solids circulation rates and low stripper gas velocities. A high value in the ratio of K_{ce}/U_{br} means that an individual bubble has a high capacity for mass transfer, and thus will remove an increased amount of the helium tracer contained in the interstitial gas. Increasing the solids circulation rate in the stripper and the stripper gas velocity generally results in a decrease in the ratio of K_{ce}/U_{br}. One notable exception to this is observed when increasing the solids circulation rate from 60 to 75 kg/(m^2·s) at a stripping gas velocity of 0.2 m/s. However, the latter simulation exhibited early signs of flooding, and thus the reliability of the data for these conditions is questionable (the simulation was fully-flooded at 0.3 m/s). The ratio of K_{ce}/U_{br} is found to decrease at elevated solids circulation rates and high gas velocities due to increasing values of both $EBD^*\Phi$ and the bubble rise velocity.

The large increases in the bubble velocity at elevated stripping gas velocities in the simulations can be attributed to an increased frequency of bubble encroachment caused by the decreased spacing of gas bubbles at elevated stripper gas velocities. Unlike the two-dimensional case simulated, however, in a three-dimensional bed the bubbles can take multiple pathways to ascend the baffles and thus there would be an increased spacing between bubbles. This would result in lower rise velocities in the three-dimensional bed than those predicted in the two-dimensional simulation, and thus a lesser influence of the gas velocity on the ratio of K_{ce}/U_{br}. However, it was observed in experiments that bubbles preferred to rise in the identical pathways of leading bubbles, giving the appearance of streaming bubble flow. This implies that, while the bubble velocity between simulations and experiments may be quantitatively erroneous, there is likely to be an influence of bubble encroachment on the true bubble velocity in the bed.

It appears from the ratio of K_{ce}/U_{br} that stripping would be most efficient at low solids circulation rates and low stripping gas velocities. While this certainly was the trend observed for the solids circulation rate, stripping efficiency was found to increase at elevated stripping gas velocities. This increase in stripper performance at elevated gas velocities must be due to other favourable characteristics not accounted for in the gas interchange coefficient. Among the most obvious of these characteristics is an increase in the bubbling frequency upon increasing the stripping gas velocity. For example, at a solids circulation rate of 45 kg/(m^2·s) the simulations

predict a peak bubbling frequency of 2.4, 3.8, and 4.9 Hz at stripping gas velocities of 0.1, 0.2, and 0.3 m/s, respectively at a measurement height of 85 mm above the disc baffle skirt. Another important effect of increasing the gas velocity is an improved use of the vessel cross-section at these elevated gas velocities. This has a considerable impact on fluidized bed operation, as non-uniform bubble distribution over the bed improves the overall mass transport between the emulsion and bubble phases since it limits concentration gradients in the radial direction. Finally, it was observed that increasing the gas velocity led to an increased number of small diameter bubbles in the bed. These bubbles arose from the frequent bubble interactions observed when spacing between the bubbles in the simulation was decreased due to the increased volume of bubbles in the bed.

Although the ratio of K_{ce}/U_{br} predicts improved stripping efficiency at low solids circulation rates due to bubble properties, it is important to note that improved stripper performance would also arise from other bed properties. These properties include a higher particle residence time in the stripper and an increased bubbling frequency at low solids circulation rates. Figure 6-8 presents the average emulsion phase residence time in the stripper. The average particle residence time was calculated from the experimentally determined pressure drop per unit height using the equation:

$$t_{res} = \frac{h_{strip} \Delta P / h}{G_s g} \tag{6.7}$$

The increased residence time at low solids circulation rates arises not only from a lower cross-sectional average catalyst velocity, but also from an increased solids concentration in the bed at low solids circulation rates. Residence time would obviously have a large influence on stripper performance since it effects the contact time between the emulsion and the bubble phases. The other characteristic that would improve contacting is a small increase in the bubbling frequency at low solids circulation rates. For example, at a stripping gas velocity of 0.1 m/s, a bubbling frequency of 2.4, 2.1, and 2.1 Hz was found at solids circulation rates 45, 60, and 75 kg/(m^2·s) in the simulations, respectively.

Although the interchange coefficient was calculated for the average bubble properties measured at a height of 85 mm above the disc baffle skirt, it is important to note that bubble properties (i.e. sphericity and bubble velocity) are expected to show sensitivity to the axial position of the bubble relative to the baffles above and below. For example, increases in the gas hold-up between an axial position of 85 and 155 mm in the baffle interspace suggest a decreased rise velocity as the upper baffle is approached. Changes in the bubble properties would alter the calculated interchange coefficient. In addition, the bubble interchange coefficient was calculated for the average bubble properties determined in the simulation. It is obvious that the true rate of mass transfer would be better predicted by calculating the interchange coefficient for the distribution of bubble sizes rather than the average value.

Figure 6-9 shows the effect of the number of baffles on the stripping efficiency for a solids circulation rate of 75 kg/(m^2·s) and a stripping gas velocity of 0.1 m/s. Operation at these conditions correspond to the least effective stripping found in the experimental stripper. For the stripper containing 2, 3, and 4 disc baffles (3, 4, and 5 donut baffles), the stripping efficiency was found to be 52%, 87%, and 91%, respectively. It is apparent that gains in the stripping efficiency

are small by increasing the number of disc baffles from 3 to 4. However, unlike the crude oil vapours that must desorb from the catalyst surface, helium is a non-adsorbing tracer gas. Therefore, additional baffle pairs beyond that required to strip only the interstitial vapours may be required to reach a satisfactory stripper performance.

This dissertation explored the hydrodynamic behaviour of the stripper using the results from CFD simulations (Chapter 4). The simulations predicted that bubbles exhibit complex behaviour in their rise path and shape as they move in the interspace between an upper and lower baffle. Many of the behaviours predicted by the CFB models were similarly observed in the experimental system. At a solids circulation rate of 45 kg/(m^2·s) operated at a stripping gas velocity of 0.2 m/s, bubbles in the experimental system were found to stream near the walls in the interspace, then suddenly move towards the outer edge of the upper baffle as the upper baffle was approached. Both spherical and elongated shaped bubbles were observed. Elongated bubbles were observed to become increasingly spherical as they approach the upper baffle. Significant variation in the bubble diameter was observed, commonly ranging from a maximum of approximately 7 cm to less than 1 cm. It was found that increasing the gas velocity in the experimental system resulted in increasingly distorted bubble shapes and larger bubble diameters.

6.5 Conclusions

The effect of operating conditions and number of baffle pairs on the stripping efficiency was tested in a cold-flow fluid catalytic cracking unit stripper containing standard disc-and-donut baffles. Stripping was found to be most efficient at low solids circulation rates and high gas velocities. For solids circulation rates of 60 and 74 kg/(m^2·s) operated at a stripping gas velocity of 0.1 m/s, stripping was found to be 71% and 57% efficient, respectively. Substantially improved stripper performance was found for elevated gas velocities at these solids circulation rates, however stripper performance is always significantly lower at these solids circulation rates compared to the stripper operated at a solids circulation rate of 43 kg/(m^2·s). For a solids circulation rate of 75 kg/(m^2·s) operated at a stripper gas velocity of 0.1 m/s, stripping was found to be 52%, 87%, and 91% efficient for the stripper containing 2, 3, and 4 disc baffles. The ratio of the cloud-emulsion gas interchange coefficient to the bubble rise velocity was calculated using the results of a two-dimensional CFD simulation of the stripper. The ratio was found sensitive to the solids circulation rate and the stripper gas velocity. In general, the ratio was highest at low solids circulation rates and low gas velocities. Mass transfer is thought to be most efficient at low solids circulation rates due to 1) smaller bubble diameters and 2) high residence time of the emulsion phase. Mass transfer is thought to be more effective at high stripper gas velocities due to 1) increased bubbling frequency, 2) improved use of the vessel cross section, and 3) increased fraction of small diameter bubbles arising from an increased frequency of bubble interactions.

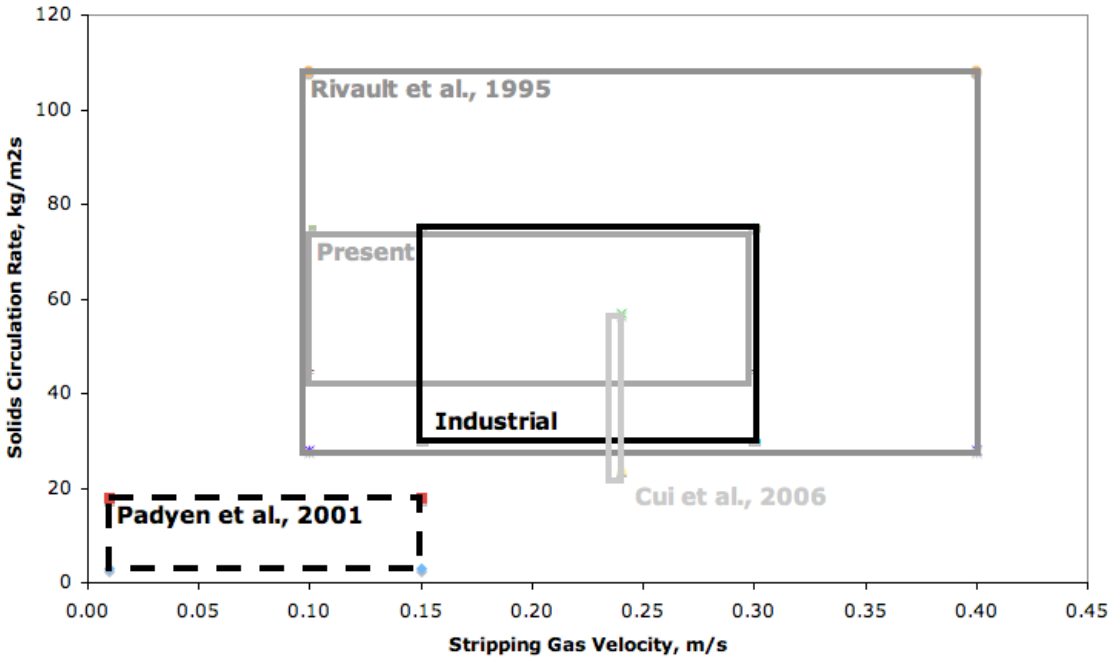

Figure 6-1: Parametric map showing the range of operating conditions (solids circulation rate and stripping gas velocity) investigated in previous studies and in the current study.

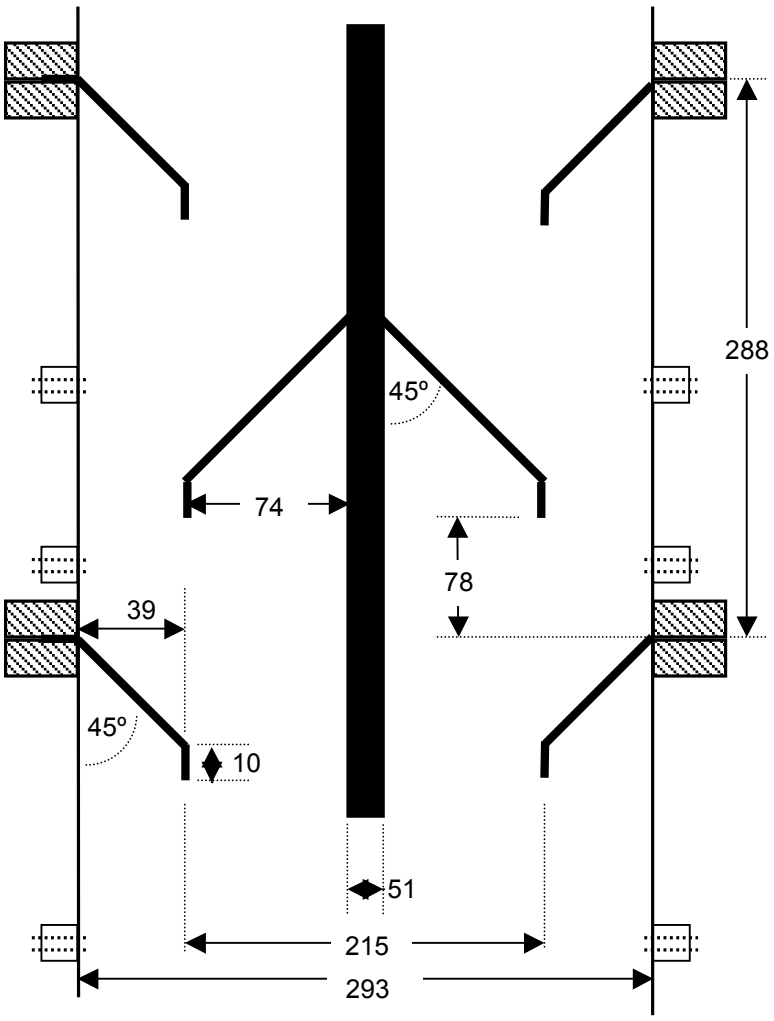

Figure 6-2: Section of the FCC stripper showing dimensions of the disc-and-donut baffles. All dimensions in mm.

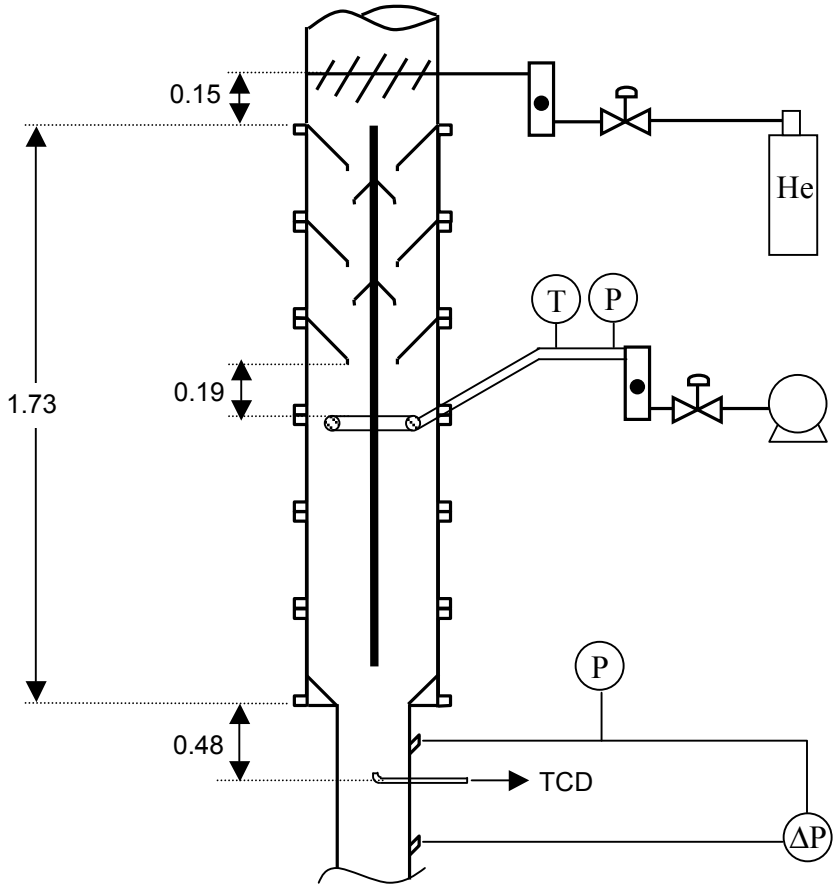

Figure 6-3: FCC stripper showing locations of instrumentation. All dimensions in m.

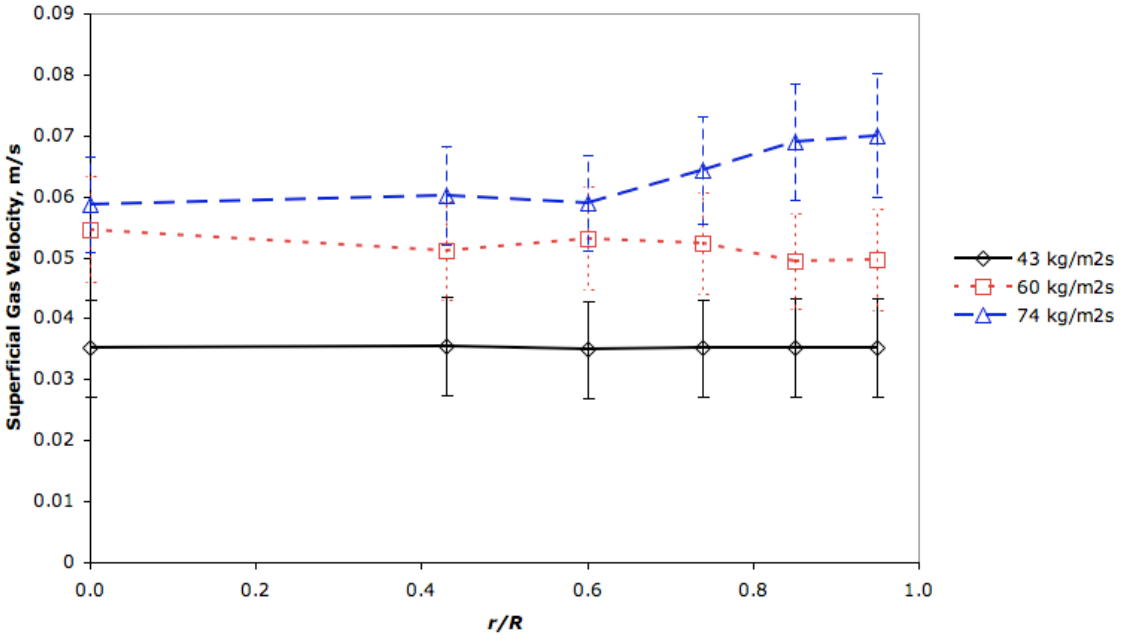

Figure 6-4: Superficial gas velocity profiles in the standpipe emulsion phase plotted with the 95% confidence intervals. Stripping gas velocity = 0.20 m/s.

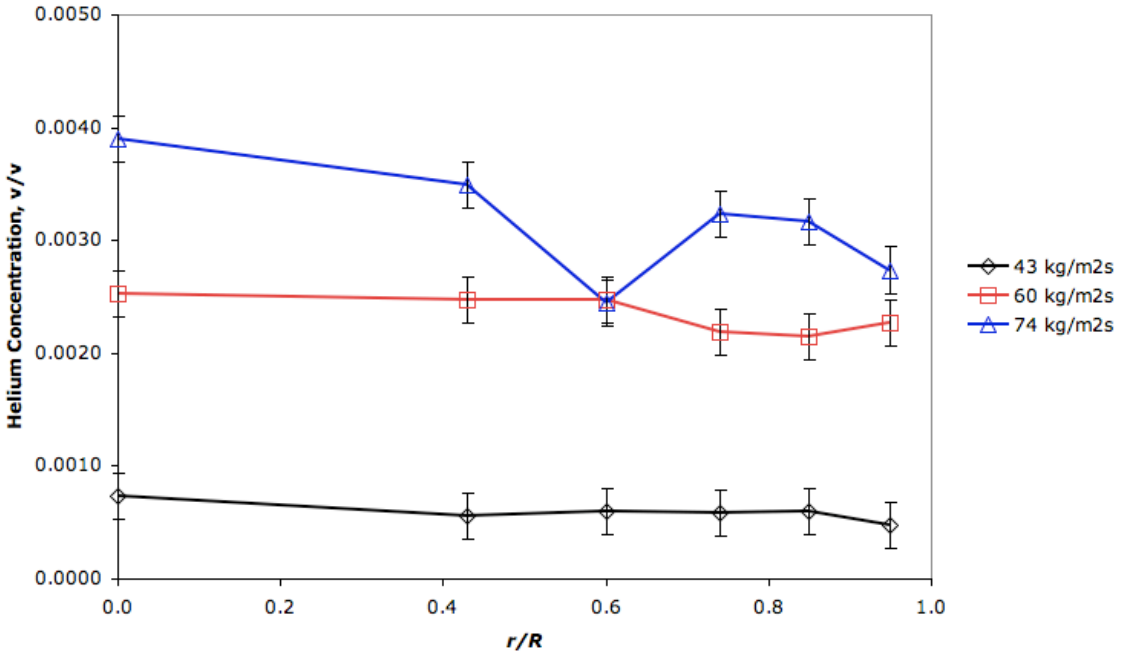

Figure 6-5: Helium concentration profiles across the radius of the standpipe plotted with 95% confidence intervals. Stripper gas velocity = 0.20 m/s.

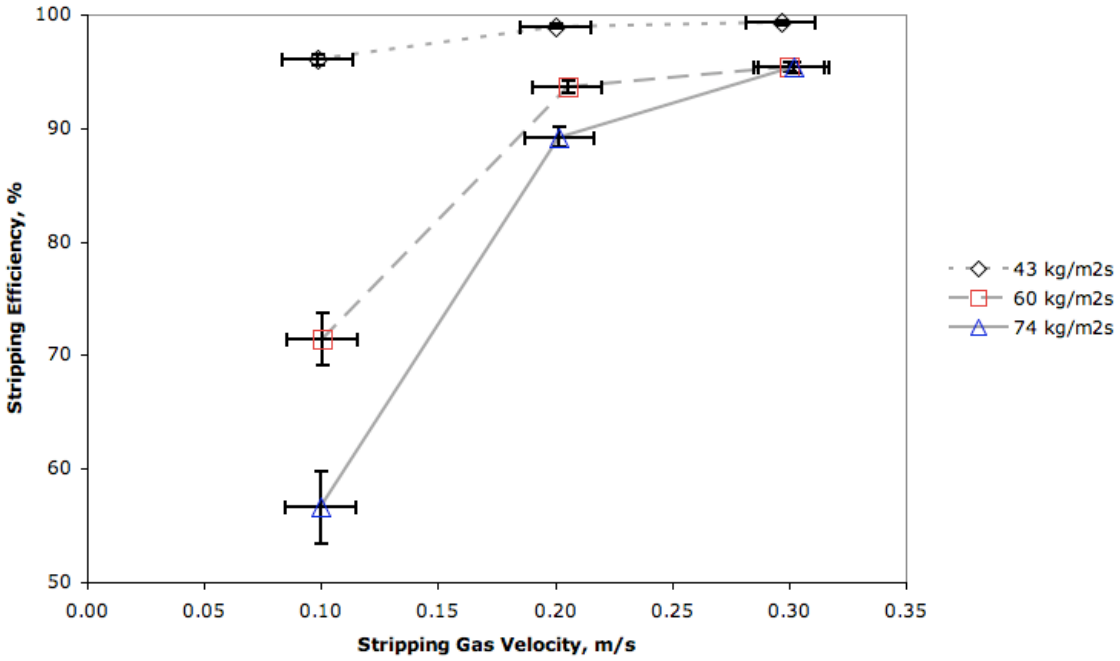

Figure 6-6: Stripping efficiency at various operating conditions plotted with the 95% confidence intervals. Stripper contains 2 disc and 3 donut baffles.

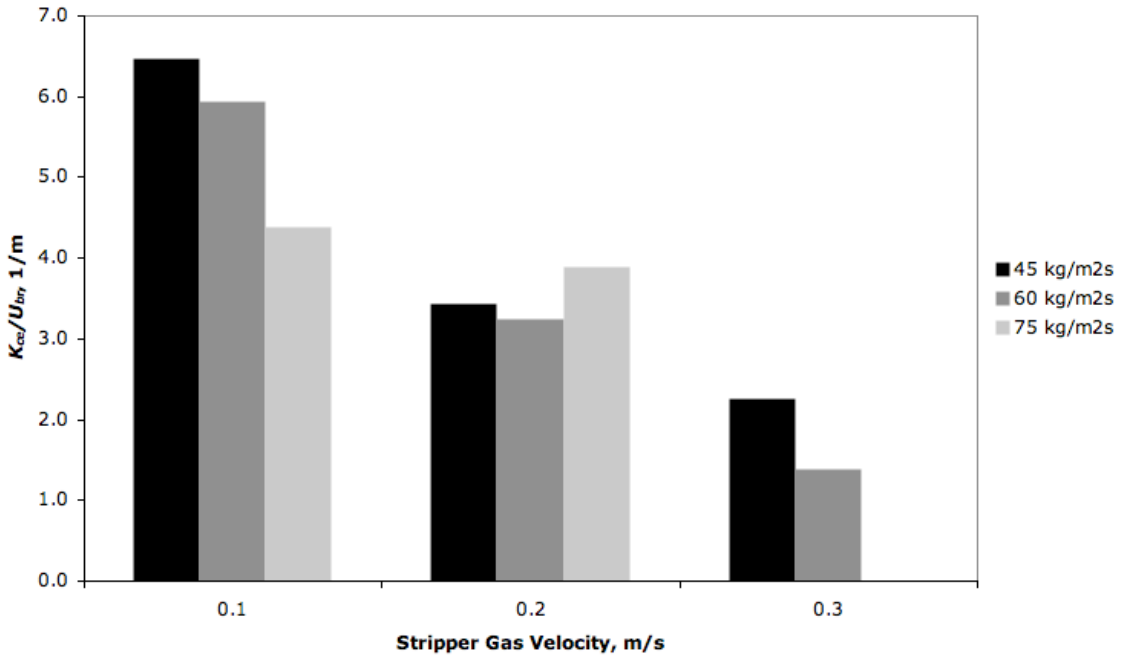

Figure 6-7: The effect of stripper operating conditions on the ratio of the cloud-emulsion gas interchange coefficient and the bubble rise velocity, calculated using the results of CFD simulations (Chapter 4).

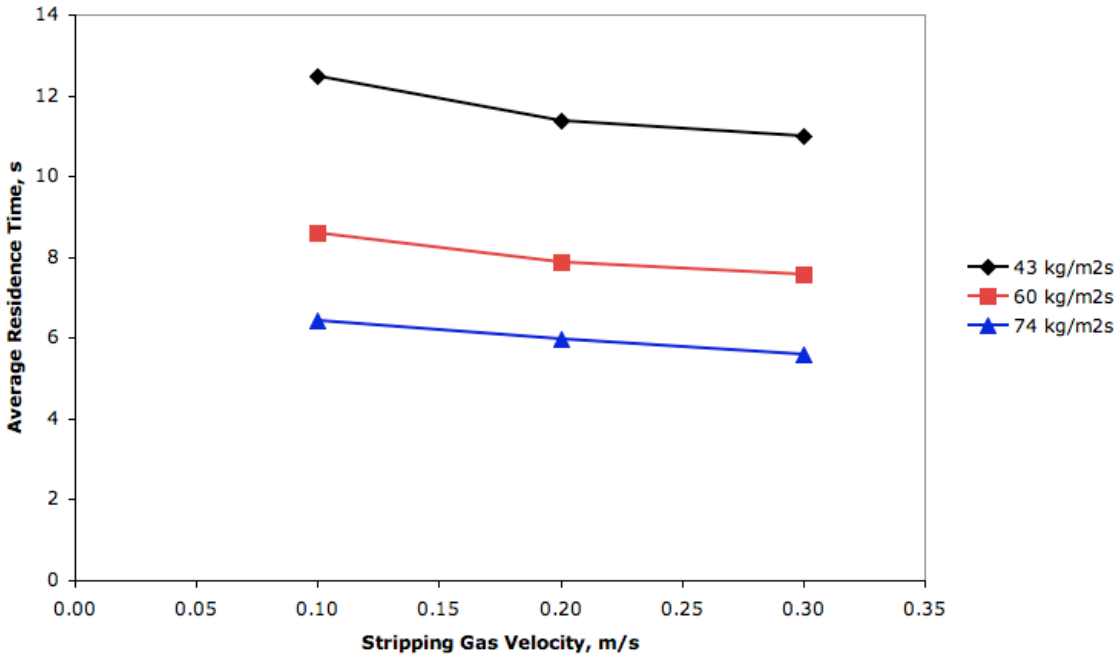

Figure 6-8: Effect of stripper operating conditions on the average emulsion phase residence time in the stripper.

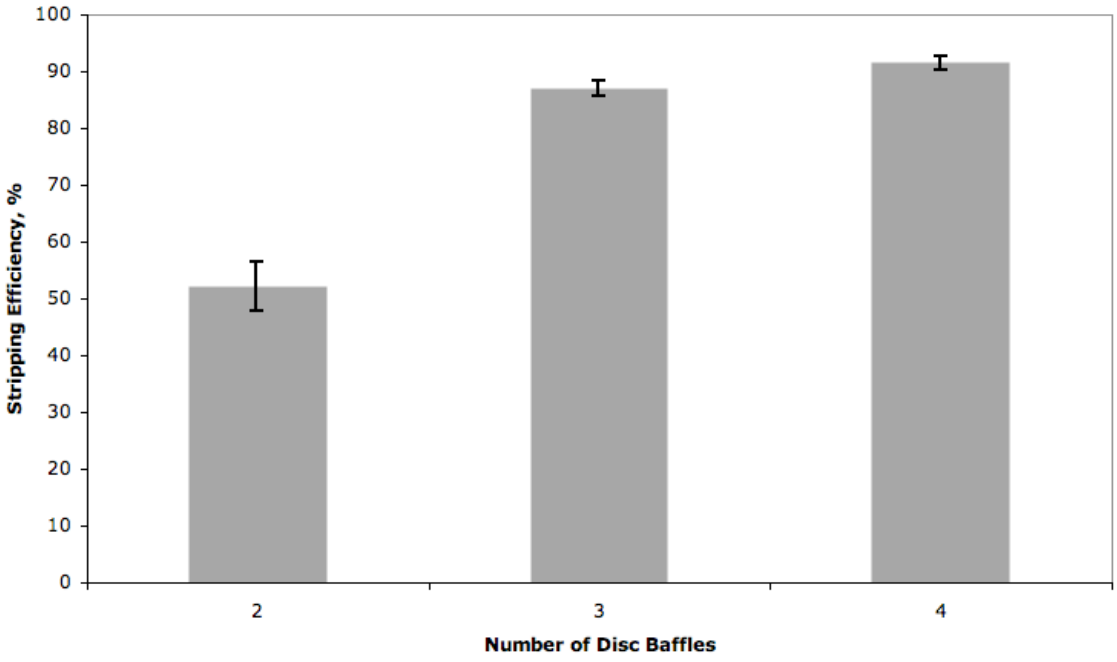

Figure 6-9: Stripping efficiency for stripper operated at varying number of baffles plotted with the 95% confidence intervals. Operating conditions: solids circulation rate = 75 kg/(m^2·s), stripper gas velocity = 0.1 m/s.

Chapter 7 – Conclusions and Recommendations

7.1 Conclusions

The study described in this dissertation was comprised of three sections. Design and calibration of the pilot-scale, cold-flow circulating fluidized bed apparatus was presented in Chapter 2. An experimental study examining the local solids flux profiles in the high-density bottom zone of the riser was presented in Chapter 3. Chapters 4 through 6 looked at the experimentally determined stripping efficiency, which was then related to the simulated hydrodynamic behaviour of the stripper. Hydrodynamics were examined using the results of a two-dimensional CFD model of the geometrically scaled experimental stripper (Chapter 4). The calculated stripping efficiency was comprised of two experimental measurements: the emulsion gas velocity profiles in the downcomer (Chapter 5), and helium concentration profiles in the standpipe (Chapter 6).

An extension of the existing 6 m tall circulating fluidized bed (CFB) in the fluidization laboratory of Saskatchewan (FLASK) was designed. The design incorporated a 0.29 m inside diameter stripping section in the downcomer, outfitted with standard disc-and-donut baffles. The CFB was able to attain a maximum solids circulation rate of 100 kg/(m^2·s) in the stripper (437 kg/(m^2·s) in the riser), however this maximum was found to be sensitive to the configuration of the riser terminator. Incorporating an internal cyclone in the downcomer reduced the maximum attainable solids circulation rate to 75 kg/(m^2·s) in the stripper (328 kg/(m^2·s) in the riser). This drop in the attainable solids circulation rate is thought to occur because of pressure drop in the underflow L-valve on the primary cyclone.

An investigation of the effect of solids circulation rate on the local solids flux profiles in a high-density bottom zone of the CFB riser was conducted. Solids circulation rates of 125, 174, 213, and 243 kg/(m^2·s) were examined for a superficial riser gas velocity of 5.3 m/s. The solids concentrations at these conditions were 0.12, 0.15, 0.16, and 0.16, respectively. In general, the radial solids flux profiles show a mostly constant net solids flux between $0.00 \leq r/R \leq 0.87$. Beyond $r/R = 0.87$, there is a sharp increase in the solids flux near the wall. The sharp increase in the solids circulation rate is thought to be an entrance effect caused by the unique solids feeding device used in the CFB. When increasing the solids circulation rate, the largest gains in the net solids flux profiles were observed near the wall. This phenomenon, as well as the increase in local solids flux near the wall, indicates developing flow in the riser.

The effect of the superficial riser gas velocity on the solids upflow at the riser centerline was examined at a static solids circulation rate of 187 kg/(m^2·s). Results show that the riser core undergoes a sharp transition from more dense conditions to more dilute conditions at a superficial gas velocity between 4.8 and 4.9 m/s. This sharp transition to a more radially uniform profile has never been reported.

The stripping efficiency was measured for stripper solids circulation rates of 44, 60, and 74 kg/(m^2·s) and superficial stripping gas velocities of 01, 0.2, and 0.3 m/s. The stripping efficiency was calculated using two experimentally determined parameters: the emulsion gas velocity in the standpipe and the concentration of helium tracer gas underflow into the standpipe. The latter was measured by sampling gas through a thermal conductivity detector. The former was tested using time-of-flight measurements of an injected helium tracer gas.

The emulsion gas velocity was determined in the un-baffled stripper and standpipe at stripper solids circulation rates of 43, 60, and 74 kg/(m^2·s). In the un-baffled stripper the solids were in a fluidized state, whereas de-fluidization of solids was found to occur in the standpipe. Results indicate a mostly constant emulsion gas velocity across the radius for both fluidized and de-fluidized solids. Two exceptions to this flat emulsion gas velocity profile were found. In the un-baffled stripper an increased downward velocity was found to occur when gas bubbles breached the measurement plane, while slip-stick flow in the standpipe caused an increase in the downward velocity near the wall.

Stripping efficiency was found to be highest at combinations of low solids circulation rates and high stripping gas velocities. Stripping efficiency ranged a high of 99.3% ± 0.18% at a solids circulation rate of 44 kg/(m^2·s) and stripper gas velocity of 0.3 m/s to a low of 56.6% ± 3.17% at a solids circulation rate of 74 kg/(m^2·s) and stripper gas velocity of 0.1 m/s. The results show that a substantial decrease in stripper performance occurs when operated beyond a solids circulation rate of 43 kg/(m^2·s). The bubble cloud – emulsion gas interchange coefficient was calculated using values of bubble diamater, bubble sphericity, and bubble rise velocity determined from CFD simulations. It was found that the interchange coefficient decreased at elevated solids circulation rates and stripper gas velocities. It is proposed that improved stripping efficiency at decreased solids circulation rates is due to the increased value of the gas interchange coefficient and the increased residence time of solids in the stripper. At elevated gas velocities, the increased bubbling frequency is mainly responsible for the improved stripping efficiency.

The stripper exhibits complex hydrodynamic behaviour in the interspace between the disc and donut baffles. It was found that bubble properties of sphericity and rise velocity are sensitive to the axial position in the baffle interspace. As the bubbles rise from the pinch point, the CFD simulations predict that they transition from an elongated shape to a more spherical shape as the upper baffle is approached. An increase in the gas hold-up indicates that the rise velocity decreases as the upper baffle is approached. Bubble interactions, predicted by the CFD simulations, appear detrimental to the capacity for mass transfer in the stripper. Bubble encroachment, occasionally resulting in coalescence of bubbles, appears to cause a sharp increase in the bubble rise velocity. Due to the increased gas hold-up, bubble encroachment is more frequent at elevated gas velocities. Because the frequency of bubble interactions would likely be lessened in a true three-dimensional bed, it is thought that the CFD simulation overestimate the influence of the stripping gas velocity on the bubble rise velocity.

7.2 Recommendations

To acquire high quality experimental results, a carefully designed apparatus is required. This is especially true of circulating systems, as the upstream and downstream hydrodynamics can vastly influence the overall behaviour of the system. Care must also be taken to ensure reliable data for troubleshooting and monitoring the operation of the system. The following modifications of the existing CFB apparatus are suggested:

1. Change the L-valve configuration on the cyclones of the riser terminator. It is believed that the pressure drop in the primary cyclone underflow L-valve inhibits the attainable solids circulation rate in the CFB. The primary cyclone should be moved closer to the freeboard section above the stripper to reduce the length of the horizontal section required on the L-valve. This horizontal length should be minimized, since the purpose is not for control of the solids circulation rate but rather for conveyance of solids. Alternatively (or additionally), the diameter of the L-valve could be increased.

2. Entrainment of solids limited the gas velocities attainable in the stripping efficiency tests. Entrainment could be reduced by increasing the diameter of the freeboard section above the stripper.

3. Some experiments showed sensitivity to the relative humidity of the fluidizing air. The humidity of the riser gas should be monitored and controlled. Alternatively, anti-static powders could be considered (for example, Larostat®).
4. Snubbers, or some sort of filtration device, should be placed on the pressure measurement lines in the riser to prevent plugging with solids. Some pressure taps on the riser are inactivated within 10 minutes of commencing operation due to plugging with solids. These filters need to be placed flush with the riser wall.

5. A different technique than that used in the present study should be employed to calibrate the solids circulation rate in the CFB. The technique used in this study was time consuming (thus allowing limited data points to create the calibration curve) and did not provide as much consistency in the results as the butterfly valve method.

This project has shown that an understanding of the operation of the many components of circulating fluidized beds is still far from being understood. Based on the results presented in this dissertation, the following are recommended to improve or extend the understanding of the various components of CFBs:

1. Tomography measurements should be employed to experimentally study the hydrodynamic behvaiour inside FCC strippers. Tomography measurements would be preferred because of the non-spherical shaped bubbles with non-vertical rise predicted in the CFD model.

2. Fibre optic probes should be used in conjunction with emulsion gas velocity measurements. The purpose of the probes would be to determine the voidage of the catalyst stream. This would enable discrimination between packed-bed and fluidized-bed

flow in the downcomer, since it is conceivable that a packed and fluidized bed could have the same value of pressure drop due to different bed voidages.

3. Extra freeboard height between the stripper bed surface and the L-valve entrances into the downcomer should be used in stripping efficiency measurements. This extra height would allow for measurement of the helium tracer gas concentration in the freeboard, thus enabling calculation of the steady-state helium tracer gas balance.

4. Experimental measurements, such as bubbling frequency profiles, should be made that enable further validation of the CFD model.

5. Three-dimensional CFD simulations of the FCC stripper should be used because of the potential magnification of the effect of bubble interactions observed in the two-dimensional simulations.

Chapter 8 – References

Abed, R., "Characterization of hydrodynamic nonuniformity in large fluidized beds", Ind. Eng. and Chem. Fundam. 24, (1985), pp. 78 – 82.

Abrahamsen, A. R. and D. Geldart, "Behaviour of gas-fluidized beds of fine powders, Part I – homogeneous expansion", Powder Tech. 26, (1980), pp. 35 – 46.

Aguillon, J., K. Shakourzadeh, and P. Guigon, "Comparative study of non-isokinetic sampling probes for solids flux measurement in circulating fluidized beds", Powder Tech. 83, (1995), pp. 79 – 84.

Arena, U., "Gas mixing", in J. R. Grace, A. A. Avidan, and T. M. Knowlton (eds.) "Circulating Fluidized Beds", Blackie Academic and Professional, (1997), pp. 86 – 118.

Avidan, A. A., "Fluid catalytic cracking", in J. R. Grace, A. A. Avidan, and T. M. Knowlton (eds.) "Circulating Fluidized Beds", Blackie Academic and Professional, (1997), pp. 466 – 488.

Azzi, M., P. Turlier, J. F. Large, and J. R. Bernard, "Use of a momentum probe and gammadensitometry to study local properties of fast fluidized beds", in P. Basu, M. Horio, and M. Hasatani (eds.) "Circulating Fluidized Bed Technology III", Pergamon Press, Oxford, (1991), pp. 189 – 194.

Baeyens, J. and D. Geldart, "An investigation into slugging fluidized beds", Chem. Eng. Sci. 29, (1974), pp. 255 – 265.

Bai, D., A. S. Issangya, and J. R. Grace, "Characteristics of gas-fluidized beds in different flow regimes", Ind. Eng. Chem. Res. 38, (1999), pp. 803 – 811.

Bai, D., E. Shibuya, Y. Masuda, K. Nishio, N. Nakagawa, and K. Kato, "Distinction between upward and downward flows in circulating fluidized beds", Powder Tech. 84, (1995), pp. 75 – 81.

Baumgarten, P. K., and R. L. Pigford, "Density fluctuations in fluidized beds", A.I.Ch.E. J. 6, (1960), pp. 115 – 123.

Bayle, J., P. Mege, and T. Gauthier, "Dispersion of bubble flow properties in a turbulent FCC fluidized bed", in M. Kwauk, J. Li, and W.-C. Yang (eds.) "Fluidization X", Engineering Foundation, (2001), pp. 125 – 132.

Benyahia, S., H. Arastoopour, T. M. Knowlton, "Simulation of particles and gas flow behaviour in the riser section of a circulating fluidized bed using the kinetic theory approach for the particulate phase", Powder Tech. 112, (2000), pp. 24 – 33.

Bi, H., H. Cui, J. Grace, A. Kern, C. J. Lim, D. Rusnell, X. Song, and C. McKnight, "Flooding of gas-solids countercurrent flow in fluidized beds", Ind. Eng. Chem. Res. 43, (2004), pp. 5611 – 5619.

Bi, H. T., N. Ellis, I. A. Abba, and J. R. Grace, "A state-of-the-art review of gas-solid turbulent fluidization", Chem. Eng. Sci. 55, (2000), pp. 4789 – 4825.

Cui, H., N. Mostoufi, and J. Chaouki, "Gas and solids between dynamic bubble and emulsion in gas-fluidized beds", Powder Tech. 120, (2001), pp. 12 – 20.

Cui, H. P., M. Strabel, D. Rusnell, H. T. Bi, K. Mansaray, J. R. Grace, C. J. Lim, C. A. McKnight, and D. Bulbuc, "Gas and solids mixing in a dynamically scaled fluid coker stripper", Chem. Eng. Sci. 61, (2006), pp. 388 – 396.

Chavarie, C. and J. R. Grace, "Interphase mass transfer in gas-fluidized beds", Chem. Eng. Sci. 31, (1976), pp. 741 – 749.

Chan, C. W., J. Seville, X. Fan, and J. Baeyens, "Solid particle motion in a standpipe as observed by positron emission particle tracking", Powder Tech. 194, (2009), pp. 58 – 66.

Chong, Y.-O., C.-S. Teo, and L.-S. Leung, "Recent advances in standpipe flow", J. of Pipelines 6, (1987), pp. 121 – 132.

Davidson, J. F., and D. Harrison, "Fluidized particles", Cambridge University Press, New York, NY, (1963)

van Deemter, J. J., "Mixing patterns in large-scale fluidized beds", in J. R. Grace and J. M. Matsen (eds.) "Fluidization", Engineering Foundation, (1980), pp. 69 – 89.

de Diego, L. F., P. Gayan, and Adanez, "Modelling of the flow structure in circulating fluidized beds", Powder Tech. 85, (1995), pp. 19 – 27.

Drinkenburg, A. A. H., and K. Rietema, "Gas transfer from bubbles in a fluidized bed to the dense phase – I. Theory", Chem. Eng. Sci. 27, (1972), pp. 1765 – 1774.

Drinkenburg, A. A. H., and K. Rietema, "Gas transfer from bubbles in a fluidized bed to the dense phase – II. Experiments", Chem. Eng. Sci. 28, (1973), pp. 259 – 273.

van Engelandt, G., J. De Wilde, G. J. Heynderickx, and G. B. Marin, "Experimental study of inlet phenomena of 35° inclined non-aerated and aerated Y-inlets in a dilute cold-flow riser", Chem. Eng. Sci. 62, (2007), pp. 339 – 355.

Fogler, H. "Elements of chemical reaction engineering, 3rd edition", Prentice Hall PTR, Upper Saddle River, NJ, (1999), pp. 596, 739.

Gamwo, I. K., Y. Soong, and R. W. Lyczkowski, "Numerical simulation and experimental validation of solids flows in a bubbling fluidized bed", Powder Tech. 103, (1999), pp. 117 – 129.

Gao, J., J. Chang, C. Xu, X. Lan, and Y. Yang, "CFD simulation of gas solid flow in FCC strippers", Chem. Eng. Sci. 63, (2008), pp. 1827 – 1841.

Geldart, D., "Types of gas fluidization", Powder Tech. 7, (1973), pp. 285 – 292.

Gibilaro, L. G., R. Di Felice, and S. P. Waldram, "Generalized friction factor and drag coefficient correlations for fluid-particle interactions", Chem. Eng. Sci. 40, (1985), pp. 1817 – 1823.

Grace, J. R., "Contacting modes and behaviour classification of gas-solid and other two-phase suspensions", Can. J. Chem. Eng. 64, (1986), pp. 353 – 363.

Grace, J. R., "Reflections on turbulent fluidization and dense suspension upflow", Powder Tech. 113, (2000), pp. 242 – 248.

Grace, J. R., and H. Bi, "Introduction to circulating fluidized beds", in J. R. Grace, A. A. Avidan, and T. M. Knowlton (eds.) "Circulating Fluidized Beds", Blackie Academic and Professional, (1997), pp. 1 – 20.

Grace, J. R., and R. Clift, "On the two-phase theory of fluidization", Chem. Eng. Sci. 29, (1974), pp. 327 – 334.

Halow, J. S. and P. Nicoletti, "Observations of fluidized bed coalescence using capacitance imaging", Powder Tech. 69, (1992), pp. 255 – 277.

Herb, B., S. Dou, K. Tuzla, and J. C. Chen, "Solid mass fluxes in circulating fluidized beds", Powder Tech. 70, (1992), pp. 197 – 205.

Incropera, F., and D. DeWitt, "Fundamentals of heat and mass transfer, 5th edition", John Wiley & Sons, New York, NY, (2002), pp. 333.

Issangya, A. S., D. Bai, and J. R. Grace, "Solids flux profiles in a high density circulating fluidized bed riser", in L.-S. Fan and T. M. Knowlton (eds.) "Fluidization IX", Engineering Foundation, (1998), pp. 197 – 204.

Johnson, D. L., and R. C. Senior, U.S. Patent 5531884, (1996)

Karri, R. S. K., and J. Werther, "Gas distributor and plenum design in fluidized beds", in W.-C. Yang (ed.) "Handbook of Fluidization and Fluid-Particle Systems", Marcel Dekker, New York, (2003), pp. 155 – 170.

Karri, S. B. R., and T .M. Knowlton, "A comparison of annulus solids flow direction and radial solids mass flux profiles at low and high mass fluxes in a riser", in J. Werther (ed.) "Circulating Fluidized Bed Technology VI", DECHEMA, Germany, (1999), pp. 71 – 77.

Karri, S. B. R., and T. Knowlton, "Comparison of group A solids flow in hybrid angled and vertical standpipes", in A. Avidan (ed.) "Circulating Fluidized Bed Technology, 4th", A.I.Ch.E., New York, NY, (1993), pp. 253 – 259.

Karri, S. B. R., T. Knowlton, and J. Litchfield, "Increasing solids flow through a hybrid angled standpipe using a bypass line", in J. F. Large and C. Laguerie (eds.) "Fluidization XIII, pre-prints, vol. 2", Engineering Foundation, (1995), pp. 1075 – 1082.

Khoe, G. K., T. L. Ip, and J. R. Grace, "Rheological and fluidization behaviour of powders of different particle size distribution", Powder Tech. 66, (1991), pp. 127 – 141.

Knowlton, T. M., "Standpipes and return systems", in J. R. Grace, A. A. Avidan, and T. M. Knowlton (eds.) "Circulating Fluidized Beds", Blackie Academic and Professional, (1997), pp. 214 – 259.

Knowlton, T. M., I. Hirsan, and L. S. Leung, "The effect of aeration tap location on the performance of a non-mechanical J-valve", in J. F. Davidson and D. L. Keairns (eds.) "Fluidization", Cambridge University Press, (1978), pp. 128 – 133.

Krishna, R., and J. M. van Baten, "Using CFD for scaling up gas-solids bubbling fluidized bed reactors with Geldart A powders", Chem. Eng. J. 82, (2001), pp. 247 – 257.

Kunni, D., and O. Levenspiel, "Effect of particles in bubbles on fluidized bed mass transfer and heat transfer kinetics", J. of Chem. Eng. of Japan 24, (1991a), pp. 183 – 188.

Kunni, D., and O. Levenspiel, "Fluidization Engineering, 2nd Edition", Butterworth-Heinemann, (1991).

Letzsch, W. S., "Revitalize stripping operations with structured packings", Hydrocarbon processing 82, (2003), pp. 69 – 72.

Leung, L. S., and P. J. Jones, "Flow of gas-solid mixtures in standpipes. A review", Powder Tech. 20, (1978), pp. 145 – 160.

Lim, K. S., and P. K. Agarwal, "Bubble velocity in fluidized beds: the effect of non-vertical bubble rise on its measurement using submersible probes and its relationship with bubble size", Powder Tech. 69, (1992), pp. 239 – 248.

Lim, K. S., and P. K. Agarwal, "Conversion of pierced lengths measured at a probe to bubble size measures. An assessment of the geometrical probability approach and bubble shape models", Powder Tech. 63, (1990), pp. 205 – 219.

Lim, K. S., J. X. Zhu, and J. R. Grace, "Hydrodynamics of gas-solid fluidization", Int. J. Multiphase Flow 21, (1995), pp. 41 – 193.

Mabrouk, R., J. Chaouki, and C. Guy, "Exit effect on hydrodynamics of the internal circulating fluidized bed riser", Powder Tech. 182, (2008), pp. 406 – 414.

Malcus, S., "Experimental and modeling study of a high suspension density CFB riser", Ph.D. dissertation, University of New Brunswick, Fredericton, NB, Canada, (2000)

Malcus, S., E. Cruz, C. Rowe, and T. S. Pugsley, "Radial solid mass flux profiles in a high-suspension density circulating fluidized bed", Powder Tech. 125, (2002), pp. 5 – 9.

Malcus, S., and T. Pugsley, "Lateral flux and velocity of FCC particles in a CFB riser", Can. J. Chem. Eng. 75, (2001), pp. 548 – 556.

Massimilla, L., "Gas jets in fluidized beds", in J. F. Davidson, R. Clift, and D. Harrison (eds.), "Fluidization, 2nd edition", Academic Press, New York, (1985), pp. 133 – 172.

Massimilla, L. and G. Donsi, "Cohesive forces between particles of fluid-bed catalysts", Powder Tech. 15, (1976), pp. 253 – 260.

McCarthy, S. J., M. F. Raterman, C. G. Smalley, J. F. Sodomin, and R. B. Miller, "Refiner improves FCC yields using latest process technologies", Oil & Gas J. 95, (1997), pp. 56 – 69.

McKeen, K. M., "Gas mixing in the bottom zone of a high density circulating fluidized bed riser", M.Sc. dissertation, University of Saskatchewan, Saskatoon, SK, Canada, (2003a).

McKeen, T. R., "Simulation of the hydrodynamics of a fluid catalytic cracker stripper using computational fluid dynamics", M.Sc. dissertation, University of Saskatchewan, Saskatoon, SK, Canada, (2003).

McKeen, T., and T. Pugsley, "Simulation and experimental validation of a freely bubbling bed of FCC catalyst", Powder Tech. 129, (2003), pp. 139 – 152.

van der Meer, E. H., R. B. Thorpe, and J. F. Davidson, "Flow patterns in the square cross-section riser of a circulating fluidised bed and the effect of riser exit design", Chem. Eng. Sci. 55, (2000), pp. 4079 – 4099.

Miller, R. B., Y. L. Yang, E. Gbordzoe, D. L. Johnson, and T. A. Mallo, "New developments in FCC feed injection and stripping technologies", NPRA 2000 annual meeting, San Antonio, TX, (2000)

Murray, J. D., "On the mathematics of fluidization, Part II. Steady motion of fully developed bubbles", J. of Fluid Mechanics 22, (1965), pp. 57 – 80.

Padyen, S., T. M. Knowlton, and H. Arastoopour, "Stripping in recirculating bubbling fluidized bed using group A particles", in M. Kwauk, J. Li, W.-C. Yang (eds.) "Fluidization X", United Engineering Foundation, New York, (2001), pp. 581 – 588.

Parssinen, J. H., and J.-X. Zhu, "Axial and radial solids distribution in a long and high-flux CFB riser", AICHE J. 47, (2001), pp. 2197 – 2205.

Peirano, E., V. Delloume, B. Leckner, "Two- or three-dimensional simulations of turbulent gas-solids flows applied to fluidization", Chem. Eng. Sci. 56, (2001), pp. 4787 – 4799.

Pell, M., and J. B. Dunson, "Gas-solids operations and equipment", in R. H. Perry and D. W. Green (eds.) "Perry's chemical engineers' handbook, 7th edition", McGraw-Hill, New York, NY, (1997), pp. 17-1 – 17-59.

Rall, R. R., and B. DeMulder, "New internal for maximizing performance of FCC catalyst strippers", 12th refining seminar, San Fransisco, CA, (2000)

Reddy, B. V., and P. K. Nag, "Effect of riser exit geometry on bed hydrodynamics and heat transfer in a circulating fluidized bed riser column", Int. J. of Energy Res. 25, (2001), pp. 1 – 8.

Rhodes, M., "What is turbulent fluidization?", Powder Tech. 88, (1996), pp. 3 – 14.

Rhodes, M. J., P. Laussmann, F. Villain, and D. Geldart, "Measurement of radial and axial solids flux variations in the riser of a circulating fluidized bed", in P. Basu and J. F. Large (eds.) "Circulating Fluidized Bed Technology II", Pergamon Press, Oxford, (1988), pp. 155 – 164.

Rietema, K., "The dynamics of fine powders", Elsevier, London, (1991).

Rivault , P., C. Nguyen, C. Laguerie, and J. R. Bernard, "Countercurrent stripping dense circulating beds, Effect of the baffles", in J. Large and C. Laguerie (eds.) "Fluidization VIII, Engineering Foundation, New York, (1995), pp. 491 – 499.

Rowe, P. N., B. A. Partridge, and E. Lyall, "Cloud formation around bubbles in gas fluidizes beds", Chem. Eng. Sci. 19, (1964), pp. 973 – 985.

Rowe, P. N., L. Santoro, and J. G. Yates, "The division of gas between bubble and interstitial phases in fluidised beds of fine powders", Chem. Eng. Sci. 33, (1978), pp. 133 – 140.

Senior, R. C., C. G. Smalley, and E. Gbordzoe, "Hardware modifications to overcome common operating problems in FCC catalyst strippers", in L. S. Fan, T. M. Knowlton (eds.), "Fluidization IX", Engineering Foundation, New York, (1998), pp. 725 – 732.

Sit, S. P., and J. R. Grace, "Effect of bubble interaction on interphase mass transfer in gas fluidized beds", Chem. Eng. Sci. 36, (1981), pp. 327 – 335.

Sit, S. P., and J. R. Grace, "Interphase mass transfer in an aggregative fluidized bed", Chem. Eng. Sci. 33, (1978), pp. 1115 – 1122.

Svensson, A., F. Johnsson, and B. Leckner, "Bottom bed regimes in a circulating fluidized bed boiler", Int. J. Multiphase Flow 22, (1996), pp. 1187 – 1204.

Toei, R. and R. Matsuno, Int. Chem. Eng. 9, (1969), pp. 358

Toomey, R. D., and H. F. Johnstone, "Gas fluidization of solid particles", Chem. Eng. Prog. 48, (1952), pp. 220 – 226.

Tsinontides, S. C., "A theoretical investigation of gas-solids flow exiting a fluidized bed into a standpipe", Powder Tech. 101, (1999), pp. 211 – 228.

Wakabayashi, T. and D. Kunni, J. Chem. Eng. of Japan 4, (1971), pp. 226 – 230.

Wei, F., L. Fangbin, J. Yong, and Y. Zhiqing, "Mass flux profiles in a high density circulating fluidized bed", Powder Tech. 91, (1997), pp. 189 – 195.

Werther, J., and B. Hirschberg, "Solids motion and mixing", in J. R. Grace, A. A. Avidan, and T. M. Knowlton (eds.) "Circulating Fluidized Beds", Blackie Academic and Professional, (1997), pp. 119 – 148.

Werther, J., and O. Molerus, "The local structure of gas fluidized beds: II. The spatial distributions of bubbles", International J. of Multiphase Flow 1, (1973), pp. 123 – 138.

Wiens, J. and T. Pugsley, "Tomographic imaging of a conical fluidized bed of dry pharmaceutical granule", Powder Tech. 169, (2006), pp. 49 – 59.

Yamazaki, R., M. Asai, M. Nakajima, and G. Jimbo, "Characteristics of regime transition in a turbulent fluidized bed", Proceedings of the 4th China – Japan Fluidization Conference, (1991), pp. 720 – 725.

Yan, A., J. H. Parssinen, and J.-X. Zhu, "Flow properties in the entrance and exit regions of a high-flux circulating fluidized bed riser", Powder Tech. 131, (2003), pp. 256 – 263.

Zhao, Y., and L. Wei, "Rheology of gas-solid fluidized beds", Fuel Processing Tech. 68, (2000), pp. 153 – 160.

Zhu, H., and J. Zhu, "Characterization of fluidization behavior in the bottom region of CFB risers", Chem. Eng. J. 141, (2008), pp. 169 – 179.

Appendix A: CFB Operating Procedures

A.1 Start-Up Procedure

1. Open valves on riser air input line and baghouse filter valve outlet line.

2. Start data acquisition system 'JasonDAQ 012009.vi'

3. Crack open valve on primary cyclone L-valve aeration line (located on the top floor of the scaffolding).

4. Turn on aeration to secondary cyclone L-valve (located in the basement). The aeration should be tuned as following: 2CEH = 5 LPM, 2CEL = 10 LPM.

5. If the stripper is being used, turn on aeration to the sparger grid located above the baffles (controls are on the 2nd floor scaffolding in the pilot plant). After ensuring all air bypass lines are initially open, turn on the blower connected to the sparger ring (controls are located on the 2nd floor scaffolding in the pilot plant). Slowly increase the air flowrate to the stripper until 200 SCFH is read on the rotameters. The final adjustments to the stripping gas flowrate are made while the CFB is operating.

6. Press 'Start' on the LEESON Speedmaster blower speed controller. Adjust the motor frequency using the '▲ or ▼' buttons. Increase the motor frequency to 10 kHz and check to see if the solids in the riser are fluidizing. If solids are not fluidizing, cycle the motor speed between 15 and 10 kHz until the solids become fluidized.

7. Increase the motor frequency to approximately 21 kHz.

8. Adjust the aeration to the annular bed to approximately 100 SCFH air.

9. Quickly adjust the aeration in the standpipe to the flowrates listed in Table A1.1. Note that if the stripper is being used, A4 should be set to 0. If the stripper sparging ring is not being used, A4 should be adjust to 6 LPM. Additional aeration ports will be required along the length of the standpipe, starting from approximately 30 cm above the standpipe/ stripper transition in approximately 1 m increments. The flowrate to these aeration taps can be initially set at 6 LPM.

10. Adjust the four aeration taps along the 45° inclined section to 6 LPM. Bubbles should reach the top of the inclined pipe and travel either upwards or downwards along the pipe. If bubbles travel upwards, they should exit the inclined standpipe through the air bypass tube.

11. Increase the aeration to the annular bed (if required) to increase the solids circulation rate in the CFB. If trying to achieve a high solids circulation rate, the aeration needs to be incremented. At each increment, wait for the CFB to maintain a constant solids circulation rate (can see this in the DAQ).

12. Aeration can be adjusted to maximize pressure build-up in the standpipe. The solids have a fluidized density of 1 psi/m. Note that excessive aeration will cause bubbles to form in the standpipe which will hinder solids flow and reduce pressure build-up.

13. An alternate method to attain a higher solids circulation rate is to increase the blower speed.

Table A1.1: Preliminary aeration scheme in the CFB standpipe.

Aeration Location (Figure A1.1)	Aeration (LPM)
0.48	7
1.48	6
2.49	6
3.44	5
4.48	0
A5	5
A4	See A.1, bullet #9
2CEH	5
2CEL	10

A.2 Shut-Down Procedure

1. Step decrease the solids circulation rate in the CFB by adjusting the aeration to the annular bed. The aeration to the annular bed should ultimately be reduced to approximately 100 SCFH.

2. After steady state is achieved, turn off aeration to the annular bed.

3. Quickly turn off aeration to the 45° inclined section.

4. Quickly turn off standpipe aeration (but keep cyclone L-valve aeration on).

5. Wait until the solids in the standpipe stop moving (they will move in high frequency oscillatory flow for a while after aeration is turned off) and the riser appears mostly empty of solids (approximately 5 minutes). Slowly decrease the electronic motor controller on the riser blower to 0.5 kHz, then turn off gas to the riser.
6. Turn off aeration to cyclones.

7. Turn off DAQ

A.3 Maintenance

After each operation of the CFB, the mesh screens on the filtration barrels coming off of the top of the downcomer should wiped clear (from inside the barrels). The baghouse filter cloth should be cleaned of solids using the shaker. Pressure taps will require periodic cleaning by blowing low pressure air through the lines. Some of the pressure lines (on the top and bottom of the riser) will plug after only a few minutes of operation, so these should be ignored. Periodically check the bolts connecting the flanged sections of the riser and standpipe, as these can loosen over time.

A.4 Troubleshooting

Table A4.1 presents a list of common problems encountered during operation of the CFB. The table lists the recommended solution to the difficulties.

Table A4.1: Problems encountered during operation of the CFB.

Symptom	Solution
Sharp drop in solids circulation rate in the CFB	Too much aeration to the annular bed. The aeration can be adjusted up to a maximum of approximately 350 SCFH. Reduce aeration in the annular bed to a low level to regain control of the solids circulation rate.
High amplitude cycling of the solids circulation rate	Defluidization in the primary cyclone L-valve. When this occurs, control of the solids flux can not be regained, and the system must be quickly shut down using the procedure outlined in A.2 (except the aeration to the annular bed and standpipe should be shut completely off, not stepped down. On the next run, aeration in the L-valve must be increased.
Air gaps in the standpipe	Defluidization/ gas bridging of the solids. When this occurs, the system must be shut down as steady state operation of the CFB can not be regained. On the next run, aeration must be added in smaller incremental levels along the axis of the standpipe.
High frequency (approx 1 – 10 Hz) oscillatory solids flow in the standpipe (slip-stick flow)	Some oscillatory flow is normal. Oscillatory flow most often occurs in the vertical section of standpipe between the 45° inclined section and the stripper. It is a symptom of defluidization of solids. Increasing the upstream aeration should reduce the problem.

Appendix B: Sample MFIX files

B.1 Sample MFIX.dat File

```
!
!  Experimental Stripper Simulation
!

! Run-control section

  RUN_NAME              = 'STRIP7510T'
  DESCRIPTION           = 'Experimental stripper, Gs-45, Ustrip-0.1'
  RUN_TYPE              = 'restart_1'
  UNITS                 = 'cgs'
  TIME                  = 60.0                    !start time
  TSTOP                 = 70.0
  DT                    = 1.0E-4                  !time step
  ENERGY_EQ             = .FALSE.                 !do not solve energy eq
  SPECIES_EQ(0)         = .TRUE.                  !solve species eq gas
  SPECIES_EQ(1)                 = .FALSE.
  DISCRETIZE                    = 9*2
  DISCRETIZE(7)                 = 0                                     !FOU species
  DEF_COR                       = .TRUE.
  MAX_INLET_VEL_FAC             = 3
  DRAG_TYPE                     = 'BVK'
  C(1)                          = 0.25
  C_NAME(1)                     = 'drag scale factor'


! Geometry Section

  COORDINATES           = 'cylindrical'
  IMAX                  = 25                      !cells in i direction
  DX                            = 2.5, 24*0.5       !dummy riser is defined first, followed by simulation cells
  YLENGTH                       = 286.0
  JMAX                  = 572                     !cells in j direction
  NO_K                  = .TRUE.                  !2D, no k direction


! Gas-phase Section

  MU_g0                 = 1.98E-04                !constant gas viscosity
  NMAX(0)                       = 2
  SPECIES_NAME(1)       = 'AIR'
  SPECIES_NAME(2)       = 'AIR'
  MW_g                          = 28.8                28.8                    !molecular weight of air


! Solids-phase Section

  RO_s                  = 1.55                    !solids density
  D_p0                  = 0.0098                  !particle diameter
  e                     = 0.95                    !restitution coefficient
  Phi                   =30.0                     !angle of internal friction
  EP_star               = 0.45                    !void fraction at Umf
  SPECIES_NAME(3)       = 'O2'
```

```
! Initial Conditions Section

   ! 1. dense bed
  IC_X_w(1)          =  0.0                  !lower half of the domain
  IC_X_e(1)          =  14.5
  IC_Y_s(1)          =  0.0
  IC_Y_n(1)          =  168.5
   !initial values in the region
  IC_EP_g(1)         =  0.45                  !void fraction
  IC_U_g(1)          =  0.0                  !radial gas velocity
  IC_V_g(1)          =  @(0.59/0.45)          !axial gas velocity
  IC_U_s(1,1)        =  0.0                  !radial solids velocity
  IC_V_s(1,1)        = 0.0                   !axial solids velocity
  IC_P_g(1)                  = 1.155E+06
  IC_T_g(1)                  = 298.0
  IC_T_s(1,1)                = 298.0
  IC_X_g(1,1)                = 1.0
  IC_X_g(1,2)                = 0.0

   !  2. Freeboard
  IC_X_w(2)          =   0.0
  IC_X_e(2)          =   14.5
  IC_Y_s(2)          =  168.5
  IC_Y_n(2)          =  286.0

  IC_EP_g(2)         =   1.0
  IC_U_g(2)          =   0.0
  IC_V_g(2)          =   0.59
  IC_U_s(2,1)        =   0.0
  IC_V_s(2,1)        =   0.0
  IC_P_g(2)                  =  1.155E+06
  IC_T_g(2)                  =  298.0
  IC_T_s(2,1)                = 298.0
  IC_X_g(2,1)                = 1.0
  IC_X_g(2,2)                = 0.0

!  Boundary Conditions Section

     ! 1. Air ring BC
  BC_X_w(1)          =  9.0
  BC_X_e(1)          =  11.0
  BC_Y_s(1)          =  10.0
  BC_Y_n(1)          =  12.0

  BC_TYPE(1)         = 'NSW'

  BC_C_X_g(1,1)              = 0
  BC_C_X_g(1,2)              = 0
  BC_hw_X_g(1,1)             = 0
  BC_hw_X_g(1,2)             = 0

          ! 2. Air inflow BC

  BC_X_w(2)                  = 9.5
  BC_X_e(2)                  = 10.5
  BC_Y_s(2)                  = 12.0
```

```
BC_Y_n(2)                = 12.0

BC_TYPE(2)               = 'MI'

BC_EP_g(2)          =  1.0
BC_U_g(2)           =  0.0
BC_V_g(2)           =  121.0        !Corresponds to a sup. gas vel. of 0.1m/s in strip
BC_P_g(2)           =  1.155E+06
BC_T_g(2)                =  298.0
BC_T_s(2,1)              = 298.0
BC_X_g(2,1)              = 1.0
BC_X_g(2,2)              = 0.0

    ! 3. Freeboard exit
BC_X_w(3)           =  2.5
BC_X_e(3)           =  14.5
BC_Y_s(3)           =  286.0
BC_Y_n(3)           =  286.0

BC_TYPE(3)          = 'PO'

BC_P_g(3)                =  1.155E+06
BC_T_g(3)                = 298.0
BC_T_s(3,1)              = 298.0

        ! 4. Dummy riser at centre
BC_X_w(4)                = 0.0
BC_X_e(4)                = 2.5
BC_Y_s(4)                = 0.0
BC_Y_n(4)                = 286.0

BC_TYPE(4)               = 'NSW'

BC_C_X_g(4,1)            = 0
BC_C_X_g(4,2)            = 0
BC_hw_X_g(4,1)           = 0
BC_hw_X_g(4,2)           = 0

        ! 10. Donut baffle 1 - above air ring
BC_X_w(10) =  10.5    11.0    11.5    12.0    12.5    13.0    13.5    14.0
BC_X_e(10) =  11.0    11.5    12.0    12.5    13.0    13.5    14.0    14.5
BC_Y_s(10) =  30.5    31.5    32.0    32.5    33.0    33.5    34.0    34.5
BC_Y_n(10) =  31.5    32.0    32.5    33.0    33.5    34.0    34.5    35.0

BC_TYPE(10) = 'NSW'  'NSW'   'NSW'   'NSW'   'NSW'   'NSW'   'NSW'   'NSW'

BC_C_X_g(10,1)           = 8*0
BC_C_X_g(10,2)           = 8*0
BC_hw_X_g(10,1)          = 8*0
BC_hw_X_g(10,2)          = 8*0

        ! 20. Disk baffle 1
BC_X_w(20) =  9.5     9.0     8.5     8.0     7.5     7.0     6.5     6.0
BC_X_e(20) =  10.0    9.5     9.0     8.5     8.0     7.5     7.0     6.5
BC_Y_s(20) =  43.5    44.5    45.0    45.5    46.0    46.5    47.0    47.5
BC_Y_n(20) =  44.5    45.0    45.5    46.0    46.5    47.0    47.5    48.0
```

```
BC_TYPE(20) = 'NSW'   'NSW'   'NSW'   'NSW'   'NSW'   'NSW'   'NSW'   'NSW'

 BC_C_X_g(20,1)        = 8*0
 BC_C_X_g(20,2)        = 8*0
 BC_hw_X_g(20,1)       = 8*0
 BC_hw_X_g(20,2)       = 8*0

 BC_X_w(30) =  5.5     5.0     4.5     4.0     3.5     3.0     2.5
 BC_X_e(30) =  6.0     5.5     5.0     4.5     4.0     3.5     3.0
 BC_Y_s(30) =  48.0    48.5    49.0    49.5    50.0    50.5    51.0
 BC_Y_n(30) =  48.5    49.0    49.5    50.0    50.5    51.0    51.5

 BC_TYPE(30) =         'NSW'   'NSW'   'NSW'   'NSW'   'NSW'   'NSW'   'NSW'

 BC_C_X_g(30,1)        = 7*0
 BC_C_X_g(30,2)        = 7*0
 BC_hw_X_g(30,1)       = 7*0
 BC_hw_X_g(30,2)       = 7*0

          ! 40. Donut baffle 2
 BC_X_w(40) =  10.5    11.0    11.5    12.0    12.5    13.0    13.5    14.0
 BC_X_e(40) =  11.0    11.5    12.0    12.5    13.0    13.5    14.0    14.5
 BC_Y_s(40) =  60.0    61.0    61.5    62.0    62.5    63.0    63.5    64.0
 BC_Y_n(40) =  61.0    61.5    62.0    62.5    63.0    63.5    64.0    64.5

 BC_TYPE(40) =         'NSW'   'NSW'   'NSW'   'NSW'   'NSW'   'NSW'   'NSW'   'NSW'

 BC_C_X_g(40,1)        = 8*0
 BC_C_X_g(40,2)        = 8*0
 BC_hw_X_g(40,1)       = 8*0
 BC_hw_X_g(40,2)       = 8*0

          ! 50. Disk baffle 2
 BC_X_w(50) =  9.5     9.0     8.5     8.0     7.5     7.0     6.5     6.0
 BC_X_e(50) =  10.0    9.5     9.0     8.5     8.0     7.5     7.0     6.5
 BC_Y_s(50) =  73.0    74.0    74.5    75.0    75.5    76.0    76.5    77.0
 BC_Y_n(50) =  74.0    74.5    75.0    75.5    76.0    76.5    77.0    77.5

 BC_TYPE(50) =         'NSW'   'NSW'   'NSW'   'NSW'   'NSW'   'NSW'   'NSW'   'NSW'

 BC_C_X_g(50,1)        = 8*0
 BC_C_X_g(50,2)        = 8*0
 BC_hw_X_g(50,1)       = 8*0
 BC_hw_X_g(50,2)       = 8*0

 BC_X_w(60) =  5.5     5.0     4.5     4.0     3.5     3.0     2.5
 BC_X_e(60) =  6.0     5.5     5.0     4.5     4.0     3.5     3.0
 BC_Y_s(60) =  77.5    78.0    78.5    79.0    79.5    80.0    80.5
 BC_Y_n(60) =  78.0    78.5    79.0    79.5    80.0    80.5    81.0

 BC_TYPE(60)= 'NSW'   'NSW'   'NSW'   'NSW'   'NSW'   'NSW'   'NSW'

 BC_C_X_g(60,1)        = 7*0
 BC_C_X_g(60,2)        = 7*0
 BC_hw_X_g(60,1)       = 7*0
 BC_hw_X_g(60,2)       = 7*0
```

```
        ! 70. Donut baffle 3
BC_X_w(70) =  10.5    11.0    11.5    12.0    12.5    13.0    13.5    14.0
BC_X_e(70) =  11.0    11.5    12.0    12.5    13.0    13.5    14.0    14.5
BC_Y_s(70) =  89.5    90.5    91.0    91.5    92.0    92.5    93.0    93.5
BC_Y_n(70) =  90.5    91.0    91.5    92.0    92.5    93.0    93.5    94.0

BC_TYPE(70) =         'NSW'   'NSW'   'NSW'   'NSW'   'NSW'   'NSW'   'NSW'   'NSW'

BC_C_X_g(70,1)        = 8*0
BC_C_X_g(70,2)        = 8*0
BC_hw_X_g(70,1)       = 8*0
BC_hw_X_g(70,2)       = 8*0

        ! 80. Disk baffle 3
BC_X_w(80) =  9.5     9.0     8.5     8.0     7.5     7.0     6.5     6.0
BC_X_e(80) =  10.0    9.5     9.0     8.5     8.0     7.5     7.0     6.5
BC_Y_s(80) =  102.5   103.5   104.0   104.5   105.0   105.5   106.0   106.5
BC_Y_n(80) =  103.5   104.0   104.5   105.0   105.5   106.0   106.5   107.0

BC_TYPE(80) =         'NSW'   'NSW'   'NSW'   'NSW'   'NSW'   'NSW'   'NSW'   'NSW'

BC_C_X_g(80,1)        = 8*0
BC_C_X_g(80,2)        = 8*0
BC_hw_X_g(80,1)       = 8*0
BC_hw_X_g(80,2)       = 8*0

BC_X_w(90) =  5.5     5.0     4.5     4.0     3.5     3.0     2.5
BC_X_e(90) =  6.0     5.5     5.0     4.5     4.0     3.5     3.0
BC_Y_s(90) =  107.0   107.5   108.0   108.5   109.0   109.5   110.0
BC_Y_n(90) =  107.5   108.0   108.5   109.0   109.5   110.0   110.5

BC_TYPE(90) =         'NSW'   'NSW'   'NSW'   'NSW'   'NSW'   'NSW'   'NSW'

BC_C_X_g(90,1)        = 7*0
BC_C_X_g(90,2)        = 7*0
BC_hw_X_g(90,1)       = 7*0
BC_hw_X_g(90,2)       = 7*0

        ! 100. Donut baffle 4
BC_X_w(100) =         10.5    11.0    11.5    12.0    12.5    13.0    13.5    14.0
BC_X_e(100) = 11.0    11.5    12.0    12.5    13.0    13.5    14.0    14.5
BC_Y_s(100) = 119.0   120.0   120.5   121.0   121.5   122.0   122.5   123.0
BC_Y_n(100) = 120.0   120.5   121.0   121.5   122.0   122.5   123.0   123.5

BC_TYPE(100) ='NSW'   'NSW'   'NSW'   'NSW'   'NSW'   'NSW'   'NSW'   'NSW'

BC_C_X_g(100,1)       = 8*0
BC_C_X_g(100,2)       = 8*0
BC_hw_X_g(100,1)      = 8*0
BC_hw_X_g(100,2)      = 8*0

        ! 110. Disk baffle 4
BC_X_w(110) =         9.5     9.0     8.5     8.0     7.5     7.0     6.5     6.0
BC_X_e(110) = 10.0    9.5     9.0     8.5     8.0     7.5     7.0     6.5
BC_Y_s(110) = 132.0   133.0   133.5   134.0   134.5   135.0   135.5   136.0
BC_Y_n(110) = 133.0   133.5   134.0   134.5   135.0   135.5   136.0   136.5
```

```
 BC_TYPE(110) ='NSW' 'NSW'   'NSW'   'NSW'   'NSW'   'NSW'   'NSW'   'NSW'

 BC_C_X_g(110,1)       = 8*0
 BC_C_X_g(110,2)       = 8*0
 BC_hw_X_g(110,1)      = 8*0
 BC_hw_X_g(110,2)      = 8*0

 BC_X_w(120) =         5.5     5.0     4.5     4.0     3.5     3.0     2.5
 BC_X_e(120) = 6.0     5.5     5.0     4.5     4.0     3.5     3.0
 BC_Y_s(120) = 136.5   137.0   137.5   138.0   138.5   139.0   139.5
 BC_Y_n(120) = 137.0   137.5   138.0   138.5   139.0   139.5   140.0

 BC_TYPE(120) ='NSW' 'NSW'   'NSW'   'NSW'   'NSW'   'NSW'   'NSW'

 BC_C_X_g(120,1)       = 7*0
 BC_C_X_g(120,2)       = 7*0
 BC_hw_X_g(120,1)      = 7*0
 BC_hw_X_g(120,2)      = 7*0

        ! 130. Donut baffle 5
 BC_X_w(130) =         10.5    11.0    11.5    12.0    12.5    13.0    13.5    14.0
 BC_X_e(130) = 11.0    11.5    12.0    12.5    13.0    13.5    14.0    14.5
 BC_Y_s(130) = 148.5   149.5   150.0   150.5   151.0   151.5   152.0   152.5
 BC_Y_n(130) = 149.5   150.0   150.5   151.0   151.5   152.0   152.5   153.0

 BC_TYPE(130) ='NSW' 'NSW'   'NSW'   'NSW'   'NSW'   'NSW'   'NSW'   'NSW'

 BC_C_X_g(130,1)       = 8*0
 BC_C_X_g(130,2)       = 8*0
 BC_hw_X_g(130,1)      = 8*0
 BC_hw_X_g(130,2)      = 8*0


        ! 140. Solids outflow
 BC_X_w(140) =         2.5
 BC_X_e(140) = 14.5
 BC_Y_s(140) = 0.000
 BC_Y_n(140) = 0.000

 BC_TYPE(140) =        'MO'

 BC_EP_g(140) =        0.45
 BC_U_g(140) =         0.00
 BC_V_g(140) =         -5.44                   !Cat velocity that corresponds to 45kg/m2s
experimental
 BC_U_s(140,1) =       0.00
 BC_V_s(140,1) =       -5.44
 BC_T_g(140)           = 298.0
 BC_T_s(140,1)         = 298.0

 BC_DT_0(140) =        0.01

        ! 150. Solids dipleg boundary
 BC_X_w(150) =         6.5     10.0    6.5
 BC_X_e(150) = 7.0     10.5    10.5
 BC_Y_s(150) = 186.0   186.0   187.0
```

```
 BC_Y_n(150) = 188.0     188.0     188.0

 BC_TYPE(150) ='NSW'  'NSW'    'NSW'

 BC_C_X_g(150,1)         = 3*0
 BC_C_X_g(150,2)         = 3*0
 BC_hw_X_g(150,1)        = 3*0
 BC_hw_X_g(150,2)        = 3*0

          ! 160. Solids dipleg inlet
 BC_X_w(160) =           7.0
 BC_X_e(160) = 10.0
 BC_Y_s(160) = 187.0
 BC_Y_n(160) = 187.0

 BC_TYPE(160) = 'MI'

 BC_EP_g(160) =          0.45
 BC_U_g(160) =           0.0
 BC_V_g(160) =           -21.76                  !Dipleg cat velocity = 45kg/m2s
 BC_U_s(160,1) =         0.0
 BC_V_s(160,1) =         -21.76
 BC_P_g(160) =  1.155E+06
 BC_T_g(160)             = 298
 BC_T_s(160,1)           = 298

 BC_X_g(160,1)           = 0.0
 BC_X_g(160,2)           = 1.0




!
!  Output Control
!
 OUT_DT            = 10.                 !write text file BUB01.OUT
                                        !  every 10 s
 RES_DT            = 0.01                !write binary restart file
                                        !  BUB01.RES every 0.01 s
 NLOG              = 25                  !write logfile BUB01.LOG
                                        !every 25 time steps
 FULL_LOG          = .TRUE.              !display residuals on screen


!SPX_DT values determine how often SPx files are written.  Here BUB01.SP1, which
!contains void fraction (EP_g), is written every 0.01 s, BUB01.SP2, which contains
! gas and solids pressure (P_g, P_star), is written every 0.1 s, and so forth.
!
     ! EP_g P_g      U_g  U_s  ROP_s    T_g  X_g
     !     P_star    V_g  V_s          T_s  X_s    Theta   Scalar
     !             W_g  W_s
 SPX_DT = 0.001 0.1     0.1  0.1  100.     100. 0.1   100.0    100.
```

B.2 Sample MFIX.out File

```
MM            MM    FFFFFFFFFF    IIIIII    XX     XX
MM            MM    FFFFFFFFFF    IIIIII    XX     XX
MMMM    MMMM    FF                II      XX     XX
MMMM    MMMM    FF                II      XX     XX
MM    MM    MM    FF                II       XX  XX
MM    MM    MM    FF                II       XX  XX
MM            MM    FFFFFFFF        II         XX
MM            MM    FFFFFFFF        II         XX
MM            MM    FF              II       XX  XX
MM            MM    FF              II       XX  XX
MM            MM    FF              II      XX     XX
MM            MM    FF              II      XX     XX
MM            MM    FF            IIIIII    XX     XX
MM            MM    FF            IIIIII    XX     XX

                Multiphase Flow with Interphase eXchanges
                        Version: 2007-4
                  Time: 21:12          Date:  8-20-2009

 Computer : ubuntu
```

---

1. RUN CONTROL

```
 Run name(RUN_NAME): STRIP7510T
 Brief description of the run (DESCRIPTION) :
   EXPERIMENTAL STRIPPER, GS-45, USTRIP-0.1
 Units (UNITS) : CGS
 Start-time (TIME) =   60.000
 Stop_time (TSTOP) =   70.000
 Time step (DT) =  0.10000E-03
 Max time step (DT_MAX) =   1.0000
 Min time step (DT_MIN) =  0.10000E-05
 Time step adjustment factor (DT_FAC) =  0.90000
 Type of run (RUN_TYPE) : RESTART_1
                 (Initial conditions from the restart (.RES) file)

 * Gas momentum equation-X is solved.

 * Gas momentum equation-Y is solved.

 * Gas momentum equation-Z is solved.
```

* Solids-1 momentum equation-X is solved.

* Solids-1 momentum equation-Y is solved.

* Solids-1 momentum equation-Z is solved.

* Energy equations are NOT solved.

* Gas Species equations are solved.

* Solids-1 Species equations are NOT solved.

* User-defined subroutines are NOT called.

* Schaeffer frictional model is solved

2. PHYSICAL AND NUMERICAL PARAMETERS

Coefficient of restitution (C_e) = 0.95000
Angle of internal friction (Phi) = 30.000
Angle of wall_particle friction (Phi_w) = 0.0000
Default turbulence length scale (L_scale0) = 0.0000
Maximum turbulent viscosity (MU_gmax) = 0.98765E+32
Reference pressure (P_ref) = 0.0000
Pressure scale-factor (P_scale) = 1.0000
Gravitational acceleration (GRAVITY) = 980.66
Under relaxation (UR_FAC) and Iterations in Leq solver (LEQ_IT):

	UR_FAC	LEQ_IT	LEQ_METHOD	LEQ_SWEEP	LEQ_TOL	DISCRETIZE
Fluid cont. and P_g	= 0.800	20	2	RSRS	0.1000E-03	Superbee
Solids cont. and P_s	= 0.500	20	2	RSRS	0.1000E-03	Superbee
U velocity	= 0.500	5	2	RSRS	0.1000E-03	Superbee
V velocity	= 0.500	5	2	RSRS	0.1000E-03	Superbee
W velocity	= 0.500	5	2	RSRS	0.1000E-03	Superbee
Energy	= 1.000	15	2	RSRS	0.1000E-03	Superbee
Species	= 1.000	15	2	RSRS	0.1000E-03	FOUP
Granular Energy	= 0.500	15	2	RSRS	0.1000E-03	Superbee
User scalar	= 0.800	15	2	RSRS	0.1000E-03	Superbee

DRAG SCALE FACTOR - C(1) = 0.25000

3. GEOMETRY AND DISCRETIZATION

Coordinates: CYLINDRICAL

X-direction cell sizes (DX) and East face locations:

I	1	2	3	4	5
DX	2.5000	2.5000	0.50000	0.50000	0.50000
X_E	0.0000	2.5000	3.0000	3.5000	4.0000

I	6	7	8	9	10
DX	0.50000	0.50000	0.50000	0.50000	0.50000
X_E	4.5000	5.0000	5.5000	6.0000	6.5000

I	11	12	13	14	15
DX	0.50000	0.50000	0.50000	0.50000	0.50000
X_E	7.0000	7.5000	8.0000	8.5000	9.0000

I	16	17	18	19	20
DX	0.50000	0.50000	0.50000	0.50000	0.50000
X_E	9.5000	10.000	10.500	11.000	11.500

I	21	22	23	24	25
DX	0.50000	0.50000	0.50000	0.50000	0.50000
X_E	12.000	12.500	13.000	13.500	14.000

I	26	27
DX	0.50000	0.50000
X_E	14.500	15.000

Number of cells in X, or R, direction (IMAX) = 25
Reactor length in X, or R, direction (XLENGTH) = 14.500

Y-direction cell sizes (DY) and North face locations:

J	1	2	3	4	5
DY	0.50000	0.50000	0.50000	0.50000	0.50000
Y_N	0.0000	0.50000	1.0000	1.5000	2.0000

J	6	7	8	9	10
DY	0.50000	0.50000	0.50000	0.50000	0.50000
Y_N	2.5000	3.0000	3.5000	4.0000	4.5000

J	11	12	13	14	15
DY	0.50000	0.50000	0.50000	0.50000	0.50000
Y_N	5.0000	5.5000	6.0000	6.5000	7.0000

J	16	17	18	19	20
DY	0.50000	0.50000	0.50000	0.50000	0.50000
Y_N	7.5000	8.0000	8.5000	9.0000	9.5000

J	21	22	23	24	25

```
 DY   0.50000      0.50000      0.50000      0.50000      0.50000
Y_N    10.000       10.500       11.000       11.500       12.000
```

...truncated

```
  J      571          572          573          574
 DY   0.50000      0.50000      0.50000      0.50000
Y_N    285.00       285.50       286.00       286.50
Number of cells in Y direction (JMAX) =  572
Reactor length in Y direction (YLENGTH) =  286.00


Z-direction cell sizes (DZ) and Top face locations:
  K        1
 DZ    6.2832
Z_T    0.0000
Number of cells in Z, or theta, direction (KMAX) =    1
Reactor length in Z, or theta, direction (ZLENGTH) =  6.2832
```

4. GAS PHASE

```
Viscosity (MU_g0) =  0.19800E-03  (A constant value is used everywhere)
Number of gas species (NMAX(0)) =   2
Gas species     Molecular weight (MW_g)
    1               28.800
    2               28.800
```

5. SOLIDS PHASE

```
Number of particulate phases (MMAX) =  1

M     Diameter (D_p0)      Density (RO_s) Close_Packed
1      0.98000E-02          1.5500           T

Void fraction at maximum packing (EP_star) =  0.45000
```

6. INITIAL CONDITIONS

7. BOUNDARY CONDITIONS

```
Boundary condition no :    1
  Type of boundary condition : NO_SLIP_WALL
    (Velocity is zero at wall)
                                Specified       Simulated
  X coordinate of west face   (BC_X_w) =   9.0000         9.0000
  X coordinate of east face   (BC_X_e) =   11.000         11.000
  Y coordinate of south face  (BC_Y_s) =   10.000         10.000
  Y coordinate of north face  (BC_Y_n) =   12.000         12.000
  Z coordinate of bottom face (BC_Z_b) =   0.0000        -6.2832
  Z coordinate of top face    (BC_Z_t) =   6.2832         0.0000
  I index of cell at west   (BC_I_w) =   16
  I index of cell at east   (BC_I_e) =   19
  J index of cell at south  (BC_J_s) =   22
  J index of cell at north  (BC_J_n) =   25
  K index of cell at bottom (BC_K_b) =    1
  K index of cell at top    (BC_K_t) =    1

Boundary condition no :    2
  Type of boundary condition : MASS_INFLOW
    (Inlet with specified gas and solids mass flux)
                                Specified       Simulated
  X coordinate of west face   (BC_X_w) =   9.5000         9.5000
  X coordinate of east face   (BC_X_e) =   10.500         10.500
  Y coordinate of south face  (BC_Y_s) =   12.000         11.500
  Y coordinate of north face  (BC_Y_n) =   12.000         12.000
  Z coordinate of bottom face (BC_Z_b) =   0.0000        -6.2832
  Z coordinate of top face    (BC_Z_t) =   6.2832         0.0000
  I index of cell at west   (BC_I_w) =   17
  I index of cell at east   (BC_I_e) =   18
  J index of cell at south  (BC_J_s) =   25
  J index of cell at north  (BC_J_n) =   25
  K index of cell at bottom (BC_K_b) =    1
  K index of cell at top    (BC_K_t) =    1
  Void fraction (BC_EP_g) =   1.0000
  Gas pressure (BC_P_g) =  0.11550E+07
  Gas temperature (BC_T_g) =   298.00
  Gas species     Mass fraction (BC_X_g)
       1              1.0000
       2              0.0000
  X-component of gas velocity (BC_U_g) =   0.0000
  Y-component of gas velocity (BC_V_g) =   121.00
  Z-component of gas velocity (BC_W_g) =   0.0000
  Solids phase-1 Density x Volume fr. (BC_ROP_s) =   0.0000
  Solids phase-1 temperature (BC_T_s) =   298.00
  X-component of solids phase-1 velocity (BC_U_s) =  0.0000
  Y-component of solids phase-1 velocity (BC_V_s) =  0.0000
```

```
  Z-component of solids phase-1 velocity (BC_W_s) =  0.0000

Boundary condition no :    3
  Type of boundary condition : P_OUTFLOW
    (Outlet with specified gas pressure)
                              Specified       Simulated
  X coordinate of west face   (BC_X_w) =   2.5000         2.5000
  X coordinate of east face   (BC_X_e) =   14.500         14.500
  Y coordinate of south face  (BC_Y_s) =   286.00         286.00
  Y coordinate of north face  (BC_Y_n) =   286.00         286.50
  Z coordinate of bottom face (BC_Z_b) =   0.0000        -6.2832
  Z coordinate of top face    (BC_Z_t) =   6.2832         0.0000
  I index of cell at west   (BC_I_w) =    3
  I index of cell at east   (BC_I_e) =   26
  J index of cell at south  (BC_J_s) =  574
  J index of cell at north  (BC_J_n) =  574
  K index of cell at bottom (BC_K_b) =    1
  K index of cell at top    (BC_K_t) =    1
  Gas pressure (BC_P_g) =  0.11550E+07
  Gas temperature (BC_T_g) =   298.00

Boundary condition no :    4
  Type of boundary condition : NO_SLIP_WALL
    (Velocity is zero at wall)
                              Specified       Simulated
  X coordinate of west face   (BC_X_w) =   0.0000         0.0000
  X coordinate of east face   (BC_X_e) =   2.5000         2.5000
  Y coordinate of south face  (BC_Y_s) =   0.0000         0.0000
  Y coordinate of north face  (BC_Y_n) =   286.00         286.00
  Z coordinate of bottom face (BC_Z_b) =   0.0000        -6.2832
  Z coordinate of top face    (BC_Z_t) =   6.2832         0.0000
  I index of cell at west   (BC_I_w) =    2
  I index of cell at east   (BC_I_e) =    2
  J index of cell at south  (BC_J_s) =    2
  J index of cell at north  (BC_J_n) =  573
  K index of cell at bottom (BC_K_b) =    1
  K index of cell at top    (BC_K_t) =    1

Boundary condition no :   10
  Type of boundary condition : NO_SLIP_WALL
    (Velocity is zero at wall)
                              Specified       Simulated
  X coordinate of west face   (BC_X_w) =   10.500         10.500
  X coordinate of east face   (BC_X_e) =   11.000         11.000
  Y coordinate of south face  (BC_Y_s) =   30.500         30.500
  Y coordinate of north face  (BC_Y_n) =   31.500         31.500
```

```
  Z coordinate of bottom face (BC_Z_b) =   0.0000        -6.2832
  Z coordinate of top face    (BC_Z_t) =   6.2832         0.0000
  I index of cell at west   (BC_I_w) =   19
  I index of cell at east   (BC_I_e) =   19
  J index of cell at south  (BC_J_s) =   63
  J index of cell at north  (BC_J_n) =   64
  K index of cell at bottom (BC_K_b) =    1
  K index of cell at top    (BC_K_t) =    1


... truncated


Boundary condition no :  152
  Type of boundary condition : NO_SLIP_WALL
    (Velocity is zero at wall)
                               Specified       Simulated
  X coordinate of west face   (BC_X_w) =   6.5000        6.5000
  X coordinate of east face   (BC_X_e) =   10.500        10.500
  Y coordinate of south face  (BC_Y_s) =   187.00        187.00
  Y coordinate of north face  (BC_Y_n) =   188.00        188.00
  Z coordinate of bottom face (BC_Z_b) =   0.0000        -6.2832
  Z coordinate of top face    (BC_Z_t) =   6.2832         0.0000
  I index of cell at west   (BC_I_w) =   11
  I index of cell at east   (BC_I_e) =   18
  J index of cell at south  (BC_J_s) =  376
  J index of cell at north  (BC_J_n) =  377
  K index of cell at bottom (BC_K_b) =    1
  K index of cell at top    (BC_K_t) =    1

Boundary condition no :  160
  Type of boundary condition : MASS_INFLOW
    (Inlet with specified gas and solids mass flux)
                               Specified       Simulated
  X coordinate of west face   (BC_X_w) =   7.0000        7.0000
  X coordinate of east face   (BC_X_e) =   10.000        10.000
  Y coordinate of south face  (BC_Y_s) =   187.00        187.00
  Y coordinate of north face  (BC_Y_n) =   187.00        187.50
  Z coordinate of bottom face (BC_Z_b) =   0.0000        -6.2832
  Z coordinate of top face    (BC_Z_t) =   6.2832         0.0000
  I index of cell at west   (BC_I_w) =   12
  I index of cell at east   (BC_I_e) =   17
  J index of cell at south  (BC_J_s) =  376
  J index of cell at north  (BC_J_n) =  376
  K index of cell at bottom (BC_K_b) =    1
  K index of cell at top    (BC_K_t) =    1
```

Void fraction (BC_EP_g) = 0.45000
Gas pressure (BC_P_g) = 0.11550E+07
Gas temperature (BC_T_g) = 298.00
Gas species Mass fraction (BC_X_g)
1 0.0000
2 1.0000
X-component of gas velocity (BC_U_g) = 0.0000
Y-component of gas velocity (BC_V_g) = -21.760
Z-component of gas velocity (BC_W_g) = 0.0000
Solids phase-1 Density x Volume fr. (BC_ROP_s) = 0.85250
Solids phase-1 temperature (BC_T_s) = 298.00
X-component of solids phase-1 velocity (BC_U_s) = 0.0000
Y-component of solids phase-1 velocity (BC_V_s) = -21.760
Z-component of solids phase-1 velocity (BC_W_s) = 0.0000

8. INTERNAL SURFACES

9. OUTPUT DATA FILES:

Extension	Description	Interval for writing
.OUT	This file (ASCII)	10.000
.LOG	Log file containing messages (ASCII)	
.RES	Restart file (Binary)	0.10000E-01
.SP1	EP_g (Binary, single precision)	0.10000E-02
.SP2	P_g, P_star (Binary, single precision)	0.10000
.SP3	U_g, V_g, W_g (Binary, single precision)	0.10000
.SP4	U_s, V_s, W_s (Binary, single precision)	0.10000
.SP5	ROP_s (Binary, single precision)	100.00
.SP6	T_g, T_s (Binary, single precision)	100.00
.SP7	X_g, X_s (Binary, single precision)	0.10000
.SP8	Theta_m (Binary, single precision)	100.00
.SP9	User Scalar (Binary, single precision)	100.00

9. OUTPUT DATA FILES:

Extension	Description	Interval for writing
.OUT	This file (ASCII)	0.10000E+33
.LOG	Log file containing messages (ASCII)	
.RES	Restart file (Binary)	0.10000E+33
.SP1	EP_g (Binary, single precision)	

10. TOLERANCES
The following values are specified in the file TOLERANCE.INC.

Minimum value of EP_s tracked (ZERO_EP_s) = 0.10000E-07
Maximum average residual (TOL_RESID) = 0.10000E-02
Maximum average residual (TOL_RESID_T) = 0.10000E-03
Maximum average residual (TOL_RESID_X) = 0.10000E-03
Minimum residual at divergence (TOL_DIVERGE) = 10000.
Tolerance for species and energy balances (TOL_COM) = 0.10000E-03

11. INITIAL AND BOUNDARY CONDITION FLAGS

The initial and boundary conditions specified are shown in the following map. Each computational cell is represented by a string of three characters. The first character represents the type of cell, and the last two characters give a number that identifies a boundary or initial condition. For example, .02 indicates a cell where Initial Condition No. 2 will be specified. Only the last two digits are written. Hence, for example, Condition No. 12, 112, 212 etc. will be represented only as 12.

First Character	Description
.	Initial condition
W	No slip wall
S	Free-slip wall
s	Partial-slip wall
c	Cyclic boundary
C	Cyclic boundary with pressure drop
I	Specified mass-flux inflow cell
O	Outflow cell
p	Specified pressure inflow cell
P	Specified pressure outflow cell

Internal surfaces at East, North or Top of each cell is is represented by the following letters to the right of the three-character string:

Side	Impermeable	Semipermeable
East	E	e
North	N	n
Top	T	t

For cells with internal surfaces on more than one side the characters will be over-written in the above order

BC/IC condition flags at K = 1

J I= 1 2 3 4 5 6 7 8 9 10 11 12 13 14 15 16 17 18 19 20 21 22 23 24

```
 574      S-- S-- P03  P03  P03  P03  P03  P03  P03  P03  P03  P03  P03  P03  P03  P03  P03
P03  P03  P03  P03  P03  P03  P03
 573      S-- W04  .--  .--  .--  .--  .--  .--  .--  .--  .--  .--  .--  .--  .--  .--  .--  .--  .--  .--  .--  .--  .--  .--
 572      S-- W04  .--  .--  .--  .--  .--  .--  .--  .--  .--  .--  .--  .--  .--  .--  .--  .--  .--  .--  .--  .--  .--  .--
 571      S-- W04  .--  .--  .--  .--  .--  .--  .--  .--  .--  .--  .--  .--  .--  .--  .--  .--  .--  .--  .--  .--  .--  .--
 570      S-- W04  .--  .--  .--  .--  .--  .--  .--  .--  .--  .--  .--  .--  .--  .--  .--  .--  .--  .--  .--  .--  .--  .--
 569      S-- W04  .--  .--  .--  .--  .--  .--  .--  .--  .--  .--  .--  .--  .--  .--  .--  .--  .--  .--  .--  .--  .--  .--
 568      S-- W04  .--  .--  .--  .--  .--  .--  .--  .--  .--  .--  .--  .--  .--  .--  .--  .--  .--  .--  .--  .--  .--  .--
```

... truncated

B.3 MFIX.log File

```
MFIX (2007-4    ) simulation on computer: ubuntu
 Run name: STRIP7510T          Time:  7:43               Date:  7-13-2009
 Memory required:   25.44 Mb
 ---------------------------------------------------------------------------

 ********************************************************************************

 From: CHECK_DATA_06
 Message: IC_X_s( 1, 1, 1) not specified
 ********************************************************************************


 ********************************************************************************

 From: CHECK_DATA_06
 Message: IC number: 1 - Sum of solids-1 mass fractions is NOT equal to one
 ********************************************************************************


 ********************************************************************************

 From: Get_Corner_Cells
 Warning: The following wall-cells are adjacent to two or
 more fluid-cells.  Mass, momentum, and energy transfer
 to these wall-cells have been set to zero.
    IJK     I     J     K
```

1252	3	104	1
1311	3	163	1
1370	3	222	1
1429	3	281	1
1825	4	103	1
1884	4	162	1
1943	4	221	1
2002	4	280	1
2398	5	102	1
2457	5	161	1
2516	5	220	1
2575	5	279	1
2971	6	101	1
3030	6	160	1
3089	6	219	1
3148	6	278	1
3544	7	100	1
3603	7	159	1
3662	7	218	1
3721	7	277	1
4117	8	99	1
4176	8	158	1
4235	8	217	1
4294	8	276	1
4690	9	98	1
4749	9	157	1
4808	9	216	1
4867	9	275	1
5263	10	97	1
5322	10	156	1
5381	10	215	1
5440	10	274	1
5836	11	96	1
5895	11	155	1
5954	11	214	1
6013	11	273	1
6114	11	374	1
6115	11	375	1
6117	11	377	1
6409	12	95	1
6468	12	154	1
6527	12	213	1
6586	12	272	1
6982	13	94	1
7041	13	153	1
7100	13	212	1

7159	13	271	1
7555	14	93	1
7614	14	152	1
7673	14	211	1
7732	14	270	1
8128	15	92	1
8187	15	151	1
8246	15	210	1
8305	15	269	1
8632	16	22	1
8635	16	25	1
8701	16	91	1
8760	16	150	1
8819	16	209	1
8878	16	268	1
9273	17	89	1
9274	17	90	1
9332	17	148	1
9333	17	149	1
9391	17	207	1
9392	17	208	1
9450	17	266	1
9451	17	267	1
10132	18	374	1
10133	18	375	1
10135	18	377	1
10354	19	22	1
10357	19	25	1
10395	19	63	1
10396	19	64	1
10454	19	122	1
10455	19	123	1
10513	19	181	1
10514	19	182	1
10572	19	240	1
10573	19	241	1
10631	19	299	1
10632	19	300	1
10971	20	65	1
11030	20	124	1
11089	20	183	1
11148	20	242	1
11207	20	301	1
11546	21	66	1
11605	21	125	1
11664	21	184	1

```
   11723    21   243     1
   11782    21   302     1
   12121    22    67     1
   12180    22   126     1
   12239    22   185     1
   12298    22   244     1
   12357    22   303     1
   12696    23    68     1
   12755    23   127     1
   12814    23   186     1
   12873    23   245     1
   12932    23   304     1
   13271    24    69     1
   13330    24   128     1
   13389    24   187     1
   13448    24   246     1
   13507    24   305     1
   13846    25    70     1
   13905    25   129     1
   13964    25   188     1
   14023    25   247     1
   14082    25   306     1
   14421    26    71     1
   14480    26   130     1
   14539    26   189     1
   14598    26   248     1
   14657    26   307     1

 ************************************************************************

 t=    0.0000  Wrote      SPx: 1, 2, 3, 4, 5, 6, 7, 8, 9, A, B,             Disk=   1.01 Mb
 t=    0.0000  Wrote RES; t=    0.0000 Dt=0.1000E-03 NIT= 15 Sm=90551.
CPU=      2. s
  MbError%(0,MMAX): 0.4137E-04 -.3165E-03
 t=    0.0030 Dt=0.1524E-03 NIT= 14 Sm=90551.                              CPU=     33. s
  MbError%(0,MMAX): 0.3782E-04 -.2787E-04
 t=    0.0040 Dt=0.1694E-03 NIT= 15MbErr%=0.4659E-05: Run diverged/stalled :-(
           Dt=0.15242E-03          Recovered           :-)
 t=    0.0073 Dt=0.2091E-03 NIT= 15 Sm=90551.                              CPU=     69. s
  MbError%(0,MMAX): -.1074E-03 0.3392E-03

 Average outflow rates at BC No. **  At Time =  0.10055E-01
  Gas : Mass flow =   2.1297         Volumetric flow =   1583.8
  Solids-1 : Mass flow =   2949.0         Volumetric flow =   1902.6
 t=    0.0101  Wrote      SPx: 1,                                  Disk=   1.06 Mb
```

```
 t=    0.0101  Wrote RES; t=    0.0101 Dt=0.2581E-03 NIT= 20MbErr%=0.3595E-05: Run
diverged/stalled :-(
           Dt=0.23231E-03          Recovered           :-)
 t=    0.0133 Dt=0.2868E-03 NIT= 23 Sm=90551.                              CPU=    111. s
   MbError%(0,MMAX): 0.3138E-04 0.2998E-04

 Average outflow rates at BC No. **  At Time =  0.20241E-01
   Gas : Mass flow =   2.1125         Volumetric flow =   1543.9
   Solids-1 : Mass flow =   3010.9         Volumetric flow =   1942.5
 t=    0.0202  Wrote      SPx: 1,                                  Disk=   1.12 Mb
 t=    0.0202  Wrote RES; t=    0.0205 Dt=0.2868E-03 NIT= 29 Sm=90550.
CPU=    173. s
   MbError%(0,MMAX): 0.1569E-04 0.1126E-04
 t=    0.0268 Dt=0.2323E-03 NIT= 22 Sm=90550.                              CPU=    236. s
   MbError%(0,MMAX): 0.6506E-05 -.9176E-05
 t=    0.0301  Wrote      SPx: 1,                                  Disk=   1.18 Mb
 t=    0.0301  Wrote RES;
 Average outflow rates at BC No. **  At Time =  0.30284E-01
   Gas : Mass flow =   2.1222         Volumetric flow =   1541.3
   Solids-1 : Mass flow =   3015.0         Volumetric flow =   1945.1
 t=    0.0319 Dt=0.1882E-03 NIT= 17 Sm=90550.                              CPU=    279. s
   MbError%(0,MMAX): 0.1615E-04 -.8304E-06
 t=    0.0368 Dt=0.2323E-03 NIT= 20 Sm=90550.                              CPU=    321. s
   MbError%(0,MMAX): 0.2319E-04 0.4926E-05
 t=    0.0395 Dt=0.2323E-03 NIT= 30MbErr%=0.2266E-04: Run diverged/stalled :-(
           Dt=0.20908E-03          Recovered           :-)
 t=    0.0402  Wrote      SPx: 1,                                  Disk=   1.24 Mb
 t=    0.0402  Wrote RES;
 Average outflow rates at BC No. **  At Time =  0.40381E-01
   Gas : Mass flow =   2.1345         Volumetric flow =   1541.6
   Solids-1 : Mass flow =   3014.5         Volumetric flow =   1944.8
 t=    0.0426 Dt=0.2091E-03 NIT= 22 Sm=90549.                              CPU=    388. s
   MbError%(0,MMAX): 0.2103E-04 -.5260E-06


...truncated


t=   69.9981  Wrote      SPx: 1,                                  Disk= 655.47 Mb
 t=   69.9991  Wrote      SPx: 1,                                   Disk= 655.52 Mb

 Average outflow rates at BC No. **  At Time =   70.000
   Gas : Mass flow =   2.3028         Volumetric flow =   1542.9
   Solids-1 : Mass flow =   3012.5         Volumetric flow =   1943.5
 t=   70.0001  Wrote      SPx: 1, 2, 3, 4, 5, 6, 7, 8, 9, A, B,            Disk= 656.53 Mb
 t=   70.0001  Wrote RES;
```

```
**********************************************************************

 Total CPU time used =     161411.593819000       seconds

**********************************************************************
```

Appendix C: Sample Matlab® Codes

C.1 Code Used to Determine the Time Lag Between Detection of the Injected Helium Pulse in Emulsion Gas Velocity Tests

```
%PURPOSE: Determine the time delay b/w injection and detection of a helium pulse

%INPUTS: text file containing 6 headers, followed by data. Data
%collected from 'emulsion gas velocity.vi' is: time, solenoid voltage,
%detection thermistor voltage, injection thermistor voltage.

%JASON WIENS
%February 19, 2008

clear;
clc;
format long;


%declare variables
i=1;    %counter variable
ii=1;   %logic variable
iii=1;  %logic variable
j=1;    %counter variable
k=1;    %counter variable
p=0;    %takes value of data for comparison purposes
q=0;    %takes value of data for comparison purposes


%open data file and retrieve data
[file, dir] = uigetfile('/Users/jsw240/Ue 04-2009/*.txt');
file2 = strcat(dir, file);
fid = fopen(file2, 'r');
date = fgetl(fid);
time_start = fgetl(fid);
header = fgetl(fid);
freq_c = fgetl(fid);
freq = str2num(freq_c);
xxxx = fgetl(fid);
channels = fgetl(fid);
lumped_data = fscanf(fid, '%f', [4,inf]);
lumped_data = lumped_data';
time = lumped_data(:,1);
v_solenoid = lumped_data(:,2);
v_det = lumped_data(:,3);
v_inj = lumped_data(:,4);


%%%%%%%%%%%%%%%%%%%%%%%%%%%%%%%%%%%%%%%%%%%%%%%%%%%%%%%%%%%%%%%%%%%%%%%%%%%

plot(time,v_det,'r',time,v_inj,'g');

%determine time of solenoid activation
[n, col] = size(v_solenoid);
```

```
while (i < n)      %while counter is less than number of data points

   p = v_solenoid(i,1);
   q = v_solenoid(i+1,1);

   if (q-p > 1.0)
      sol_open_t(j,1) = time(i+1,1);    %TIME solenoid opens is recorded in matrix 'sol_open'
      sol_open_n(j,1) = i+1;          %DATA element location where solenoid opens
      j=j+1;
   end

   i=i+1;
end


%reset variables
i=1;
j=1;
k=1;
p=0;
q=0;


%retrieve data before solenoid activation for statistical analysis of
%thermistor voltage signals
%CHECKED JSW :)
[n, col] = size(sol_open_n);
p = 1000;   %number of data points retrieved before injection for statistical analysis

if (sol_open_n(1,1)-p < 0)
   i=i+1;
   ii=2;
end

while (i <= n)
   q = sol_open_n(i,1) - p;

   while (j <= p)
      pre_sol_inj(j,k) = v_inj(q,1);
      pre_sol_inj_t(j,k) = time(q,1);
      j=j+1;
      q=q+1;
   end

   j=1;
   k=k+1;
   i=i+1;
end


%reset variables
i=1;
j=1;
k=1;
p=0;
q=0;
```

```
%calculate the standard deviation of the pre-solenoid activation and
%calculate the 95% confidence interval for detection of helium
[n, col] = size(pre_sol_inj)

while (i <= col)
   mean_inj(i,1) = mean(pre_sol_inj(:,i));
   linreg_inj(i,:) = polyfit(pre_sol_inj_t(:,i),pre_sol_inj(:,i),1);
   stdev_inj(i,1) = std(pre_sol_inj(:,i));
   ci95_inj(i,1) = 2*stdev_inj(i,1);
   tolerance_inj(i,1) = mean_inj(i,1) + ci95_inj(i,1);
   i=i+1;
end


%reset variables
i=1;
j=1;
k=1;
p=0;
q=0;
n=0;


%retrieve data after solenoid activation for detection of helium pulse
[n, col] = size(sol_open_n);
[nn, colcol] = size(v_inj);
p = 30000;          %number of data points AFTER injection to retrieve

if (sol_open_n(n,1)+p > nn)     %check for sufficient data on tail
   n=n-1;
   iii=2;
end


if (ii == 2)                    %check that sufficient header data was found
   i=i+1;
end


while (i <= n)
   q = sol_open_n(i,1);

   while (j <= p)
      post_sol_inj(j,k) = v_inj(q,1);
      post_sol_time_inj(j,k) = time(q,1);
      j=j+1;
      q=q+1;
   end

   j=1;
   k=k+1;
   i=i+1;
end
```

```
%reset variables
i=1;
j=1;
k=1;
p=0;
q=0;


%determine when the inj thermistor voltage is below the 95% ci for each inj
[n, col] = size(post_sol_inj);

if (ii==2)
   k=i+1;
end

while (j <= col)

   while (i <= n-4)
      p = post_sol_inj(i,j);
      w = post_sol_inj(i+1,j);
      v = post_sol_inj(i+2,j);
      y = post_sol_inj(i+3,j);
      z = post_sol_inj(i+4,j);

      if (p > tolerance_inj(j,1) && w > tolerance_inj(j,1) && v > tolerance_inj(j,1) && y > tolerance_inj(j,1) && z > tolerance_inj(j,1))
         therm_detection(j,1) = post_sol_time_inj(i,j);
         node_inj(j,1) = i;
         node_absolute_inj(j,1) = sol_open_n(k,1)+i;
         break
      end

      if (i == n-4)
         therm_detection(j,1) = -99999999;
         node_inj(j,1)=0;
         break
      end

   i=i+1;
   end

   i=1;
   j=j+1;
   k=k+1;
end


%reset variables
i=1;
j=1;
k=1;
p=0;
q=0;


%%%%%%%%%%%%%%%%%%%%%%%%%%%%%%%%%%%%%%%%%%%%%%%%%%%%%%%%%%%%%%%%%%%%%%%%%%%
```

```
%retrieve data before node where injection was found for statistical analysis of
%thermistor voltage signals
[n, col] = size(node_absolute_inj);
p = 1000;   %number of data points retrieved before injection for statistical analysis

if (node_absolute_inj(23,1)==0)
   node_absolute_inj(23,1)=1001;
end

while (i <= n)
   q = node_absolute_inj(i,1) - p;

   while (j <= p)
       pre_sol_det(j,k) = v_det(q,1);
       pre_sol_det_t(j,k) = time(q,1);
      j=j+1;
      q=q+1;
   end

   j=1;
   k=k+1;
   i=i+1;
end


%reset variables
i=1;
j=1;
k=1;
p=0;
q=0;


%calculate the standard deviation of the pre-solenoid activation and
%calculate the 95% confidence interval for detection of helium
[n, col] = size(pre_sol_det)

while (i <= col)
  mean_det(i,1) = mean(pre_sol_det(:,i));
  linreg_det(i,:) = polyfit(pre_sol_det_t(:,i),pre_sol_det(:,i),1);
  stdev_det(i,1) = std(pre_sol_det(:,i));
  ci95_det(i,1) = 2*stdev_det(i,1);
  tolerance_det(i,1) = mean_det(i,1) + ci95_det(i,1);
   i=i+1;
end


%reset variables
i=1;
j=1;
k=1;
p=0;
q=0;
n=0;
```

```
%retrieve data after injection found for detection of helium pulse
[n, col] = size(node_absolute_inj);
[nn, colcol] = size(v_inj);
p = 10000;          %number of data points AFTER injection to retrieve


while (i <= n)
   q = node_absolute_inj(i,1);

   while (j <= p)
      post_sol_det(j,k) = v_det(q,1);
      post_sol_time_det(j,k) = time(q,1);
      j=j+1;
      q=q+1;
   end

   j=1;
   k=k+1;
   i=i+1;
end


%reset variables
i=1;
j=1;
k=1;
p=0;
q=0;


%%%%%%%%%%%%%%%%%%%%%%%%%%%%%%%%%%%%%%%%%%%%%%%%%%%%%%%%%%%%%%%%%%%%%%%%%%%%%%%


%determine when the det thermistor voltage is below the 95% ci for each inj
[n, col] = size(post_sol_det);

while (j <= col)

   while (i <= n-4)
      p = post_sol_det(i,j);
      w = post_sol_det(i+1,j);
      v = post_sol_det(i+2,j);
      y = post_sol_det(i+3,j);
      z = post_sol_det(i+4,j);

      if (p > tolerance_det(j,1) && w > tolerance_det(j,1) && v > tolerance_det(j,1) && y > tolerance_det(j,1) && z >
tolerance_det(j,1))
         therm_detection(j,2) = post_sol_time_det(i,j);
         node_det(j,1) = i;
         break
      end

      if (i == n-4)
         therm_detection(j,2) = -99999999;
         node_det(j,1)=0;
         break
```

```
        end

    i=i+1;
    end

    i=1;
    j=j+1;
end


%reset variables
i=1;
j=1;
k=1;
p=0;
q=0;


%retrieve data for linear regression on post - 95%ci data
%DATA CHECKED JSW :)
[n,col] = size(node_det);
p = 1000          %number of data points to include in the linear regression

while (i <= n)
    q_inj = node_inj(i,1);
    q_det = node_det(i,1);

    while (j <= p)

        if ((q_inj || q_det)==0)
            linreg_post_inj_datav(1:p,i)=0;
            linreg_post_det_datav(1:p,i) =0;
            break
        end

        linreg_post_inj_datav(j,i) = post_sol_inj(q_inj+j,i);
        linreg_post_det_datav(j,i) = post_sol_det(q_det+j,i);
        linreg_post_inj_datat(j,i) = post_sol_time_inj(q_inj+j,i);
        linreg_post_det_datat(j,i) = post_sol_time_det(q_det+j,i);
        j=j+1;
    end

    j=1;
    i=i+1;
end


%reset variables
i=1;
j=1;
k=1;
p=0;
q=0;


%perform linear regression on post - 95%ci data
```

```
[n,col] = size(linreg_post_inj_datav);

while (i <= col)
   linreg_post_inj(i,:) = polyfit(linreg_post_inj_datat(:,i),linreg_post_inj_datav(:,i),1);
   linreg_post_det(i,:) = polyfit(linreg_post_det_datat(:,i),linreg_post_det_datav(:,i),1);
   i=i+1;
end


%reset variables
i=1;
j=1;
k=1;
p=0;
q=0;


%determine time of helium injection via linear regression method
[n,nol] = size(linreg_post_inj)

while (i <= n)
    therm_detection_regression(i,1) = (linreg_post_inj(i,2) - linreg_inj(i,2))/(linreg_inj(i,1) - linreg_post_inj(i,1));
    therm_detection_regression(i,2) = (linreg_post_det(i,2) - linreg_det(i,2))/(linreg_det(i,1) - linreg_post_det(i,1));
    therm_detection_regression(i,3) = therm_detection_regression(i,2) -   therm_detection_regression(i,1);
   i=i+1;
end


%reset variables
i=1;
j=1;
k=1;
p=0;
q=0;


%determine time lag between injection and detection using the thermistor
%voltages. These values are found in the 'therm_detection' matrix: column 1
%- INJECTION, column 2 - DETECTION, column 3 - DET-INJ (time delay)
[n, col] = size(therm_detection);

while (i <= n)
   therm_detection(i,3) = therm_detection(i,2) - therm_detection(i,1);
   i=i+1;
end

therm_detection
stdev_95ci_method = std(therm_detection(:,3))
mean_95ci_method = mean(therm_detection(:,3))
therm_detection_regression
stdev_regression_method = std(therm_detection_regression(:,3))
mean_regression_method = mean(therm_detection_regression(:,3))
avg_preinj_mean_inj = mean(mean_inj(:,1))
avg_preinj_mean_det = mean(mean_det(:,1))

%reset variables
```

```
i=1;
j=1;
k=1;
p=0;
q=0;


fclose all;
```

C.2 Code Used to Determine the Bubble Area and Circumference From MFIX Simulation Data

```
%PURPOSE: Map bubbles by defining contours - determines circumference and
%bubble area

%Uses 71 rows of cells (#s 110 - 180) - top cell starts immediately below
%the donut baffle

%INPUTS: text file from post MFIX

%JASON WIENS
%June 25, 2009      final edit: Sept 19, 2009

clear;
clc;
format short g;

y_start = 16;       %axial element defining north boundary used to determine db - cell# 42 is midpoint between disc and donut
baffle
x_start = 3;       %radial element defining west boundary used to determine db
x_max = 26;
x_lims = x_max+2;
n_pixels = 71;

%%%%%%%%%%%%%%%%%%%%%%%%%%%%%%%%%%%%%%%%%%%%%%%%%%%%%%%%%%%%%%%%%%%%%%%%%%%

%BEGIN RETRIEVE DATA - EP_g_reverse.m

%declare variables
i=1;    %counter variable
ii=1;   %logic variable
iii=1;  %logic variable
j=1;    %counter variable
k=1;    %counter variable
p=0;    %takes value of data for comparison purposes
q=0;    %takes value of data for comparison purposes
```

```
frames=10000;


%open data file and retrieve data
[file, dir] = uigetfile('/Users/jsw240/cfd models/*.*');
file2 = strcat(dir, file);
fid = fopen(file2, 'r');
blank1 = fgetl(fid);
blank2 = fgetl(fid);
Z_loc = fgetl(fid);
time = fgetl(fid);
header = fgetl(fid);


%sort data into 3d matrix(x,y,t)
x=n_pixels;
y=1;
t=1;

while (t <= frames)

   while (x>=1)
      xx=fscanf(fid, '%f',[4,27]);
      if (size(xx)==[0,0])
         break
      end

      data(x,:,t)=xx(4,:);
      x=x-1;
   end

   i=i+1;
   x=n_pixels;
   blank=fgetl(fid);
   time=fgetl(fid)
   header=fgetl(fid);
   t=t+1;

   if (size(xx)==[0,0])
      break
   end

end


%END RETRIEVE DATA

%%%%%%%%%%%%%%%%%%%%%%%%%%%%%%%%%%%%%%%%%%%%%%%%%%%%%%%%%%%%%%%%%%%%%%%%%%%%%%%


%MODIFY THE RETRIEVED DATA TO EXCLUDE GAS TRAPPED UNDER BAFFLES (Aug '09)
[f,g,h] = size(data);
i=1;
j=1;
x=1;
y=1;
```

```
i=1;
t=1;
n=0;

while (t <= h)
   data(51,3:17,t)=0;
   data(50,3:17,t)=0;
   data(49,3:17,t)=0;
   data(48,3:17,t)=0;
   data(47,3:17,t)=0;
   data(46,3:17,t)=0;
   data(45,3:17,t)=0;
   data(44,3:17,t)=0;
   data(43,3:17,t)=0;
   data(42,3:17,t)=0;
   data(41,3:17,t)=0;
   data(40,3:17,t)=0;
   data(39,3:17,t)=0;
   data(38,3:17,t)=0;
   data(37,3:17,t)=0;
   data(36,3:17,t)=0;
   data(35,3:17,t)=0;
   data(34,3:17,t)=0;
   data(33,3:17,t)=0;
   data(32,3:17,t)=0;
   data(31,3:16,t)=0;
   data(30,3:15,t)=0;
   data(29,3:14,t)=0;
   data(28,3:13,t)=0;
   data(27,3:12,t)=0;
   data(26,3:11,t)=0;
   data(25,3:10,t)=0;
   data(24,3:9,t)=0;
   data(23,3:8,t)=0;
   data(22,3:7,t)=0;
   data(21,3:6,t)=0;
   data(20,3:5,t)=0;
   data(19,3:4,t)=0;
   data(18,3,t)=0;
   t=t+1;
end

%END MODIFY DATA (Aug 7, 2009)


%%%%%%%%%%%%%%%%%%%%%%%%%%%%%%%%%%%%%%%%%%%%%%%%%%%%%%%%%%%%%%%%%%%%%%%%%%%

%BEGIN MAP BUBBLES
[f,g,h]=size(data);
i=1;
j=1;
x=1;
y=1;
i=1;
t=1;
n=0;
```

```
u=1;

while (i <= (x_max-x_start+1))
   void_t1(1,i) = 1.0;
   i=i+1;
end

i=1;

%start loop
while (t <= h)
   i=1;
   a=0;
   u=1;

   while (i <= (x_max-x_start+1))
      void(1,i) = data(y_start, x_start+i-1, t);
      voidyplus(1,i) = data(y_start-1, x_start+i-1, t);   %added Aug'09

      if (void(1,i) >= 0.8)
         a(1,u)=i;
         u=u+1;
      end

      i=i+1;
   end

   i=1;
   u=1;

   voidcheck=1;

   if (any(void >= 0.8))
      [row,col] = size(a);

      while (i <= (col))
         aa = a(1,i);
         voidcheck(1,i) = voidyplus(1,aa);
         i=i+1;
      end

   end

   i=1;


   if (any(void >= 0.8) && all(voidcheck < 0.8))    %mod && voidyplus Aug'09
      drop2(1,1)=1;
      n=n+1;

      while (any(drop2(1,:) >= 0.8))

         if (any(void_t1(1,:) >= 0.8))   %start here to make a time-lapse of bubble
            n=n-1;
         break
         end
```

```
        if (t+1 > frames)            %mod Aug 13 '09
           break
        end

        while (i <= (x_max-x_start+1))
           drop2(1,i) = data(y_start, x_start+i-1, t);
           i=i+1;
        end
        i=1;

        while (i <= (x_max-x_start+1))

           if (drop2(1,i) < 0.8)
              bubble(j,i,n) = 0;
           end

           if (drop2(1,i) >= 0.8)
              bubble(j,i,n) = 1;
           end

           if (drop2(1,i) > 1.0)
              bubble(j,i,n) = 0;
           end

           i=i+1;
        end

        i=1;
        t=t+1;
        j=j+1;

        if (j > 100000)
           break
        end

     end

     j=1;
  end

  t=t+1;
  void_t1 = void;
end

%add a row of zeros beneath the final contour     mod Aug 13 '09
i=1;
j=1;
x=1;
y=1;
i=1;
t=1;
[y,x,z]=size(bubble);

while (i <= z)
  bubble(y+1,:,z)=0;
```

```
   bubble(:,x+1,z)=0;
   i=i+1;
end


%END MAP BUBBLES

%%%%%%%%%%%%%%%%%%%%%%%%%%%%%%%%%%%%%%%%%%%%%%%%%%%%%%%%%%%%%%%%%%%%%%%%%%%%%%%

%BEGIN DETERMINE BUBBLE PROPERTIES

i=1;
j=1;
x=1;
y=1;
i=1;
t=1;

%determine bubble volume
sum1=sum(bubble);
sum2=sum(sum1);
[q,w,e]=size(sum2);

while (i <= e)
   dimension(i,1,1)=sum2(1,1,i);
   i=i+1;
end

volume = dimension*0.000025     %determines bubble area (m2), each cell area =0.000025 m (0.5cm X 0.5cm)
i=1;

%determine bubble contour
[q,w,e]=size(bubble);

while (t <= e)
      if (j==1)
         if (i==1)
            if (bubble(j,i,t)==1)
               circum(j,i,t)=1;
            else
               circum(j,i,t)=0;
            end
         i=i+1;
         end


         while (i <= w)
            if (i==w)
               if (bubble(j,i,t)==1)
                  circum(j,i,t)=1;
               else
                  circum(j,i,t)=0;
               end
               i=1;
               j=j+1;
            break
```

```
        end

        if (bubble(j,i,t)==1)
            circum(j,i,t)=1;
        else
            circum(j,i,t)=0;
        end
        i=i+1;
    end
end


while (j<q)
    if (i==1)
        if (bubble(j,i,t)==1)
            circum(j,i,t)=1;

        else
            circum(j,i,t)=0;
        end
        i=i+1;
    end


    while (i <= w)

        if (i==w)
            if (bubble(j,i,t)==1)
                circum(j,i,t)=1;
            else
                circum(j,i,t)=0;
            end
            i=1;
            j=j+1;
        break
        end
        if (bubble(j,i,t)==1)
            if (bubble(j+1,i,t)==0 | bubble(j,i+1,t)==0 | bubble(j-1,i,t)==0 | bubble(j,i-1,t)==0)
                circum(j,i,t)=1;
            else
            circum(j,i,t)=0;
            end
        end

        if (bubble(j,i,t)==0)
            circum(j,i,t)=0;
        end
            i=i+1;
    end

end


if (j==q)
    if (i==1)
        if (bubble(j,i,t)==1)
```

```
            circum(j,i,t)=1;
        else
            circum(j,i,t)=0;
        end
    i=i+1;
    end


    while (i <= w)
        if (i==w)
            if (bubble(j,i,t)==1)
                circum(j,i,t)=1;
            else
                circum(j,i,t)=0;
            end
            i=1;
            j=1;
        break
        end

        if (bubble(j,i,t)==1)
            circum(j,i,t)=1;
        else
            circum(j,i,t)=0;
        end
        i=i+1;
    end
  end

  t=t+1;
end


%end determine bubble contour

i=1;
j=1;
x=1;
y=1;
i=1;
t=1;
n=1;

while (n <= e)

  perim(n,1)=0;

  %locate first perimeter element
  while (i <= w)
    if (circum(j,i,n)==1)
      location(1,:)=[j,i];
      break
    end
    i=i+1;
  end
  i=1;
```

```
logic = 1;
pos = 1;
current_loc = [location(1,1), location(1,2)];
counter=1;


while (logic==1)

   if (pos == 1)
      if (circum(current_loc(1,1), current_loc(1,2)+1,n)==1)
         perim(n,1)=perim(n,1)+0.00500;
         current_loc = [current_loc(1,1)+0,current_loc(1,2)+1];
         pos=6;
      else
         pos=2;
      end
   end

   if (pos == 2)
      if (circum(current_loc(1,1)+1, current_loc(1,2)+1,n)==1)
         perim(n,1)=perim(n,1)+0.00707;
         current_loc = [current_loc(1,1)+1, current_loc(1,2)+1];
         pos=7;
      else
         pos=3;
      end
   end

   if (pos == 3)
      if (circum(current_loc(1,1)+1, current_loc(1,2)+0,n)==1)
         perim(n,1)=perim(n,1)+0.00500;
         current_loc = [current_loc(1,1)+1, current_loc(1,2)+0];
         pos=8;
      else
         pos=4;
      end
   end

   if (pos == 4)
      if (circum(current_loc(1,1)+1, current_loc(1,2)-1,n)==1)
         perim(n,1)=perim(n,1)+0.00707;
         current_loc = [current_loc(1,1)+1, current_loc(1,2)-1];
         pos=1;
      else
         pos=5;
      end
   end

   if (current_loc(1,1)==1)
      pos=1;
   end

   if (pos == 5)
      if (circum(current_loc(1,1)+0, current_loc(1,2)-1,n)==1)
         perim(n,1)=perim(n,1)+0.00500;
         current_loc = [current_loc(1,1)+0, current_loc(1,2)-1];
```

```
            pos=2;
        else
            pos=6;
        end
    end

    if (pos == 6)
        if (circum(current_loc(1,1)-1, current_loc(1,2)-1,n)==1)
            perim(n,1)=perim(n,1)+0.00707;
            current_loc = [current_loc(1,1)-1, current_loc(1,2)-1];
            pos=3;
        else
            pos=7;
        end
    end

    if (pos == 7)
        if (circum(current_loc(1,1)-1, current_loc(1,2)+0,n)==1)
            perim(n,1)=perim(n,1)+0.00500;
            current_loc = [current_loc(1,1)-1, current_loc(1,2)+0];
            pos=4;
        else
            pos=8;
        end
    end

    if (pos == 8)
        if (circum(current_loc(1,1)-1, current_loc(1,2)+1,n)==1)
            perim(n,1)=perim(n,1)+0.00707;
            current_loc = [current_loc(1,1)-1, current_loc(1,2)+1];
            pos=5;
        else
            pos=1;
        end
    end

    logic = any(location ~= current_loc);

    counter=counter+1;

    if (counter > 500)
        break
    end
  end
  n=n+1;
  counter=1;
end


fclose all;
```

C.3 Code Used to Determine the Bubbling Frequency and Pierced Chord Length from MFIX Simulation Data

```
%PURPOSE: determine bubbling frequency and pierced chord length

%INPUTS: text file from post MFIX

%JASON WIENS
%June 17, 2009

clear;
clc;
format short g;

i_west = 3;
i_east = 26;
j_north1 = 30;        %upper meas. plane
j_south1 = 31;          %lower meas. plane
j_north2 = 23;
j_south2 = 24;
j_north3 = 16;
j_south3 = 18;
j_north4 = 9;
j_south4 = 11;
j_north5 = 2;
j_south5 = 3;

frames = 10000;     %nuber of data frames to analyze (100 frames/ s)


%declare variables
i=1;    %counter variable
ii=1;   %logic variable
iii=1;  %logic variable
j=1;    %counter variable
k=1;    %counter variable
p=0;    %takes value of data for comparison purposes
q=0;    %takes value of data for comparison purposes


%open data file and retrieve data
[file, dir] = uigetfile('/Users/jsw240/cfd models/*.*');
file2 = strcat(dir, file);
fid = fopen(file2, 'r');
blank1 = fgetl(fid);
blank2 = fgetl(fid);
Z_loc = fgetl(fid);
time = fgetl(fid);
header = fgetl(fid);


%sort data into 3d matrix(x,y,t)
x=71;
y=1;
```

```
t=1;
while (t <= frames)
   rel_time(t,1)=0+(t-1)*0.001;
   while (x>=1)
      xx=fscanf(fid, '%f',[4,27]);
      if (size(xx)==[0,0])
         break
      end
      data(x,:,t)=xx(4,:);
      x=x-1;
   end
   i=i+1;
   x=71;
   blank=fgetl(fid);
   time=fgetl(fid)
   header=fgetl(fid);
   t=t+1;
   if (size(xx)==[0,0])
      break
   end
end


%%%%%%%%%%%%%%%%%%%%%%%%%%%%%%%%%%%%%%%%%%%%%%%%%%%%%%%%%%%%%%%%%%%%%%%%%%%%%%%

%START PIERCED LENGTH MEASUREMENT

n=0;
t=1;
i=1;
p=1;

%bubble pierced length at upper plane (j_north1)
while (i <= (i_east - 16 + 1))

   while (t <= frames)

      if (data(j_north1, 16+i-1, t) >= 0.8)
         n=n+1;
         p=1;
         bubble_pierce_upper1(n,16-2+i-1,1)=0;
         while (data(j_north1, 16+i-1, t) >= 0.8)

            if (p==1)                              %Mod. July 13/2009
               if (data(j_north1-1, 16+i-1, t) >= 0.8)  %Test to see if the 'bubble' is from the tray above
                  n=n-1;
                  t=t+1;
                  break
               end
            end

            if (p==1)
               bubble_time_upper1(n,16-2+i-1,1) = rel_time(t,1);
            end
            p=p+1;
```

```
            bubble_pierce_upper1(n,16-2+i-1,1) = bubble_pierce_upper1(n,16-2+i-1,1)+1;
            t=t+1;

            if (t > frames)
               bubble_pierce_upper1(n,16-2+i-1,1) = 999;
               break
            end

         end
      else
         t=t+1;
      end

   end
   t=1;
   i=i+1;
   n=0;

end

[row,col] = size(bubble_pierce_upper1);
if (col < 24)
   bubble_pierce_upper1(1,24)=0;
end

n=0;
i=1;
t=1;
p=1;


%bubble pierced length at upper plane (j_north2)
while (i <= (i_east - 9 + 1))

   while (t <= frames)

      if (data(j_north2, 9+i-1, t) >= 0.8)
         n=n+1;
         p=1;
         bubble_pierce_upper2(n,9-2+i-1,1)=0;
         while (data(j_north2, 9+i-1, t) >= 0.8)

            if (p==1)                              %Mod. July 13/2009
               if (data(j_north2-1, 9+i-1, t) >= 0.8)  %Test to see if the 'bubble' is from the tray above
                  n=n-1;
                  t=t+1;
                  break
               end
            end

            if (p==1)
               bubble_time_upper2(n,9-2+i-1,1) = rel_time(t,1);
            end
            p=p+1;

            bubble_pierce_upper2(n,9-2+i-1,1) = bubble_pierce_upper2(n,9-2+i-1,1)+1;
```

```
            t=t+1;

            if (t > frames)
               bubble_pierce_upper2(n,9-2+i-1,1) = 999;
               break
            end

         end
      else
         t=t+1;
      end

   end
   t=1;
   i=i+1;
   n=0;

end

[row,col] = size(bubble_pierce_upper2);
if (col < 24)
   bubble_pierce_upper2(1,24)=0;
end

n=0;
i=1;
t=1;
p=1;


%bubble pierced length at upper plane (j_north3)
while (i <= (i_east - i_west + 1))

   while (t <= frames)

      if (data(j_north3, i_west+i-1, t) >= 0.8)
         n=n+1;
         p=1;
         bubble_pierce_upper3(n,i,1)=0;
         while (data(j_north3, i_west+i-1, t) >= 0.8)

            if (p==1)                                %Mod. July 13/2009
               if (data(j_north3-1, i_west+i-1, t) >= 0.8)  %Test to see if the 'bubble' is from the tray above
                  n=n-1;
                  t=t+1;
                  break
               end
            end

            if (p==1)
               bubble_time_upper3(n,i,1) = rel_time(t,1);
            end
            p=p+1;

            bubble_pierce_upper3(n,i,1) = bubble_pierce_upper3(n,i,1)+1;
            t=t+1;
```

```
            if (t > frames)
               bubble_pierce_upper3(n,i,1) = 999;
               break
            end

         end
      else
         t=t+1;
      end

   end
   t=1;
   i=i+1;
   n=0;

end

[row,col] = size(bubble_pierce_upper3);
if (col < 24)
   bubble_pierce_upper3(1,24)=0;
end

n=0;
i=1;
t=1;
p=1;


%bubble pierced length at upper plane (j_north4)
while (i <= (i_east - i_west + 1))

   while (t <= frames)

      if (data(j_north4, i_west+i-1, t) >= 0.8)
         n=n+1;
         p=1;
         bubble_pierce_upper4(n,i,1)=0;
         while (data(j_north4, i_west+i-1, t) >= 0.8)

            if (p==1)                              %Mod. July 13/2009
               if (data(j_north4-1, i_west+i-1, t) >= 0.8)  %Test to see if the 'bubble' is from the tray above
                  n=n-1;
                  t=t+1;
                  break
               end
            end

            if (p==1)
               bubble_time_upper4(n,i,1) = rel_time(t,1);
            end
            p=p+1;

            bubble_pierce_upper4(n,i,1) = bubble_pierce_upper4(n,i,1)+1;
            t=t+1;
```

```
            if (t > frames)
               bubble_pierce_upper4(n,i,1) = 999;
               break
            end

         end
      else
         t=t+1;
      end

   end
   t=1;
   i=i+1;
   n=0;

end

[row,col] = size(bubble_pierce_upper4);
if (col < 24)
   bubble_pierce_upper4(1,24)=0;
end

n=0;
i=1;
t=1;
p=1;


%bubble pierced length at upper plane (j_north5)
while (i <= (i_east - i_west + 1))

   while (t <= frames)

      if (data(j_north5, i_west+i-1, t) >= 0.8)
         n=n+1;
         p=1;
         bubble_pierce_upper5(n,i,1)=0;
         while (data(j_north5, i_west+i-1, t) >= 0.8)

            if (p==1)                              %Mod. July 13/2009
               if (data(j_north5-1, i_west+i-1, t) >= 0.8)  %Test to see if the 'bubble' is from the tray above
                  n=n-1;
                  t=t+1;
                  break
               end
            end

            if (p==1)
               bubble_time_upper5(n,i,1) = rel_time(t,1);
            end
            p=p+1;

            bubble_pierce_upper5(n,i,1) = bubble_pierce_upper5(n,i,1)+1;
            t=t+1;
```

```
            if (t > frames)
               bubble_pierce_upper5(n,i,1) = 999;
               break
            end

         end
      else
         t=t+1;
      end

   end
   t=1;
   i=i+1;
   n=0;

end

[row,col] = size(bubble_pierce_upper5);
if (col < 24)
   bubble_pierce_upper5(1,24)=0;
end

n=0;
i=1;
t=1;
p=1;


%bubble pierced length at lower plane (j_south1)
while (i <= (i_east - 17 + 1))

   while (t <= frames)

      if (data(j_south1, 17+i-1, t) >= 0.8)
         n=n+1;
         p=1;
         bubble_pierce_lower1(n,17-2+i-1,1)=0;
         while (data(j_south1, 17+i-1, t) >= 0.8)

            if (p==1)                              %Mod. July 13/2009
               if (data (j_south1-1, 17+i-1, t) >= 0.8)  %Test to see if 'bubble' is from tray above
                  n=n-1;
                  t=t+1;
                  break
               end
            end

            if (p==1)
               bubble_time_lower1(n,17-2+i-1,1) = rel_time(t,1);
            end
            p=p+1;

            bubble_pierce_lower1(n,17-2+i-1,1) = bubble_pierce_lower1(n,17-2+i-1,1)+1;
            t=t+1;
```

```
            if (t > frames)
               bubble_pierce_lower1(n,17-2+i-1,1) = 999;
               break
            end

         end
      else
         t=t+1;
      end

   end
   t=1;
   i=i+1;
   n=0;

end

[row,col] = size(bubble_pierce_lower1);
if (col < 24)
   bubble_pierce_lower1(1,24)=0;
end


i=1;
n=1;
p=1;
j=1;
t=1;


%bubble pierced length at lower plane (j_south2)
while (i <= (i_east - 10 + 1))

   while (t < frames)

      if (data(j_south2, 10+i-1, t) >= 0.8)
         n=n+1;
         p=1;
         bubble_pierce_lower2(n,10-2+i-1,1)=0;
         while (data(j_south2, 10+i-1, t) >= 0.8)

            if (p==1)                              %Mod. July 13/2009
               if (data (j_south2-1, 10+i-1, t) >= 0.8)  %Test to see if 'bubble' is from tray above
                  n=n-1;
                  t=t+1;
                  break
               end
            end

            if (p==1)
               bubble_time_lower2(n,10-2+i-1,1) = rel_time(t,1);
            end
            p=p+1;

            bubble_pierce_lower2(n,10-2+i-1,1) = bubble_pierce_lower2(n,10-2+i-1,1)+1;
```

```
            t=t+1;


            if (t > frames)
               bubble_pierce_lower2(n,10-2+i-1,1) = 999;
               break
            end

         end
      else
         t=t+1;
      end

   end
   t=1;
   i=i+1;
   n=0;

end

[row,col] = size(bubble_pierce_lower2);
if (col < 24)
   bubble_pierce_lower2(1,24)=0;
end

i=1;
n=1;
p=1;
j=1;
t=1;


%bubble pierced length at lower plane (j_south3)
while (i <= (i_east - i_west + 1))

   while (t <= frames)

      if (data(j_south3, i_west+i-1, t) >= 0.8)
         n=n+1;
         p=1;
         bubble_pierce_lower3(n,i,1)=0;
         while (data(j_south3, i_west+i-1, t) >= 0.8)

            if (p==1)                              %Mod. July 13/2009
               if (data (j_south3-1, i_west+i-1, t) >= 0.8)  %Test to see if 'bubble' is from tray above
                  n=n-1;
                  t=t+1;
                  break
               end
            end

            if (p==1)
               bubble_time_lower3(n,i,1) = rel_time(t,1);
            end
            p=p+1;
```

```
            bubble_pierce_lower3(n,i,1) = bubble_pierce_lower3(n,i,1)+1;
            t=t+1;


            if (t > frames)
               bubble_pierce_lower3(n,i,1) = 999;
               break
            end

         end
      else
         t=t+1;
      end

   end
   t=1;
   i=i+1;
   n=0;

end

[row,col] = size(bubble_pierce_lower3);
if (col < 24)
   bubble_pierce_lower3(1,24)=0;
end

i=1;
n=1;
p=1;
j=1;
t=1;


%bubble pierced length at lower plane (j_south4)
while (i <= (i_east - i_west + 1))

   while (t <= frames)

      if (data(j_south4, i_west+i-1, t) >= 0.8)
         n=n+1;
         p=1;
         bubble_pierce_lower4(n,i,1)=0;
         while (data(j_south4, i_west+i-1, t) >= 0.8)

            if (p==1)                              %Mod. July 13/2009
               if (data (j_south4-1, i_west+i-1, t) >= 0.8)  %Test to see if 'bubble' is from tray above
                  n=n-1;
                  t=t+1;
                  break
               end
            end

            if (p==1)
               bubble_time_lower4(n,i,1) = rel_time(t,1);
            end
            p=p+1;
```

```
            bubble_pierce_lower4(n,i,1) = bubble_pierce_lower4(n,i,1)+1;
            t=t+1;


            if (t > frames)
               bubble_pierce_lower4(n,i,1) = 999;
               break
            end

         end
      else
         t=t+1;
      end

   end
   t=1;
   i=i+1;
   n=0;

end

[row,col] = size(bubble_pierce_lower4);
if (col < 24)
   bubble_pierce_lower4(1,24)=0;
end

i=1;
n=1;
p=1;
j=1;
t=1;


%bubble pierced length at lower plane (j_south5)
while (i <= (i_east - i_west + 1))

   while (t <= frames)

      if (data(j_south5, i_west+i-1, t) >= 0.8)
         n=n+1;
         p=1;
         bubble_pierce_lower5(n,i,1)=0;
         while (data(j_south5, i_west+i-1, t) >= 0.8)

            if (p==1)                              %Mod. July 13/2009
               if (data (j_south5-1, i_west+i-1, t) >= 0.8)  %Test to see if 'bubble' is from tray above
                  n=n-1;
                  t=t+1;
                  break
               end
            end

            if (p==1)
               bubble_time_lower5(n,i,1) = rel_time(t,1);
            end
```

```
            p=p+1;

            bubble_pierce_lower5(n,i,1) = bubble_pierce_lower5(n,i,1)+1;
            t=t+1;


            if (t > frames)
               bubble_pierce_lower5(n,i,1) = 999;
               break
            end

         end
      else
         t=t+1;
      end

   end
   t=1;
   i=i+1;
   n=0;

end

[row,col] = size(bubble_pierce_lower5);
if (col < 24)
   bubble_pierce_lower5(1,24)=0;
end

i=1;
n=1;
p=1;
j=1;
t=1;



%determine bubble frequency at i

[m,mm] = size(bubble_pierce_upper1);

while (j <= m)

   while (i <= mm)
      if (bubble_pierce_upper1(j,i) > 0)
         bubble_pass_upper1(j,i) = 1;
      else
         bubble_pass_upper1(j,i) = 0;
      end
      i=i+1;
   end
   j=j+1;
   i=1;
end

i=1;
j=1;
```

```
[m,mm] = size(bubble_pierce_upper2);

while (j <= m)

   while (i <= mm)
      if (bubble_pierce_upper2(j,i) > 0)
         bubble_pass_upper2(j,i) = 1;
      else
         bubble_pass_upper2(j,i) = 0;
      end
      i=i+1;
   end
   j=j+1;
   i=1;
end

i=1;
j=1;

[m,mm] = size(bubble_pierce_upper3);

while (j <= m)

   while (i <= mm)
      if (bubble_pierce_upper3(j,i) > 0)
         bubble_pass_upper3(j,i) = 1;
      else
         bubble_pass_upper3(j,i) = 0;
      end
      i=i+1;
   end
   j=j+1;
   i=1;
end

i=1;
j=1;

[m,mm] = size(bubble_pierce_upper4);

while (j <= m)

   while (i <= mm)
      if (bubble_pierce_upper4(j,i) > 0)
         bubble_pass_upper4(j,i) = 1;
      else
         bubble_pass_upper4(j,i) = 0;
      end
      i=i+1;
   end
   j=j+1;
   i=1;
end
```

```
i=1;
j=1;

[m,mm] = size(bubble_pierce_upper5);

while (j <= m)

   while (i <= mm)
      if (bubble_pierce_upper5(j,i) > 0)
         bubble_pass_upper5(j,i) = 1;
      else
         bubble_pass_upper5(j,i) = 0;
      end
      i=i+1;
   end
   j=j+1;
   i=1;
end

i=1;
j=1;


n_bubbles_upper1 = sum(bubble_pass_upper1);
n_bubbles_upper2 = sum(bubble_pass_upper2);
n_bubbles_upper3 = sum(bubble_pass_upper3);
n_bubbles_upper4 = sum(bubble_pass_upper4);
n_bubbles_upper5 = sum(bubble_pass_upper5);

[q,qq] = size(rel_time);
tot_time = rel_time(q,1);

while (i <= mm)
   freq_upper1(1,i) = n_bubbles_upper1(1,i)/tot_time;
   freq_upper2(1,i) = n_bubbles_upper2(1,i)/tot_time;
   freq_upper3(1,i) = n_bubbles_upper3(1,i)/tot_time;
   freq_upper4(1,i) = n_bubbles_upper4(1,i)/tot_time;
   freq_upper5(1,i) = n_bubbles_upper5(1,i)/tot_time;
   i=i+1;
end

i=1;
j=1;


fclose all;
```